THE APPLIED COMPUTATIONAL ELECTROMAGNETICS SOCIETY
JOURNAL AND NEWSLETTER

Vol.3 No.2 Fall 1988

EDITORS

THE APPLIED COMPUTATIONAL ELECTROMAGNETICS SOCIETY
JOURNAL AND NEWSLETTER

Vol. 3 No.2 Fall 1988

* FROM THE EDITOR 7

* PRESIDENT'S CORNER 8

* *THE NEWSLETTER*

* ACES NEWS 9

* CORRESPONDENCE 9

* ACES SOFTWARE LIBRARY 10

* SOFTWARE EXCHANGE COMMITTEE by C.H. Vandament 11

* LONG RANGE PLANNING COMMITTEE by R.Dawson Coblin 13

* ACES SOFTWARE-PERFORMANCE STANDARDS COMMITTEE by E.K. Miller 14

* PANDORA'S BOX by R. Dawson Coblin 17

* EM MODELING NOTES by Gerald Burke 18

* *THE JOURNAL*

"A Dual Normal Mode Representation for Electromagnetic Scattering: Some Initial Considerations" by T.H. Lehman 28

"Comparison of Methods for Far Zone Scattering from a Flat Plate and Cube" by R.J. Marhefka and T.J. Brinkley 57

"On the Comparison of Numerical Methods" by Ch. Hafner 79

"Implementation of GEMACS 3.3 on Personal Computers" by Adel F. Armanious and Peter S. Excell 83

"Numerical Electromagnetics Computation Using the Inmos T800 Transputer on an Olivetti M24 Personal Computer" by J.J. Le Roux and J.H. Cloete 88

"Obtaining Scattering Solutions for Perturbed Geometrics and Materials from Moment Method Solutions" by Elizabeth Yip and Brian Tomas 95

"The Effects of Heavy Charged Particle Irradiation of MOSFET Devices" by William Eichinger, Patrick O'Reilly and Christopher Lehner 119

"HF Ground Constant Measurements at the Lawrence Livermore National Laboratory (LLNL) Field Site" by George H.Hagn 131

"Numerical Integration of Marcuse's Power Loss Formula" by James P. Coughlin, Albert Krall and Robert H. Baran 166

* INSTITUTIONAL MEMBERS 197

APPLIED COMPUTATIONAL ELECTROMAGNETICS SOCIETY

OFFICERS AND COMMITTEE CHAIRMEN

OFFICERS:

James C. Logan
President (1990)
NOSC, Code 822
271 Catalina Blvd.
San Diego, CA 92152
Office: (619) 553-3780

Stan Kubina
Vice President (1990)
Concordia University
7141 Sherbrooke St WEST
Montreal, Quebec
CANADA H4B 1R6
Office: (514) 848-3093

Richard W. Adler
Secretary (1990)
Naval Postgraduate School
Code 62AB
Monterey, CA 93943
Office: (408) 646-2352

James K. Breakall
Treasurer (1990)
Naval Postgraduate School
Code 62BK
Monterey, CA 93943
Office: (408) 646-2383

MEMBERS AT LARGE:

Robert Bevensee
Lawrence Livermore National Lab, L-156
PO Box 5504,
Livermore, CA 94550
Term: 3 years (expires 1989)
Office: (415) 422-6787

Lee Corrington
COMMANDER
USAISE C/ASB SET-P
Ft. Huachuca, AZ 85613-5300
Term: 3 years (expires 1990)
Office: (602) 538-7682

Pete Cunningham
COMMANDER
USACECOM AMSEL-RD-C3-TA-1
Ft. Monmouth, NJ 07703
Term: 3 years (expires 1991)
Office: (201) 544-5415

APPLIED COMPUTATIONAL ELECTROMAGNETICS SOCIETY
OFFICERS AND COMMITTEE CHAIRMEN

PAST PRESIDENT:

Edmund K. Miller
General Research Corporation
5383 Hollister Ave.
Santa Barbara, CA 93111
Office: (805) 964-7724

PUBLICATIONS COMMITTEE:

David E. Stein
Transactions Editor
LTV Aircraft Products Group
P.O. Box 530685
Grand Prairie, TX 75073-0685
Office: (214) 266-4309

Michael Thorburn
Advertising Editor
Electrical & Computer Engineering Dept
Oregon State University
Corvallis, OR 97331-3202
Office: (503) 754-3617

MEETINGS COMMITTEE:

Bob Noel, Chairman
Rockwell International
3370 Miraloma Ave
Mail Stop OA13
Anaheim, CA 92803
Office: (714) 779-3073

COMMITTEE ON LONG RANGE PLANNING:
(Technical Activities Committee)

R. Dawson Coblin, Chairman
Lockheed
Missiles & Space Co. Inc.
O/62-42 B/o76
111 Lockheed Way
Sunnyvale, CA 94089-3504
Office: (408) 742-2689

APPLIED COMPUTATIONAL ELECTROMAGNETICS SOCIETY
OFFICERS AND COMMITTEE CHAIRMEN

CONSTITUTION AND BYLAWS COMMITTEE:

Janet McDonald, Chairman
COMMANDER
USAISEC/ASB-SET-P
Ft. Huachuca, AZ 85613-5300

Office: (602) 538-7639

SOFTWARE EXCHANGE COMMITTEE:

(Previously established under E. Miller)

C.H. Vandament, Chairman
Rockwell International
802 Brentwood
RIchardson, TX 75080

Office: (214) 705-3952

SOFTWARE PERFORMANCE STANDARDS COMMITTEE:
(Established by ADCOM 3-24-88)

Ed Miller, Chairman
General Research Corporation
5383 Hollister Ave.
Santa Barbara, CA 93111

Office: (805) 964-7724

NOMINATING COMMITTEE:
(For replacement of one Member at Large, to be elected at next general meeting.)

Robert Bevensee
Lawrence Livermore National Lab. L-156
P.O. Box 5504
Livermore, CA 94550

Office: (415) 422-6787

APPLIED COMPUTATIONAL ELECTROMAGNETICS SOCIETY

OFFICERS AND COMMITTEE CHAIRMEN

AWARDS COMMITTEE:

Lee Corrington, Chairman
COMMANDER
USAISE C/ASB SET-P
Ft. Huachuca, AZ 85613-5300

Office: (602) 538-7682

1989 SYMPOSIUM PROGRAM COMMITTEE:

Michael Thorburn, Chairman
Electrical and Computer Engineering Dept.
Oregon State University
Corvallis, OR 97331-3202

Office: (503) 754-3617

FROM THE EDITOR

The papers in this issue continue our tradition of featuring the latest computational electromagnetics techniques, applications, and insights. Meanwhile, the response to our forthcoming special issue on Electromagnetics Computer Code Validation, scheduled for publication in January 1989, has been far greater than expected. Equally impressive has been the interest shown in a second special issue for early 1990. To date, ten candidate topics have been proposed. We are still accepting recommendations for topics and for special guest editors. Selection will proceed in the near future.,

The recent upsurge of interest in such ACES activities is a consequence of two developments, one of which is a general increase of interest in computational electromagnetics. However, this interest is not unique among ACES members but instead is shared by other publications and symposia. Furthermore, the interest level has thus far been sufficient to support several publications and symposia, including our own. Even so, our success has been possible only because of the second development -- your increased support of ACES, a one-of-a-kind, interdisciplinary professional society devoted entirely to computational electromagnetics, particularly from a "user" standpoint.

Lest we be viewed as merely one of several publications and/or symposia, we must realize our full potential as a professional society. This is possible only if certain critical ACES committees (above and beyond those responsible for our publication and our annual symposium) are active. It is the activities of these other committees, more than anything else, which makes ACES unique. For this reason, the renewed efforts of various committees are most encouraging.

At the same time, the ACES Journal and Newsletter will continue striving to be the best possible publication that we can be. Indeed, it is largely because of the authors who have published with us -- and those to follow -- that we can even speak in terms of excellence. We shall also seek new ways to complement the efforts of those other publications with similar interests, in manners which enable us to maintain our existing niche and scope.

As we complete our third year, we face new opportunities. The number of papers submitted and accepted for publication may soon be sufficient to support a quarterly publication schedule. This would shorten the "lead time" for publication. Authors could disseminate their findings more rapidly, and ACES members could "hear from ACES" more often -- all for the price of a modest dues increase. Other tentative projects include the publication of peer-reviewed software (as is already done by a physics publication), the inclusion of the ACES Journal and Newsletter in literature-search data bases, and the publication of code user group news (which requires that we identify various code user groups). Meanwhile, there remains unfinished business. The ACES Modeling Short Note, which would have additional value in compiling a user-experience data base, has not yet received much support, nor has "Pandora's Box". We still seek to publish other regular feature columns dealing with modeling guidelines, particular codes, input/output issues, and relevant hardware issues. Finally, in keeping with an initial purpose of ACES, we would like to publish more codes, algorithms, and solved problems which would make it unnecessary for others to "re-invent the wheel".

Most of these things will eventually come to pass, either in ACES or elsewhere. The choice rests with us.

David E. Stein
Editor-in-Chief

PRESIDENT'S CORNER

James C. Logan

Here it is December already and we are publishing our second Journal and Newsletter for 1988. Soon to be on the street is the special issue of our Journal on Software Validation. Our Software Exchange Committee and Software Performance Standards Committee are very active. Planning and preparation for the 1989 ACES Symposium is also well under way. There is a lot of activity going on due to the efforts of many volunteers serving on ACES committees.

I wish to especially mention the efforts of the Meetings Committee. They are trying to line up symposium sites for future ACES for the next three to five years. The intent is to alternate between the East and West Coasts, so that the ACES Symposium may be more accessible to more members. Suggestions should be directed to Bob Noel. Volunteers to serve on the Program Committee for future Symposium should also contact Bob Noel.

The ranks of ACES membership is growing in leaps and bounds. As ACES grows, we are experiencing some growing pains. This may be especially true for the newer committees. At the 1988 ACES Symposium and again in the last newsletter, we issued an appeal for volunteers to serve on various committees. I wish to renew the invitation to get involved and make your contribution to your Society. Please do so by directly contacting the Chairman of the committee of your choice. If you previously offered to help and for some reason you have not heard from the Committee Chairman recently, please drop a line or make a phone call. Get involved. It's good for you and for ACES too.

I extend my best wishes to all fellow ACES members for a happy Holiday season. I hope to see all of you in Monterey in March 1989.

ACES NEWS

1. Membership has now reached the "magic mark" of 500! Our Journal/Newsletter printing volume is at a level where we can begin to benefit from offset printing. This will help up to keep our subscription/membership rates low.

2. NEEDS 2.0 is nearing release. We have updates completed for IGUANA 5.4, GRAPS 2.0, ANTMAT 2.0 and MININEC 3.12. NEC2-PC has been successfully compiled under Microsoft FORTRAN 4.01 and equals or exceeds 32-bit PC versions of NEC3 in terms of accuracy for problems that push the capability of the code" to the limit, such as a 299-segment half-wave dipole. Additional user features are now being added and tested. Release is expected in February.

3. In the 1988 CONFERENCE PROCEEDINGS we goofed and printed a 1987 paper by George Hagn. His '88 paper is being included in this J/NL and a copy will be sent to all who attended the '88 CONFERENCE or who purchased the PROCEEDINGS. Our apologies to George. (BLUSH!).

4. The SPRING '88 J/NL (Vol 3, No.1) contained a paper by Art Ludwig (pp.46-54), but it did not appear in the Table of Contents. Please pencil it into your copy.

5. The 5th Annual Review, 21-23 March 1989, features a day of Short Courses on Monday, 20th. The PC Demo room is much larger than at previous conferences and will easily accommodate upwards of 75 people.

CORRESPONDENCE

Robert M. Bevensee
Lawrence Livermore National Lab

Corrections to Electromagnetic Theory, by J. A. Stratton, McGraw Hill, 1941.

Page 346. The integrand of $I_0(x) = J_0(ix)$ should be $\cosh(x \cos \lambda)$, not $\cos(x \cos \lambda)$.

Page 411. The right side of Eq. (69), $j_n(kR)P_n^m(\cos\theta)$ for $m \geq 0$, should be multiplied by

$$(-)^{m/2}, \ m \text{ even} \qquad i = \sqrt{-1}$$
$$+i(-)^{(m-1)/2}, \ m \text{ odd}$$

Page 413. In Eq. (84) for $P^m_{n+m}(0)$, the factor (n+2m-1)! should be multiplied by $(-)^{n/2}$ (n even). This can be verified by Tables of Functions, by E. Jahnke and F. Emde, fourth edition, Dover Publications, 1945, p 110, $P_n^m(x=0)$.

Page 465. In the right side of Eq. (16) the term $i\omega\mu$ (n x H) should be $i\omega\mu$ (n x H)ϕ.

Page 469. In the right side of Eq. (31) the first integrand, $\phi\, E_1 \cdot dS$ should be $\nabla\phi(E_1 \cdot dS)$.

Page 571. In Eq. (35) for $j_n(\rho)$ the denominator factor (2n+1) should be (2n+2); the $h_n^{(1)}(\rho)$- formula should have the factor -i instead of i. I believe that the a_n^r- expression of Eq. (39) should contain the term $2(\mu_1-\mu_2)$ instead of $\mu_1-\mu_2$ on the right side. And b_1^r of Eq. (40) should contain the additional term

$$+\frac{1}{10}\frac{N^2(N^2-1)(N^2+4)}{(N^2+2)^2}\rho^5$$

within the parentheses.

ACES SOFTWARE LIBRARY

CURRENT INDEX OF ITEMS IN LIBRARY:

Item#	Description	Computer
002	MININEC2F frequency sweep	IBM-PC
003	ENHANCED MININEC2 double ARRAY size to 20 wires, etc.	IBM-PC
004	ENHANCED MININEC2	IBM-PC
005	THIN WIRE MININEC2	IBM-PC
006	NEC2	DEC VAX
007	NEC3	DEC VAX
008	NEEDS 1.0 MININEC3, NEC-PC, IGUANA, GRAPS	IBM-PC/XT or AT
009	MININEC3/GRAPS	IBM-PC/XT or AT
011	NAC-3 ver. 1.3 Updated version (see this issue)	IBM-PC/AT or XT
012	SIGDEMO	IBM-PC
013	Misc BASIC programs RF Designers Toolbox	IBM-PC
014	AT-ESP	IBM-PC/XT or AT
015	VMAP 2-D vector field plot	IBM-PC
016	DRESP,DRESV2 Dielectric resonators, field distribution plots	IBM-PC
017	NEC-AM AM Broadcast array design	IBM-PC/XT or AT
018	RF65FT v2.0 RF power density for FM/TV via FCC OST BULL.65	IBM-PC/XT or AT

SOFTWARE EXCHANGE COMMITTEE REPORT

Charles M. Vandament

A letter was sent to all members of the committee, first thanking them for their interest and then asking for their help in compiling a comprehensive catalog of software descriptions of all programs related to the very general field of electromagnetics. Eight members have agreed to contribute; most of them have been telephoned and have started writing or at least started organizing their thoughts to start writing. The major programs are now covered by at least one experienced user of the code; to wit, NEC-MOM, NEC-BSC, GEMACS, and MININEC/NEEDS/IGUANA. We are also including some descriptions of more specialized codes, such as those relating to the analysis of electromagnetics in particle accelerator design.

One purpose of this catalog is to list concisely the information needed, steps to be followed, and people to contact in order to procure the various codes. Each code's capabilities and limitations are to be described, but we especially desire knowledgeable comparisons between various codes which can accomplish the same purpose. Handy ancillary codes are also to be included for such mundane things as transmission line analysis, preprocessors and postprocessors for the major codes, etc. Our target date for a first draft is January 10, 1989.

If anyone has a desire to contribute to the catalog, or to assist the contributers, they should contact the appropriate person listed below.

Chuck Vandament - Catalog Manager
Mainframe NEC-MOM

Jim Akers - Personal Computer NEC-MOM

Bob Balestri - GEMACS (Lightning, EMP)

Richard Cooper - Accelerator Codes

Ron Marhefka, et. al. - NEC-BSC

Bob Noel - GEMACS (Antennas, EMI)

Michael Thorburn - Microwave Circuit Design EM programs.

A complete listing of the committee members is listed below:

C.H. (Chuck) Vandament, CHMN
Rockwell International
802 Brentwood Ln.
Richardson, TX 75080
214-231-1907

Richard K. Cooper
MS H829
Los Alamos National Laboratory
Los Alamos, NM 87545
505-667-2839

Thomas K Pollock
505 Camino del Mar
Del Mar, CA 92014-3005
619-259-6886

William J Ball
Carl J. Jones Corp
SAIC
7901 Yarnwood CT.
Springfield, VA 22153
703-569-7704

Deb Shortess
Science and Engineering Assoc.
701 Dexter Avenue N., Suite 400
Seattle, WA 98109
206-285-8686

Jim Akers
Drawer EE
Mississippi State University
Mississippi State, MS 39762
601-325-3669

Bob Balestri
Booz, Allen and Hamilton
4330 East-West Highway
Bethesda, MD 20814
301-951-2547

Ronald J. Marhefka
ElectroScience Laboratory
1320 Kinnear Rd
Columbus, OH 43212
614-292-5752

Robert A. Noel
Rockwell International
3370 Miraloma Ave.
MS OA13
Anaheim, CA 92803
714-779-3073

Janet McDonald
COMMANDER
USAISEC/ASB-SET-P
Ft. Huachuca, AZ 85613-5300
602-538-7680

Alex Woo
NASA Ames Research Center MS 227-2
Moffett Field, CA 94035
415-694-6010

Paul N. Demmie
Division 9141
Sandia National Laboratories
Albuquerque, NM 87185
505-844-5554

Ted Roach
Microcube Corporation
P.O. Box 488
Leesburg, VA 22075
703-777-7157

Jim Hatfield
4226 6th Avenue NW
Seattle, WA 98107
206-783-9151

Ruediger Anders
Vorder Halden 11
D-7777 Salem 1
W. Germany
Int+49 (7553) 7349

Jim Logan
NOSC Code 822
271 Catalina Blvd.
San Diego, CA 92152
619-553-3780

Michael Thorburn
ECE Dept.
Oregon State University
Corvallis, OR 97331-3202
503-754-3617

Melvin W. Dill
9 Hartford St.
Bedford, MA 01730
617-455-3609

LONG RANGE PLANNING COMMITTEE REPORT

R. Dawson Coblin

The Long Range Planning Committee was formed after the 1988 ACES meeting. Dawson Coblin was appointed chairman of this committee. The purpose of the committee is to identify long range objectives for ACES and present them to the ADCOM. Specific tasks are:

1. Update and publish Five-year Goals and Plans;
2. Update and publish One-year Goals and Plans;
3. Identify other overlapping and complimentary interests with other organizations;
4. Identify and promote new and developing technical areas.

The first on-going activity is to find volunteers for the committee. Interest survey results were acquired from Dave Stein and Dick Adler. Coblin is sending out a mailing to 35 interested people to solicit committee volunteers. Once active members are identified, the tasks listed above will be addressed for 1988/89.

ACES SOFTWARE-PERFORMANCE STANDARDS COMMITTEE PLANS FOR 1989 MEETING

Introductory Comments

The primary focus of the new ACES Committee is that of validation as elaborated on further below. As an organization however, ACES has other interests in software, among them being acquisition and distribution, I/O technology, and hardware options. The Software Performance Standards Committee that was approved at our 1988 meeting in Monterey has been tasked specifically with validation. You might be interested to know that at the June 1988 Antennas and Propagation Society AdCom meeting at Syracuse, the Electromagnetic Modeling Software Modeling Committee was approved and I was designated as chairman, going beyond the performance-validation function which I had proposed. The AP-S Committee is tasked to look at the same kinds of issues as are of concern to ACES, and it is my intention to develop some appropriate collaboration. The purpose of this report is to give you my present thoughts on how the ACES Committee might work and on arranging a specific function for our 1989 meeting. Because ACES has a parallel interest in the kinds of issues to be considered by the AP-S Committee, I include some discussion of activities other than validation since where we have no identified committee or working group, we may want to form one.

Software Performance Validation

It would be agreed I think, that the most important single attribute of model performance is that of accuracy, for which some validation "protocol" is necessary. The value of a given code is first of all directly determined by the numerical accuracy and physical relevancy of the results it produces. Fancy user interfaces and graphical displays are irrelevant when the model produces misleading or wrong results. On the other hand, a model that satisfies all accuracy requirements but which requires so much computer time and/or storage that its routine use is inhibited, may be similarly devalued. That is why the most meaningful comparison of alternate models for solving the same problem is probably from the viewpoint of comparing the solution accuracy provided as a function of the associated computer cost, which is why this category includes both performance and validation.

If we are in agreement that validation is a key attribute of modeling, then we must develop systematic and consistent ways of quantifying what we mean by validation. I won't attempt doing that in this brief discussion, but do expect that our new committee will need to do some hard and thoughtful work on this topic. The outcome would be, I hope, an "experimental protocol" for guiding how models are validated, by comparison with other models, by using experimental measurements, or by analytical requirements.

Among the other issues this process should raise are identification and development of "benchmark" problems and solutions which could provide physically meaningful tests of any applicable model. Most important I think, is that model performance and validation be done from an applications viewpoint, since it is the end user who most needs help in model selection and application. That's not to say that this area is not of interest to model developers also, as any deficiencies identified by a validation exercise should help guide future needs and research. However, the end user has different interests, revolving not around selection of basis and testing functions, iteration versus inversion of model matrices,etc. but rather: for what problems can the model be used, at what cost, and to provide what accuracy?

An additional component of model performance and validation would be to develop a library of solved problems. I have used the term "user-experience data base" in the past to describe this library. The goal would be to collect information helpful to others in modeling the same or similar kinds of problems with respect both to what was found to work as well as what difficulties were encountered. By including negative as well as positive results, this data base would be much more useful than would be the case were it to contain only successes. If the problems could be organized into various categories and into some logical progression of increasing complexity in each, the collection would eventually become a "modeling handbook" which could give guidance to the experienced and novice modeler alike. Results presented in the modeling handbook could be "keyed" to the codes included in the catalog described below. It should be observed that handbook results as well as those for benchmark solutions should be available in hard copy as well as in electronic form.

Software Acquisition and Distribution

For the same reason that an accurate but computationally unaffordable model may be largely of only

academic value, an otherwise useful model that is unknown beyond its developer(s) or unavailable for whatever reason, is of similarly limited value. As a minimum first step, there is needed a computer-code catalog in which modeling software can be described in some consistent, uniform fashion. This would then provide prospective users with the the information necessary for making informed comparisons and code selections, as well as directions on how to acquire software of interest.

The catalog might have software of the following three (at least) types:

Public domain--available to anyone for at most a nominal charge;

Limited distribution--available to contractors and others approved by the sponsor, usually the US government;

Vendor--available for purchase or lease from the developer/marketer.

While these various types of codes might naturally be distributed in different ways, it would be desirable for those in the public domain to be made available via electronic mail. Possibly *netlib* at Argonne National Laboratory (see December 1987 PCs for AP) would provide a way to do this, but other outlets might also be developed.

Input/Output Options

Probably the most labor-intensive part of modeling, especially as problems become electrically larger and geometrically more complex, is that of model description (input) and results presentation (output). The efficiency of both input and output can be immeasurably increased by use of computer graphics, interactive digitizers, automatic mesh generators, etc. Decisions by users about which code is most appropriate for a given application will increasingly be driven by the user interface provided by the various alternatives available. As a matter of fact, the overall efficiency of the modeling process has an often-overlooked component whose cost can greatly exceed that of the computer resources themselves, this being of course the cost of the human resources incurred in exercising the model.

This activity would deal with the general problem of workstation environments designed for running EM computer models. It would involve collecting information about software available for this purpose in any of the three categories mentioned above. In addition, we could expect to consider the problem of validating the input data needed for model description and whether some standards for model description would be appropriate. Another area of concern would be graphics packages for displaying not only the input, but especially the output as the amount of EM data produced for a given problem can greatly exceed that needed to describe the problem itself. We need to explore unconventional ways of presenting model-related data and results for improving our interpretation and understanding of what is being computed.

Computer Hardware

As the bottleneck imposed by raw component speed is approaching, it is becoming apparent that alternate architectures will be needed to continue the past exponential growth of computer throughput into the future. Parallel and array processing offers some hope that the number of unknowns solvable per unit clock time will continue to increase at least as fast as it has over the past 30 years if not more so. At the same time, PCs, workstations, and minicomputers have greatly increased the scope of problems that can be solved outside the mainframe environment. These are topics of general interest to users and developers alike and therefore appropriate as well as another ACES activity.

Particular areas of interest in this activity would include the various parallel architectures that are becoming available and whether they might be better suited for one kind of model/formulation than another. These designs include those like the Hypercube, the Connection Machine, and possibly even neural nets as well as array processors and special parallel/parallelable microprocessors like the INMOS Transputer. If it happens that such designs are significantly better suited for one kind of model than another, this could be significant in determining where the greatest modeling improvements will be realized.

A PROPOSAL FOR YOUR CONSIDERATION

We learned in the special session on software validation at the AP-S Meeting in Syracuse, that both the Acoustical Society and the eddy-current community have already initiated some activities to develop benchmark solutions and intercompare models and codes. This seems like an appropriate kind of thing for the EM modeling community to undertake. One possibility would be to develop a list of test problems for

which solutions would be solicited and presented at a special session in Monterey in 1989. It would be necessary to specify parameters to be used, observables to be computed, and how the results are to be presented to ensure that convenient comparison could be made.

As a specific example, suppose that we consider the modeling of wire objects. Among the list of geometries that could be considered are the linear dipole and circular loop, collinear and coplanar arrays, conical spirals, and other more complex shapes, possibly including wire-mesh models of surfaces. Results could be obtained for excitation as antennas or scatterers over some size-to-wavelength range in a free-space as well as a half-space environment. Scattering and radiation patterns, near fields, and current and charge distributions (including input impedance for the antenna) could be the observables chosen for comparison. How this might be done and what is intended to be demonstrated are aspects of the "experimental protocol" to which I referred above.

Similar sets of problems could be developed for 2D and 3D surface and volumetric problems involving perfect conductors, and dielectric and lossy objects. In any case, the emphasis should not be on how the answer is obtained, but on quantitatively determining how well it compares with other model results, exhibits analytically required behavior, or agrees with physical reality. If you think that this would be a worthwhile exercise, and if you would be willing to participate, please let me know.

In order to help structure the many responses that will be forthcoming (I am an optimist), I request your input be provided via completing either, or both, of the sections below and mailing to the address above.

SOFTWARE VALIDATION COMMITTEE--Request for Input

NAME _____
ORGANIZATION _____
ADDRESS _____
_____
_____

TELEPHONE _____

I suggest that that the following problem(s) would be appropriate for use in developing a set of test/benchmark results for model validation--

PROBLEM GEOMETRY (e.g, a straight wire of specified length-to-diameter ratio; provide the information needed to define the geometry):

_____
_____

ELECTROMAGNETIC PROPERTIES (e.g., length-to-wavelength range of straight wire, impedance value(s) and location(s) if discretely loaded, impedance/unit length if distributed loading, etc.):

_____
_____

EXCITATION (e.g., if straight wire as scatterer, angles of incidence, or if straight wire as antenna, source location):

_____
_____

OBSERVABLES TO BE USED (e.g., current and charge distributions, near fields, far fields, integrated far-field power, etc., in order of their importance as a validating test relevant to a particular application):

_____
_____

I would_____ would not_____ (please check one) like to present results for one or more test problems (to be determined based in part on input received) at a special function at the 1989 meeting.

Please return to: E. K. Miller, General Research Corporation, 5383 Hollister Avenue, Santa Barbara, CA 93111, Telephone (805) 964-7724.

PANDORA'S BOX

Dawson Coblin

According to Greek mythology, Pandora opened her box only long enough for evil to escape and roam the world. By closing it, she trapped hope in the box. So man is doomed to live in an evil world without hope. In their less sanguine moments, code users feel the same way; lost, abandoned and despairing. It is intended that in this column Pandora's box can be opened again and hope allowed to excape.

The purpose of this column is to concentrate on unsuccessful applications of commonly used codes. The goal will be to determine areas where the application may have forced the code to break down and to make suggestions for improving the results. The success of this approach depends on the responsiveness of the ACES members to share their less successful attempts and quandaries.

The membership is therefore solicited to send their problem cases to me for review. Please include the name of the code used (and version, if applicable), the specifics of the test case, examples of the output, a list of the problems and contradictions observed, and your name, address, and telephone number. Please respond to the following address:

R.Dawson Coblin
O/62-42 B/o76
Lockheed Missiles & Space Co.
111 Lockheed Way
Sunnyvale, CA 94089-3504

MODELING NOTES

The Primary purpose of ACES and the Journal/Newsletter is to foster information exchange among workers involved in developing and applying computer codes to model electromagnetic problems.

This section features short articles about particular aspects of the more popular codes and short notes which summarize user experience with specific codes. To facilitate the submission of short notes in a standard form which can be easily referenced later, we include the ACES MODELING SHORT-NOTES form for 1-3 page submittals.

Readers are encouraged to report their code experiences in these ACES MODELING SHORT-NOTE forms and send them to the ACES Secretary, whose address is listed in the FRONTISPIECE. Camera-ready SHORT-NOTE forms are preferred.

EM Modeling Notes*

Gerald Burke
Lawrence Livermore National Laboratory
Livermore, CA 94550

Work on NEC has continued in an effort to improve the accuracy in modeling wires with discontinuous radii and tightly coupled junctions, an effort sponsored by the U. S. Army, Ft. Huachuca, ISEC. Developments, including modifications in the evaluation of the kernel of the integral equation and a new condition on charge in the basis functions, were sumarized in the last Newsletter. The results appear encouraging. While there will still be lots of ways to get wrong results from NEC, this should correct some particularly troublesome problems. The code with these and other enhancements should eventually be released as NEC–4. An update of progress is given below.

As usual, there are a couple of errors to report in existing codes, although these should not effect too many NEC users. The bad news is at the end of this column.

Junction Model Update

The problems with the present NEC model for a stepped-radius wire can be seen by comparing the solution for charge with that from an accurate solution of a surface model. Glisson and Wilton in [1] present results from a careful numerical solution for a straight wire with a step in radius. They solved a surface integral equation for the body of revolution with high sampling density at the step in radius and with no *a priori* conditions on the charge density. Their results show that the charge density is singular at the outer edge of a step in radius and goes to zero at the inner edge in a way similar to the edge conditions at on infinite wedge.

Similar, although probably less accurate, results can be obtained from NEC by modeling the stepped-radius wire as a cage of thin wires. Such a model is shown in Fig. 1 where twelve wires were used to model a monopole with the radius reduced by a factor of two. The monopole in Fig. 1 is viewed at one degree from end on, but is actually very thin relative to its length. As shown by A. Ludwig in [2], the error in modeling a thick wire as a cage of n thin wires is least when the radius of the thin wires is approximately equal to the radius of the thick wire divided by n. Since the radius of the monopole changes in this case, and we did not want to change the radius of the individual wires, an average radius of $(a_1 + a_2)/24$ was used. In order to resolve the behavior of charge at the step

* Work performed under the auspices of the U. S. Department of Energy by the Lawrence Livermore National Laboratory under Contract W-7405-Eng-48.

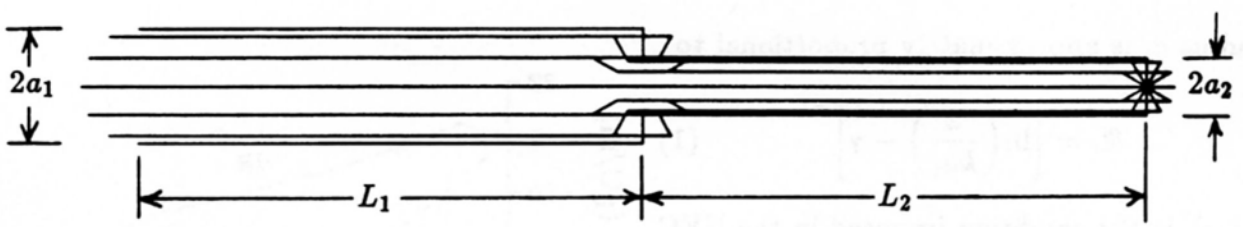

Fig. 1. A twelve-wire cage model of a monopole with stepped radius. The monopole is fed against a ground plane at its thick end. Dimensions are $a_1 = 0.00025\lambda$, $a_2 = 0.000125\lambda$ and $L_1 = L_2 = 0.125\lambda$.

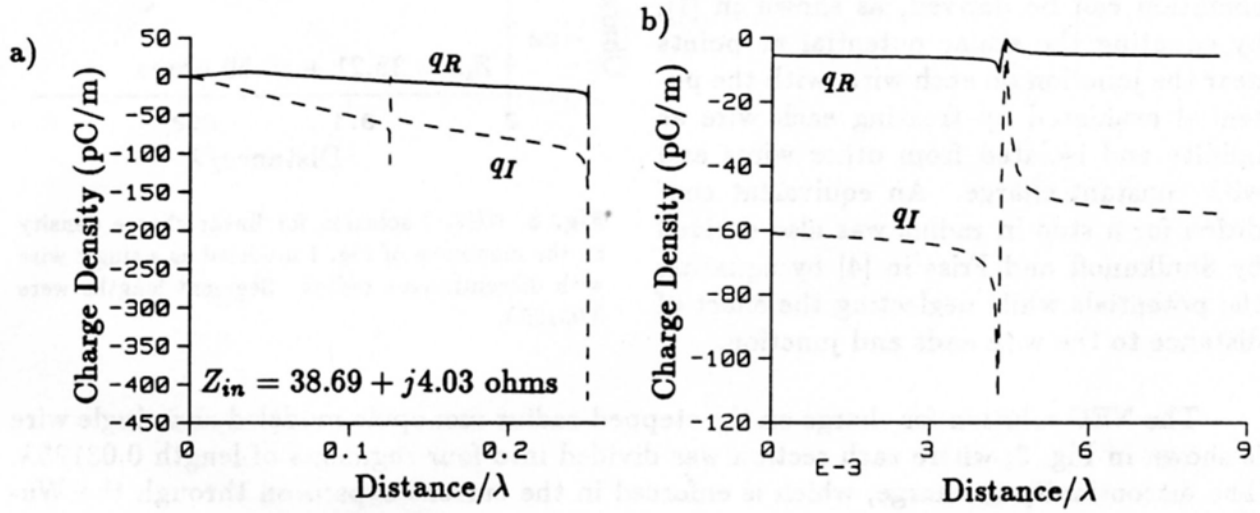

Fig. 2. Charge distribution determined by NEC for the twelve-wire model of the stepped-radius monopole; a) total charge density on the monopole, b) detail of charge density at the step in radius.

in radius and at the wire end, the short radial wires at these points were modeled with two segments each. The axial segments were tapered to have lengths equal to those of the radial segments at their connections.

The solution for charge density on the monopole is shown in Fig. 2, where a continuous curve has been plotted from the derivative of the NEC current expansion. The charge is seen to have a sharp peak at the outer corners of the step in radius and the end of the monopole and to go to zero at the inner corner of the step. Glisson and Wilton show in [1], with a more finely resolved solution at the step in radius, that the surface charge density is singular at the outer edge as $|s - s_2|^{-1/3}$ and goes to zero at the inner edge as $|s - s_1|$ where s represents distance along the wire surface and s_1 and s_2 are the values at the inner and outer corners of the step, respectively. This behavior, which matches the behavior of charge on an infinite wedge, holds over a distance of about one wire radius from the step. Over a considerably larger region the charge no longer conforms to the singularity for an infinite wedge, but is strongly affected by the proximity of the step.

At still larger distances from the step the charge has a slower, nearly sinusoidal variation characteristic of a continuous wire. Glisson and Wilton show in [1] that if this sinusoidal variation of charge is extrapolated to the junction the value on the wire with

radius a_i is approximately proportional to

$$\Psi_i = \left[\ln\left(\frac{2}{ka_i}\right) - \gamma\right]^{-1} \qquad (1)$$

which is the condition imposed in the NEC basis functions. This condition was derived by Wu and King in [3] by analysis of a wire with continuously tapered radius. The same condition can be derived, as shown in [1], by equating the scalar potential at points near the junction on each wire, with the potential evaluated by treating each wire as infinite and isolated from other wires and with constant charge. An equivalent condition for a step in radius was also derived by Shulkunoff and Friss in [4] by equating the potentials while neglecting the effect of distance to the wire ends and junction.

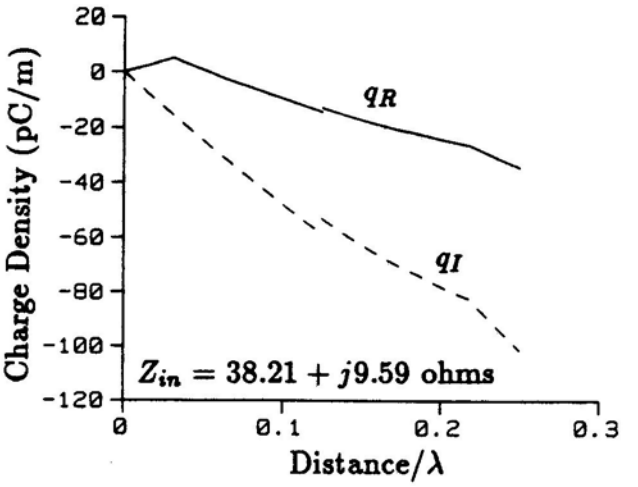

Fig. 3. NEC–3 solution for linear charge density on the monopole of Fig. 1 modeled as a single wire with discontinuous radius. Segment lengths were 0.03125λ.

The NEC solution for charge on the stepped-radius monopole modeled as a single wire is shown in Fig. 3, where each section was divided into four segments of length 0.03125λ. The discontinuity in charge, which is enforced in the current expansion through the Wu-King condition, is evident in this plot, but the edge singularities could not be resolved due to the segment length. The change in slope of the charge curve on the last segment can be considered to represent the end singularity spread over the segment length. This behavior is typical of moment-method solutions in which the edge singularity is not resolved. Examination of the near electric field along the wire would show a large error in the boundary condition near the end but little error in a power integral since the current is small at the end. Good results for the overall current distribution can generally be obtained from such solutions.

The segment length at the step in radius was then reduced to 0.0005λ by putting twenty segments on each section and tapering the lengths for shorter segments at the junction. Two problems are evident in the solution for charge shown in Fig. 4. Excluding the segments adjacent to the junction, the charge has become nearly continuous, while the discontinuity of the Wu-King condition is enforced at the junction where it is inappropriate. Similar results are obtained when NEC's extended thin-wire kernel is used.

The convergence of the NEC–3 solution to continuous charge at a step in radius appears to be the most serious failure of the model and points to a problem in the implementation of the thin-wire approximation. The moment-method solution should converge to the correct result despite the choice of basis functions, but it does not. With large segments, as for the results in Fig. 3, the Wu-King condition in the current expansion is able to force an appropriate discontinuity in the charge distribution. The input impedance obtained from this model, shown on Fig. 3, is in reasonable agreement with the impedance

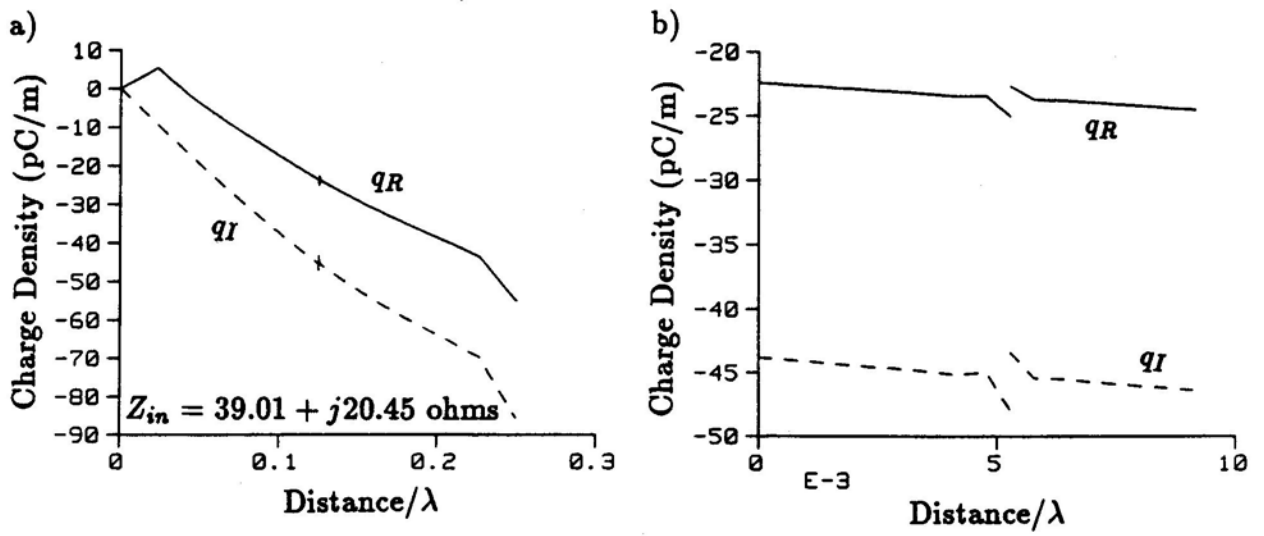

Fig. 4. NEC–3 solution for linear charge density on the monopole of Fig. 1 modeled as a single wire with discontinuous radius; a) Charge density along the monopole, b) detail at the step in radius. Segment lengths were tapered with lengths of 0.0005λ adjacent to the step.

from the twelve-wire cage model of Fig. 2. As the segment length is reduced the charge becomes nearly continuous, and the impedance, as in Fig. 4, is closer to that for a wire with continuous radius of either a_1 or a_2.

To correct these problems, a new thin-wire kernel evaluation was developed with the current treated as a tubular distribution on the wire surface and the boundary condition enforced on the axis. This convention, when all openings in the wire surface are closed by end caps, can represent an exact model in the sense of the extended boundary condition developed by P. C. Waterman [5]. Waterman noted that, due to the analytic continuability of the solution of the integral equation, forcing the field to vanish over any region within a closed surface is sufficient to make it vanish everywhere within the surface. The electric field then must also vanish on the outside of the surface. Waterman develops this approach to avoid singularities of the operator at internal resonances of the structure. For the thin wire, it is a convenient way to avoid problems with the singularity of the integral equation kernel.

While wire ends and the annular surface at a change in radius should be closed with caps, it is interesting to examine the result of simply locating the current on the surface and match points on the axis. With this change, the solution for charge on the stepped-radius monopole is shown in Fig. 5. It is seen that the smoothly varying charge on opposite sides of the junction now differs by approximately the ratio predicted by the Wu-King condition. Closer to the junction there is some suggestion of the correct behavior of charge at the inner and outer corners of the step, while at the junction the charge is discontinuous by the ratio set in the current expansion. Locating the current on the surface in NEC–3 would not work, since the point charges at the displaced ends of the current tube would introduce errors. However, the present code is built on NECVLF [6] in which the fields of these point charges have been dropped.

Wire ends were then closed with caps, using a simple approximation that would be

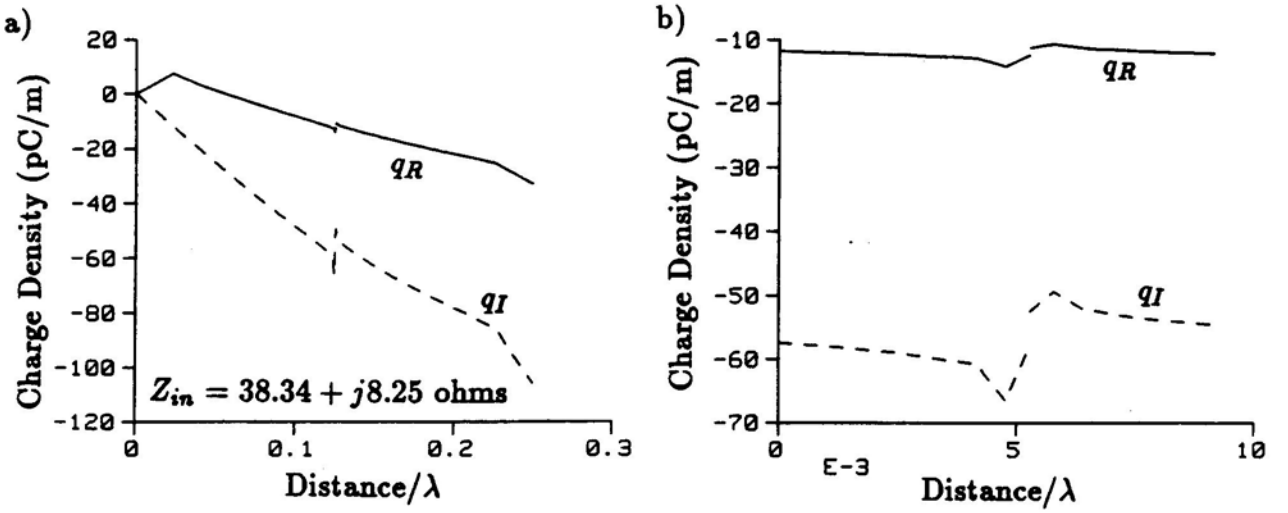

Fig. 5. Solution for linear charge density on the stepped-radius monopole as in Fig. 4 but with current on the surface and match points on the axis; a) Charge density along the monopole, b) detail at the step in radius. Segment lengths were tapered with lengths of 0.0005λ adjacent to the step.

practical for large complex models. Flat end caps were assumed with constant charge density to maintain continuity of current and charge density with the wire. Thus the actual singularity of charge density was neglected, the objective being the minimum complexity that would do the job. The field of the charge on the end caps is included in the moment-method impedance matrix. Caps were also included on voltage sources to prevent the source field from exciting the inside of the wire. The charge on the source caps is determined by the capacitance of the gap and the source voltage. Since the voltage is a known value, the field due to the charge on the source caps is added to excitation vector on the right-hand side of the matrix equation. As expected the end caps have a significant effect on the solution only when segment lengths are on the order of the wire radius or less.

The effect of including end caps on wire ends and voltage sources is shown in Figs. 6 and 7 for a quarter wave monopole with a wire radius of 0.01λ. The monopole was divided into 80 segments so that the ratio of segment length to radius was 0.3125. Since the radius is constant, the thin-wire kernel (TWK) in NEC–3 is equivalent to putting the current on the surface and the match points on the axis. The invalid condition of zero field on the axis of an open cylinder results in non-physical oscillations of the current. These oscillations become apparent for segment lengths shorter than about two times the radius. The extended thin-wire kernel (ETWK) represents a physically valid condition, with the current and match points on the surface of the cylinder. However, the field is evaluated with only the first two terms of a series expansion in radius. Hence oscillations in the current are greatly reduced but are still present. Similarly, with the new code NEC-4X the oscillations are reduced at the end and eliminated at the voltage source. That the oscillations are not completely eliminated at the end is probably the result of the approximation of a constant charge density on the end cap, neglecting the actual singular behavior of charge at the edge.

To completely close the wire surface, the field due to charge on the annular surface at a change in radius should also be included in the solution. Work on this is underway,

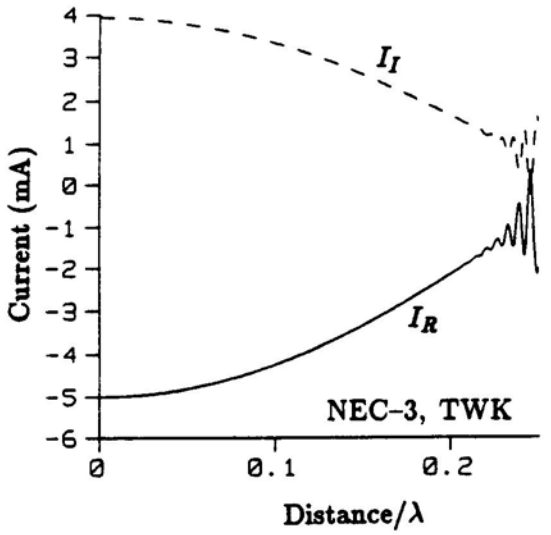

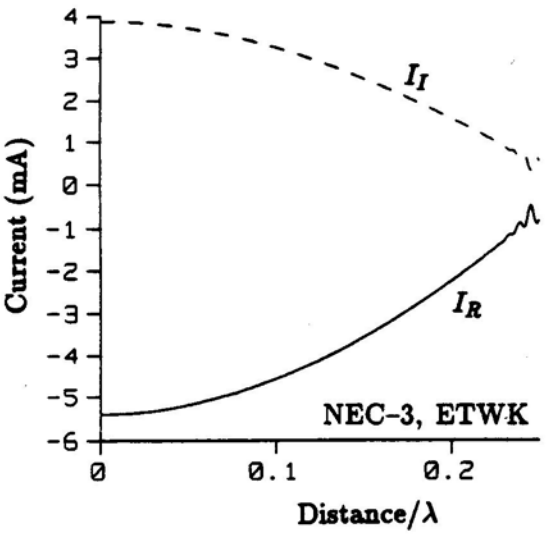

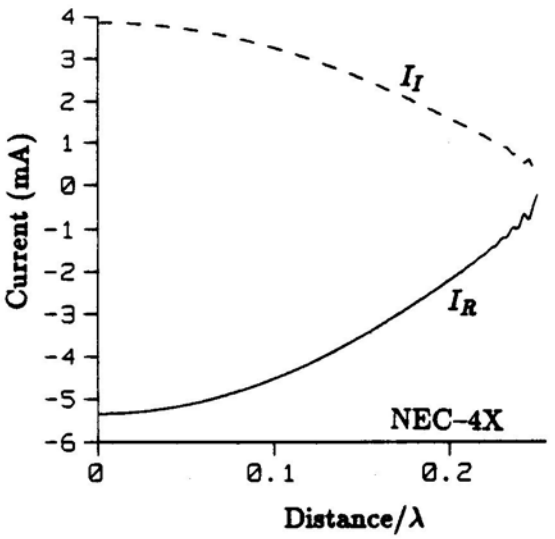

Fig. 6. Current on a $\lambda/4$ monopole excited by an incident plane wave with 2 V/m. The monopole had a radius of 0.01λ and was modeled with 80 segments.

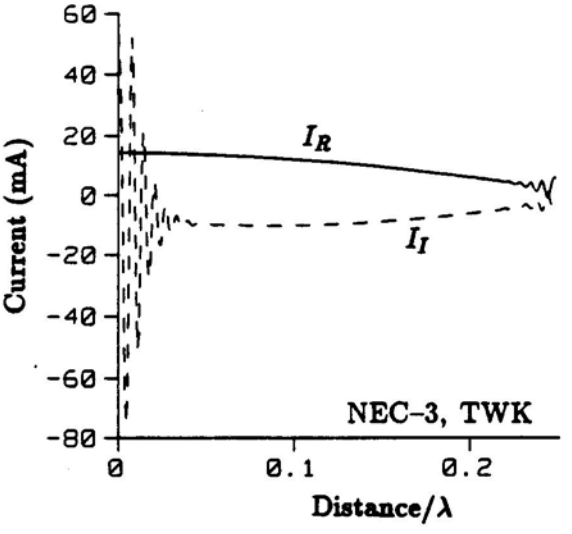

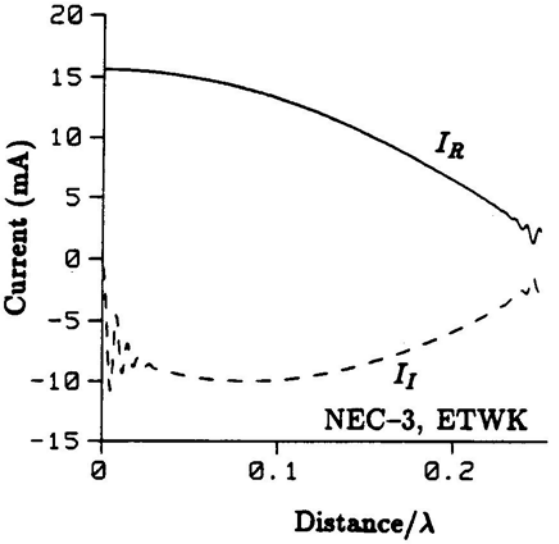

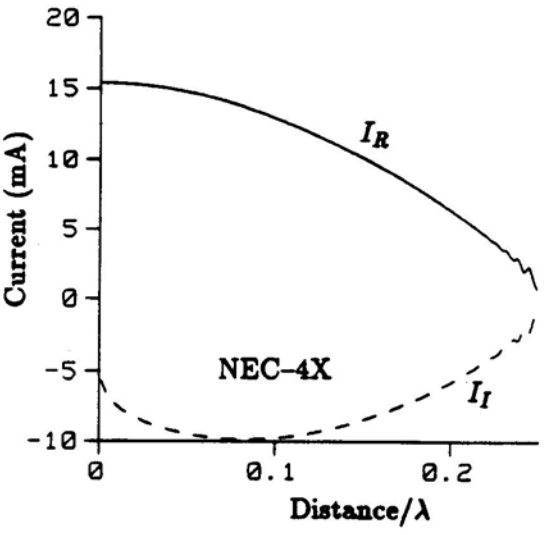

Fig. 7. Current on a $\lambda/4$ monopole excited by a 1 V source at its base. The monopole had a radius of 0.01λ and was modeled with 80 segments.

and initial results show a cleaner behavior of the charge near the step in radius when the segment lengths are short.

While the solution now appears to converge to the right result, the convergence would be very slow without a better condition than that of Eq. (1) for the charge at junctions. This condition fails to take into account the effect on charge due to the proximity of a step in radius. It also does not account for coupling of closely spaced wires which results in a greater charge density on the outer wires at a fan-shaped junction. In NEC–4X, accurate charge distributions for the basis functions are determined with minimal computational overhead by executing a small moment-method solution for each junction. Any junction on which the charge cannot be determined as uniform due to symmetry is considered isolated from the rest of the structure with the wires extended to infinity away from the junction. An integral equation based on continuity of scalar potential is then solved to determine the distribution of charge. The charge is represented in a piece-wise linear expansion, with triangular basis functions and one semi-infinite basis function on each wire. A single half-triangle and the semi-infinite function were found to be sufficient for convergence.

The new code has been tested on a number of wire structures for which results could be validated against available measurements or independent numerical solutions. One antenna of interest is the stepped radius monopole shown in Fig. 1. It was shown in [7] that NEC–3 yields an inaccurate input reactance for this monopole when it is modeled as a single wire. Results for input impedance and resonant frequency, computed by NEC–3D and NEC–4X, are shown in Table 1 for varying length of the segments adjacent to the junction. For Δ less than 0.00625 m the segment lengths were tapered for shorter segments toward the junction. These results should be compared with the twelve-wire cage model of Fig. 1 which yielded an impedance of $38.69 + j4.03$ ohms. Improved accuracy and convergence are apparent.

Table 1. Input impedance and resonant frequency of the stepped radius monopole computed by NEC–3D and NEC–4X. Monopole length is 0.25 m with radius 0.00025 m on the lower half and 0.000125 m on the upper half. Each section was divided into N segments with segment length Δ at the junction. The impedance was computed at 299.8 MHz.

		NEC–3D			NEC–4X		
N	Δ (m)	R (ohms)	X (ohms)	f_{res} (MHz)	R (ohms)	X (ohms)	f_{res} (MHz)
2	0.0625	39.05	7.66	296.15	38.91	2.89	298.44
4	0.0312	38.21	9.58	295.08	37.88	3.21	298.23
8	0.0156	38.24	11.56	294.06	37.73	3.59	298.02
20	0.00625	38.54	14.22	292.73	37.80	4.31	297.65
20	0.002	38.80	17.47	291.18	38.02	5.52	297.08
20	0.001	38.92	19.24	290.34	38.11	5.67	297.01
20	0.0005	39.01	20.45	289.77	38.09	3.78	297.95
20	0.00025	39.06	20.89	289.59	38.08	1.43	299.10
20	0.000125	39.11	20.97	289.58	38.18	0.93	299.35

The decrease in reactance in the NEC–4X results for segment lengths less than 0.001 m may indicate the need for including the field due to the charge on the annular surface of the step in radius for such short segments. This comparison will be repeated when we have closed the annular gap. For a monopole with continuous radius of 0.000125 m, NEC–3D predicts an impedance of $40.16 + j23.05$ ohms and resonant frequency of 289.54 MHz, while for a continuous radius of 0.00025 m the impedance is $40.76 + j23.45$ ohms and resonant frequency of 288.24 MHz. Hence, the NEC–3 results for the stepped-radius monopole appear to converge toward the result for a continuous radius.

A test of modeling a tightly coupled junction is provided by the strip-line EMP simulator constructed from 18 wires, as shown in Fig. 8. This structure was built at the Commissariat a L'Energie Atomique in France [8] where measured fields were compared with results obtained from NEC–2. The NEC results for the vertical electric field within the simulator were about a factor of two larger than measured values. Also, NEC–2 predicted nearly equal current in the 18 wires, while measurements showed that currents in the outer wires were about three times as large as on the wires at the center.

Results from NEC–3D and NEC–4X are shown in Fig. 9 for the currents in the wires when the line is driven by a one volt source at 4 MHz. NEC–3D is seen to produce nearly equal currents while results of NEC–4X show larger currents in the outer wires as had been measured. Integrating the vertical component of electric field from the ground plane to the center of the wire nearest the center plane at $x = 0$ m, $y = 0.02$ m yielded 1.93 volts in NEC–3D and 1.05 volts in NEC–4X further confirming the accuracy of NEC–4X.

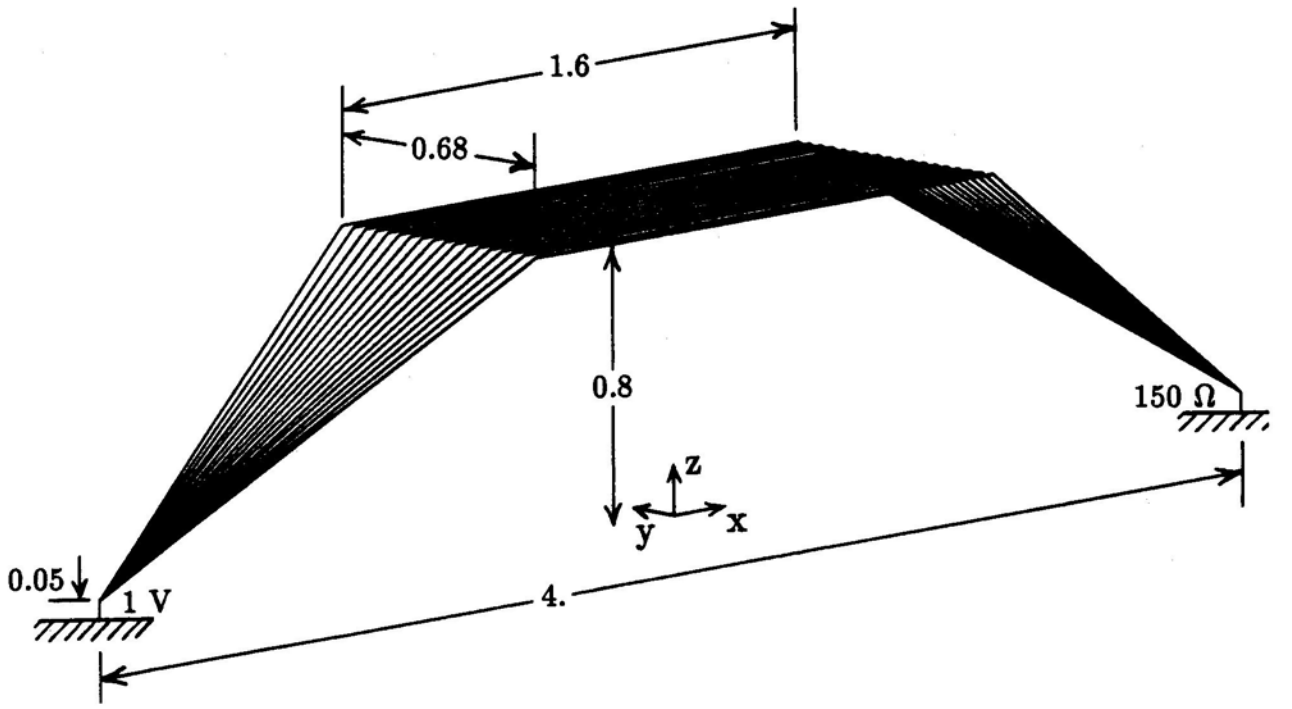

Fig. 8. Strip-line EMP simulator constructed from 18 wires. The line is driven by a voltage source against the ground plane and the other end is terminated in a 150 ohm load. All dimensions are in meters, and the wire radius is 0.0008 m.

Junctions of wires driven against a ground plane can sometimes be modeled more accurately in NEC–3 if the vertical wire is omitted and the individual wires are connected to the ground plane. This cannot be done with the terminating load, however, since the currents in the wires would then be forced to be equal by circuit considerations. Hence an accurate model of the junctions is necessary to model the strip line.

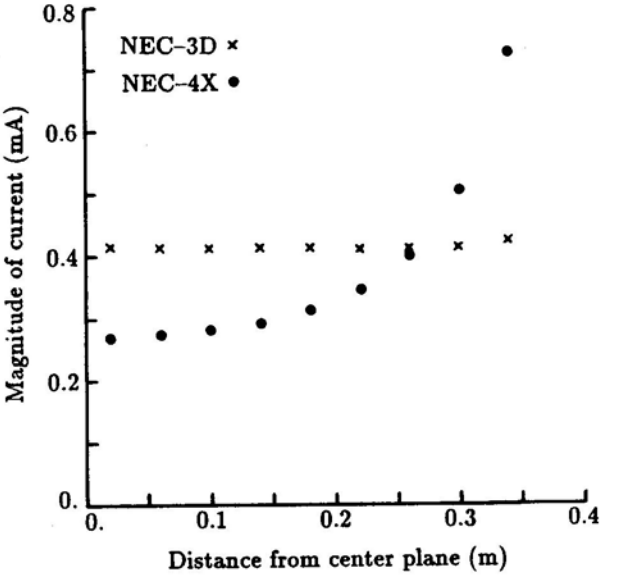

Fig. 9. Magnitude of current on the wires of the strip-line EMP simulator. Current is computed at a point 0.4 m from the center of the simulator toward the source.

Several tasks remain to be completed before NEC–4X can be released as NEC–4. One is to investigate the importance of including the field due to charge at the annular surface at a change in radius. The extended thin wire kernel evaluation, that is an option in NEC–3 for segments that are short relative to their radius, has been eliminated in NEC–4X due to the effectiveness of caps on wire ends and voltage sources. Caps could also be included on segments with impedance loads or connections to network ports.

The new solution for charge density at a junction, based on continuity of scalar potential, considers the junction to be in an infinite medium. The result should be appropriate for junctions above or below an air-ground interface unless some junction wires are very close to the interface. However, a condition taking the interface into account may be needed for a model such as a monopole on a wire ground screen. For such cases, an option should be available to leave the charge density as an unknown to be determined in the full moment-method solution. This can be done by including an additional basis function and match point at the junction. Such a treatment might also be useful for modeling an insulated wire with discontinuous sheath, for which an appropriate condition on charge is not presently known.

If time permits, we would like to include other recent NEC developments, including loop basis and weighting functions, the model for insulated wires and some restructuring of the Fortran. Of course, much more testing and debugging is needed. When finished, the NEC–4 code should offer substantial advantages over NEC–3 for some of the modeling situations that have caused problems in the past.

Code Error Reports

An old error has come back to haunt us in the code NEC–GS for modeling monopoles on radial wire ground screens. Several errors were found in this code in December 1986 that effected models with sources or loads located on the radial wires. However, only the single precision source file was corrected on our distribution directory on the VAX.

The double precision source and all executable and object library files were not corrected. Persons having NEC–GS should contact Jerry Burke (415-422-8414) for corrections.

An error of a more esoteric nature has been pointed out by Dr. Melvin Weiner of MITRE Corporation. He noted that when the reflection coefficient approximation in NEC is used with a negative permittivity and zero conductivity the wrong branch of the square root is used in calculating the reflection coefficient. Negative permittivities can occur in equivalent ground parameters to approximate a wire ground screen, and the conductivity would be zero if the screen was in free space rather than over ground.

This problem can be fixed by testing each result of a complex square root and chosing the sign to give a negative imaginary part. In NEC–3, this must be done in the calculation of the wavenumber in the main program as well as in the reflection coefficients. Alternatively you can avoid the problem by making sure that there at least a small amount of conductivity when the permittivity is negative. The accuracy of the reflection coefficient approximation for negative permittivity also remains to be determined.

References

[1] A. W. Glisson and D. R. Wilton, *Numerical Procedures for Handling Stepped-Radius Wire Junctions*, Department of Electrical Engineering, University of Mississippi, March 1979.

[2] A. C. Ludwig, "Wire Grid Modeling of Surfaces," *IEEE Trans. Antennas and Propagation*, Vol. AP-35, pp. 1045-1048, 1987.

[3] T. T. Wu and R. W. P. King, "The Tapered Antenna and its Application to the Junction Problem for Thin Wires," *IEEE Trans. Antennas and Propagation*, Vol. AP-24, pp. 42-45, 1976.

[4] S. A. Schelkunoff and H. T. Friis, *Antennas: Theory and Practice*, Wiley, New York, 1952.

[5] P. C. Waterman, "Matrix Formulation of Electromagnetic Scattering," *Proceedings of the IEEE*, Vol. 53, pp. 805-812, August 1965.

[6] G. J. Burke, *Enhancements and Limitations of the Code NEC for Modeling Electrically Small Antennas*, Lawrence Livermore National Laboratory, Rept. UCID–20970, January 1987.

[7] J. K. Breakall and R. W. Adler, "A comparison of NEC and MININEC on the Stepped Radius Problem," *Applied Computational Electromagnetics Society Journal and Newsletter*, Vol. 2, No. 2, Fall 1987.

[8] J. P. Desmettre, Commissariat a L'Energie Atomique, Private Communication.

A DUAL NORMAL MODE REPRESENTATION FOR ELECTROMAGNETIC SCATTERING: SOME INITIAL CONSIDERATIONS

T. H. Lehman
927 Camino Del Rio NW
Albuquerque, NM 87114

ABSTRACT

This paper presents a new technique for characterizing the electromagnetic interaction with and scattering from objects of finite extent. By exploiting the structure of the operators (in this case matrices) associated with the interaction, it is shown that both the system (impedance) matrix and the transfer (admittance) matrix can be partitioned into the sum of two matrices such that each of the resulting matrices can be decomposed into a set of normal modes. As a result, the number of parameters needed to describe the interaction is now significantly reduced and the parameters identified by this technique are model independent, i.e. they are measurable parameters. Potential applications of the technique include EM computations, compact descriptions of scatterers and antennas, interpretation of measured data, and algorithm development applicable to scattering and inverse scattering problems.

INTRODUCTION

There are a number of numerical methods available for determining the induced currents on or fields scattered from a wide class of objects. Direct applications of all of these methods – which include method of moments, finite element, finite difference, etc. – yield interaction or scattering representations which are exclusively in terms of a large number of abstract parameters (model dependent parameters). Although, in principle, these parameters can be related to the measured or observed parameters (model independent parameters) of the interaction, this usually is very difficult to accomplish when it can be done at all. This disparity between measured and model parameters significantly reduces the utility of these models for most applications to practical problems other than as computational tools for specific cases.

This requirement for an "observable parameter based EM model" is not new and has provided the impetus for considerable research in the area. Two methods resulting from this research are worth noting. The first of these methods is the Eigenmode Expansion Method (EEM) which is simply a re–statement of the fact that a non–normal matrix, say Z, can be diagonalized by a similarity transformation or

$$e = T^{-1}ZT \tag{1}$$

where the elements of the diagonal matrix e are the eigenvalues of Z, T is the matrix of right eigenvectors and T^{-1}, the inverse of T, is the matrix of left eigenvectors. If Z is the impedance matrix obtained by application of the frequency domain method of moments formulation to an antenna or scatterer, then not only is Z a function of the frequency, f,

but in general, e and T are also functions of f (usually complicated and irrational functions). The only real advantage of this formulation is that each eigenvector $(T)_j$ is orthogonal with respect to all other eigenvectors $(T)_k$.

The second method worth noting is the Singularity Expansion Method (SEM) [Baum (1971)]. It is intimately related to the EEM method in that it decomposes Z (the system matrix) or $Y = Z^{-1}$ (the transfer matrix) into a set of time invariant vectors (independent of f or the complex frequency s) and a diagonal matrix representation that contains all of the time or frequency dependence. For the interior problem with only ohmic losses (restricts Z(s) to be second order in s), it is straight–forward but tedious to show [Richardson and Potter (1974)] that each element of the admittance matrix Y can be expanded into a partial fraction expansion about each pole of Z(s) so that Y can be written in the form

$$Y = \sum_{k=1}^{M} A_k/(s-s_k) \quad , \qquad (2)$$

where $M = 2N$, the A_k's are matrices independent of s, and the s_k's are the poles of Z(s). The A_k's are evaluated by setting $s=s_k$ in the following equation

$$A_k = T(s)(s-s_k)e^{-1}(s)T^{-1}(s) \qquad (3)$$

where T and e are defined by equation (1). In this formulation, the s_k's are referred to as the complex natural frequencies of the system.

Applications of this methodology to the exterior problem where ohmic losses are replaced by radiation losses significantly increases the complexity of the formulation and its understanding. First of all, the impedance matrix Z is no longer second order in s and is at least of order N [Cordaro and Davis (1981)] where N is the dimensionality of the impedance matrix. There are now on the order of $2N^2$ natural frequencies instead of the 2N natural frequencies associated with the internal problem (the factor of 2 arises because the poles occur in conjugate pairs). Secondly, the mode shapes associated with the natural frequencies are no longer orthogonal or real (this was also true for the interior problem). Lastly, only the first row of the natural frequencies s_{1k} have been observed experimentally. As a consequence, the admittance matrix has been written in the form

$$Y = \sum_{k=1}^{M} A_{1k}/(s-s_{1k}) + \text{"entire function"} \quad . \qquad (4)$$

Here the "entire function" somehow accounts for the driven response of the scatterer while the sum over the poles accounts for the undriven response. The functional form of the entire function has yet to be uniquely defined. To date the SEM representation has proven to be too complex and too difficult both theoretically and experimentally to be of much practical value except for a few specific cases. It seems rather obvious that the "entire function" in equation (4) arises because the A_{1k}'s do not form a complete set of natural frequency mode shapes. If all of these mode shapes are required, then the SEM formulation

results in replacing one NxN frequency dependent full matrix by N NxN frequency dependent diagonal matrices and N NxN frequency independent full complex matrices. But, "Is this representation simpler than the original matrix?"

The next question is "Where does one go from here?" It appears that the cure is worse than the disease. There are three possible cases. The first is that there are no "measurable parameter based EM models" that are simple and easy to apply. Certainly, the results obtained to date seem to support this argument. The second is that simple and easy to apply "measurable parameter based EM models" do exist but that the theoretical and experimental tools necessary for developing these models currently do not exist. The third is that these models have not been developed primarily because of misconceptions held about the nature and existence of normal modes. It is this last case that is examined in some detail in the remainder of this paper.

We begin by examining the concept of classical normal modes. It is well–known that for a linear phenomenon which obeys the wave equation and for which the interaction takes place within a bounded region of space (an interior problem), the "system response" can be decomposed into an infinite number of normal modes as long as all losses or damping mechanisms are ignored. As the name implies, these modes represent independent degrees of freedom (they are orthogonal to each other) and they are defined to be measurable parameters because they do not depend on the analytical formulation of the problem. If a loss or damping mechanism is now introduced into the interaction, then, in general, the response can no longer be decomposed into normal modes and the modes are no longer independent (although for most problems of interest, orthogonality is a good approximation even for the case of large damping coefficients). As a result, it is generally accepted that normal modes exist only for those interactions for which there is no loss or damping, although it has been shown [Caughey and O'Kelly (1965)] that this is not universally true. It should be noted that for interior problems, damping is directly related to the constitutive parameters of the media; for example, for a cavity problem we have no damping if we assume that the cavity walls are perfectly conducting. For the exterior problem (scattering), we know that radiation damping is always present independent of the nature of the media parameters. Therefore, it is easy to assume that the response of scatterers cannot be decomposed into normal modes, even though a few objects (most notably a circular wire loop and a perfectly conducting sphere) do exhibit normal mode behavior.

The behavior of the circular wire loop and the sphere pose some interesting questions. "Is it an accident of nature that their response can be decomposed into normal modes?" These two objects still radiate, so is there some property of their radiation mechanism that makes them different than say a thin straight wire? Or is it possible that the response of all perfectly conducting scatterers can be decomposed into normal modes and that the wire loop and the sphere are limiting cases of some yet to be determined higher order normal mode theory (i.e. for these geometries the higher order theory reduces to the canonical form of normal mode theory)? We now investigate this possibility.

THE DUAL NORMAL MODE REPRESENTATION OF THE IMPEDANCE MATRIX

Consider a thin straight wire defined by a length 2L, a radius a and an impedance matrix $Z_w(f)$ obtained from discretizing Pocklington's equation with the reduced kernel. We do not have to specify the discretization procedure since the structure of Z_w is form invariant with respect to the method of discretization. In other words, Z_w is a Toeplitz matrix irrespective of how it was obtained. The second attribute of Z_w of note, is that if we evaluate it at two different frequencies, say f_1 and f_2, then the two matrices that result from this calculation, do not commute:

$$[Z_w(f_1),Z_w(f_2)] = Z_w(f_1)Z_w(f_2) - Z_w(f_2)Z_w(f_1) \neq 0$$

unless $f_1 = f_2$. Therefore, we know that $Z_w(f_1)$ and $Z_w(f_2)$ cannot be diagonalized by the same similarity transformation and that "classical" normal mode theory is not applicable to a thin wire scatterer.

Since Z_w does not exhibit normal mode behavior, the next question is "does any part of Z_w exhibit normal mode behavior?" The answer to this question is yes. By carefully examining the structure of Z_w, it can be shown that Z_w can be partitioned into the sum of two matrices (see Appendix A) such that each matrix can be diagonalized by a frequency independent similarity transformation:

$$Z_w(f) = Z_1(f) + Z_2(f) \tag{5}$$

where

$$[Z_1(f_1),Z_1(f_2)] = 0 \tag{6}$$

and

$$[Z_2(f_1),Z_2(f_2)] = 0 \tag{7}$$

for arbitrary f_1 and f_2. Therefore, there exists two time or frequency independent matrices, T_1 and T_2, [Arfken (1966)] such that

$$T_1^t Z_1(f) T_1 = z_1(f) \tag{8}$$

and

$$T_2^t Z_2(f) T_2 = z_2(f) \tag{9}$$

for all values of the frequency, f, where $z_1(f)$ and $z_2(f)$ are diagonal matrices and

$$T_1^t = T_1^{-1} = \text{transpose of } T_1 \tag{10}$$

$$T_2^t = T_2^{-1} = \text{transpose of } T_2. \tag{11}$$

Therefore, both Z_1 and Z_2 are diagonalizable by orthogonal similarity transformations.

Equations (8), (9), (10) and (11) allow us to write the impedance matrix, Z_w, for the thin wire in a very simple and compact form:

$$Z_w(f) = T_1 z_1(f) T_1^t + T_2 z_2(f) T_2^t \quad . \tag{12}$$

Thus Z_w can be expressed in terms of two frequency dependent diagonal matrices and two frequency independent orthogonal matrices. Some of the interesting properties of these matrices are:

(1) The matrix elements of both T_1 and T_2 are real.

(2) The first N/2 columns of T_1 and T_2 represent symmetric mode shapes and the second N/2 columns of T_1 and T_2 represent anti–symmetric mode shapes.

(3) Both T_1 and T_2 form complete sets of eigenvectors; so that the current and the incident field can be expanded in terms of either set.

(4) Both the symmetric $(T_1)_s$ and anti–symmetric $(T_1)_a$ modes of Z_1 are analytic functions of the position, x, along the length of the wire and are of the form

$$(T_1)_s = \cos((2n+1)\,\pi\, x/2L),\ n = 0,1,2,...$$

$$(T_1)_a = \sin((2n+1)\,\pi\, x/2L),\ n = 0,1,2,...$$

i.e. they are symmetric and anti–symmetric odd multiple half wavelength (spatial) modes. Note that the anti–symmetric modes do not vanish at the ends of the wire.

(5) Both the symmetric $(T_2)_s$ and anti–symmetric $(T_2)_a$ modes of Z_2 are also analytic functions of the position, x, along the length of the wire and are of the form

$$(T_2)_s = \cos(n\,\pi\, x/L)\ ,\ n = 0,1,2,....$$

$$(T_2)_a = \sin(n\,\pi\, x/L)\ ,\ n = 0,1,2,....$$

i.e. they are symmetric and anti–symmetric full wave–length (spatial) modes. Note that the symmetric modes do not vanish at the ends of the wire for this case.

(6) The matrix elements of the diagonal matrices z_1 and z_2 are complex; so that radiation damping is included in this representation.

(7) The set of eigenvalues z_1 and the set of eigenvalues z_2 are both doubly degenerate. The eigenvalue $(z_1)_n$ of the eigenvector $(T_1)_s$ is equal to the eigenvalue of the eigenvector $(T_1)_a$ for the same mode number n. Similarly, $(T_2)_s$ and $(T_2)_a$ have equal eigenvalues for the same mode number n.

(8) The resonances of the z_1 eigenvalues occur exactly at odd multiples of the half wavelength for the thin wire (Figure 1). Similarly, the resonances of the z_2 eigenvalues occur exactly at multiples of the full wavelength (Figure 2). These eigenvalues do not exhibit any mode–to–mode coupling. In both Figures 1 and 2, the inverses of the eigenvalues, z_1^{-1} and z_2^{-1}, are presented so that the resonances are easier to identify.

Two aspects of this dual normal mode representation of the impedance matrix require more discussion: (1) the resonant frequencies of the impedance matrix eigenvalues are not equal to the measured values of the resonant frequencies for the thin wire and (2) the $(T_1)_a$ and the $(T_2)_s$ mode shapes do not have zero amplitudes at the ends of the wire. Of the two, the first is the least disturbing since we will show later that the resonant frequencies of the admittance matrix do indeed correspond to the measured values. The physical significance of the impedance matrix eigenvalues is unclear at this time. The second aspect of the dual normal mode representation is more disturbing. One would feel more comfortable if all the mode shapes vanished at the ends of the wire. However, the "unnatural" mode shapes are just the derivatives of the "natural" mode shapes suggesting

that they are somehow related to the charge distribution on the wire. Another possible explanation is that one set of modes corresponds to magnetic field modes and the other to electric field modes. This imposed duality is not new in electromagnetics and raises the serious question as to whether a first order time formulation is more natural than a second order time formulation. Perhaps a formulation fashioned after the Hamiltonian theory of classical mechanics [Goldstein (1957)] would shed some light on this subject.

Before concluding our discussion of the impedance matrix, we return once again to our original supposition that the impedance matrix Z_{loop} of a circular wire loop is just some limiting case of a higher order normal mode theory. To support this supposition we note that in the limit as the thin straight wire evolves into a circular loop

$$Z_w = Z_2$$

and the Z_1 contribution to the impedance matrix vanishes. But Z_2 is just equal to Z_{loop} so that for thin wire scatterers our initial supposition is true.

THE DUAL NORMAL MODE REPRESENTATION OF THE ADMITTANCE MATRIX

We have been able to demonstrate up to this point that the impedance matrix for the thin wire can be put into an extremely simple form. A more important question is what about the admittance matrix, Y_w, which is, of course, just the inverse of Z_w? The most desirable behavior would be that the structure of the impedance matrix is form invariant under inversion. This would imply that for the thin wire, Y_w would also be a Toeplitz matrix. From experience, we know that, in general, this is not true.

The next best situation would be that the form of the normal mode decomposition as defined by equations (5),(6),(7) and (12) is preserved under inversion. This would imply that Y_w could be partitioned into the sum of two commuting matrices as before or

$$Y_w(f) = Y_1(f) + Y_2(f) \tag{13}$$

where

$$[Y_1(f_1), Y_1(f_2)] = 0 \tag{14}$$

and

$$[Y_2(f_1), Y_2(f_2)] = 0 \tag{15}$$

for arbitrary f_1 and f_2. We would also require that Y_1 is diagonalizable by the same orthogonal similarity transformation that diagonalized Z_1 and similarly, that Y_2 is diagonalizable by the same similarity transformation that diagonalized Z_2 or

$$y_1(f) = T_1^t Y_1(f) T_1 \tag{16}$$

and

$$y_2(f) = T_2^t Y_2(f) T_2 \tag{17}$$

where $y_1(f)$ and $y_2(f)$ are frequency dependent diagonal matrices and T_1 and T_2 are

frequency independent orthogonal matrices as before. If equations (13) through (17) prove to be true, then the admittance matrix $Y_w(f)$ for the thin wire can be written in a compact form given by

$$Y_w(f) = T_1 y_1(f) T_1^t + T_2 y_2(f) T_2^t \tag{18}$$

As was the case for the impedance matrix, the admittance matrix can also be written in terms of two frequency dependent diagonal matrices and two orthogonal frequency independent matrices.

The proof of the identity

$$[T_1 z_1(f) T_1^t + T_2 z_2(f) T_2^t]^{-1} = T_1 y_1(f) T_1^t + T_2 y_2(f) T_2^t \tag{19}$$

turned out to be non–trivial. However, for the decomposition of the impedance matrix as presented in the previous section to be of more than just academic interest, the admittance matrix must also exhibit a similar behavior. Therefore, the proof of the above identity or a similar identity is a very crucial step in the development of this dual normal mode theory.

The first thing of note about the above identity is that

$$y_1(f) = z_1^{-1}(f)$$

and

$$y_2(f) = z_2^{-1}(f)$$

is not a solution. Therefore, in general, y_1 and y_2 are probably non–linear functions of z_1 and z_2.

A review of the literature on inverse matrix theory failed to provide any insight into the proof of the identity given by equation (19). Finally, a numerical demonstration of the validity of the identity was attempted. To do this, we pre–multiply equation (18) by T_1^t and post–multiply by T_1 which results in the equation

$$y_1(f) + T_1^t T_2 y_2(f) T_2^t T_1 = T_1^t Y_w(f) T_1 \tag{20}$$

Next, we pre–multiply equation (18) by T_2^t and post–multiply by T_2 which results in the equation

$$T_2^t T_1 y_1(f) T_1^t T_2 + y_2(f) = T_2^t Y_w(f) T_2 \tag{21}$$

First of all we note that $S^t = T_2^t T_1$ and $S = T_1^t T_2$ are both frequency independent orthogonal matrices with $S^t S = S S^t = I$ (the identity matrix). Next, we note that equations (20) and (21) yield $2N^2$ equations for the $2N$ unknowns y_1 and y_2. Using only the $2N$ equations provided by the diagonal elements of the matrices defined by equations (20) and (21), y_1 and y_2 can be determined from solutions of the equation

$$Hy(f) = h(f) \tag{22}$$

where y(f) and h(f) are 2Nx1 column vectors and H is a 2Nx2N frequency independent matrix. The first N elements of y(f) correspond to the N diagonal elements of $y_1(f)$ and the second N elements of y(f) correspond to the N diagonal elements of $y_2(f)$. The first N elements of h(f) correspond to the N diagonal elements of the matrix $T_1{}^tY_w(f)T_1$ and the second N elements of h(f) correspond to the N diagonal elements of $T_2{}^tY_w(f)T_2$. If H is partitioned into the four NxN matrices: $H_{11},H_{12},H_{21},H_{22}$; then H_{11} and H_{22} are equal to the NxN identity matrix I, or

$$H_{11} = H_{22} = I,$$

the elements of H_{12} are given by

$$(H_{12})_{ij} = (S_{ij})^2$$

and the elements of H_{21} are given by

$$(H_{21})_{ij} = (S_{ji})^2$$

where

$$S_{ij} = (T_1{}^tT_2)_{ij}.$$

Equation (22) was solved numerically over a frequency range corresponding to a wire length–to–wavelength ratio of 0.05 to 2.0. The impedance matrix, $Z_w(f)$, was derived from a hybrid finite difference/method of moments technique using pulse expansion functions with point matching. The wire was divided into 20 segments and the wire radius–to–length ratio was 0.005. Since H is independent of frequency, the resulting 40x40 matrix only had to be inverted once. The values of $y_1(f)$ and $y_2(f)$ obtained from equation (22) were inserted into equation (18) and the resulting values obtained for $Y_w(f)$ were then compared to the values $Y_w(f)$ obtained by directly inverting $Z_w(f)$. The results for 6 elements of the admittance matrix are shown in Figures 3 through 8. Comparisons for other matrix elements showed similar agreement.

Although the comparison of the results of the two calculations was excellent, they still were not exact. This could either be attributed to numerical round–off error since the calculations were performed on a PC AT computer using single precision or it could be attributed to small contributions to the admittance matrix that were not included in equation (18). Another literature search on the subject of inverse matrix theory failed to provide any new insight. Then it was discovered that another matrix besides the identity matrix commutes with both $Z_1(f)$ and $Z_2(f)$ of equation (5), therefore, it is also diagonalizable by both the orthogonal similarity transformations defined by T_1 and T_2 of equations (8) and (9). This matrix is the cross identity matrix, E, i.e. the major cross diagonal elements of E are equal to one and all other elements are zero. With the aid of this matrix, one can then show that if a matrix Z can be partitioned into the sum of two commuting matrices as defined by equations (5),(6) and (7), then Z^2 can also be partitioned into the sum of two matrices (but not the same two matrices) that have the same properties. If this is true for Z^2, it is also true for Z^3 and all higher powers of Z (the

proof for a 4x4 matrix is shown in Appendix B). Using the Cayley–Hamilton theorem [Wilson, Decius and Cross (1955)], the inverse of the NxN matrix, Z_w, can be written in the form

$$Z_w^{-1} = Y_w = -[C_{N-1} + C_{N-2}Z_w + C_{N-3}Z_w^2 + ...$$

$$..+ C_1 Z_w^{N-2} + Z_w^{N-1}]/C_N \qquad (23)$$

and therefore, equations (13) through (17) follow and we have proved the identity given by equation (19). In equation (23), all of the C's are scalars and they are the coefficients of the characteristic equation for Z_w; for example, C_1 is the negative of the trace of Z_w and C_N is the negative of the determinant of Z_w. Equation (18) also follows and we have succeeded in demonstrating that the admittance matrix can be written in the very simple form

$$Y_w(f) = T_1 y_1(f) T_1^t + T_2 y_2(f) T_2^t \qquad (18)$$

which only requires two frequency dependent diagonal matrices and two frequency independent orthogonal real matrices as compared to the 2N frequency dependent diagonal matrices and the 2N frequency independent non–orthogonal complex matrices that result from the SEM formulation.

The eigenvalues, $y_1(f)$ and $y_2(f)$, of the two admittance matrices $Y_1(f)$ and $Y_2(f)$ were calculated over the frequency range corresponding to a wire length to wavelength ratio of 0.05 to 2.0. The calculations were performed for a 20 segment wire, again using a hybrid finite difference/method of moments technique with pulse expansion functions and point matching. Results of the calculations are presented in Figures 9 through 12. Some of the interesting behavior exhibited by these eigenvalues is:

(1) The response resonances of these eigenvalues occur at the same frequencies as observed in measured data, i.e. they are no longer "exact" multiples of half and full wavelengths as was the case for the eigenvalues of the impedance matrix.

(2) The eigenvalues (Figures 9 and 11) associated with the symmetric mode shapes exhibit odd multiple of half wavelength resonances while the eigenvalues (Figures 10 and 12) associated with the anti–symmetric mode shapes exhibit multiple of full wavelength resonances. Remember that this was not true for the impedance matrix eigenvalues.

(3) While the impedance matrix eigenvalues did not exhibit any mode–to–mode coupling, the eigenvalues of the admittance matrix exhibit strong mode–to–mode coupling behavior for some of the eigenvalues.

(4) The admittance matrix appears to exhibit a very high degree of degeneracy (or "near" degeneracies) over the frequency range for which the eigenvalues were calculated. This degeneracy persists even for the phase of the eigenvalues (Figure 9.b) with similar results for the other set of eigenvalue phases (not shown).

It will be interesting to see if the redundancy which manifests itself through the degeneracies of the admittance matrix eigenvalues persists over a higher frequency range. The thin straight wire is only a two parameter problem, namely length to wavelength ratio and length to radius ratio, therefore one would expect considerable redundancy in its response characterization over a considerable frequency range.

One of the features that will require more investigation is the strong mode–to–mode coupling exhibited by the symmetric modes (Figures 9 and 11) at frequencies near the first resonance (approximately half wavelength) of the thin wire. It appears that all of the symmetric modes contribute significantly to the first resonance response. For frequencies near the second symmetric resonance (Figures 9 and 11), the nearest neighbor modes, modes 0 and 2, are coupled more strongly than the higher order modes. For the anti–symmetric modes (Figures 10 and 12), the modal coupling is also the strongest for the nearest neighbor modes.

POTENTIAL APPLICATIONS

For many years, normal mode techniques have played a powerful role in the analysis of the dynamic response of complex structural systems and their environments. This role is not limited to numerical response predictions but has included test definition, data analysis and system identification. These normal mode techniques provide a convenient bridge between model predictions and test results which is always an important consideration in any area of physics. Although, there is no guarantee that normal mode techniques will display a similar robust character when applied to the exterior EM interaction problem, there is also no reason, at this time, to assume otherwise.

The first and most obvious benefit of the technique would result if it provides better understanding and insight into the physics and the nature of EM coupling problems. This could potentially lead to the development of good self–consistent approximate models and to simpler and more meaningful measurement techniques.

From strictly a computational point of view, there are several possibilities. First a significant reduction in the number of unknowns can usually be achieved by making the transformation to normal coordinates. For example, if the expansion functions used in the discretization require 10 segments per wavelength from accuracy considerations, then only the first N/10 modal coordinates need to be retained in the calculations since the higher order mode contributions will be in error. Also, it maybe possible to partition a complex scatterer into several distinct regions such that the total system can be reconstructed by using the modal coordinates of each region as the expansion functions. Another possibility includes reducing matrix fill time for applications that require the prediction of responses over a wide frequency range. Also, it may be possible to treat the mode density as a continuum (rather than discrete) which potentially could provide us with a method for increasing the upper frequency limits for the numerical techniques currently in use.

One area that has a great practical potential is the whole field of EM measurements. If it can be shown that the eigenvalues of the admittance matrix can be directly or easily related to measurements, then the technique will provide a simple format for categorizing the response of radiating structures. This will be useful as a tool for retaining information about general classes of radiating objects, for extrapolating near field measurements to far field responses and possibly for identifying objects from far field measurements. However, for the last application to be feasible, algorithms that relate the impedance matrix eigenvalues to the admittance matrix eigenvalues will be required, since the impedance matrix "footprint" is significantly simpler than that of the admittance matrix.

SUMMARY

We have demonstrated that both the impedance and admittance matrices for a straight thin wire can be put into a simple form by using a dual normal mode formulation. The mode shapes associated with the normal modes are real and are neither functions of time nor frequency. They can be represented numerically by real orthogonal matrices. The dynamic or transient part of the interaction can be characterized by diagonal matrices which are complex numbers (in the frequency domain) and are functions of either time or frequency. These elements of the diagonal matrices could be referred to as the modal frequencies. However, one must keep in mind that there is no one–to–one correspondence between the modal frequencies associated with the impedance matrix and the modal frequencies associated with the admittance matrix. The impedance matrix modal frequencies have only one resonant frequency but that frequency does not coincide with measured resonant frequencies. The resonances of the admittance matrix modal frequencies do coincide with the measured resonant frequencies but each of these modal frequencies possess multiple resonances. Maybe it would be less confusing to refer to the impedance matrix modal frequencies as the system frequencies and the admittance matrix modal frequencies as the transfer frequencies.

In many respects, the dual normal mode representation is much simpler than the representation provided by the Singularity Expansion Method. However, the transfer frequencies (eigenvalues of the admittance matrix) are no longer one–parameter rational functions of the frequency. The functional behavior of the transfer frequencies needs to be determined.

Clearly, much work on the dual normal mode representation needs to be done. Issues regarding its extension to more complex scatterers need to be investigated. The physical significance of the system frequencies (eigenvalues of the impedance matrix) and the mode shapes that do not satisfy the boundary conditions at the end of the wire needs to be determined. The relationship between the transfer frequencies and measured data must be established. However, if it can be demonstrated that the dual normal mode representation simply and efficiently bridges the gap between models and measurements, it has the potential of providing us with a very powerful tool applicable to almost every facet of the EM interaction and scattering problem.

REFERENCES:

Baum, C. E., "On the Singularity Expansion Method for the Solution of Electromagnetic Interaction Problems," Interaction Note 88, Air Force Weapons Laboratory, Albuquerque, NM, December 1971.

Richardson, M. and R. Potter, "Identification of the Modal Properties of an Elastic Structure from Measured Transfer Function Data," Presented at the 20th International Instrumentation Symposium, Instrument Society of America, Albuquerque, NM, May 1974 (pp. 239).

Cordaro, J. T. and W. A. Davis, "Time–Domain Techniques in the Singularity Expansion Method," IEEE Transactions on Antennas and Propagation, Vol. AP–29, No. 3, May 1981.

Caughey, T.K. and M.E.J. O'Kelly, "Classical Normal Modes in Damped Linear Systems," Journal of Applied Mechanics, September 1965.

Arfken, G., Mathematical Methods for Physicists, Academic Press, New York, NY, 1966.

Goldstein, H., Classical Mechanics, Addison–Wesley, Reading, MA, 1957.

Wilson, E. B. , Decius, J. C. and Cross, P. C., Molecular Vibrations, The Theory of Infrared and Raman Vibrational Spectra, McGraw–Hill, New York, NY, 1955.

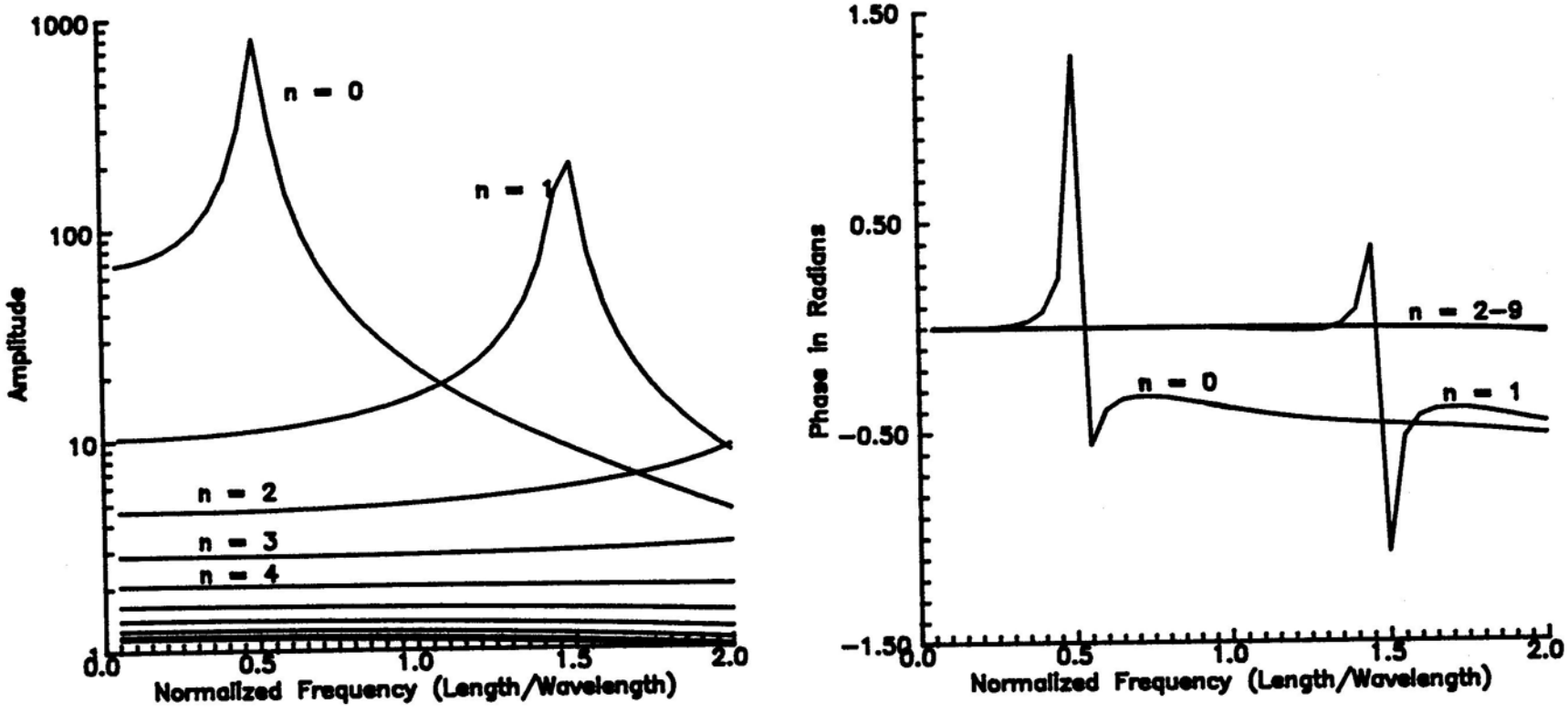

Figure 1. The inverse of the first ten eigenvalues of the Z_1 impedance matrix.

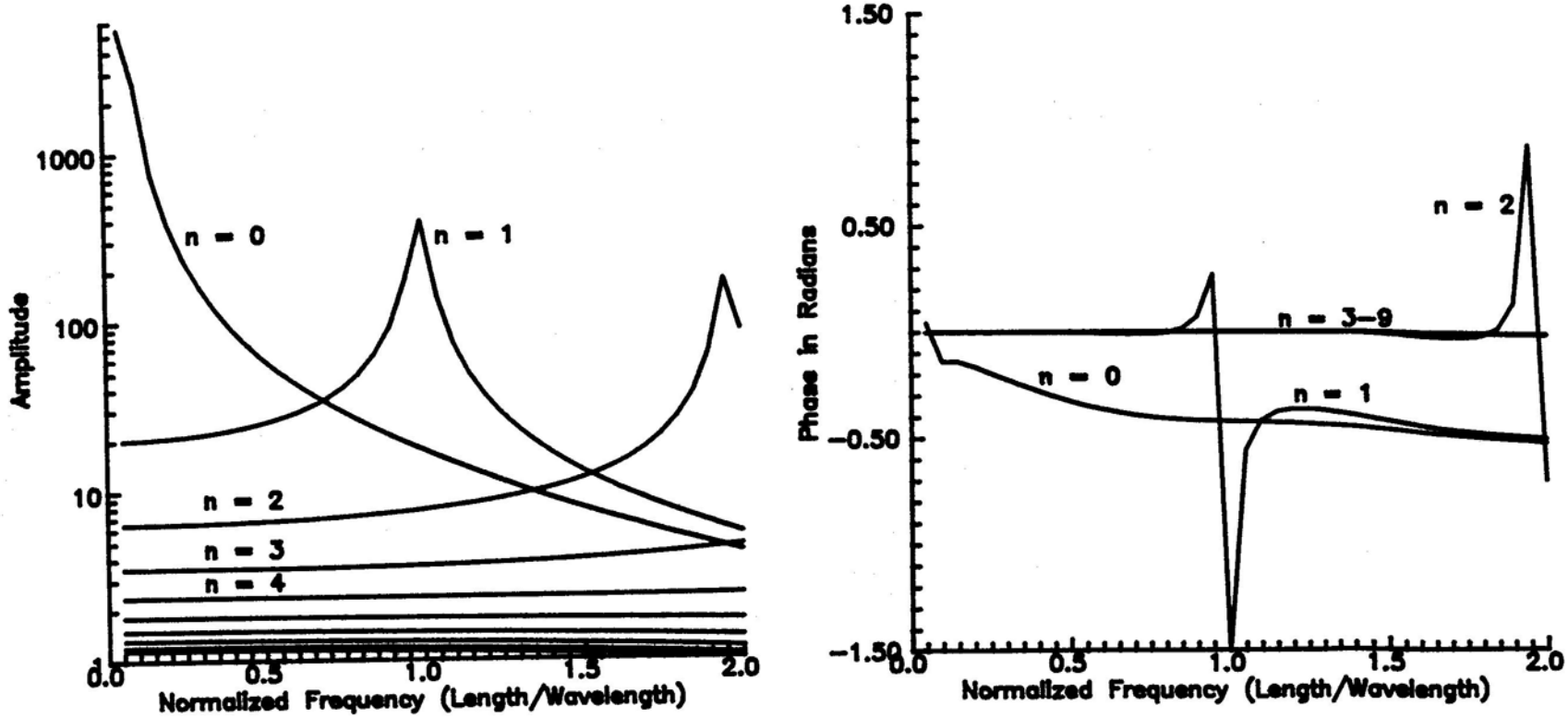

Figure 2. The inverse of the first ten eigenvalues of the Z_2 impedance matrix.

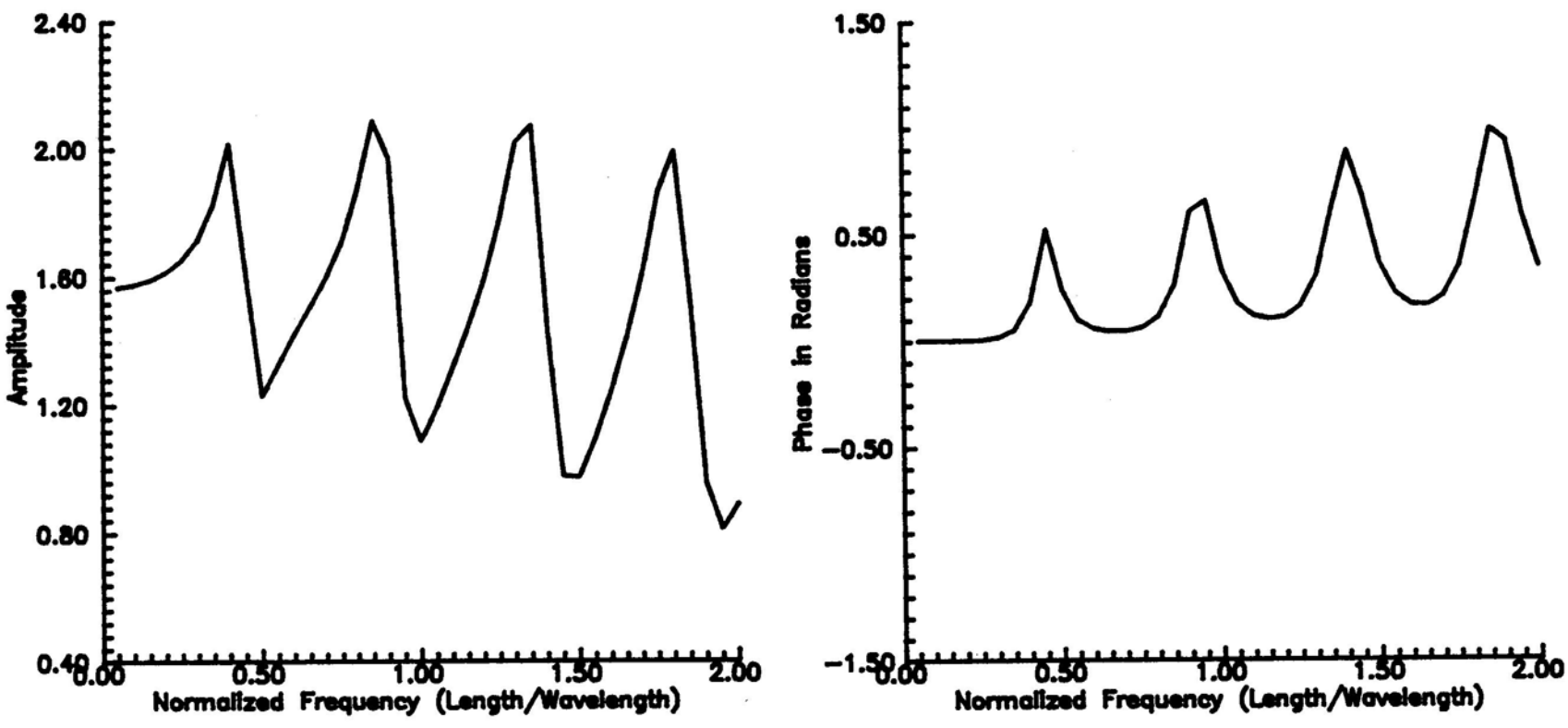

Figure 3. Comparison of the inverse method (–) vs. eigenvalue method (– – –) for the $Y_{1,1}$ element for the admittance matrix.

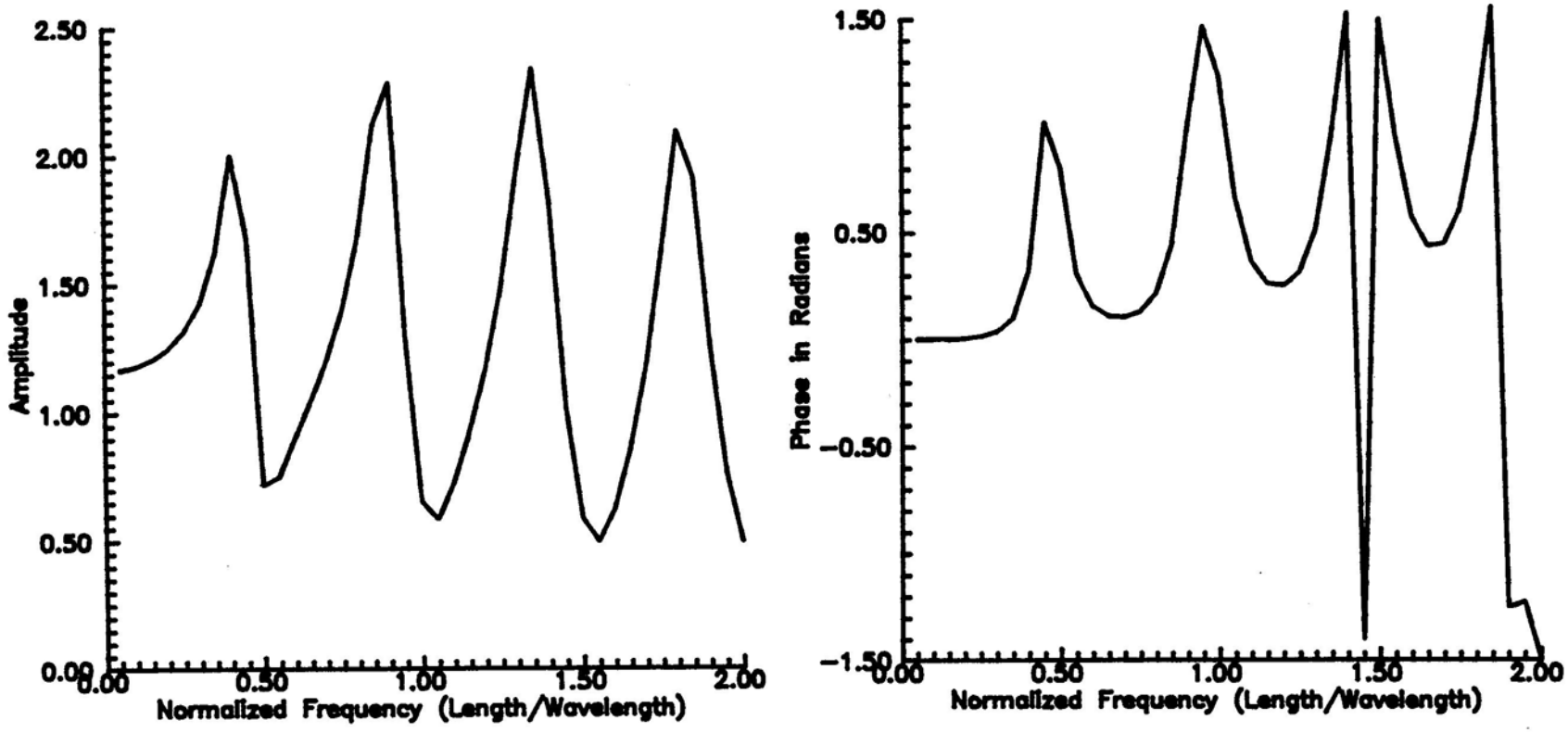

Figure 4. Comparison of the inverse method (–) vs. the eigenvalue method (– – –) for the $Y_{1,2}$ element of the admittance matrix.

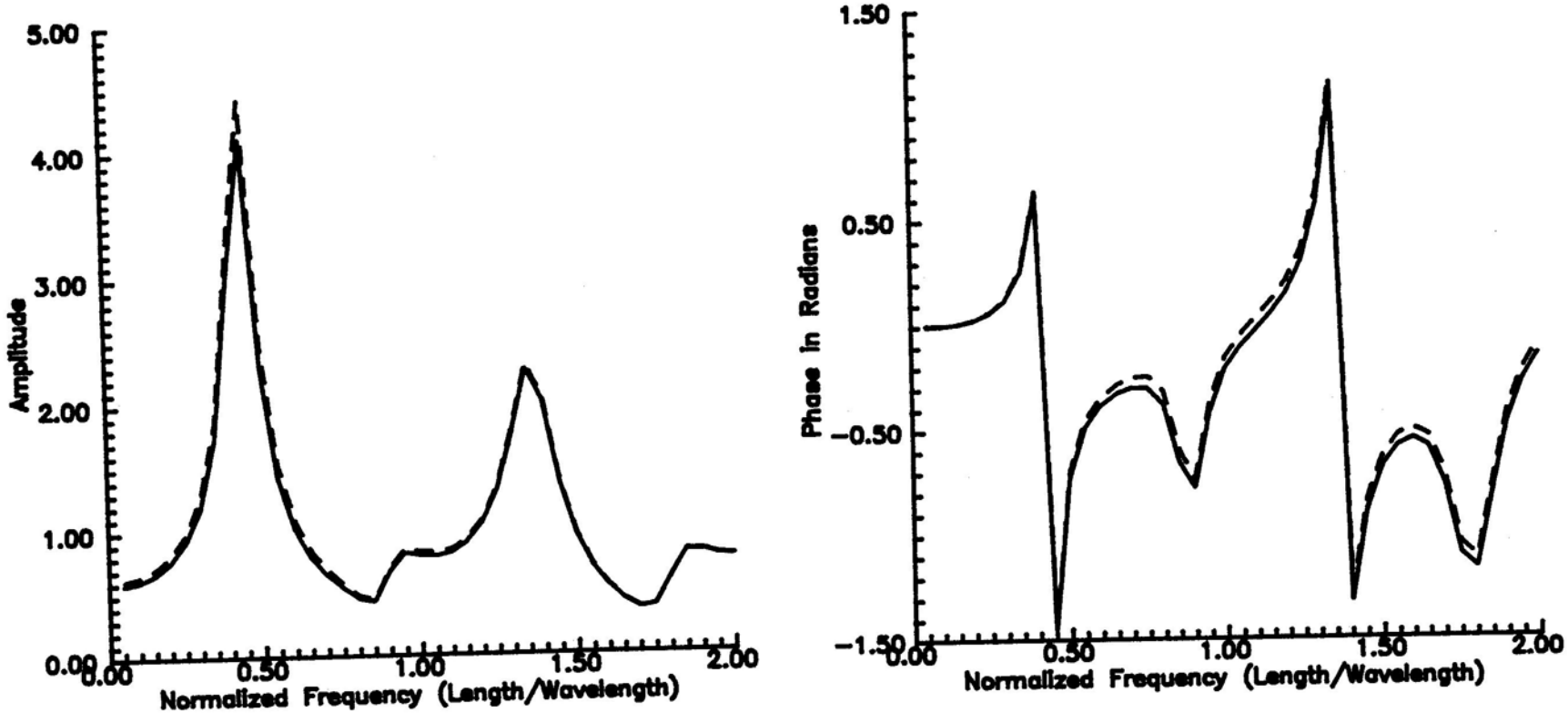

Figure 5. Comparison of the inverse method (–) vs. the eigenvalue method (– – –) for the $Y_{1,\,10}$ element of the admittance matrix.

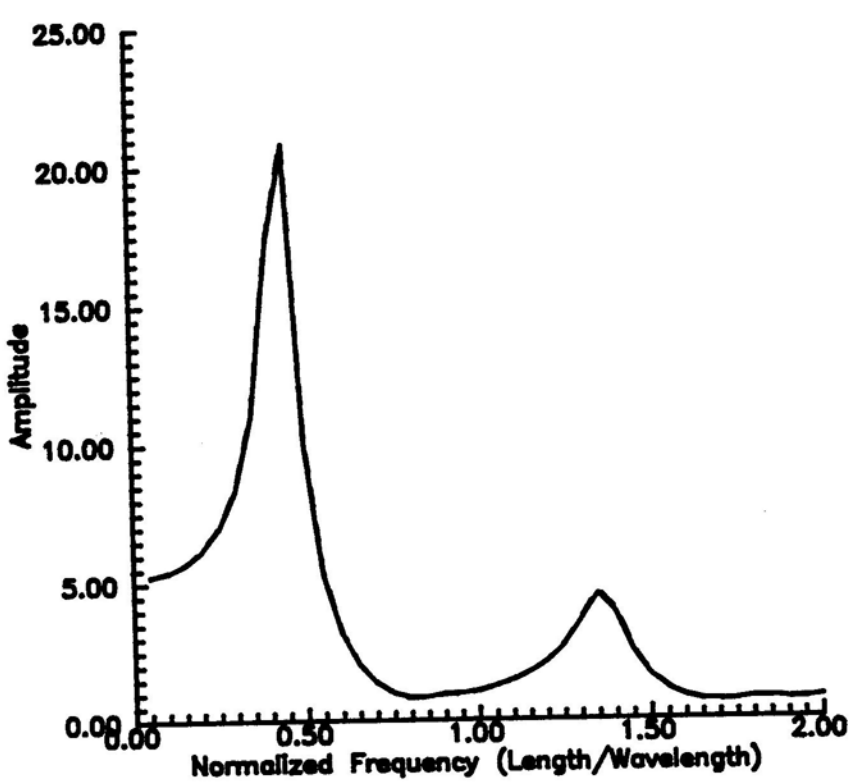

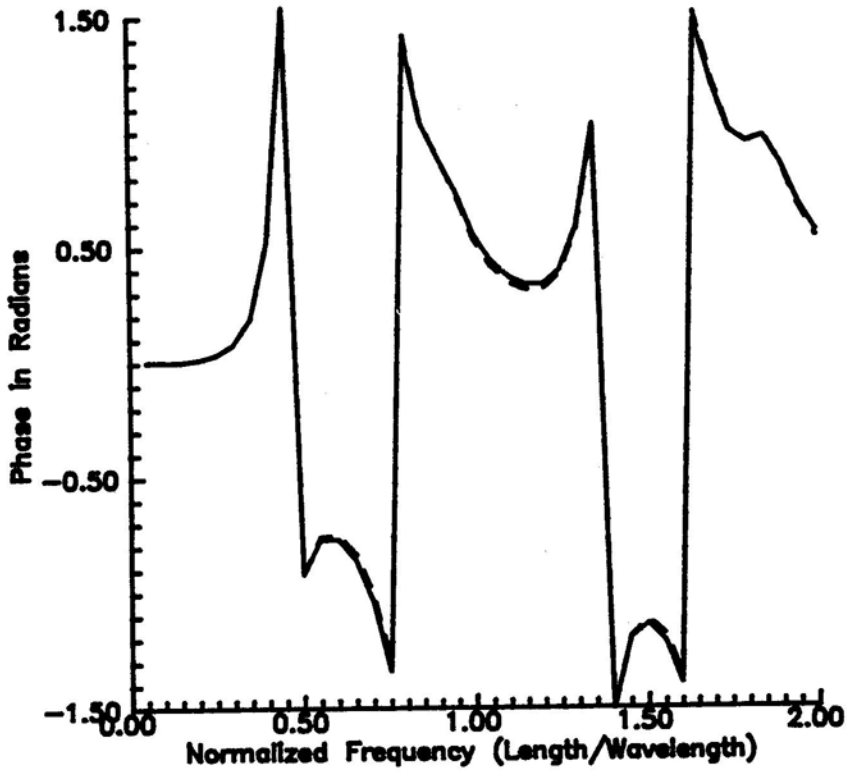

Figure 6. Comparison of the inverse method (–) vs. the eigenvalue method (– – –) for the $Y_{10,\,10}$ element of the admittance matrix.

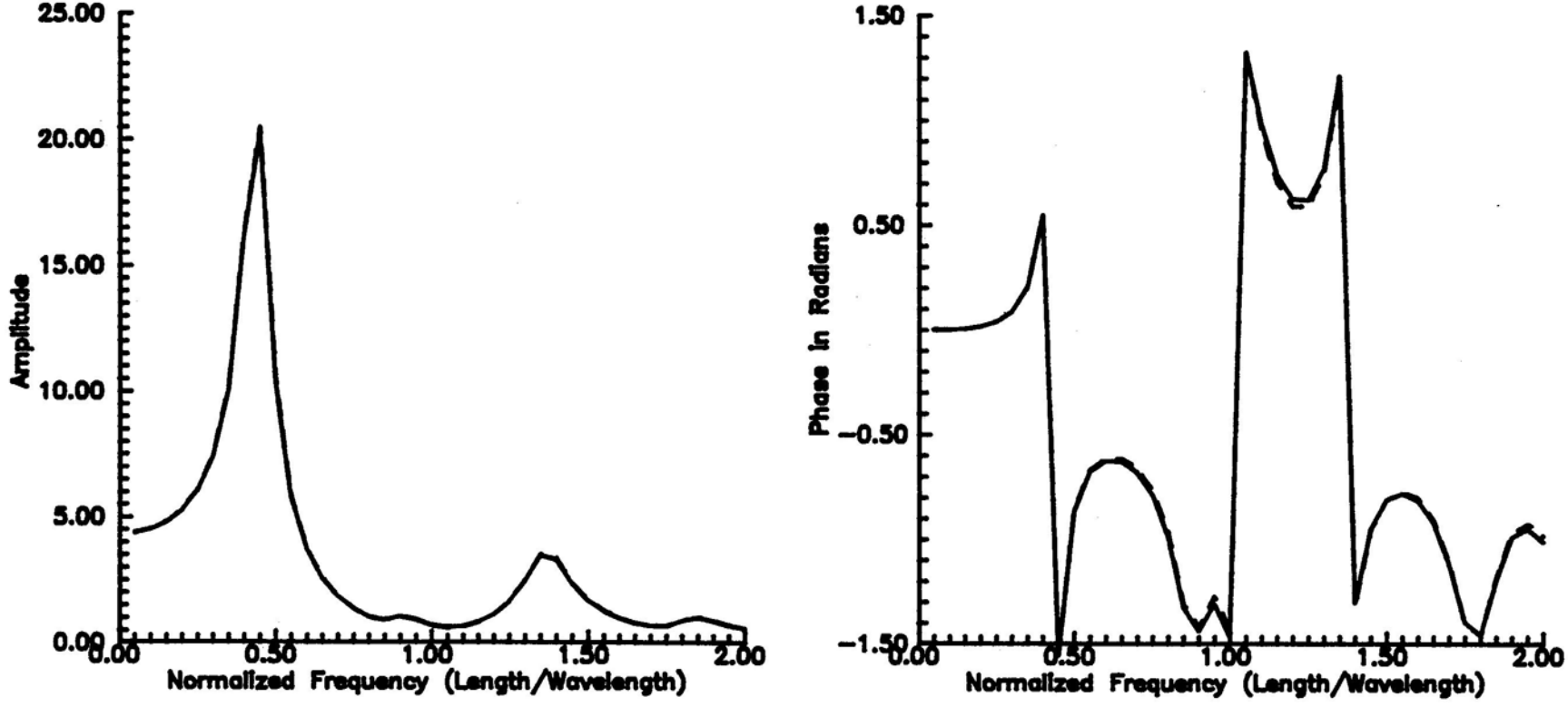

Figure 7. Comparison of the inverse method (–) vs. the eigenvalue method (– – –) for the $Y_{10,\,9}$ element of the admittance matrix.

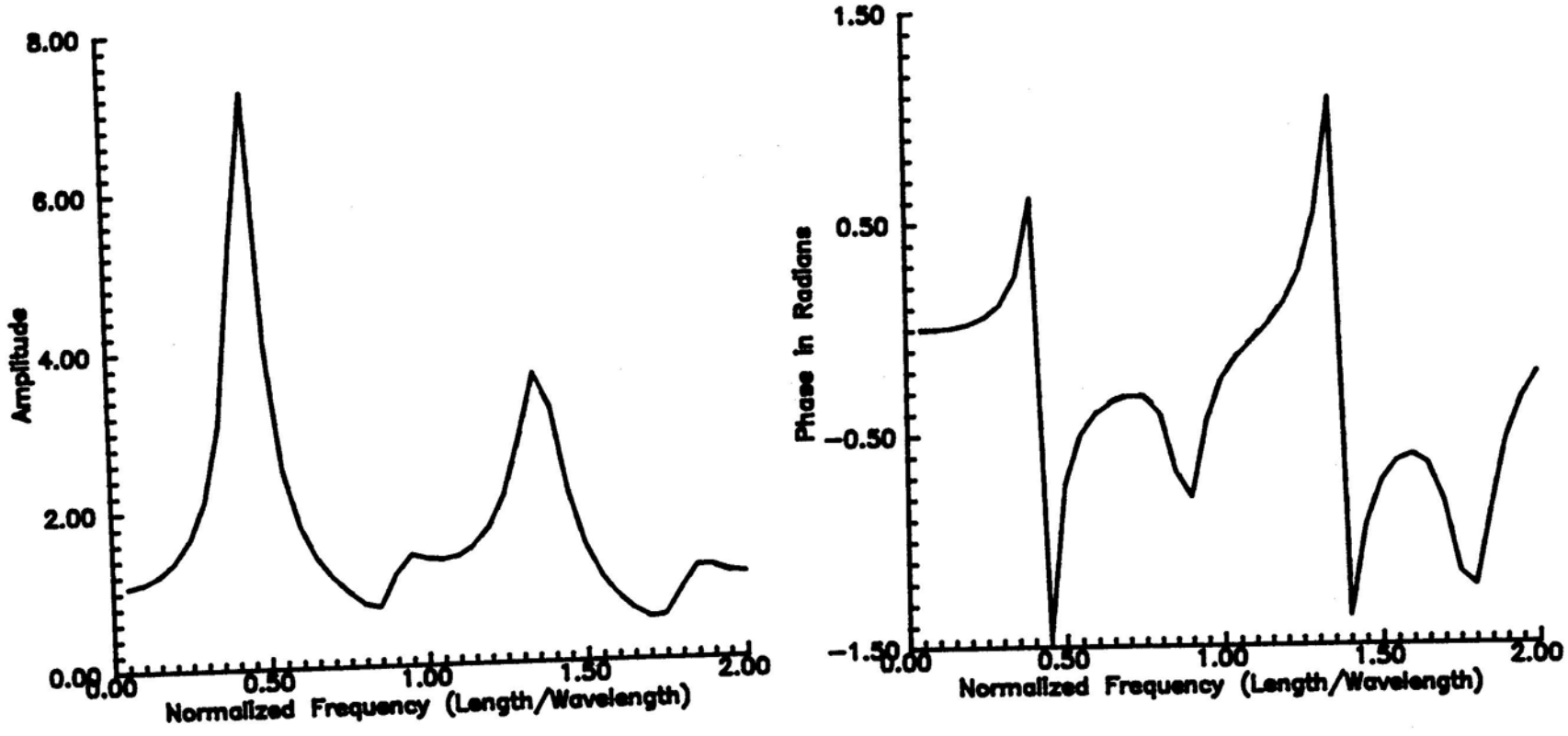

Figure 8. Comparison of the inverse method (–) vs. the eigenvalue method (– – –) for the $Y_{10,\,2}$ element of the admittance matrix.

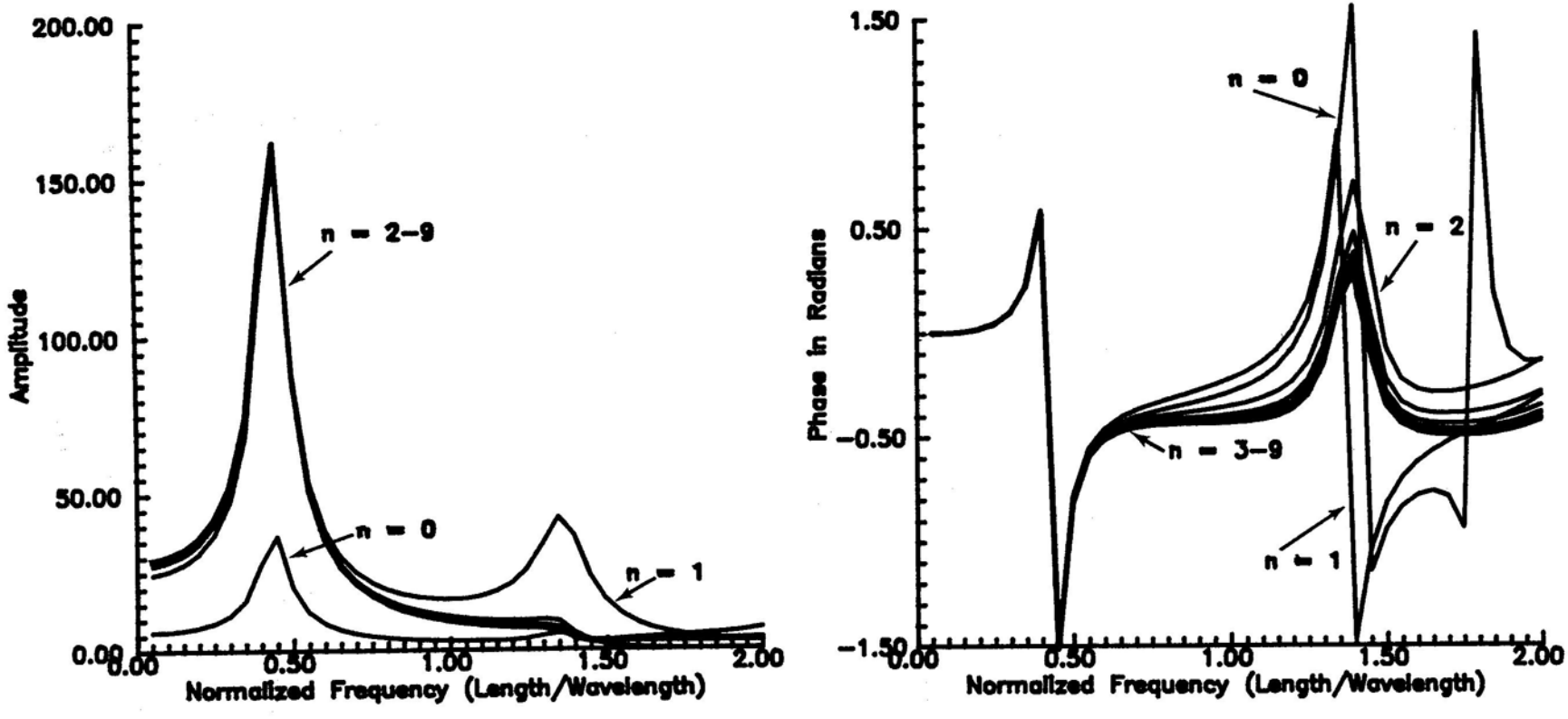

Figure 9. The first ten eigenvalues of the Y_1 matrix.

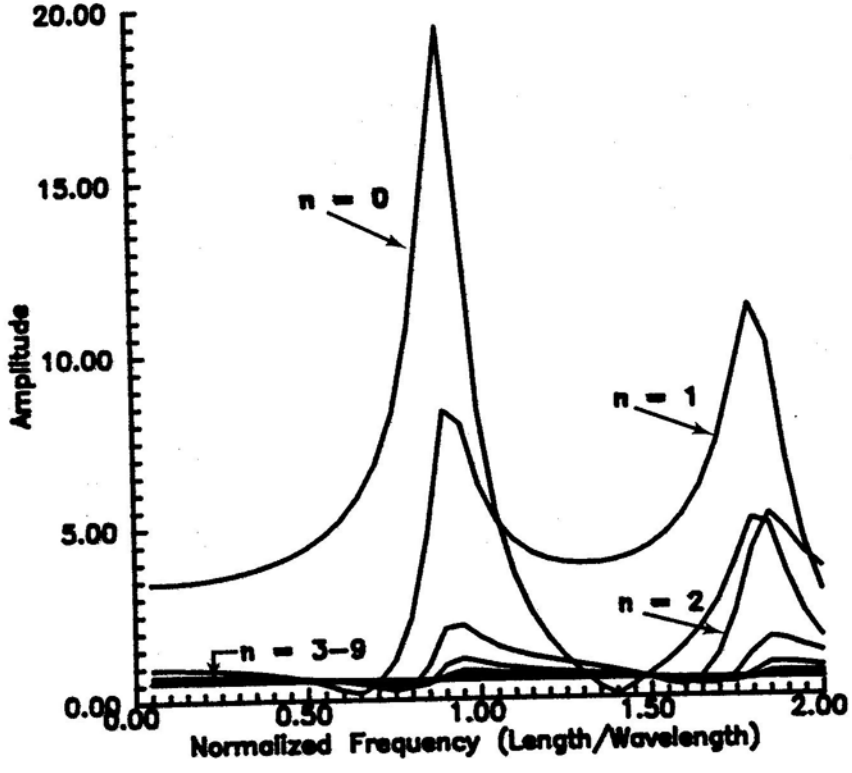

Figure 10. The amplitudes of the second ten eigenvalues for the Y_1 matrix.

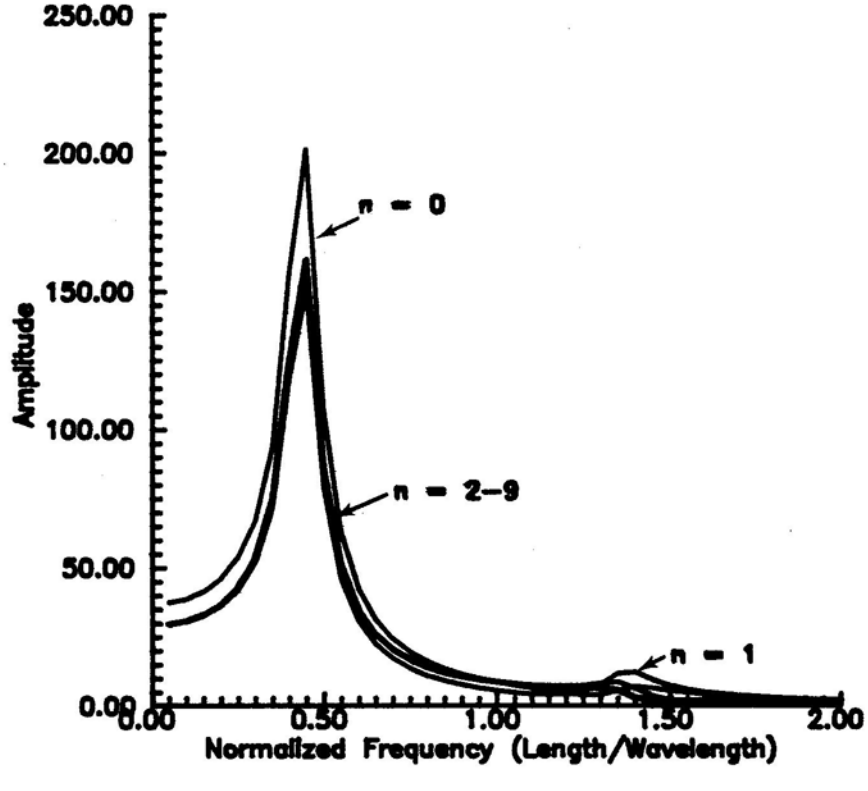

Figure 11. The amplitude of the first ten eigenvalues for the Y_2 matrix.

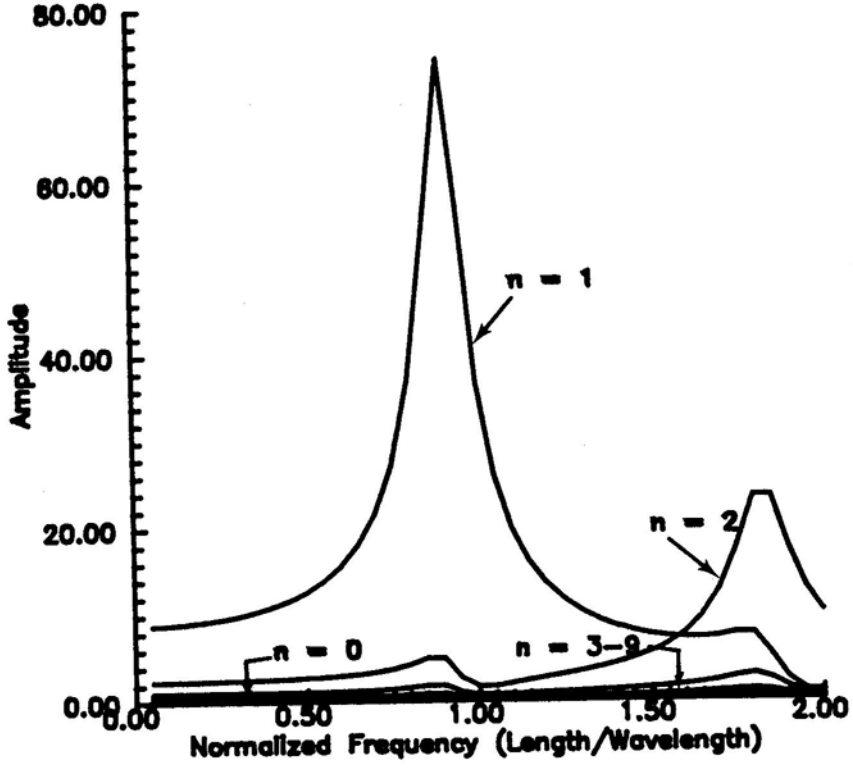

Figure 12. The amplitude of the second ten eigenvalues for the Y_2 matrix.

APPENDIX A

To prove that the impedance matrix, Z_w, can be partitioned into the sum of two commuting matrices as defined by equations (5), (6) and (7), we begin by writing Z_w in the form:

$$Z_w(f) = \sum_{n=0}^{N-1} \alpha_n(f)\, \phi_n \qquad (A.1)$$

where the α's are just frequency dependent scalars and the ϕ's are frequency independent NxN matrices of the form

$$\phi_0 = I \text{ (identity matrix)},$$

$$\phi_1 = \begin{bmatrix} 0&1&0&0&\cdots&0&0 \\ 1&0&1&0&\cdots&0&0 \\ 0&1&0&1&\cdots&0&0 \\ \cdot&\cdot&\cdot&\cdot&\cdot&\cdot&\cdot \\ \cdot&\cdot&\cdot&\cdot&\cdot&\cdot&\cdot \\ \cdot&\cdot&\cdot&\cdot&\cdot&\cdot&\cdot \\ 0&0&\cdots&1&0&1&0 \\ 0&0&\cdots&0&1&0&1 \\ 0&0&\cdots&0&0&1&0 \end{bmatrix}$$

$$\phi_2 = \begin{bmatrix} 0&0&1&0&0&\cdots&0&0 \\ 0&0&0&1&0&\cdots&0&0 \\ 1&0&0&0&1&\cdots&0&0 \\ \cdot&\cdot&\cdot&\cdot&\cdot&\cdot&\cdot&\cdot \\ \cdot&\cdot&\cdot&\cdot&\cdot&\cdot&\cdot&\cdot \\ \cdot&\cdot&\cdot&\cdot&\cdot&\cdot&\cdot&\cdot \\ 0&0&\cdots&1&0&0&0&1 \\ 0&0&\cdots&0&1&0&0&0 \\ 0&0&\cdots&0&0&1&0&0 \end{bmatrix}$$

.

.

.

$$\phi_{N-2} = \begin{bmatrix} 0\,0\cdots\cdots 0\,1\,0 \\ 0\,0\cdots\cdots 0\,0\,1 \\ \cdots\cdots\cdots \\ \cdots\cdots\cdots \\ \cdots\cdots\cdots \\ \cdots\cdots\cdots \\ \cdots\cdots\cdots \\ 1\,0\,0\cdots\cdots 0\,0 \\ 0\,1\,0\cdots\cdots 0\,0 \end{bmatrix}$$

$$\phi_{N-1} = \begin{bmatrix} 0\,0\cdots\cdots 0\,1 \\ 0\,0\cdots\cdots 0\,0 \\ \cdots\cdots\cdots \\ \cdots\cdots\cdots \\ \cdots\cdots\cdots \\ \cdots\cdots\cdots \\ \cdots\cdots\cdots \\ 0\,0\cdots\cdots 0\,0 \\ 1\,0\cdots\cdots 0\,0 \end{bmatrix}$$

$$\phi_N = 0 \text{ (null matrix).}$$

The ϕ's do not commute or

$$[\phi_n, \phi_m] = \phi_n\phi_m - \phi_m\phi_n \neq 0 \tag{A.2}$$

unless $n = m$ or $n = 0$ or $n = N$ or $m = 0$ or $m = N$. If we define two new sets of matrices, $\bar{\chi}_n$ and χ_n, by the relationships

$$\chi_n = \phi_n - \phi_{N-n} \tag{A.3}$$

and

$$\bar{\chi}_n = \phi_n + \phi_{N-n} \tag{A.4}$$

and add equations (A.3)and (A.4) we can write ϕ_n in terms of these new matrices or

$$\phi_n = (\chi_n + \bar{\chi}_n)/2. \tag{A.5}$$

substituting equation (A.5) into equation (A.1) yields

$$Z_w(f) = 1/2 \sum_{n=0}^{N-1} \alpha_n(f)\,\chi_n + 1/2 \sum_{n=0}^{N-1} \alpha_n(f)\,\bar{\chi}_n \tag{A.6}$$

and by defining

$$Z_1(f) = 1/2 \sum_{n=0}^{N-1} \alpha_n(f)\, \chi_n$$

and

$$Z_2(f) = 1/2 \sum_{n=0}^{N-1} \alpha_n(f)\, \bar{\chi}_n$$

equation (5) follows or

$$Z_w(f) = Z_1(f) + Z_2(f) \tag{5}$$

But

$$[\chi_n, \chi_m] = 0$$

and

$$[\bar{\chi}_n, \bar{\chi}_m] = 0$$

for all n and m. Therefore, equations (6) and (7) follow or

$$[Z_1(f_1), Z_1(f_2)] = 0 \tag{6}$$

and

$$[Z_2(f_1), Z_2(f_2)] = 0 \tag{7}$$

for all f_1 and f_2. One possible generalization of equation (A.5) to arbitrarily shaped wires was suggested by J. W.Williams [private communication]. This generalized form is given by

$$\phi_n = g\, \chi_n + (1-g)\, \bar{\chi}_n \tag{A.7}$$

where g is now a geometric shape factor. For a straight wire, $g = 1/2$ and equation (A.5) follows. For a wire loop, $g = 0$ and Z_w reduces to

$$Z_w(f) = \sum_{n=0}^{N-1} \alpha_n(f)\, \bar{\chi}_n \tag{A.8}$$

which is the form of the impedance matrix for a wire loop.

APPENDIX B

To show that the admittance matrix, Y_w, can be written in the form

$$Y_w = T_1 y_1 T_1^t + T_2 y_2 T_2^t \tag{18}$$

for the case of a 4x4 impedance matrix, we begin by writing the normalized impedance matrix, Z, given by

$$\begin{aligned} Z &= Z_w/\alpha_o \\ &= I_4 + X_4 \end{aligned} \tag{B.1}$$

where

$$X_4 = \beta_1\phi_1 + \beta_2\phi_2 + \beta_3\phi_3,$$

$$\beta_1 = \alpha_1/\alpha_0,\ \beta_2 = \alpha_2/\alpha_0,\ \beta_3 = \alpha_3/\alpha_0,$$

$$I_4 = \begin{bmatrix} 1&0&0&0 \\ 0&1&0&0 \\ 0&0&1&0 \\ 0&0&0&1 \end{bmatrix} \qquad \phi_1 = \begin{bmatrix} 0&1&0&0 \\ 1&0&1&0 \\ 0&1&0&1 \\ 0&0&1&0 \end{bmatrix}$$

$$\phi_2 = \begin{bmatrix} 0&0&1&0 \\ 0&0&0&1 \\ 1&0&0&0 \\ 0&1&0&0 \end{bmatrix} \qquad \phi_3 = \begin{bmatrix} 0&0&0&1 \\ 0&0&0&0 \\ 0&0&0&0 \\ 1&0&0&0 \end{bmatrix}$$

and the α's are the frequency dependent coefficients defined by equation (A.1) of Appendix A. The Cayley–Hamilton theorem states that a matrix satisfies its own characteristic equation or

$$Z^4 + C_1Z^3 + C_2Z^2 + C_3Z + C_4 = 0 \tag{B.2}$$

where the C's are scalars. Therefore,the inverse of Z, $Y = Z^{-1}$, is given by

$$\begin{aligned} Y &= -[C_3 + C_2Z + C_1Z_2 + Z^3]/C_4 \\ &= -[(I_4+C_1+C_2+C_3) + (C_2+2C_1+3)X_4 + (C_1+3)X_4^2 + X_4^3]/C_4 \end{aligned} \tag{B.3}$$

We have already shown in Appendix A that the first two terms of equation (A.3) can be reduced to the desired form; therefore we will address only the X_4^2 and X_4^3 terms.

X_4^2:

Expanding X_4^2 in terms of its primitive matrices we have

$$X_4^2 = \beta_1^2 \phi_1^2 + \beta_2^2 \phi_2^2 + \beta_3^2 \phi_3^2 + \beta_1 \beta_2 (\phi_1\phi_2 + \phi_2\phi_1)$$
$$\beta_1 \beta_3 (\phi_1\phi_3 + \phi_3\phi_1) + \beta_2\beta_3 (\phi_2\phi_3 + \phi_3\phi_2) \qquad \text{(B.4)}$$

with

$$\phi_1^2 = 2I_4 - E_4 + \phi_2$$
$$\phi_2^2 = I_4$$
$$\phi_3^2 = E_4\phi_3$$
$$\phi_1\phi_2 + \phi_2\phi_1 = 2E_4 + 2E_4\phi_2$$
$$\phi_1\phi_3 + \phi_3\phi_1 = \phi_2$$
$$\phi_2\phi_3 + \phi_3\phi_2 = E_4\phi_2$$

where

$$E_4 = \begin{bmatrix} 0 & 0 & 0 & 1 \\ 0 & 0 & 1 & 0 \\ 0 & 1 & 0 & 0 \\ 1 & 0 & 0 & 0 \end{bmatrix}.$$

X_4^3:

Similarly, expanding X_4^3 in terms of its primitive matrices we have

$$\begin{aligned} X_4^3 \quad &= \beta_1^3\phi_1^3 + \beta_2^3\phi_2^3 + \beta_3^2\phi_3^2 + \beta_1\beta_2^2 (\phi_1\phi_2^2 + \phi_2\phi_1\phi_2 + \phi_2^2\phi_1) \\ &+ \beta_1\beta_3^2(\phi_1\phi_3^2 + \phi_3\phi_1\phi_3 + \phi_3^2\phi_1) + \beta_1^2\beta_2(\phi_2\phi_1^2 + \phi_1\phi_2\phi_1 + \phi_1^2\phi_2) \\ &+ \beta_2\beta_3^2(\phi_2\phi_3^2 + \phi_3\phi_2\phi_3 + \phi_3^2\phi_2) + \beta_1^2\beta_3(\phi_3\phi_1^2 + \phi_1\phi_3\phi_1 + \phi_1^2\phi_3) \\ &+ \beta_2^2\beta_3(\phi_3\phi_2^2 + \phi_2\phi_3\phi_2 + \phi_2^3\phi_3) \\ &+ \beta_1\beta_2\beta_3(\phi_1\phi_2\phi_3 + \phi_1\phi_3\phi_2 + \phi_2\phi_1\phi_3 + \phi_2\phi_3\phi_1 + \phi_3\phi_1\phi_2 + \phi_3\phi_2\phi_1) \end{aligned} \qquad \text{(B.5)}$$

with

$$\phi_1^3 = 2\phi_1 + E_4$$
$$\phi_2^3 = \phi_2$$
$$\phi_3^3 = \phi_3$$
$$\phi_1\phi_2^3 + \phi_2\phi_1\phi_2 + \phi_2^2\phi_1 = \phi_1 + E_4 + 2E_4\phi_2$$
$$\phi_1\phi_3^2 + \phi_3\phi_1\phi_3 + \phi_3^2\phi_1 = E_4\phi_2$$
$$\phi_2\phi_1^2 + \phi_1\phi_2\phi_1 + \phi_1^2\phi_2 = 4I_4 + 4\phi_2 - 2E_4\phi_3$$

$\phi_2\phi_3^2 + \phi_3\phi_2\phi_3 + \phi_3^2\phi_2 = \phi_2$

$\phi_3\phi_1^2 + \phi_1\phi_3\phi_1 + \phi_1^2\phi_3 = \phi_1 + 2\phi_3$

$\phi_3\phi_2^2 + \phi_2\phi_3\phi_2 + \phi_2^2\phi_3 = \phi_3 + E_4$

$\phi_1\phi_2\phi_3 + \phi_1\phi_3\phi_2 + \phi_2\phi_1\phi_3 + \phi_2\phi_3\phi_1 + \phi_3\phi_1\phi_2 + \phi_3\phi_2\phi_1 = 2I_4 + \phi_2 + 2E_4\phi_3.$

Collecting terms, equation (B.3) can now be written in the form

$$Y = \sum_{n=0}^{3} \Gamma_n(f;I_4,E_4)\phi_n. \tag{B.6}$$

But since

$$[I_4,\phi_n] = 0$$

and

$$[E_4,\phi_n] = 0$$

for all n, the results of Appendix A also hold for equation (B.6) and equation (18) follows:

$$Y_w = T_1 y_1 T_1^t + T_2 y_2 T_2^t \tag{18}$$

Comparison of Methods for Far Zone Scattering from a Flat Plate and Cube *

R. J. Marhefka
T. J. Brinkley
The Ohio State University ElectroScience Laboratory
Department of Electrical Engineering
Columbus, Ohio 43212

Abstract

Different high frequency methods are used to analyze the backscatter and bistatic scattering from a flat plate and a cube. The results are compared and their validity is checked against method of moments and measurements. A newly developed far zone corner diffraction coefficient based on the latest equivalent current and PTD solutions cast in UTD form is discussed.

I Introduction

The validity of various methods for determining the far zone bistatic scattering from a flat plate and convex flat plate structure such as a cube is presented in this paper. This is accomplished by comparing the methods in various basic situations. The specific techniques to be compared in this study are the classical equivalent currents with "stripping" [1], the previous corner diffraction coefficient [1], the newly developed equivalent currents by Michaeli [2], and an extension to this method cast in the form of

*This work was supported in part by Contract No. F33615-86-K-1023 between Wright Patterson Air Force Base and The Ohio State University Research Foundation.

a Uniform Geometrical Theory of Diffraction (UTD) far zone corner diffraction coefficient [3]. In addition, the Method of Moments (MOM) using the Electromagnetic Surface Patch (ESP) code [4] and measurements from The Ohio State University ElectroScience Laboratories compact range are used to further validate the results.

A recent paper by Ludwig [5] compares three methods for backscattering from a cube, that is, the MOM using the Numerical Electromagnetics Code (NEC-MOM), physical optics (PO), and the previous UTD corner diffraction solution. In this paper, it will be shown that methods which give comparable results for backscatter can differ for bistatic scattering. The emphasis here is to present basic examples that can be used to validate existing codes and to suggest a numerically efficient and accurate method for convex flat plate structures to first order.

An approximate expression for the far zone field scattered by the vertex of a finite perfectly conducting wedge is presented in this regard. The solution is cast in the form of the UTD and is based on asymptotic equivalent currents found using modified Physical Theory of Diffraction (PTD) concepts [2,3]. The faces of the wedge must be flat (the normal to each individual face is a constant everywhere on the face except at the edge) and the edges must be straight. For plane wave incidence from an arbitrary direction, the first order contribution from each vertex to the far zone scattered field is obtained.

Since diffraction is a local phenomena at high frequencies the results obtained for a finite wedge may be applied to much more complex bodies made up of simple shapes. The field scattered by a three-dimensional shape constructed from flat plates may be approximated to first order as the sum of the contributions from each individual corner. The first order solution should be reasonably accurate in or near the specular regions as long as the object is convex. A convex body is defined here as a closed surface made up of flat plates such that all of the exterior wedge angles, taken between faces and exterior to the surface, are greater than 180 degrees. A simple example of an object that does not meet this requirement is a corner reflector. In this case, the effect of the interaction between the faces must be taken into account. Higher order effects such as double diffraction [6] and edge waves [7] are not considered here.

Note that the results presented in this paper are for a parallel ray type

solution, that is, for a radar cross section result. The NEC - Basic Scattering Code (NEC-BSC)[8] is a near zone formulated code, that is it has a finite range involved. The UTD solutions are slightly different for this non-parallel ray case. The capabilities of the NEC-BSC and a comparable far zone code called the RCS-BSC are discussed in Reference [9].

II Theoretical Background

There are many approximate solutions to the scattered field from a finite perfectly conducting wedge. Physical Optics and its extension the Physical Theory of Diffraction [10] is surface and edge current based. Geometrical Optics (GO) and its extensions the Geometrical Theory of Diffraction (GTD) [11] and the Uniform Geometrical Theory of Diffraction [12] are ray based. The Method of Equivalent Currents (MEC) [13] is an intermediate type solution that was developed to handle caustic regions in the GTD. This has been augmented with the concept of stripping to provide better answers for flat plate problems [1]. Recently, Michaeli [14] showed a more rigorous approach in deriving equivalent currents. This was shown to be related to the incremental length method of Mitzner [15] by Knott [16]. These equivalent currents still had singularity problems that have been remedied by Michaeli [2] using a skewed coordinate system. Ufimtsev also derived a similar solution [17,18].

The above solutions can be cast in a corner diffraction coefficient form. These UTD ray type solutions have the advantage of being efficient for far zone flat plate problems since only the fields scattered from the corners need to be added. It also has the advantage that the results correlate to the scattering centers seen in high resolution measurements. Just the corner diffraction coefficient forms are outlined in this section.

A previous diffraction coefficient for a corner formed by the intersection of two straight edges was derived by Burnside and Pathak [1]. It is based on the asymptotic evaluation of the radiation integral containing the equivalent currents of Ryan and Peters [13]. The result was then empirically modified so that the diffraction coefficient would not change sign abruptly as it passes through the false shadow boundaries. It was derived for spherical wave incidence and remains valid for cases when the diffraction point is near the

corner since the integral was evaluated for a saddle point near an end point; however, only the far zone result is shown here. The corner diffracted field due to one corner and one edge in the case of plane wave incidence and a far zone receiver is given by

$$
\begin{aligned}
\begin{bmatrix} E^c_{\beta_o} \\ E^c_{\phi} \end{bmatrix} &= -\begin{bmatrix} E^i_{\beta'_o}(Q_c)\, D^c_s(\phi,\phi',\beta_o,\beta_{oc}) \\ E^i_{\phi'}(Q_c)\, D^c_h(\phi,\phi',\beta_o,\beta_{oc}) \end{bmatrix} \frac{e^{-jks}}{s} \\
\begin{bmatrix} D^c_s \\ D^c_h \end{bmatrix} &= \mp \begin{bmatrix} C_s(Q_e) \\ C_h(Q_e) \end{bmatrix} \frac{\sqrt{\sin\beta_o \sin\beta_{oc}}}{(\cos\beta_{oc}+\cos\beta_o)} \frac{e^{-j\frac{\pi}{4}}}{\sqrt{2\pi k}} \qquad (1) \\
C_{s,h}(Q_e) &= \frac{-e^{-j\frac{\pi}{4}}}{2n\sqrt{2\pi k}\sin\beta_a} \{[D^c_o(\phi-\phi') + D^c_n(\phi-\phi')] \\
&\mp [D^c_o(\phi+\phi') + D^c_n(\phi+\phi')]\} \\
D^c_{o,n}(\psi) &= D_{o,n}(\psi)\left| F\left[\frac{\sin^2\beta_a a^{\mp}(\psi)}{2\pi a(\beta_{oc}+\beta_o)}\right]\right| \\
a(\beta) &= 2\cos^2\left(\frac{\beta}{2}\right), \quad a^{\mp}(\psi) = 2\cos^2\left(\frac{2n\pi N^{\mp}-\psi}{2}\right)
\end{aligned}
$$

where $N^{\mp}$ is the integer which most nearly satisfies $2n\pi N^{\mp} - \psi = \mp\pi$, and

$$
\begin{aligned}
D_{o,n}(\psi) &= \cot\left[\frac{\pi \mp \psi}{2n}\right] \\
\beta_a &= \frac{\pi + \beta_o - \beta oc}{2} \\
F(x) &= 2j\left|\sqrt{x}\right| e^{jx} \int_{|\sqrt{x}|}^{\infty} e^{-j\tau^2} d\tau
\end{aligned}
$$

where the angles are shown in Figure 1. The sign on the diffraction coefficient may be plus or minus depending on which endpoint of the edge is being considered. The correct sign in front of the $C_{s,h}$ terms in Equation 1 is chosen based on the direction edge vector shown in Figure 1.

It is assumed that the incident field, and therefore the scattered field, is a time harmonic field with time dependence given by $e^{j\omega t}$, which is suppressed.

The new far zone corner diffraction solution is based on the PTD and cast into the form of the MEC and then into a UTD diffraction coefficient. The details of this procedure are given in [3], while a brief outline of how this

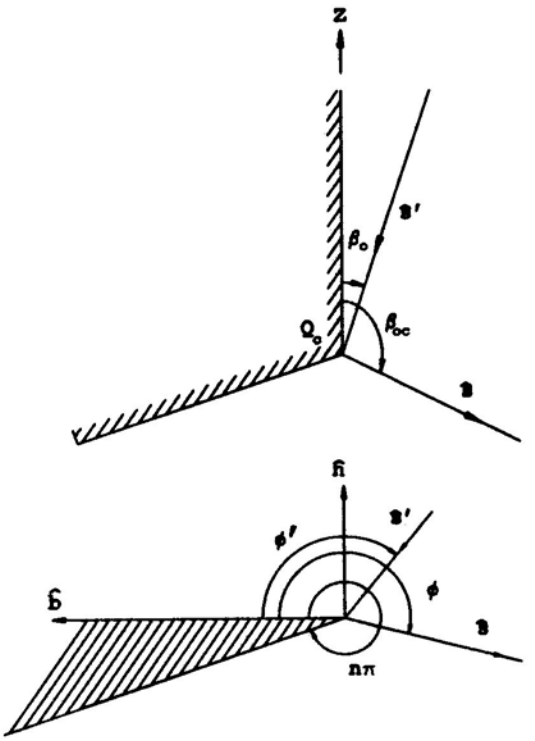

Figure 1: Definition of angles for the Previous Corner Diffraction Coefficients.

is done follows. The PO is first used to approximate the currents resulting in a double integral over the surface. Stokes theorem is then applied to reduce the equation to a line integral [19,20]. The Michaeli currents are added to produce a total first order MEC result. This integral is then evaluated using the method of stationary phase to obtain the contribution from each corner [21].

The new corner diffraction coefficients are given in a form similar to previous expressions for diffraction coefficients:

$$\begin{bmatrix} E^c_\beta \\ E^c_\phi \end{bmatrix} = \begin{bmatrix} D^c_s & D^c_2 \\ 0 & D^c_h \end{bmatrix} \begin{bmatrix} E^i_{\beta'} \\ E^i_{\phi'} \end{bmatrix} \frac{e^{-jks}}{s}$$

$$D^c_{s,h,2} = \pm \frac{j}{4\pi k} \left(\frac{1}{\cos\beta - \cos\beta'} \right) \left[d^{LPO}_{s,h,2} + d^{UTD}_{s,h,2} - d^{PO}_{s,h,2} \right]$$

where the plus or minus sign is chosen depending on which endpoint contribution is being calculated. The minus sign is used for the corner contribution associated with the negative t-axis, while the plus sign is used for the corner contribution associated with the positive t-axis. The edge

fixed coordinates shown in Figure 2 are chosen such that $\hat{n}$ is the outward normal of the O-face, $\hat{t}$ is tangent to the edge, the positive b-axis lies on the O-face, and $\hat{t} = \hat{b} \times \hat{n}$. The expressions for $d^{LPO}_{s,h,2}$, $d^{UTD}_{s,h,2}$, and $d^{PO}_{s,h,2}$ are given by (O-face contribution only)

$$
\begin{aligned}
d^{LPO}_{\substack{s \\ h,2}} &= \frac{1}{2} U^i c_{\substack{s \\ h,2}}(\gamma, \phi') \left\{ \left[\cot\left(\frac{\pi - (\gamma - \phi')}{4} \right) - \cot\left(\frac{\pi + (\gamma - \phi')}{4} \right) \right] \right. \\
&\mp \left. \left[\cot\left(\frac{\pi - (\gamma + \phi')}{4} \right) - \cot\left(\frac{\pi + (\gamma + \phi')}{4} \right) \right] \right\} \\
d^{UTD}_{\substack{s \\ h,2}} &= \frac{1}{n} c_{\substack{s \\ h,2}}(\alpha, \pi - \alpha) \left[\cot\left(\frac{\pi - (\alpha - \phi')}{2n} \right) \right. \\
&\mp \left. \cot\left(\frac{\pi - (\alpha + \phi')}{2n} \right) \right] \\
d^{PO}_{\substack{s \\ h,2}} &= \frac{1}{2} U^i c_{\substack{s \\ h,2}}(\alpha, \phi') \left\{ \left[\cot\left(\frac{\pi - (\alpha - \phi')}{4} \right) - \cot\left(\frac{\pi + (\alpha - \phi')}{4} \right) \right] \right. \\
&\mp \left. \left[\cot\left(\frac{\pi - (\alpha + \phi')}{4} \right) - \cot\left(\frac{\pi + (\alpha + \phi')}{4} \right) \right] \right\}
\end{aligned}
$$

where the + sign is associated with d^{LPO}_h, d^{LPO}_2, d^{UTD}_h, d^{UTD}_2, d^{PO}_h, and d^{PO}_2 while the − sign is associated with the d^{LPO}_s, d^{UTD}_s, and d^{PO}_s terms. The functions c_s, c_h, and c_2 are given by

$$
\begin{aligned}
c_s(\delta, \epsilon) &= -\frac{\sin\beta}{\sin\beta'} \\
c_h(\delta, \epsilon) &= \frac{\sin\phi}{\sin\delta} \\
c_2(\delta, \epsilon) &= -\frac{\sin\beta}{\sin\delta} (\cot\beta \cos\phi + \cot\beta' \cos\epsilon) \\
U^i &= \begin{cases} 0 & , \pi - \phi' < 0 \\ 1 & , \pi - \phi' > 0 \end{cases} \\
\cos\gamma &= \frac{\sin\beta \cos\phi}{\sin\beta'} + \frac{(\cos\beta - \cos\beta')^2}{\sin\beta'(\sin\beta \cos\phi + \sin\beta' \cos\phi')} \\
\cos\alpha &= \frac{\sin\beta \cos\phi}{\sin\beta'} + \frac{(\cos\beta - \cos\beta')\cos\beta'}{\sin^2\beta'}
\end{aligned}
$$

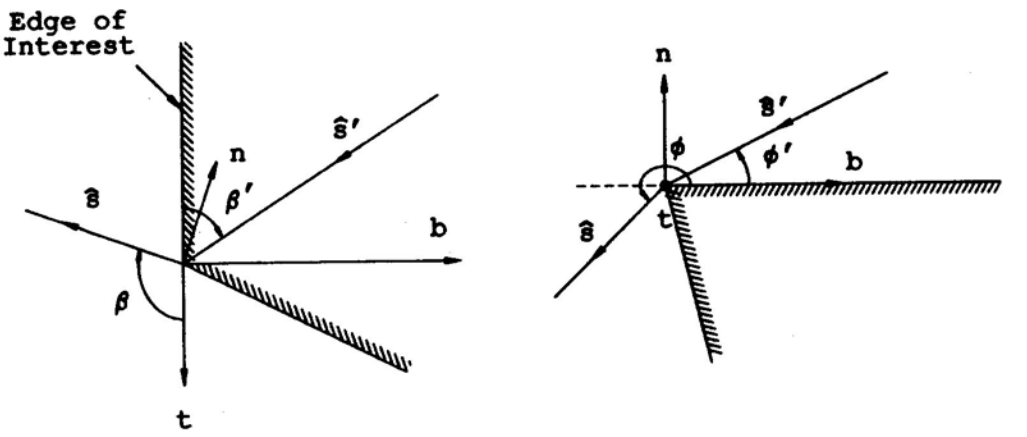

Figure 2: Definition of the Angles used in the New Corner Diffraction Coefficients.

from which γ and α are determined using

$$\cos^{-1}\mu = -j\ln\left(\mu+\sqrt{\mu^2-1}\right)$$

$$\sqrt{\mu^2-1} = \begin{cases} -\left|\sqrt{\mu^2-1}\right| & \mu<-1 \\ j\left|\sqrt{1-\mu^2}\right| & -1\le\mu\le 1 \\ \left|\sqrt{\mu^2-1}\right| & \mu>1 \end{cases}$$

Notice that γ and α do not correspond to physical angles and become complex for some cases. The angles β', ϕ', β, and ϕ are defined in Figure 2. Since only convex structures are considered here proper shadowing of the rays is fairly simple. The shadowing of the incident field is accounted for by $\vec{E}^i_{\beta'}$ and $\vec{E}^i_{\phi'}$ which are the components of the GO incident field. The shadowing of the diffracted ray is more complicated. The contributions from the LPO and PO components, $d^{LPO}_{h,s,2}$ and $d^{PO}_{h,s,2}$, are present everywhere. The UTD components, $d^{UTD}_{h,s,2}$, are shadowed like diffracted fields. They do not contribute if the observation point is inside the wedge ($\phi > n\pi$).

For the special case of a flat plate ($n = 2$) the contribution from both

faces may be found using

$$
\begin{aligned}
d_{\substack{s\\h,2}}^{LPO} &= \frac{1}{2}S^i c_{\substack{s\\h,2}}(\gamma,\phi')\left\{\left[\cot\left(\frac{\pi-(\gamma-\phi')}{4}\right)-\cot\left(\frac{\pi+(\gamma-\phi')}{4}\right)\right]\right. \\
&\mp \left.\left[\cot\left(\frac{\pi-(\gamma+\phi')}{4}\right)-\cot\left(\frac{\pi+(\gamma+\phi')}{4}\right)\right]\right\} \\
d_{\substack{s\\h,2}}^{UTD} &= \frac{1}{n}c_{\substack{s\\h,2}}(\alpha,\pi-\alpha)\left\{\left[\cot\left(\frac{\pi-(\alpha-\phi')}{4}\right)+\cot\left(\frac{\pi+(\alpha-\phi')}{4}\right)\right]\right. \\
&\mp \left.\left[\cot\left(\frac{\pi-(\alpha+\phi')}{4}\right)+\cot\left(\frac{\pi+(\alpha+\phi')}{4}\right)\right]\right\} \\
d_{\substack{s\\h,2}}^{PO} &= \frac{1}{2}S^i c_{\substack{s\\h,2}}(\alpha,\phi')\left\{\left[\cot\left(\frac{\pi-(\alpha-\phi')}{4}\right)-\cot\left(\frac{\pi+(\alpha-\phi')}{4}\right)\right]\right. \\
&\mp \left.\left[\cot\left(\frac{\pi-(\alpha+\phi')}{4}\right)-\cot\left(\frac{\pi+(\alpha+\phi')}{4}\right)\right]\right\} \\
S^i &= \begin{cases} -1 & ,\pi-\phi'<0 \\ 1 & ,\pi-\phi'>0 \end{cases}
\end{aligned}
$$

where γ, α, and the other variables have been defined previously.

It is interesting to note that by writing the equations for the Michaeli equivalent currents and the new corner diffraction coeffients in cotangent form provide more insight into the connection of the new solutions with the previous methods. The new parameters separate out the optics currents and diffraction currents. This separation manifests itself in new parameters for the ϕ angles. They arise from the asymptotic evaluation of the currents in the skewed coordinate system chosen in physically meaningful directions. The LPO factor (γ) is related to the projection of the average of the incident and diffraction planes on to the plane of the plate [3]. The PO and UTD factor (α) relates to the projection of the Keller diffraction cone on to the plane of the plate. It is easy to see in this form that in the Keller directions the LPO and PO cancel, leaving the UTD result formally used in many solutions.

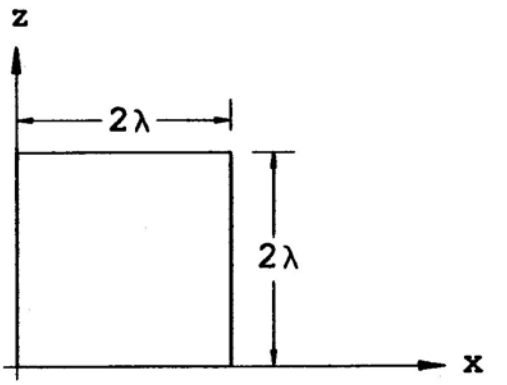

Figure 3: Two wavelength plate in the x-z plane.

III Comparisons

The first example compares the Ryan and Peters equivalent currents, the previous and new corner diffraction solutions. The simple example of backscatter from a two wavelength square plate lying in the x-z plane, as shown in Figure 3, is used. This illustrates that for backscatter these different methods produce very similar results, except for the very low level regions.

The co-polarized fields, in the principal plane, calculated using the three different methods are shown in Figures 4 and 5. All three methods give essentially the same results for the principal plane pattern cuts shown here. This is not surprising since the major contributions to the fields are the scattering from the two edges in their Keller cone directions. The new corner diffraction solution reduces to the Ryan and Peters equivalent current solution for points on the Keller cone [3], and the previous corner diffraction solution is essentially the same as Ryan and Peters equivalent current solution for most regions of space. The results in Figure 5 are for the horizontal ($\sigma_{\phi\phi}$) polarization. For a knife edged plate such as this, the scattered field should be zero in the plane of the plate. Note that this is not the case in

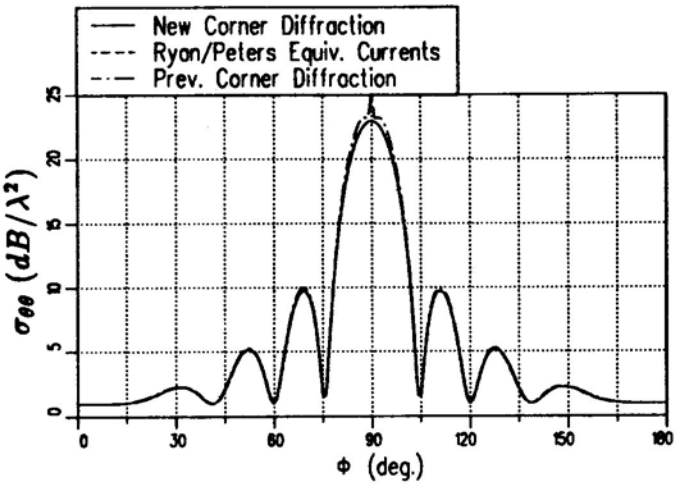

Figure 4: Backscatter from a 2 wavelength plate ($\theta = 90°$ pattern).

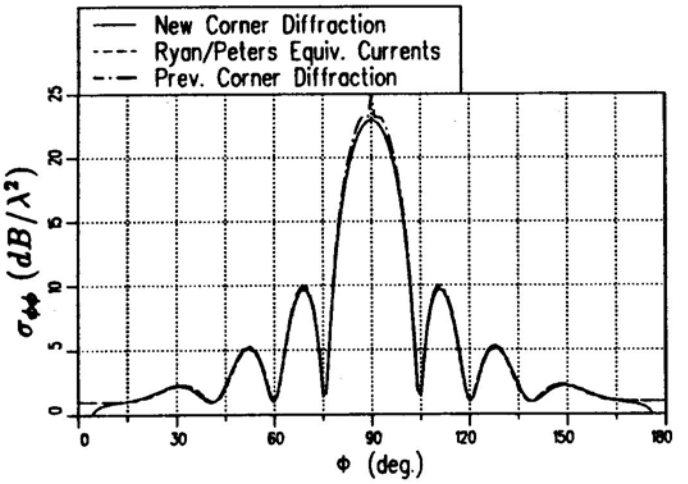

Figure 5: Backscatter from 2 wavelength plate ($\theta = 90°$ pattern).

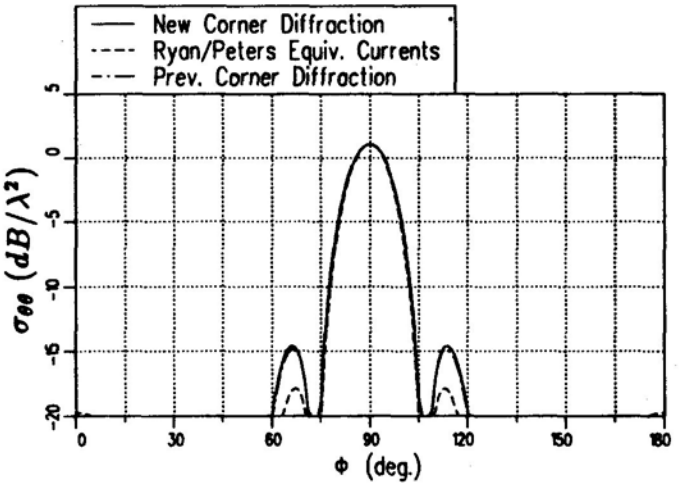

Figure 6: Backscatter from 2 wavelength plate ($\theta = 60°$ pattern).

these first order results. The higher order terms (i.e. the double, triple etc. diffractions) produce the null for this polarization when they are included.

For patterns away from the principal plane, the higher levels are the same but the lower levels differ. This is illustrated by taking a conical cut ($\theta = 60°$) for the two wavelength plate. The results for the same three methods used previously are shown in Figures 6 and 7. In this case the methods agree well for the main lobe, however, they differ in the lower levels of the pattern.

The differences in the three methods mentioned earlier are greatly increased for bistatic scattering problems. The bistatic scattering from a square plate two wavelengths on a side is examined to illustrate the point. The complete scattering matrix (all four values of σ) is found for a plate in the x-y plane with a fixed source located at $\theta^i = 45°$ and $\phi^i = 0°$ as shown in Figure 8. The results for the $\phi = 60°$ pattern cut are compared with the previous corner diffraction solution and Method of Moment calculations for co-polarized fields in Figures 9 and 10. Similarly the results for the cross-polarized fields are given in Figure 11 and Figure 12. Overall the new solution agrees well with the Method of Moment calculations and does not exhibit the discontinuities which appear near $\theta = 240°$ and $\theta = 300°$

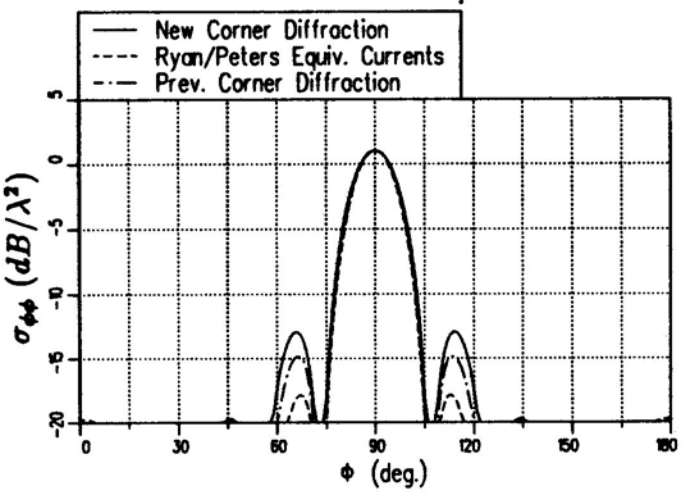

Figure 7: Backscatter from a 2 wavelength plate ($\theta = 60°$ pattern).

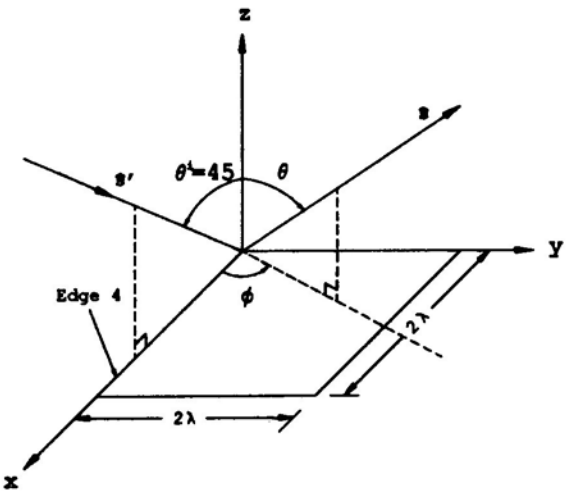

Figure 8: 2λ square plate in the x-y plane with a fixed source at $\theta^i = 45°$ and $\phi^i = 0$.

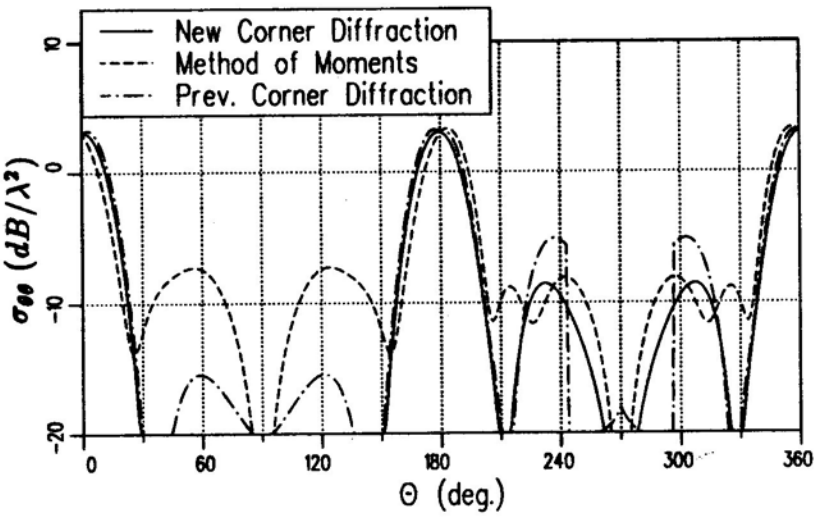

Figure 9: Co-polarized RCS in the $\phi = 60°$ plane of a 2λ square plate with a $\hat{\theta}^i$ polarized fixed source at $\theta^i = 45°$, $\phi^i = 0°$.

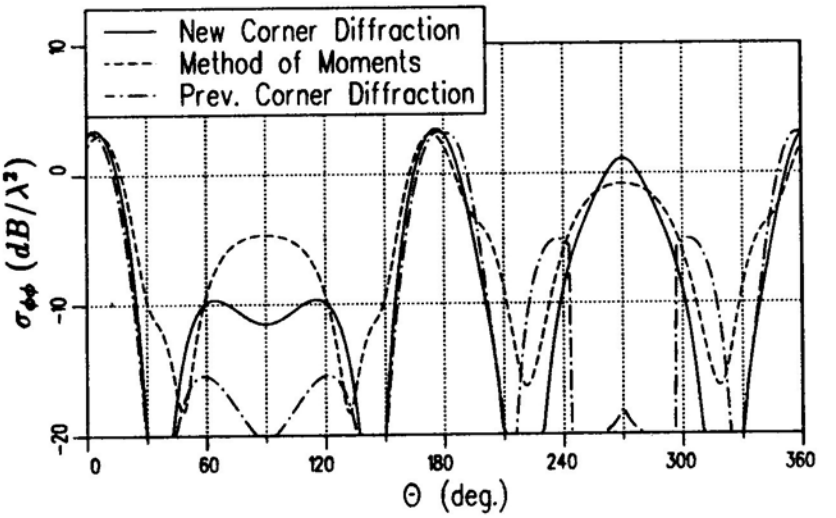

Figure 10: Co-polarized RCS in the $\phi = 60°$ plane of a 2λ square plate with a $\hat{\phi}^i$ polarized fixed source at $\theta^i = 45°$, $\phi^i = 0°$.

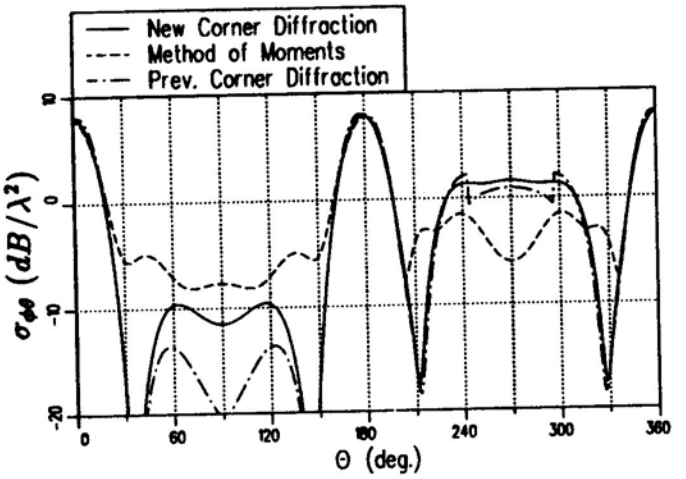

Figure 11: Cross-polarized RCS in the $\phi = 60°$ plane of a 2λ square plate with a $\hat{\theta}^i$ polarized fixed source at $\theta^i = 45°$, $\phi^i = 0°$.

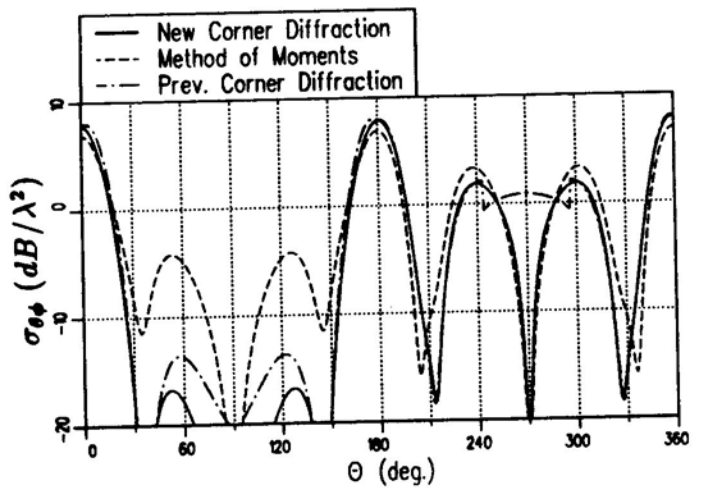

Figure 12: Cross-polarized RCS in the $\phi = 60°$ plane of a 2λ square plate with a $\hat{\phi}^i$ polarized fixed source at $\theta^i = 45°$, $\phi^i = 0°$.

in the previous corner diffraction solution. The discontinuities in the previous corner diffraction solution are caused by the so called false shadow boundaries where the associated two-dimensional problem passes through a shadow boundary, but the three-dimensional problem in reality does not. The Ryan and Peters equivalent current results are not shown here, but they behave differently for similar reasons; that is, the solution still contains two dimension information in regions that it should not. In the region from $\theta \approx 60°$ to 120° (i.e. near the plane of the plate) the new solution and the Method of Moments solution differ by more than 20 dB. It is suspected that most of these differences are due to the effects of higher order terms (double and triple diffraction, edge waves) which are not included in the new solution.

In this example the new solution is compared to backscatter measurements [22] made at 10 GHz on a 6" cube. The geometry of the cube, tilted 45° in the x-z plane, is illustrated in Figure 13. The results for the H-plane and E-plane patterns taken in the x-y plane are given in Figures 14 and 15, respectively. The results agree well to first order over most regions of the pattern. The discrepancies are probably due to a combination of higher order terms not being included in the analysis and in measurements errors. The error in the measurements is likely two fold. First the faces of the cube model were misaligned slightly so they did not form edges as sharp as may be required. Secondly, it seems that there was some deviation from the desired pattern cuts as can be seen from the lack of symmetry in the measured patterns. In any case, they confirm the validity of the new corner diffraction solution within first order accuracy for wedge type structures.

IV Discussion

The new corner diffraction coefficient in the above examples has been shown to provide improved results over other methods, especially in bistatic situations. The Michaeli equivalent currents have not been shown since they provide the same results as the new corner diffraction coefficient. Certain properties of these new solutions, however, may still cause patterns taken in some regions of space to be discontinuous.

It has been shown [2,3] that D_2^c and D_h^c do not tend to definite limits

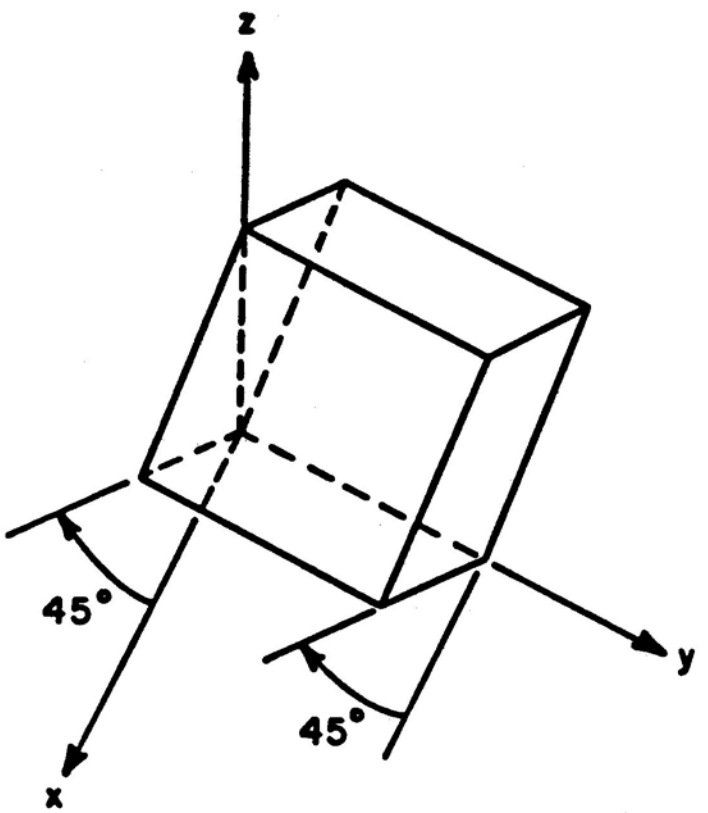

Figure 13: 6" Cube tilted 45° in the x-z plane.

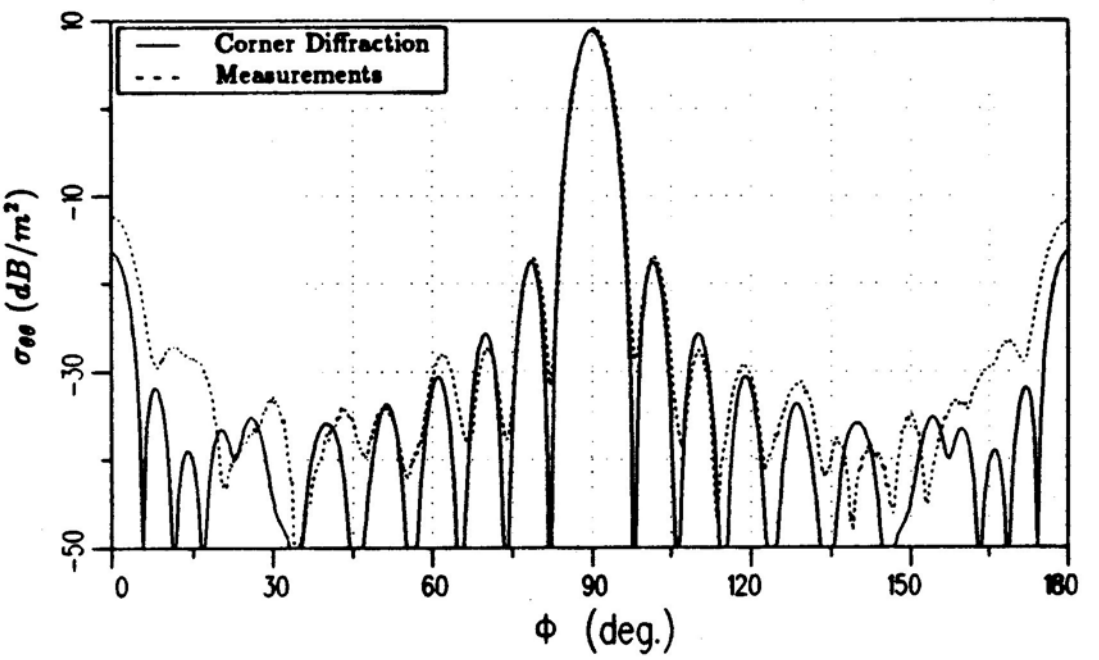

Figure 14: H-plane pattern for 6" cube tilted 45° in the x-z plane.

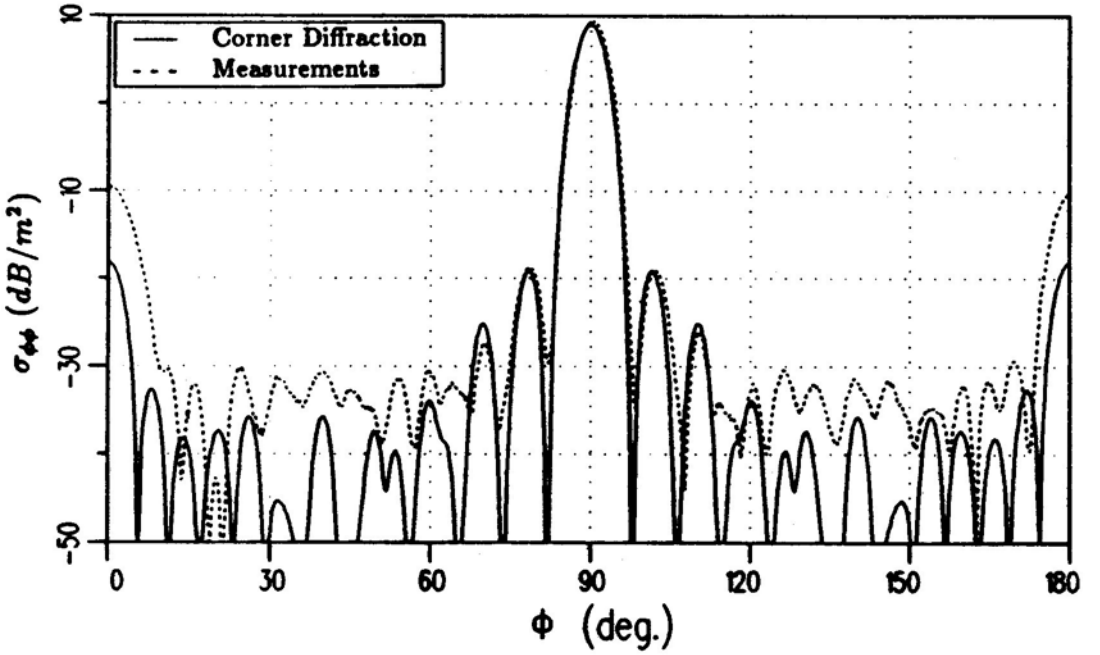

Figure 15: E-plane pattern for 6" cube tilted 45° in the x-z plane.

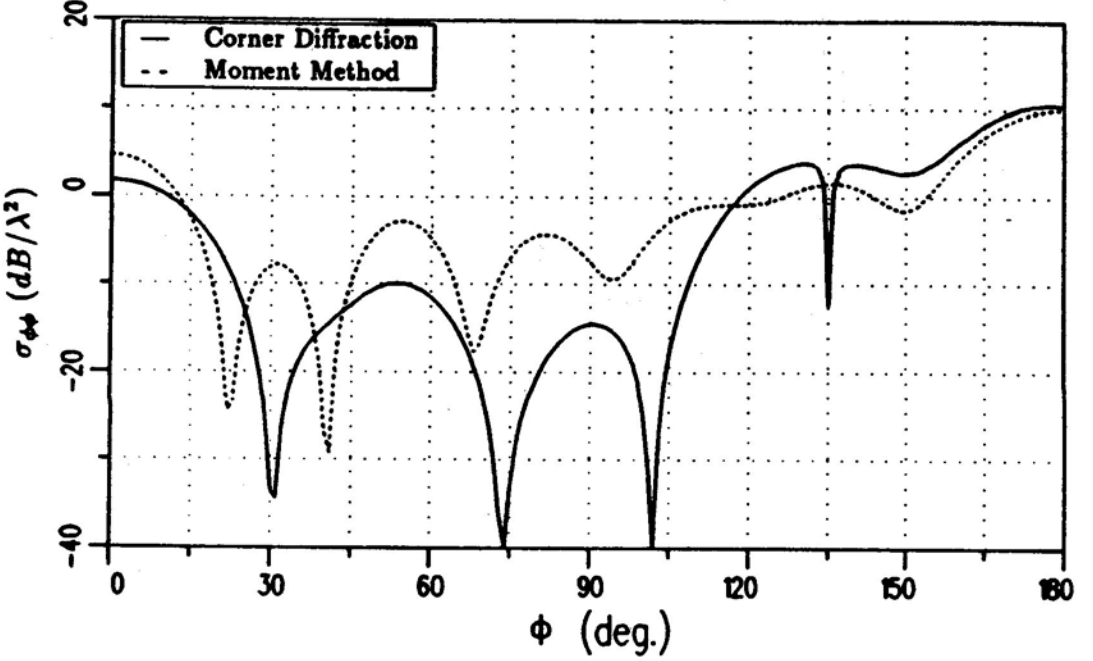

Figure 16: RCS for the $\theta = 89°$ cut of a 2λ square plate with a $\hat{\phi}^i$ polarized fixed source at $\theta^i = 45°$, $\phi^i = 0°$.

as $\hat{s} \rightarrow \hat{\sigma}$ (i.e. the intersection of the associated half-plane and the Keller cone), where $\hat{\sigma} = \hat{t}\sin\beta' + \hat{b}\cos\beta'$, but they remain bounded. In practice, this means that both D_2^c and D_h^c, and therefore E_β^c and E_ϕ^c, are discontinuous at this point in the pattern. A simple example illustrates how this discontinuity can affect a pattern. The bistatic RCS from the flat plate shown earlier in Figure 8 is considered. The source, linearly polarized in the $\hat{\phi}^i$ direction, remains fixed at $\theta^i = 45°$ and $\phi^i = 0°$ while the pattern is taken near the x-y plane ($\theta = 89°$). The bistatic RCS is given in Figures 16 and 17 for the co-polarized and cross polarized fields, respectively. The abrupt null at $\phi \approx 135°$ in the co-polarized pattern and the spike at the same location in the cross-polarized pattern are due to discontinuities in the contribution from edge 4 (indicated in Figure 8). The point $\phi \approx 135°$ coincides with $\beta_4 = \beta_4'$ and $\phi_4 \approx 0$ where β_4, β_4', and ϕ_4 are the edge fixed coordinates for edge 4. Due to the geometry $\hat{\beta}_4 \approx \hat{\phi}$ and $\hat{\phi}_4 \approx \hat{\theta}$ so the discontinuity in $\sigma_{\phi\phi}$ is due to the discontinuity in D_2^c and, likewise, the discontinuity in $\sigma_{\theta\phi}$ is due to the discontinuity in D_h^c.

Therefore, the discontinuity in the new diffraction coefficients at the

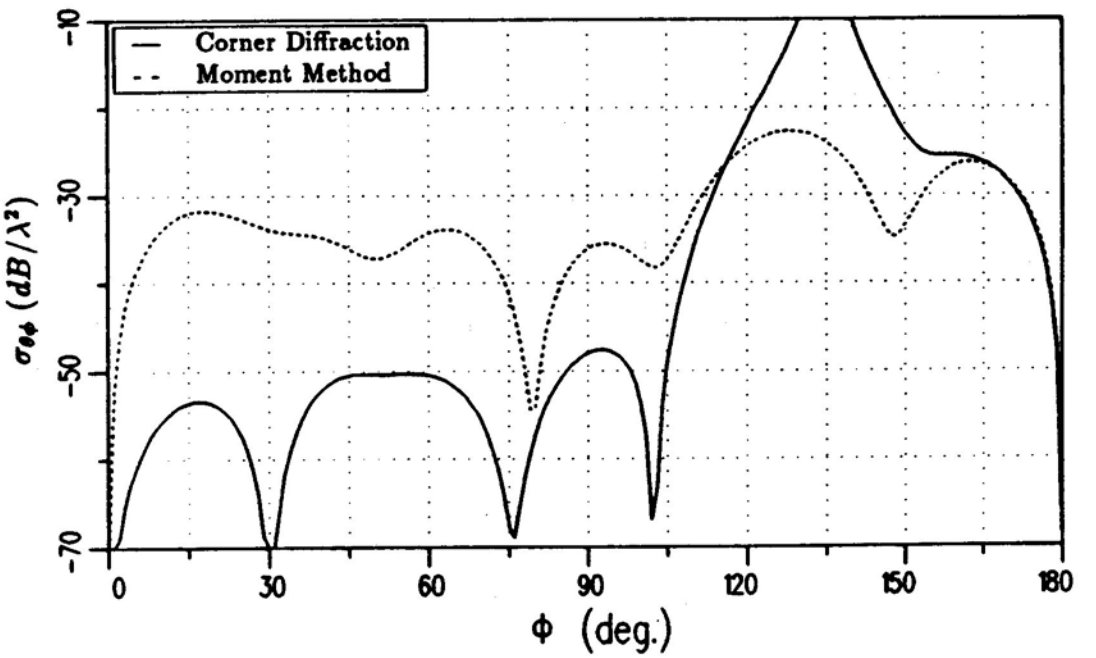

Figure 17: RCS for the $\theta = 89°$ cut of a 2λ square plate with a $\hat{\phi}^i$ polarized fixed source at $\theta^i = 45°$, $\phi^i = 0°$.

intersection of the Keller cone and the infinite half plane associated with the edge ($\beta = \beta'$ and $\phi = 0$) may be expected to cause discontinuities or narrow spikes depending on the polarization and the pattern cut. As the examples illustrate these disturbances only affect a typical pattern cut for around 5° to 10°. In addition, they are in the low level regions of the returns.

It is easily seen that the diffraction coefficients D_2^c and D_h^c are discontinuous as the source passes through the half plane $\phi' = \pi$. In the general case of bistatic scattering, these discontinuities in the sign of the field scattered by a corner will result in discontinuities in the total scattered field. However, the diffraction coefficients are continuous here ($\phi' = \pi$) for the special case of backscatter.

V Conclusions

The objective of this paper has been to compare different methods for the analysis of the high frequency far zone scattering from flat plate and convex flat plate type structures. Ryan and Peters equivalent currents and the previous corner diffraction coefficient are compared with the Michaeli equivalent currents and the new corner diffraction coefficient. The method of moments and measurements are also used to validate the solutions.

It has been shown that for backscatter all the methods compare reasonably within engineering accuracy. For bistatic scattering, however, the two dimensional nature of the old methods lead to inaccuracies. The newer methods, based on more rigorous three dimensional analysis, remove most of these problems.

A new corner diffraction coefficient is presented that provides an efficient and accurate solution to within first order. It provides the same level of accuracy as the Michaeli equivalent currents with the added benefit of not needing integrations for flat plates. All the optics and edge scattering effects have been lumped into the corners of the plate with nice physical interpretations.

References

[1] Sikta, F. A., W. D. Burnside, T. T. Chu, and L. Peters, Jr., "First-Order Equivalent Current and Corner Diffraction Scattering from Flat Plate Structures," *IEEE Trans. on Antennas and Propagation*, Vol. AP-31, No. 4, pp. 584–589, July 1983.

[2] Michaeli, A., "Elimination of Infinities In Equivalent Edge Currents, Part I: Fringe Current Components," *IEEE Trans. on Antennas and Propagation*, Vol. AP-34, No. 7, pp. 912–918, July 1986.

[3] Brinkley, T. J. and R. J. Marhefka, "Far Zone Bistatic Scattering from Flat Plates," Technical Report 718295-8, July 1988, The Ohio State University, ElectroScience Laboratory, Department of Electrical Engineering, prepared under Contract No. F33615-86-K-1023 for Wright Patterson Air Force Base.

[4] Newman, E. H. and R. L. Dilsavor, "A user's manual for the electromagnetic surface patch code: ESP version III," Report 716148, May 1987, The Ohio State University, ElectroScience Laboratory, prepared under Grant No. NSG 1613 with the National Aeronautics and Space Administration, Langley Research Center.

[5] Ludwig, A. C., "Backscattering from a Cube," Applied Computational Electromagnetic Society Journal and Newsletter, Vol. 2, No. 2, Fall 1987, pp. 55–73.

[6] Tiberio, R., M. Giuliano, G. Pelosi, and R. G. Kouyoumjian, "High-Frequency Electromagnetic Scattering of Plane Waves From Double Wedges," to be published.

[7] Sikta, F. A., "UTD Analysis of Electromagnetic Scattering by Flat Plate Structures," Ph.D. dissertation, The Ohio State University, Department of Electrical Engineering, Columbus, Ohio, 1981.

[8] R. J. Marhefka and W. D. Burnside, "Numerical Electromagnetic Code - Basic Scattering Code, NEC - BSC (Version 2), Part I: User's Manual," Technical Report 712242-14, December 1982, The Ohio State University ElectroScience Laboratory, Department of Electrical Engineering; prepared under Contract No. N00123-79-C-1469 for Naval Regional Contracting Office.

[9] Newman, E. H. and R. J. Marhefka, "An Overview of MM and UTD Methods at The Ohio State University," Proc. of the IEEE, to be published.

[10] Ufimtsev, P. Ya., "Method of Edge Waves in the Physical Theory of Diffraction," Air Force Systems Command, Foreign Tech. Div., Document ID No. FTD-HC-23-259-71, 1971 (Translation from the Russian "Method Krayevykh voin v fizicheskoy teorii difraktsi," Soviet Radio Publication House, Moscow, 1962).

[11] Keller, J. B., "Geometrical Theory of Diffraction," *J. Opt. Soc. of America*, Vol. 52, No. 2, pp. 116–130, Feb. 1962.

[12] Kouyoumjian, R. G., and P. H. Pathak, "A Uniform Geometrical Theory of Diffraction for an Edge in a Perfectly Conducting Surface," *Proc. IEEE*, Vol. 62, pp. 1448–1461, Nov. 1974.

[13] Ryan, C. E., Jr., and L. Peters, Jr., "Evaluation of Edge Diffracted Fields Including Equivalent Currents for the Caustic Regions," *IEEE Trans. on Antennas and Propagation*, Vol. AP-17, pp. 292–299, May 1969.

[14] Michaeli, A., "Equivalent Edge Currents for Arbitrary Aspects of Observation," *IEEE Trans. on Antennas and Propagation*, Vol. AP-32, No. 3, pp. 252–258, March 1984.

[15] Mitzner, K. M., "Incremental Length Diffraction Coefficients," Northrop Corp., Aircraft Division, Tech. Rep. No. AFAL-TR-73-296, April 1974.

[16] Knott, E. F., "The Relationship Between Mitzner's ILDC and Michaeli's Equivalent Currents," *IEEE Trans. on Antennas and Propagation*, Vol. AP-33, No. 1, pp. 112–114, January 1985.

[17] Ufimtsev, P. Ya., and D. I. Butorin, "Explicit Expressions for an Acoustic Edge Wave Scattered by an Infinitesimal Edge Element," *Sov. Phys. Acous.*, Vol. 34, No. 4, pp. 283–287, July–August 1986.

[18] Ufimtsev, P. Ya., "A New Mathematical Formulation of the Physical Theory of Diffraction," submitted to *IEEE Proc.* for publication.

[19] Buyukdura, O. M., R. J. Marhefka, and W. Ebihara, "Radar Cross Section Studies, Phase III," Technical Report 716622-1, The Ohio State University, ElectroScience Laboratory, April 1986.

[20] Gordon, Willliam B., "Far-Field Approximations to the Kirchoff-Helmholtz Representations of Scattered Fields," *IEEE Trans. on Antennas and Propagation*, pp. 590–592, July 1975.

[21] Buyukdura, O. M., personal communication.

[22] Dominek, A.K., personal communication.

On the Comparison of Numerical Methods

Ch.Hafner, Swiss Federal Institute of Technology, CH-8092 Zurich, Switzerland

Abstract

Serious comparisons of numerical methods are important for scientists who develop new codes as well as for those who use programs. Historical considerations show some errors which were made in the past and should be avoided in the future. Every numerical code is based not only on numerical but also on analytical considerations. Both of them have to be taken into account. As a result, benchmarks for complicated topics (numerical calculations of electromagnetic fields) should give more informations than just numbers like 'speed', 'memory requirement', etc.

Historical considerations

In the early times of numerical calculations many codes were implemented and tested. They were all based on a mixture of ideas and were usually named after the most important idea. Several people believed that their method was the best and many of them tried to show this 'analytically'. But very often the mathematical knowledge of engineers dealing with numerical techniques was insufficient and sometimes the questions which arose simply could not be answered by analytical considerations. To overcome such problems the application of physical knowledge was helpful in many cases. For example, the simple Point Matching (PM) technique was used together with 'circular harmonic' analysis (Rayleigh hypothesis) in the sixties. Different people 'showed analytically' that PM could be used only for circular domains while non circular problems were solved sucessfully. Others claimed that only 'single valued' boundaries should be admitted, that 'non integer orders' should be used and so on. In fact, Russian mathematicians [1] had already given a strong analytical basis for this technique years ago. The experience with elaborated PM programs [2] made clear that the method failed in complicated cases for numerical reasons (bad convergence, under- and overflows, cancellations). The treatment of numerical details seemed to be even more important than the main ideas (This might be true for any numerical method.). At that time, the PM had already been pushed aside by the Method of Moments (MM) which seemed to have a more physical basis. The consequent improvement of both the analytical and numerical parts of the PM led to the Multiple MultiPole (MMP) method (better known in the USA as SPEX (SPherical wave EXpansion) for 3D scattering [3]) which has been sucessfully applied to various problems of 2D and 3D, static and dynamic, scattering and guided waves etc. [4].

A second approach to show the superiority of a method lies in a generalization which allows to consider 'concurrents' as special cases of the 'favorite'. For example if a Projection Technique (PT) is used (like in the MM) the PM is a special case if Dirac functions are used as testing functions. Since Dirac functions are known to be

simple but otherwise not very good testing functions, the superiority of PT over PM seems to be clear. The best choice of testing functions are the expansion functions themselves (Galerkin). The disadvantage of this choice is the occurance of integrals (scalar products of functions) which usually have to be solved numerically. On the other hand, it has been shown [4] that the generalization of PM (overdetermined systems of weighted equations) leads to the same results as PT with Galerkin's method if an adequate weighting is chosen. This means that generalized PM is superior to PT because it avoids time consuming numerical integrations without lack of quality.

A third attempt in knocking out concurrents consisted of specially tailored numerical 'comparisons': Elaborated forms of the 'favorite' were compared with weak forms of the 'concurrents'. Examples which were known to be easily solvable by the 'favorite' have been preferred and so on.

It may be surprising but the described proceeding was successful in many cases. As a result, only a few methods survived, or, more precisely, the names of only a few methods survived, because sometimes people saved their programs by simply renaming them. This is of course a legitimate consequence of the generalization of the methods. For the users it has, however, become very difficult to see which program is most suitable for their problems. Codes with the same name may differ one from another much more than codes with different names.

In the last years it has been recognized that every elaborated program has its own advantages and disadvantages too. The hope of finding 'the one and only' method seems to disappear because the implementation of huge programs show a very annoying effect: The probability of errors and the possibility of generating new errors while attempting to eliminate other errors increase with the length of the code. Though it has become possible to reanimate old ideas, to combine different methods, to look for new directions, and to compare numerical programs seriously. The question is now: How should such a comparison look like? It seems to be clear that both analytical and numerical considerations are important and that the 'dirty tricks' mentionned above should be avoided.

Analytical considerations

If a numerical program is designed, various considerations show different ways and choices are necessary to get a certain code. The program usually gets a name which does not say anything about these choices and the details of implementation, but such informations are very important and should be known for serious comparisons. In most of the methods for calculating electromagnetic fields, the following choices are important:

1.) Field equations: Maxwell's equations in differential or integral form, wave equations, Helmholtz equations, variational integrals, other integral equations etc.

2.) Continuity/boundary equations: Continuity of certain components of the electric or magnetic field, potentials, derivatives of potentials, current density, energy

flow etc.

3.) Primary functions (functions which are approximated directly by a series of expansion functions): Certain field components, potentials, charges, currents, energy densities etc.

4.) Type of expansion functions: Dirac functions, piecewise constant functions, linear functions, continuous functions, differentiable functions, solutions of the field equations, Green functions, etc.

5.) Method to get a system of equations for the unknown parameters in the expansions: Error Method (EM), PT, PM etc. (The EM defines a certain error which has to be minimized.) Since different forms of these methods exist some more information is necessary here: Definition of the error (EM), the scalar product and the testing functions (PT), the weighting (generalized PM) etc.

6.) Algorithm to solve the system of equations: Gauss, Cholesky, least squares, iterative methods etc.

In practice, different approaches sometimes lead to identical solutions. Good codes should usually be derivable with different approaches. For example, the MMP programs were designed with this intention. They use analytical solutions of the field equations (This means that automatically different forms of field equations may be used with identical results.). These solutions are continuous, differentiable Green functions. Usually but not necessarily the continuity of all field components is used and certain field components are chosen as primary functions. The system of equations in the MMP programs may be derived with EM, PT or generalized PM and is solved by fast updating routines using Given's plane rotations.

Numerical considerations

To get information about the speed and application range of numerical programs, numerical comparison standards seem to be useful. The problem of benchmarks for computers is already well known: Tests which give one single number which represents the 'speed' of a machine are misleading in many cases. For example benchmarks show that an 80286 based AT personal computer is much faster than an 8088 based XT. The MMP programs have been implemented and tested on such machines. It has been shown [5] that these programs run faster on an XT (with 8MHz clock) than on an AT (with 8MHz clock) for not too small problems. Comparisons of the MMP programs on very different machines showed astonishing effects which usually depended on the size and type of the considered problem. On the other hand it may be expected that the comparison of different programs will depend not only on the problem to be calculated but also on the machine and on the compiler which is used.

In fact 'speed' is not the only important feature of a program. Users usually want to get a program on the machine they already have. New and faster machines very often require time consuming adaptions of the codes. For these reasons it is

essential that a program is written in a way that it may be easily implemented on other machines (which even might not exist when the program is created). From this follows that common languages should be preferred and special features of a compiler on a certain machine should be ignored.

At present, very often two different types of examples are proposed as benchmarks for numerical field calculations:

1.) Examples which have a well known 'analytic' solution. They allow a calculation of the errors made by the considered program. Usually such examples can be treated by new and not yet highly sophisticated techniques. Because they are not really difficult to solve (otherwise an analytic solution would not be known) they give not much information on the application range.

2.) Examples without an 'analytic' solution which are well known from measurements and from calculations with mature programs. It is clear that such examples are much more important from a practical point of view. But they may be crucial for newly born codes. For this reason, they are preferred by some established scientists who try to defend their methods from being threatened by new promising ones.

To avoid benchmarks which result in meaningless numbers, a serious comparison of numerical calculations must be based on very different examples and should give much more information ('choices' of the method, application range, used machines, compilers, memory requirements, error checks, input/output support etc.) then just some numbers. Testing examples should include 'analytically' solved problems as well as 'practically well known' problems. They should include various configurations, both 2D and 3D geometries, open and closed structures, harmonic and impulsive time dependencies, scattering and eigenvalue problems, perfect and imperfect conductors, lossless and lossy dielectrics, etc. Of course, no program will be able to solve all the testing examples effectively. But this will just give the desired information for the users.

References

[1] I.N.Vekua: *New Methods for solving Elliptic equations*, North-Holland Publ. Comp., Amsterdam, 1967.

[2] Ch.Hafner: SFIT thesis 6683, Zurich, 1980.

[3] A.C.Ludwig: IEEE Trans. AP 34, NO 34, 1986.

[4] Ch.Hafner: *Numerische Berechnung elektromagnetischer Felder*, Springer, Berlin, 1987.

[5] Ch.Hafner: URSI Radio Science Meeting, Syracuse, 1988.

IMPLEMENTATION OF GEMACS 3.3 ON PERSONAL COMPUTERS

Adel F Armanious and Peter S Excell
Department of Electrical Engineering
University of Bradford, UK

Abstract

GEMACS 3.3* is a powerful MM/GTD hybrid package which can model a wide range of antenna and scattering problems. It is intended for use on large mainframe computers but an implementation on a personal computer has advantages in the possibilities of interactive use and graphical output. An approach to this implementation is presented, together with benchmark test results from typical PCs, a mainframe and a supercomputer.

1. Introduction

GEMACS is a very powerful and flexible code for electromagnetic modeling, not only because it allows flexible hydridization of different approaches, but also because it incorporates powerful geometry pre- and post-processors and other features which aid execution of large problems [1]. The code is very large and is normally intended to be run on a large mainframe computer or vector processor. However, there are attractions in being able to use it on a personal copmputer since the possibility of interactive dialogue and graphics compensates for the reduced processing power in many applications. The latest version of the code (Version 4.0) includes a finite-difference (FD) module which adds substantially to its length [2]: the running of this on larger personal computers (based on the Intel 80286 or 80386 microprocessor) has recently been reported [3]. For many applications, however, FD is not needed and a more compact code can be realized which will run on smaller PCs. In the work reported here, the earlier Version 3.3 of GEMACS was modified for implementation on a standard IBM-type PC, originally based around the Intel 8086 microprocessor. This version of the code contains only Moment-Method and GTD modeling modules. The personal computer used was fitted with an Intel 8087 co-processor but, more significantly, the 8086 processor was replaced by an NEC (i.e. Nippon Electrical Corporation) V30 accelerated-architecture microprocessor that is pin-compatible with the 8086. The use of this processor in standard IBM-type PCs has been found to give a great improvement in performance [4].

GEMACS 3.3 consists of five modules which are executed sequentially:

1. Input module (geometry processor and command language interpreter)
2. GTD module, which also supports a hybrid MM-plus-GTD solution
3. MM module, using wire grids and/or surface patches
4. Solution module, exploiting banded matrix iteration
5. Output module

---

*This version has now been superseded by version 4.0 and is no longer supported. There is, however, not a great deal of difference between these versions apart from the addition of the finite-difference module to the latter.

In operation, the code is strongly file-oriented. The starting point whenever running any module is a check point file which is updated whenever there is an exit from the module. The user is able to designate a certain run time and, if the execution is unfinished at the end of this time, the check point file is updated and the current values of the internal variables are saved, thus permitting execution to be recommenced at a later time. The flexible hybridization of GTD and MM techniques makes the code particularly powerful and useful for handling objects that are too large to be analyzed by MM alone.

2. A PC Version of GEMACS 3.3

GEMACS 3.3 was written in Fortran 4 and hence, as a preliminary, statements which contained obsolete features of Fortran 4 were modified so that they conformed to the current Fortran-77 standard. The code was then transferred to a PC where non-standard modifications had necessarily to be made in order to make optimum use of the limited power available. To simplify this, all the DIMENSION and COMMON statements of the routines were taken out of the program and an INCLUDE statement used which makes the compiler read the DIMENSION and COMMON statements from a specified file. In order to compile each module with a limited DOS memory the modules were divided into groups of routines which were compiled separately and subsequently linked.

2.1 Hardware and PC Configuration

An IBM PC/XT or PC/AT or compatible computer is required, with the following specifications and extensions:

1. 640Kb of RAM memory
2. Mathematical co-processor (8087 or 80287)
3. 10Mb (or larger) hard disk
4. Printer with either wide (132 characters/line) paper or normal paper if compressed mode is available.

A large and fast hard disk is recommended if very large structures are to be analyzed. Table 1 shows the size of each module in Fortran lines, RAM bytes and compressed disk bytes.

Table 1 Sizes of GEMACS 3.3 PC Modules

Module	Source Code Lines*	Minimum memory required bytes (in RAM)	EXE file size on hard disk (bytes)
INPUT	14109	343879	254679
GTD	17356	577187	407843
MOM	12135	319539	234739
SOLN	9143	260683	179931
OUTPUT	7037	216773	136245

*excluding comment lines

2.2 Choice of Fortran Compiler

An attempt was made to compile the code using RM Professional Fortran 1.0 but unfortunately this failed due to the size of the common block data segments. Another attempt was made using Microsoft Fortran Version 3.31 but this gave difficulties due to the restricted subset of Fortran-77 implemented. Finally, an optimized Microsoft Fortran Version 4.0 was used. This was successful and it has the additional advantage of options for optimization to achieve maximum speed or minimum size: speed optimization was used for the present work.

Problems arose in implementing the GTD module with the maximum number of plates (51) permitted in the mainframe version. For this, 720Kb would be required which is clearly outside the ability of DOS on a PC/XT-type system. The use of overlay was tried but this had a severe effect on run-time performance. As a compromise, the maximum permitted number of plates was reduced to 14 (as in GEMACS 3.1 [1]), which permits the program to run without overlay. Some other problems were encountered due to the optimization option in the compiler: these were tackled by disabling the optimization in a small number of routines. The executable files were stored in compressed format in order to reduce hard disk space requirements.

2.3 Code Operation

GEMACS uses unformatted indirect access files to store the check point data file and all of the data sets produced, including the interaction matrix. The minimum number of files needed for a MM/GTD problem is 16, however it is very likely that additional files will be required, e.g. for structure loads, additional excitations or additional field patterns. It is therefore advisable to specify that at least 20 files will be used when loading DOS: this is done in the CONFIG.SYS file.

2.4 Code Limitation

As mentioned above, the number of plates permitted in the GTD module was limited to 14 (c.f. 51 in the mainframe version). The maximum number of corners that each plate may have was also reduced to 6 in the PC version (as in GEMACS 3.1, c.f. 16 in the standard version 3.3). All of the other limitations are the same as those in the mainframe version [1].

2.5 Benchmark Testing

The test example cited in the GEMACS manual [1] was used for comparative tests. This consists of a 0.25m monopole located over a square conducting plate of side length 1.5m and driven at 500MHz. A hybrid solution was used, the plate being modeled as a single GTD plate and the monopole being modeled as a wire with six segments using the Method of Moments. The published test solves for the current distribution on the monopole and calculates the far field and input parameters.

Test results and timings were available* for a Honeywell 6180 mainframe (this was actually running GEMACS Version 3.1). Two personal computers were used to test the present code and, for comparison, results from a Cray X-MP/48 were also obtained. The personal computers used were as follows:

---

*Provided by K R Siarkiewicz, USAF Rome Air Development Center

1. A standard IBM PC/AT (6MHz clock) with the enhancements specified in Section 2.1.
2. An Amstrad PC1512 with the same enhancements.

The Amstrad PC1512 is compatible with the IBM PC/XT but it has an 8MHz clock and, for the present tests, the 8086 microprocessor was replaced by a V30 as discussed in Section 1. Comparative results are given in Table 2 and the corresponding timings are given in Table 3.

Table 2 Comparative Results for Benchmark Test

Result	IBM PC/XT	Amstrad PC 1512 with V30	Honeywell 6180*	Cray X-MP/48
Input Impedance (ohms)	300.876	300.876	300.877	300.877
Input phase (deg)	17.676	17.676	17.676	17.676
Input power (W)	0.158E-02	0.158E-02	0.158E-02	0.158E-02

*running GEMACS 3.1

Table 3 Comparative Timings (sec) for Benchmark Test

Module	IBM PC/XT	Amstrad PC 1512 with V30	Honeywell 6180	Cray X-MP/48
INPUT	4.8	7.9*	1.91	0.03
GTD	503	273	133.26	1.60
MOM	4.3	4.8*	8.44†	0.04
SOLN	3.2	3.7*	(inc. in MOM)	0.03
OUTPUT	2.6	3.0*	1.02	0.09
Total time	518	292	145	1.79

*Dominated by slow hard disk
†Time for MOM and SOLN

It is seen that the GTD module dominates the processing time on all of the computers: Fig. 1 shows comparative timings for the routines within this module, excluding routines involving disk access (results for the Cray are not shown).

It is seen that the results produced by the personal computers are almost identical to those from the mainframes (detailed results for the far fields are not shown, but were also identical within the range of the printed output (four significant figures)) and the timings are of a similar order of magnitude to those achieved by the Honeywell mainframe: the Cray is, of course, very much faster. The performance of the V30 microprocessor is particularly remarkable since it achieves almost twice the speed of an 80286-architecture machine when it is not hindered by disk access times. Allowing for the faster clock rate in the Amstrad PC1512, the speed improvement with the V30 is less (1.4 times faster) but still substantial.

References

1. Kadlec, D L & Coffey, E L: 'General electromagnetic model for the analysis of complex systems (GEMACS), version 3', USAF Rome Air Development Center, Report No. RADC-TR-83-217, 1983.

2. Siarkiewicz, K R: 'GEMACS - an executive summary', IEEE Int. Symp. on EMC, Wakefield, MA, 1985, pp. 75-81.

3. Coffey, E L: 'GEMACS on a personal computer', Proc. 4th Annual Review of Progress in Applied Computational Electromagnetics, Monterey, CA, 1988.

4. Rock, I: 'V-series microprocessors', Electronics & Wireless World, Vol. 94, No. 1625, pp. 256-260, 1988.

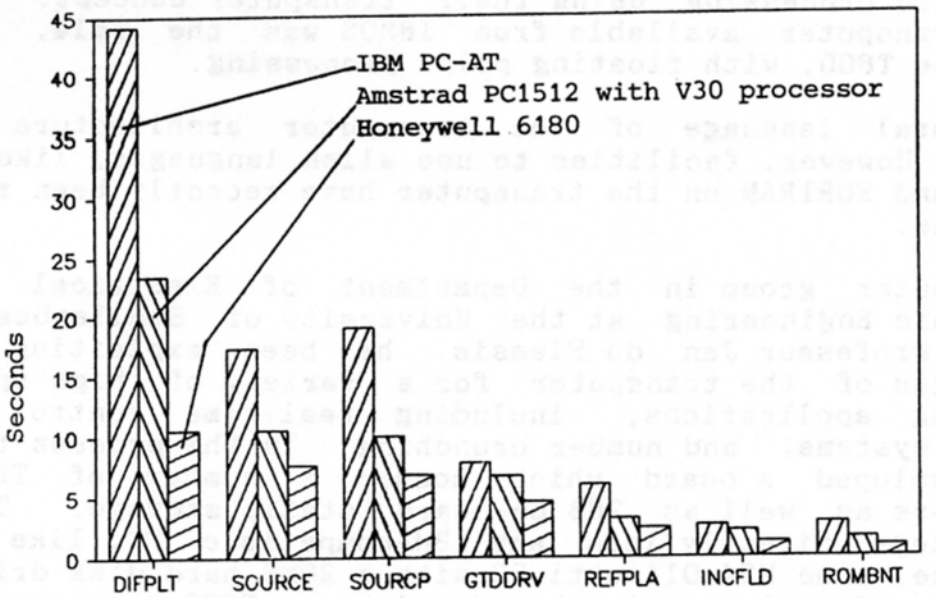

Fig. 1 Comparative timings for routines within the GTD module. (The times for DIFPLT have been divided by 10)

12 APRIL 1988
UPDATED 9 NOVEMBER 1988

NUMERICAL ELECTROMAGNETICS COMPUTATION USING THE INMOS T800 TRANSPUTER ON AN OLIVETTI M24 PERSONAL COMPUTER

M.ENG PROGRESS SUMMARY

J.J. LE ROUX
ANTENNA AND MICROWAVE GROUP
DEPARTMENT OF ELECTRICAL AND ELECTRONIC ENGINEERING
UNIVERSITY OF STELLENBOSCH, STELLENBOSCH, 7600
REPUBLIC OF SOUTH AFRICA

STUDY LEADER : Prof. J.H. CLOETE

INTRODUCTION : As is known to most engineers and scientists interested in computational electromagnetics analysis, G.J. Burke and A.J. Poggio developed a code called NEC2 at the Lawrence Livermore Laboratory in California [1]. This code was developed using a mainframe computer and was written in FORTRAN. The code has subsequently been used on a VAX785 mainframe at this University.

Recent developments at INMOS in the field of fast 32-bit parallel processors however opened up a new avenue of arithmetic processing using their transputer concept. The first transputer available from INMOS was the T414, and later the T800, with floating point processing.

The natural language of the transputer architecture is OCCAM. However, facilities to use alien languages, like C, PASCAL and FORTRAN on the transputer have recently been made available.

The computer group in the Department of Electrical and Electronic Engineering at the University of Stellenbosch, led by Professor Jan du Plessis, has been exploiting the advantages of the transputer for a variety of high speed computing applications, including real-time control of dynamic systems, and number crunching. In the process they have developed a board which houses a number of T800-processors as well as 2MB on-board static storage. This board plugs directly into any IBM-compatible PC, like in this case, the M24 Olivetti PC with a 20MB hard disk drive. The cost of a transputer board with one T800 processor is about $US2000.

At the suggestion of Professor du Plessis, a study was initiated to investigate the feasibility of running NEC2 on the T800 transputer.

In order to test this idea, a transputer board, containing a single T800, was plugged into an Olivetti M24 PC, with the following additional hardware : 2 x 360kB floppy drives; 1 x 20MB hard drive; 1 x 8087 co-processor; and 640kB of RAM.

PROCEDURE TO TRANSFER NEC2 TO T800 TRANSPUTER : After less than 1 month's work, NEC2 was successfully run on the T800 transputer, using the following procedure :

1. Firstly the necessary software for FORTRAN use on the transputer, as supplied by INMOS, was loaded and installed on the hard drive.

2. To load NEC2 onto the PC hard drive, it was found that it would be easier to transport the PC to a mainframe serial port, and transfer the program serially from the VAX785 magnetic storage to the PC hard drive, using a suitable error-free transfer packet.

3. Having transferred the program onto the PC hard disk, the use of NEC2 on the transputer was investigated. The program was renamed NEC2.F77 to comply with INMOS terminology. The logical first step seemed to be to try compiling the program using the transputer's FORTRAN compiler. Obviously there were a lot of errors and warnings, but at least it proved that the compiler accepted the NEC2 package.

4. The nature of the warnings and errors after compilation were the following :

a. The compiler did not accept the REAL*8 statement. This was replaced with the DOUBLE PRECISION statement.

b. Some of the declared constants were too large for single precision format. All these were replaced with double precision format, i.e.

DATA TA/1.745329252E-02 replaced with

DATA TA/1.745329252D-02
^

(The E replaced by a D)

c. The compiler has an alternative protocol for READ/WRITE statements which involves the exclusion of a comma, i.e.

WRITE (6,*),'WHAT TO BE WRITTEN ON SCREEN' becomes

WRITE (6,*) 'WHAT TO BE WRITTEN ON SCREEN'
^

(Comma removed)

d. The OPEN statement does not allow the RECORDTYPE and CARRIAGECONTROL options, as found on the VAX785.

e. The compiler does not accept the use of Hollerith constants. All these were replaced with CHARACTER declarations and the H-characters in the DATA-statements were removed. Use was also made of type conversions, i.e. conversion from CHARACTER to INTEGER and vice versa, to bypass the Hollerith constraints.

f. Line 66 of subroutine COUPLE was changed to the following form :

```
FORMAT (2(1X,I4,1X,I4,1X,I5,2X),45H**ERROR** COUP.....
```

(inclusion of a comma after the first closing bracket)

g. The transputer clock procedure, ICLOCK, produces a time value (seconds) in an integer format, as opposed to the VAX785 real format. All the time printout FORMAT statements were modified to accommodate the integer format.

5. After all the above errors and warnings were rectified, it was possible to compile the program, but the compiler failed to generate the binary code, NEC2.BIN. (It was not necessary to debug the warnings, as they were, in fact, just warnings. They would not have prevented the creation of an executable file.) After checking the diagnostic printout and consulting with Mr. Pieter Bakkes, one of the lecturers involved with the transputer project, the conclusion was drawn that the source code, NEC2.F77, was too large for compilation (690kB). It was thus decided to divide the whole program into 17 separate segments and compile each segment separately, after which all segments were linked together to create the executable file NEC2.B4. This proved to be successful, and a file NEC2.B4 of size 340kB was created.

6. The file NEC2.B4 was subsequently executed, and at first everything seemed to indicate that NEC2 was running. However, about a quarter of the way through the run execution terminated. After a lengthy investigation inside the source code using several WRITE statements to follow the progress of the program, it became clear from the INMOS literature that only 2kB of on-chip (T800) storage is used for the stack. To use external storage for the stack, a NEC2.EXE file has to be created (by copying and renaming the link file, LINKT.EXE to NEC2.EXE) and executed. This proved to be successful, and NEC2 ran for the first time from beginning to end, using the 12-element log-periodic antenna example in the NEC2-users manual [1].

Note that because this particular example employs 78 segments, it would mean a matrix size of 6084 elements, which is more than the maximum of 4000 possible elements budgeted for in the original NEC2-version. The dimensions of the variables CM and IRESRV were changed to 10000 to avoid the use of external file storage. Provision still has to be made for the opening of files for disk storage.

RESULTS : The 12-element log-periodic antenna example in the NEC2 users manual [1] was used as a benchmark.

The results obtained from analysing the 12-element log-periodic antenna,using NEC2, on the T800 transputer were compared with those published in the NEC2-users manual [1], as well as those obtained from microVAX and VAX785 executions. The results agreed excellently in all three cases.

The runtime comparisons are as follows [2]:

Transputer T800 using static storage	32s

(In the original report, the T800 execution time was stated as 42s. However, a memory clock jumper on the transputer board was incorrectly set for the type of memory used, hence the radical improvement from 42s to 32s.)

microVAX using core storage	47s
VAX785 using magnetic tape storage (with 11 other users on the VAX)	40s
" " (with no other users)	34s
VAX785 using core storage (with 2 other users on the VAX)	18s

RECENT DEVELOPMENTS : The Department recently acquired the new INMOS Parallel FORTRAN compiler for use on the T800-transputer. This compiler was originally developed for use with several transputers in a parallel environment, with the added advantage of being able to write software in FORTRAN for parallel processes. The feasibility of compiling NEC2 with this compiler was investigated.

It was found that it was possible to compile the entire NEC2 source code, unsegmented, using this compiler. The execution time with this compiler is, however, about 3 seconds slower than the above benchmark, using the same log-periodic antenna (i.e. ± 35s). Other advantages for use with NEC2 could not be detected.

Additionally, the Group recently acquired the NEEDS package, as distributed by the Applied Computational Electromagnetic Society. This consists of an excellent pre-processor, IGUANA, for creating, editing and plotting the required NEC2 data cards for a given structure, accessing NEC2 or MININEC for execution and a graphics package, GRAPS, for plotting of the results. This package also includes SOMNEC, a FORTRAN program which creates an interpolation table for use by NEC2, for the cases where a non-ideal earth surface is used. This program was immediately transferred to the hard disk, debugged and successfully compiled on the transputer.

An obvious next step was to integrate the transputer-NEC2 and -SOMNEC into the NEEDS-facility. The status of this exercise is as follows :

a) It is now possible to access the transputer-NEC2 as well as the transputer-SOMNEC from the NEEDS menu; it involved a simple modification of the path to the transputer directory in the relevant menu-batch files.

b) Unfortunately the card deck output format of IGUANA is not the same as that required by the transputer-NEC2 (possibly to be compatible with the MININEC input format). An interface program was written to reconvert the IGUANA output deck (containing commas between fields) to the format required by the transputer-NEC2 (with spaces between fields, as in the NEC2 users manual [1]). This seemed to be less troublesome than to alter the READ and FORMAT statements in NEC2 in order to accommodate the commas in the IGUANA deck format. This interface program is automatically executed immediately after using IGUANA, just before returning to the main menu.

c) NEEDS contains an updated version of NEC2, with the added facilities of a helix generation card (GH) as well as a plotting card (PL) to facilitate storage of current, near-fields, far-fields or field strengths on disk for later plotting. As it was too much trouble to recommence debugging of this version for compilation on the transputer, it was decided to copy the subroutine HELIX, as well as all statements relating to this subroutine and the PL card to the existing transputer version of NEC2, debugging these additions where necessary.

Initially a problem was experienced in that only a maximum of 7 files could be opened, regardless of the number of OPEN-statements in the program. After initially blaming the transputer compiler, it later transpired that the CONFIG.SYS-file in the MS-DOS root directory did not make provision for enough files to be created. This error was promptly rectified by editing this file.

After the abovementioned modifications and additions were performed, a totally PC-based antenna analysis workstation was obtained, with performance comparable to a mainframe system. The program components which are primarily used, are the following :

IGUANA - this NEEDS-based program is used to to create, edit, view and plot the structure to be analysed. The final structure file is saved as NAME.DAT, where NAME is any user-defined name, and is stored in the transputer directory. This program is executed in the DOS-environment.

SOMNEC - this program is used to create non-ideal earth interpolation tables, which is saved as SOMNEC.DAT, for use by NEC2 where necessary. This program is executed on the transputer.

NEC2 - using the transputer, this program calculates currents, radiation patterns etc. This program makes MININEC obsolete. The output listing is saved as LISTING.DAT.

NECPP - this handy post-processor program in NEEDS searches through the output listing, LISTING.DAT, for the relevant data to be plotted. After finding the data, it is saved in the GRAPS-directory for subsequent plotting. It operates in the DOS-environment.

GRAPS - this is the graphical plotting sub-program in NEEDS, with several options for plotting of the results obtained from the execution of NEC2. It also operates in the DOS-environment.

The only limitation is a maximum segment dimension of 300, but this will be extended by the planned acquisition in the near future of a transputer board containing about 4MB of on-board memory.

CONCLUSIONS : The transputer compares very favourably with the mainframe systems, and can be thought of as the poor man's VAX. In effect microVAX performance can be obtained by using a standard PC as host for the University of Stellenbosch, Department of Electrical and Electronic Engineering T800 transputer board. The total investment is less than $US5000.

ACKNOWLEDGEMENT

The valuable assistance of Mr Pieter Bakkes, Senior Lecturer in the Department, is gratefully acknowledged.

REFERENCES

[1] Burke, G.J. and Poggio, A.J. ; Numerical Electromagnetics Code (NEC) - Method of Moments , 3 Program Description Manuals, NOSC, San Diego, California, USA.

[2] J.J. le Roux et al, Electronics Letters, 4 August 1988 , Vol 24, no 16, pp 991-992

Obtaining Scattering Solutions for Perturbed Geometries and Materials from Moment Method Solutions.

ELIZABETH YIP [1]

BRIAN TOMAS [2]

[1] Boeing Advanced Systems,

P.O. Box 3707, M.S. 4C-01,

Seattle, Wa. 98124-2207

[2] Boeing Aerospace,

P.O. Box 3999, M.S. 8K-17,

Seattle, Wa. 98124-2499

Abstract. In this paper, we present an efficient method for computing the solution to scattering problems using a perturbation scheme based on the solution of related original problems. Assuming the radar cross section has been computed for a particular scatterer associated with a moment method matrix B , we call the computation of the radar cross section of a slightly perturbed scatterer a "perturbed problem of B". If the original problem has n unknowns, and the perturbed problem is formed by changing p cells of the original problem, then our method requires an operation count of $O(n^2p + p^3)$ while a direct moment method solution requires an operation count of $O(n^3)$. Our method involves application of the Sherman-Morrison-Woodbury formula for inverses of perturbed matrices. We show that the method can be easily implemented in any moment method code, and the user does not have to learn a new input procedure.

Further, the modified code can provide a basis for a non-linear optimization procedure which minimizes the radar cross section of an obstacle by varying the surface impedances. An appropriate objective function in this problem depends on the radar cross section at the angles and frequencies of interest. Let n be the number of cells in the obstacle and let p be the number of cells with variable impedance, with $n >> p$. Then application of the Sherman-Morrison-Woodbury formula results in objective function evaluations requiring an $O(np + p^3)$ operation count. In contrast, application of the classical moment method results in objective function evaluations requiring an $O(n^3)$ operation count.

Numerical results from large practical problems demonstrate the efficiency and stability of the new method.

The work of the first author was funded by Rome Air Development Center/OCTM under contract number F30602-85-C-0225. Both authors wish to thank Dr. Robert J. Chiavetta for suggesting an appropriate title and for reading and commenting on earlier drafts of this paper. Parts of this material have been presented by the authors at the 3rd and 4th Annual Reviews of Progress in Applied Computational Electromagnetics, Monterey, Ca..

1. INTRODUCTION

Let MOM be a generic moment method code that solves its matrix equation by Gaussian elimination. Suppose MOM has solved a certain scattering problem. A second scattering problem is called a perturbed scattering problem of the first if the scatterer of the second problem is a slight perturbation of the first, geometrically and/or electrically. In this paper, we present an easy modification of MOM, which we call UMOM, for the solution of perturbed scattering problems. The method employed is based on the Sherman- Morrison-Woodbury updating formula (which we will abbreviate as SMW in the rest of this paper).

We show that appropriate application of the SMW yields a method that is efficient and easy to use. If the original problem has n unknowns, and the perturbed problem is formed by changing p unknowns of the orginal problem, then our method requires an operation count of $O(n^2p + p^3)$ while a direct moment method solution requires an operation count of $O(n^3)$.

The SMW was the work of Sherman, Morrison [1],[2] and Woodbury [3], which is not well-known outside the community of numerical linear algebra. The formula was rediscovered and applied to different engineering disciplines. A partial list of references on the applications of the SMW is:

(1) R. Hockney 1970 [4],

(2) B.Buzbee, F.Dorr, J.George and G.Golub, 1971 [5],

(3) W.Proskurowski, O. Widlund 1976 [6],

(4) E.L. Yip 1986 [7],

(5) E.L. Yip and B. Tomas, 1987 [9],

(6) B.Tomas and E.L.Yip 1988 [10],

(7) R. Kastner 1988 [11].

Kastner's work on large planar structures uses a specialized form of the SMW, which is simpler than the application of the SMW to general moment method codes discussed in this section.

Section 2 contains a discussion of the classical theory of the SMW and one of its implementations. Section 3 presents its application to scattering problems. In Sections 4 and 5, we present the solution of two scattering problems: the perturbed problem and the optimal loading problem. Section 6 contains numerical results.

2 THEORY

This section presents the Sherman-Morrison-Woodbury updating formula, and an algorithm for its general implementation. The efficiency of the method in terms of operation count is also discussed.

If A and B are $n \times n$ matrices, and if $A - B$ is a rank p matrix, there exist $n \times p$ matrices U and V such that

$$A = B - UV^T, \tag{1}$$

(where the superscript T signifies the transpose of the corresponding matrix). The Sherman-Morrison-Woodbury updating formula expresses A^{-1} in terms of B^{-1}, U and V:

$$A^{-1} = B^{-1} + B^{-1}U(I - V^T B^{-1} U)^{-1} V^T B^{-1} \tag{2}$$

(For the sake of completeness, we derive the Sherman-Morrison-Woodbury formula in the Appendix.)

There are many different methods of implementing of the above equation for the solution of $Ax = b$. Algorithm 1 below is an implementation for the most general case, that is, when $B - A$ is an arbitrary rank p matrix.

Algorithm 1.

Step 1. Compute for $BZ = U$.

Step 2. Compute the matrix $K = (I - V^T Z)$, and its LU factors.

Step 3. Solve $By = b$ for y.

Step 4. Compute $w = V^T y$.

Step 5. Solve $Ks = w$ for s.

Step 6. The solution for $Ax = b$ can be computed as $x = y + Zs$.

Postmultiply both sides of equation (2) by b,

$$A^{-1}b = B^{-1}b + B^{-1}U(I - V^T B^{-1}U)^{-1}V^T B^{-1}b. \tag{3}$$

Substituting the matrices Z and K and the vectors y, w, and s which are defined in Algorithm 1 into equation (3), we see that, in the absence of numerical round-off, the vector x defined in Step 6 of Algorithm 1 satisfies $Ax = b$.

If A and B are full matrices, and if B has already been factored, then the amount of work in Algorithm 1 is of the order $p(n^2 + p^2/3)$; if p is small, this can be much less costly than factoring A.

3 Application to Scattering Problems

Let B and A be the coefficient matrices of the original and perturbed problems, respectively. If both the material and geometric properties of the two problems are different,

then the matrix $B - A$ consists of a few non-zero rows and a few non-zero columns. If only the material properties of the two problems are different, the the matrix $B - A$ will consists of only a few non-zero columns. In order to apply the SMW, the matrices U and V in equation (1) need to be defined.

Before we proceed with our discussion, it is pertinent to indicate the following:

(1) If an $n \times n$ matrix C has only one non-zero column, say the j-th column, then if u is a vector of length n and equals the non-zero column of C, and v is a vector of length n with the value 1 at its j-th entry and zero everywhere else, then $C = uv^T$.

(2) If an $n \times n$ matrix R has only one non-zero row, say the i-th row, then if v is a vector of length n and its transpose equals the non-zero row R, and u is a vector of length n with the value 1 at its i-th entry and zero everywhere else, then $R = uv^T$.

Consider first the case when only the material properties are different in the two problems. Suppose there are q non-zero columns, $j_1, j_2, \ldots, j_q$, in $B - A$. Let U be a $n \times q$ matrix whose columns are the q non- zero columns of $B - A$. Let V be an $n \times q$ matrix whose k-th column, $k = 1, 2, \ldots, q$, has the value 1 at its j_k-th entry and zero everywhere else. Then $B - A = UV^T$.

The case when both the geometric and/or material properties are different is more complicated. Suppose $B - A$ has p non-zero rows, $i_1, i_2, \ldots, i_p$, and q non-zero columns, $j_1, j_2, \ldots, j_q$. Let R be a matrix whose rows are the non-zero rows of $B - A$. Let C be a matrix whose columns are the non-zero columns of $B - A$ minus the intersection of the non-zero rows and non-zero columns of $B - A$. (See Fig. 1) Then

$$B - A = R + C. \tag{4}$$

Let U be an $n \times (p + q)$ matrix of the form:

$$U = [P_1, U_1], \tag{5}$$

where P_1 is a $n \times p$ matrix whose k-th column, $k = 1, 2, \ldots, q$, has the value 1 at its i_k entry and zero everywhere else, and U_1 is an $n \times q$ matrix whose columns are the non-zero columns of C in equation (4). Similarly, let V be an $n \times (p+q)$ matrix whose transpose is of the form:

$$V^T = \begin{bmatrix} V_1 \\ Q_1 \end{bmatrix} \tag{6}$$

where V_1 is an $p \times n$ matrix whose rows are just the non-zero rows of R in equation (4), and Q_1 is an $q \times n$ matrix whose k-th row, $k = 1, 2, \cdots, q$ has the value 1 at its j_k-th row and zero everywhere else. Then from equations (4) to (6),

$$\begin{aligned} UV^T &= P_1 V_1 + U_1 Q_1 \\ &= R + C \\ &= B - A \end{aligned} \tag{7}$$

Once U and V are identified, Algorithm 1 may be applied.

4 Solving the Perturbed Problem

This section shows that the basic properties of the matrices U and V defined in section 3 provide a user-friendly and portable computer implementation for practical problems. In this implementation, the user describes the perturbed problem to UMOM in exactly the same way he describes the original problem to MOM. UMOM will figure out the differences between the two problems. This implementation is also portable in the sense that, in order to apply the SMW updating formula to another moment method code, one need only modify the subroutines of UMOM slightly.

For the convenience of discussion, we shall refer to the part of the scatterers which is

different in the two problems as the "perturbed" part, and the other part as the "unperturbed" part.

The steps the user takes to solve his new problem are :

(1) Solve the original problem with MOM; specify that the problem and immediate computation information are to be saved.

(2) Use UMOM to solve the perturbed problem. The input process for UMOM includes defining the new problem and specifying the disk file on which the old problem is stored.

Generation of the pertinent information for the SMW requires the user's input to be processed by the routines: SORT, COMPARE, and INDEX. Each of these is explained in detail below.

The structural differences between the two problems are obtained first. UMOM SORTs (by the Shell sorting algorithm) the discrete points which describe the scatterers in the two problems, and then COMPAREs them. This is a very efficient procedure. Without the sorting, a brute force comparison requires $O(n^2)$ operations, where n is the number of points which describe the scatterering problem. With sorting , the comparison takes an average of $O(n \log n)$ operations.

Any sorting algorithm requires an ordering for the objects to be sorted. UMOM assumes the following ordering on the $x - y$ plane:

We say $(x_1, y_1) > (x_2, y_2)$ if and only if $x_1 > x_2$ or $(x_1 = x_2 \quad \text{and} \quad y_1 > y_2)$.

For example, in Fig. 2, point 1 is less than point 2 which is less than point 3.

The INDEX process establishes the link between the matrices of the original and the

perturbed problems. Write

$$A = A_0 + A_1 \tag{8.1}$$

$$B = B_0 + B_1 \tag{8.2}$$

where A_0 and B_0 contain matrix elements which correspond to the unperturbed part of the two scatterers, and A_1 and B_1 contain matrix elements which correspond to the perturbed part of the two scatterers.

Mathematically, INDEX generates a set of indices from which a permutation matrix P is defined with A_0 and B_0 related as:

$$P^T A_0 P = B_0. \tag{9}$$

(Note that the inverse of P is its transpose.)

The matrix equation we are interested in solving is

$$Ax = b \tag{10}$$

which is equivalent to

$$\begin{aligned} P^T A P P^T x &= P^T b \\ (P^T A_0 P + P^T A_1 P) P^T x &= P^T b \\ (B_0 + P^T A_1 P) P^T x &= P^T b \\ (B + P^T A_1 P - B_1) y &= P^T b, \end{aligned} \tag{11}$$

where $y = P^T x$. $P^T A_1 P - B_1$ in equation (11) has only non-zero rows and non-zero columns corresponding to the perturbed part of the scatterers. And according to section

3, matrices U and V can be found so that

$$B_1 - P^T A_1 P = UV^T.$$

The SMW can then be applied.

Note that only A_1 and B_1 in equation (8) need to be generated. This can easily be accomplished by modifying the appropriate DO-loops in the code which generate the matrix elements in MOM.

Before applying the SMW, premultiply the right-hand-side vector b by P^T. Then in place of the regular linear equation solver, use the SMW updating formula to solve for y in equation (11). Then the true solution x is obtained as

$$x = Py \tag{12}$$

In summary, Fig. 3 illustrates the flow of MOM and UMOM and the structure of UMOM. The procedures in UMOM can be modified with minimal effort for adaptation to other moment method codes.

In our previous discussion, we assume the two problems generate matrices of the same dimensions. In the case in which they generate matrices of different dimensions, we show that minor modifications to the smaller matrix afford the use of the SMW.

In the case in which the dimension of B is greater than that of A, append an identity matrix to the right lower corner of A so that the two matrices have the same dimensions and replace equation (10) with

$$\begin{bmatrix} A & 0 \\ 0 & I \end{bmatrix} \begin{bmatrix} x \\ z \end{bmatrix} = \begin{bmatrix} b \\ 0 \end{bmatrix} \tag{13}$$

Note that the solution of equation (13) is of the form

$$\begin{bmatrix} x \\ 0 \end{bmatrix}$$

where x is the solution of equation (10).

In the case where the dimension of A is greater than that of B, append an identity matrix to the lower right corner of B so that the two matrices have the same dimensions. Note that the necessary criterion for the application of the SMW updating formula is that $B^{-1}b$ can be computed efficiently. Note that

$$\begin{bmatrix} B & 0 \\ 0 & I \end{bmatrix}^{-1} = \begin{bmatrix} B^{-1} & 0 \\ 0 & I \end{bmatrix}.$$

Thus the modified coefficient matrix for the original problem is as easy to "invert" as its unmodified form.

5 Optimal Loading

An immediate application of UMOM is to the optimal loading problem. We are interested in minimizing the scattering cross section of an obstacle by varying its surface impedance. The discrete approximation to this problem is a nonlinear optimization problem. This problem can be solved by applying UMOM. In the analysis below we consider a single angle and a single frequency; practical applications usually consider a range of angles and frequencies. For simplicity, only examples with real-valued impedances are considered in the analysis. The general case is solved by treating the real and imaginary parts as separate variables.

Let μ be the vector of discrete impedances of the cells in the scattering obstacle. Let B be the impedance matrix associated with the obstacle geometry and μ. Then the objective

function for the optimization problem is

$$\sigma = \sigma(\mu)$$

where $\sigma = |L(x)|^2$, L is a linear functional independent of μ, and x solves $Ax = b$ with b the usual excitation vector. In practice the impedance varies over p cells with $n >> p$, where n is the total number of cells in the problem.

At each iteration, the bulk of computation in the optimal loading problem involves the computation of the objective function, which involves solutions to the matrix equation $Ax = b$, requiring $O(n^3)$ operations. We present an efficient method of computing of the objective function using the SMW which requires $O(np+p^3)$ operations: the first solution of the linear system is computed by MOM; subsequent solutions for different values of μ are computed by SMW.

For simplicity, assume below that the cells in the model are ordered so that the only the first p cells have variable impedance, and that these impedances vary independently. The general case can be handled by the INDEX process discussed in Section 3.

Let B be the impedance matrix associated with an initial impedance μ_0 and let A be the impedance matrix for an updated value of μ. Then from the discussion in section 2, $B - A = UV^T$ where U is an $n \times p$ matrix related to the basis and testing functions; in the case when both are pulse functions, the j-th column, $j = 1, 2, \ldots, p$, has the value 1 at its j-th entry and zero everywhere else, and

$$V^T = [D|0] \tag{14}$$

where D is a $p \times p$ diagonal matrix whose diagonal entries are the components of μ.

Note that U and b are independent of μ.

The flow of the optimization calculations proceeds as follows.

Algorithm 2.

Step 1 Initialization: Compute U, b, $\hat{U} = B^{-1}U$, $\hat{b} = B^{-1}b$ by MOM, with U and b overwritten by $\hat{U}$ and $\hat{b}$.

Step 2 Iteration: Compute the objective function, applying the SMW to compute

$$x = A^{-1}b = \hat{b} + \hat{U}(I - V^T\hat{U})^{-1}V^T\hat{b}. \tag{15}$$

Step 3 Test for Optimality: If the solution is optimal, stop. Otherwise recompute new μ and V^T as defined in equation (14) and go to Step 2.

Note that B^{-1} is no longer needed in Step 2, so the memory used by B^{-1} can be used to store $B^{-1}U$ if the appropriate I/O procedure is used.

The flow of the above calculations is summarized in Fig. 4.

From Step 2, it can be seen that using the SMW formula for the computation of $A^{-1}b$ results in an $O\left(np + p^3\right)$ operation count compared with an $O\left(n^3\right)$ operation count using MOM.

The use of objective function gradients in optimization algorithms is well known. We now investigate the computation of the objective function gradient using the SMW formula. A finite difference approximation to the gradient of σ requires $O\left(np^2\right)$ operations. The gradient can also be computed in $O\left(np^2\right)$ operations by applying the SMW formula and observing that required intermediate quantities are already stored for objective function evaluations.

Recall that

$$\sigma = |L(x)|^2 = L(x)\,\overline{L(x)}$$

from which

$$\frac{\partial \sigma}{\partial \mu_k} = L\left(\frac{\partial x}{\partial \mu_k}\right)\overline{L(x)} + L(x)\,\overline{L\left(\frac{\partial x}{\partial \mu_k}\right)}$$

by the linearity of L. The derivatives of x are obtained by implicitly differentiating $Ax = b$:

$$\frac{\partial A}{\partial \mu_k}x + A\frac{\partial x}{\partial \mu_k} = 0$$

$$\frac{\partial x}{\partial \mu_k} = -A^{-1}\left(\frac{\partial A}{\partial \mu_k}x\right).$$

From the decomposition $B - A = UV^T$, the form of V^T as defined in equation (14), and the fact that U is independent of μ, it can be seen that $\frac{\partial A}{\partial \mu_k}$ has only one nonzero column, and it is just the k-th column of U which we call u_k. That is,

$$\frac{\partial A}{\partial \mu_k} = [0, \ldots, u_k, 0, \ldots]. \tag{16}$$

If we write $x = (x_1, \ldots, x_n)^T$ then $\frac{\partial A}{\partial \mu_k}x = x_k u_k$. From this it follows that

$$\frac{\partial x}{\partial \mu_k} = -x_k A^{-1}(u_k). \tag{17}$$

Now the SMW formula can be applied to compute $A^{-1}(u_k)$ in $O(np)$ operations using the fact that $B^{-1}(u_k)$ is already stored for use in evaluating the objective function. Assuming that $\left(I - V^T B^{-1} U\right)^{-1}$ is also already stored, the gradient of σ can be calculated as above in $O\left(np^2\right)$ operations.

We have shown that the well known technique of impedance loading can be efficiently applied using moment method techniques. The implementation can use subroutines from existing moment method codes and existing optimization software. Unlike earlier techniques [12], a separate analysis is not required for each new geometry.

We have incorporated the SMW into three moment method codes currently in use:

(1) RAMZ - a modification of RAMVS [13] which is a 2D moment method code for scatterers treated with absorbing materials that satisfy an impedance boundary condition,

(2) DMS2 - a 2D volumetric moment method code internal to the Boeing Company,

(3) NEC - written by Burke and Poggio [14] which we use as a 3D moment method code for structures modeled as wire grid surfaces in free space or over a ground plane.

The modification made to NEC is for the optimal loading problem.

The following is a discussion of three examples, one corresponding to each of the the above codes and its corresponding modifications:

(1) The original problem is a perfectly conducting sheet of 10 wavelengths lying on the x-axis. The perturbed problem is obtained by replacing the leftmost 10 cells (1 wavelength) with a material whose electric and magnetic impedances are $(.5, .6)$ and $(1.65, 1.65)$. Both problems have 100 cells. The H-pol monostatic scattering pattern is computed from 0 to 30 degrees at 10 degree intervals. See Fig. 5 for a description of the geometry and angle orientation.

(2) The original problem is a perfectly conducting ellipse whose major and minor axes are respectively 4 wavelengths and 2 wavelengths. The major and minor axes lie respectively on the y- and x- axes. The perturbed problem is obtained by removing 4 cells on the right of the ellipse above the x-axis. The original problem has 101 cells and the perturbed problem has 97 cells. The E-pol monostatic RCS for incidence angles from zero to 10 degrees are computed. See Fig. 6 for a description of the

geometry and the angle orientation.

(3) This example is motivated by Schindler, Mack and Blacksmith [12]. A pair of parallel dipoles is viewed in the plane of the dipoles, polarized also in the plane of the dipoles. The dipoles are 1 meter long, spaced .2 meters apart, and are divided into 6 segments. The center two segments of each dipole are loaded with impedances of $200 + j200$ at initialization. The scattering is optimized over the sector from 0 to 40 degrees using 5 angles at a single frequency, 300 mhz. See Fig. 7 for a description of the geometry and the angle orientation.

All three examples were run on the VAX 11-785. The table below summarizes the matrix dimensions, perturbation order and CPU time. n and p are respectively the dimensions of the original matrix and the perturbed part. MOM and UMOM respectively represent the original moment methods code and their corresponding SMW modification.

TABLE 1. CPU SECOND PERFORMANCE COMPARISON

Example	n	p	MOM sec.	UMOM sec.
1	200	20	36.9	26.7
2	101	4	19.6	8.7
3	12	4	1.56	0.07

The timing for Example 3 is the timing per iteration. This example ran for 201 iterations.

The scattering patterns of the above examples verify the accuracy of the methods presented in this paper. Fig. 8 shows the scattering pattern of the perfectly conducting sheets and the treated sheet (example 1). The treated case was run through the original moment method code and the answers coincides with those obtained by the SMW-modified moment method code. Fig. 9 shows the scattering pattern of the closed elliptic conductor and the elliptic conductor with an aperture. The optimal impedances for the center 2

segments of each dipole in example 3 are $78 + 407j$ and $56 + 487j$. Fig. 10 illustrates the effect of this optimal loading.

7 Conclusion

The classical theory of the Sherman-Morrison-Woodbury updating formula and its application to scattering problems have been presented. Two examples have been considered: the perturbed problem and the optimal loading problem. It has been shown that an easy modification to a basic moment method code yields an efficient solution method for the perturbed problem and the optimal loading problem. Our numerical examples have demonstrated that the new method is numerically stable and is between 1.5 to 22 times faster than the classical approach.

Note that for any matrix X such that $I - X$ is nonsingular, we have

$$(I - X)^{-1} = I + X + X^2 + X^3 + \cdots . \tag{A.1}$$

The right hand side of equation (A.1) is the Taylor series of $(I - X)^{-1}$.

Recall that

$$\begin{aligned} A &= B - UV^T \\ &= B(I - B^{-1}UV^T). \end{aligned}$$

Thus the inverse of A can be written as

$$\begin{aligned} A^{-1} &= [B(I - B^{-1}UV^T)]^{-1} \\ &= [I - B^{-1}UV^T]^{-1}B^{-1}. \end{aligned} \tag{A.2}$$

Note that since A is nonsingular, the inverse of $I - B^{-1}UV^T$ exists and can be written as an infinite series:

$$\begin{aligned} [I - B^{-1}UV^T]^{-1} &= I + B^{-1}UV^T + B^{-1}UV^TB^{-1}UV^T + \cdots + (B^{-1}UV^T)^k + \cdots \\ &= I + B^{-1}U[I + V^TB^{-1}U + \cdots + (V^TB^{-1}U)^{k-1} + \cdots]V^T \\ &= I + B^{-1}U[I - V^TB^{-1}U]^{-1}V^T \end{aligned} \tag{A.3}$$

Substitute A.3 into A.2 we obtain:

$$A^{-1} = B^{-1} + B^{-1}U(I - V^TB^{-1}U)^{-1}V^TB^{-1}$$

which is the SMW.

REFERENCES

1. J. Sherman and W.J. Morrison, *Adjustment of an Inverse Matrix Corresponding to Changes in the Elements of a Given Column or a Given Row of the Original Matrix*, Ann. Math. Stat. 20 (1949), p. 621.

2. J. Sherman and W.J. Morrison, *Adjustment of an Inverse Matrix Corresponding to a Change in One Element of a Given Matrix*, Ann. Math. Stat. 21 (1950), p. 124.

3. W. Woodbury, *Inverting Modified Matrices,*, in "Memorandum Report 42," Statistical Research Group, Princeton., 1950.

4. R. Hockney, *The Potential Calculation and some Applications*, Math. Comput. Phys. 9 (1970 pages 135–211).

5. B. Buzbee, F. Dorr, J. George and G. Golub, *The Direct Solution of the Discrete Poisson Equation for Irregular Regions*, SIAM J. Numer. Anal. 8 (1971), 722-736.

6. J.R. Bunch and D.J. Rose, *Partitioning, Tearing and Modification of Sparse Linear Systems*, J. Math. Anal. Appl. 48 (1974), 574–593.

7. W. Proskurowski and O. Widlund, *On the Numerical Solution of Helmholtz's Equation by the Capacitance Matrix Method*, Math. Comput. 30 (1976), 433–468.

8. E.L. Yip, *A Note on the Stability of Solving a Rank-p Modification of a Linear System by the Sherman-Morrison-Woodbury Formula*, SIAM J. Sci. Stat. Comput. 7 2 (1986), 507–513.

9. E. Yip and B. Tomas, *Solving Perturbed Problems in a Moment Method Code*, in "3rd Annual Review of Progress in Applied Computational Electromagnetics, Montery, Ca.," 1987.

10. B. Tomas and E. Yip, *Optimal Loading*, in "4-th Annual Review of Progress in Applied Computational Electromagnetics, Montery, Ca.," 1988.

11. R. Kastner, *An "Add On" Method for the Analysis of Scattering form Large Planar Structures*, IEEE Trans. Antennas Propagat. (1989) (to appear).

12. J.K. Schindler, R.B. Mack and P. Blacksmith, Jr., *The Control of Electromagnetic Scattering by Impedance Loading*, Proc. IEEE 53 (1965), 993-1004,.

13. V.V. Liepa, E.F. Knott and T.B.A. Senior, "Scattering from 2 Dimensional Bodies with Absorber Sheets," Air Force Avionics Laboratory, Report No. AFAL-TR-74-119, 1974.

14. G.J. Burke and A.J. Poggio, "Numerical Electromagnetics Code - Method of Moments," Lawrence Livermore National Laboratory, Report No. UCID-18834, 1981.

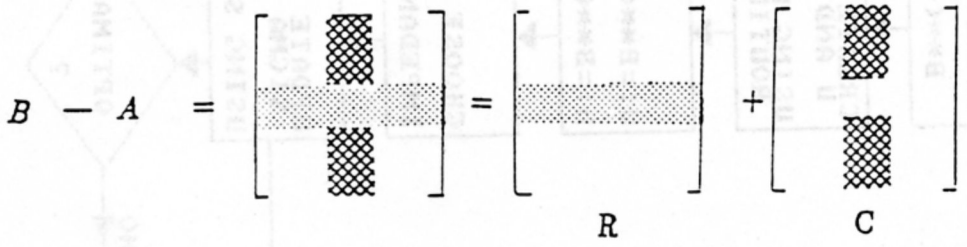

Fig. 1 The Perturbed Parts of the New Matrix

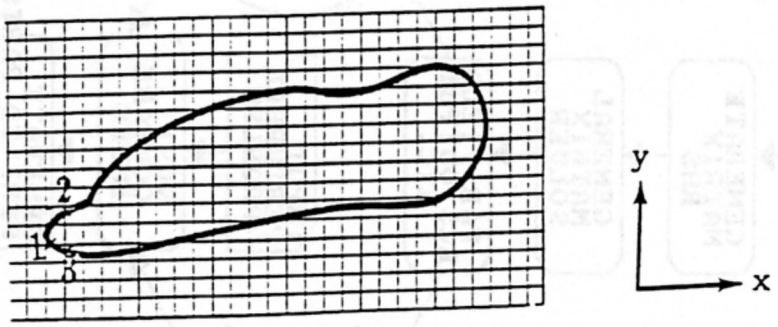

Fig. 2 An Example of Ordering Points in the $x - y$ Plane

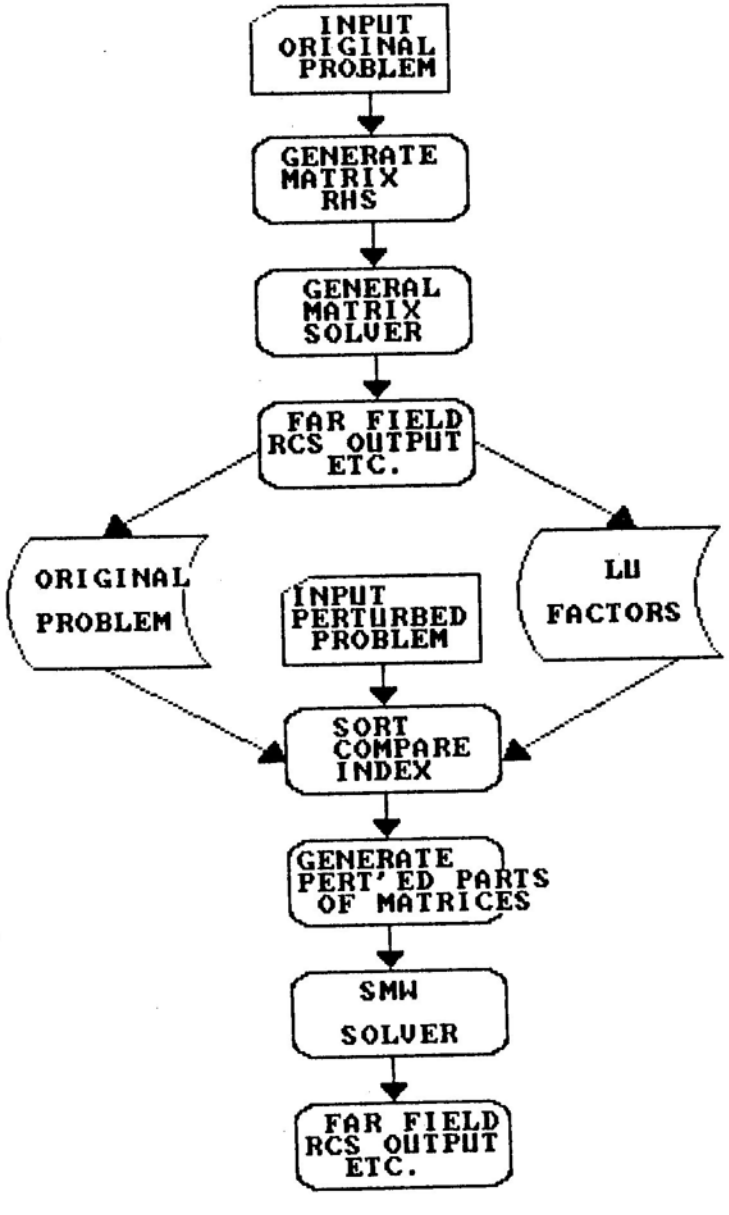

Fig. 3 Flow Diagram for MOM-UMOM

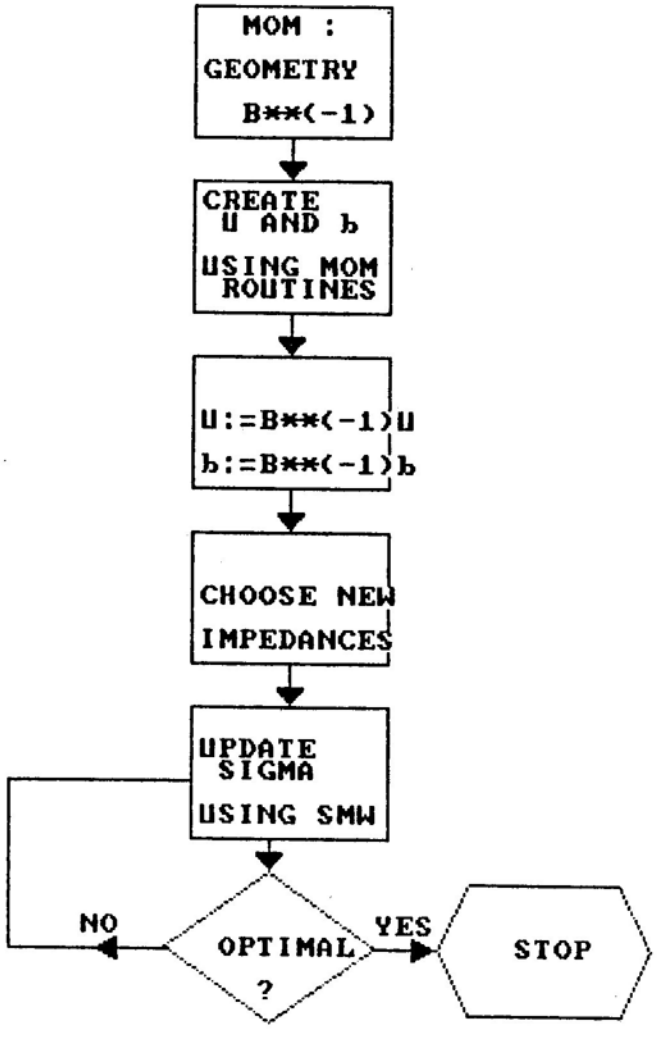

Fig. 4 Flow Diagram for The Optimal Loading Calculation

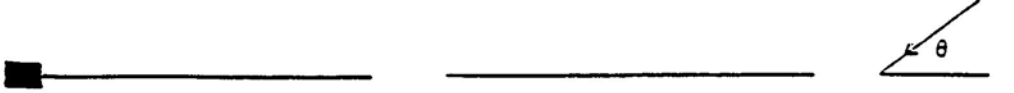

Fig. 5 Geometry and Angle Orientation of Example 1

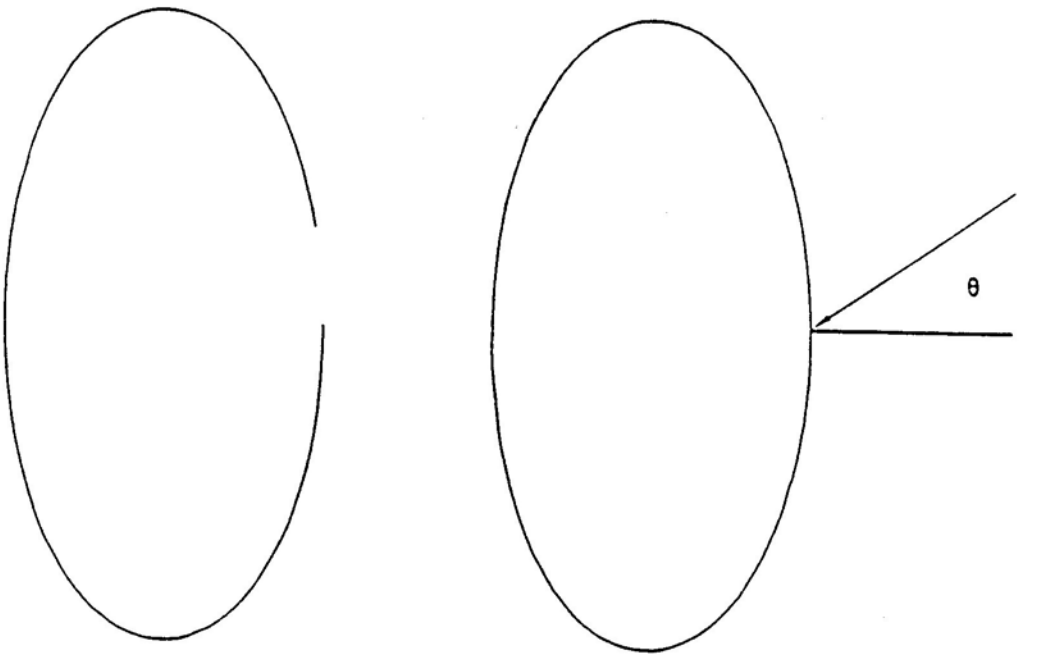

Fig. 6 Geometry and Angle Orientation of Example 2

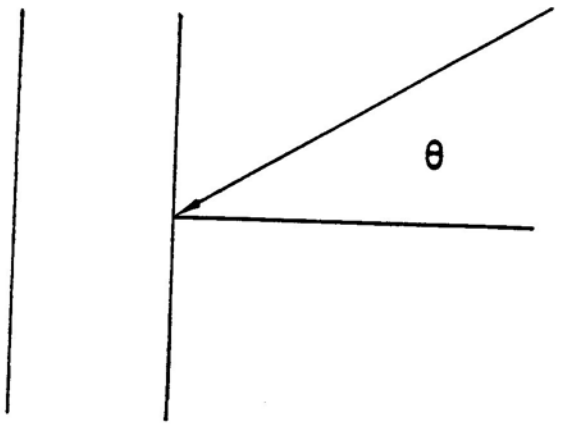

Fig. 7 Geometry and Angle Orientation of Example 3

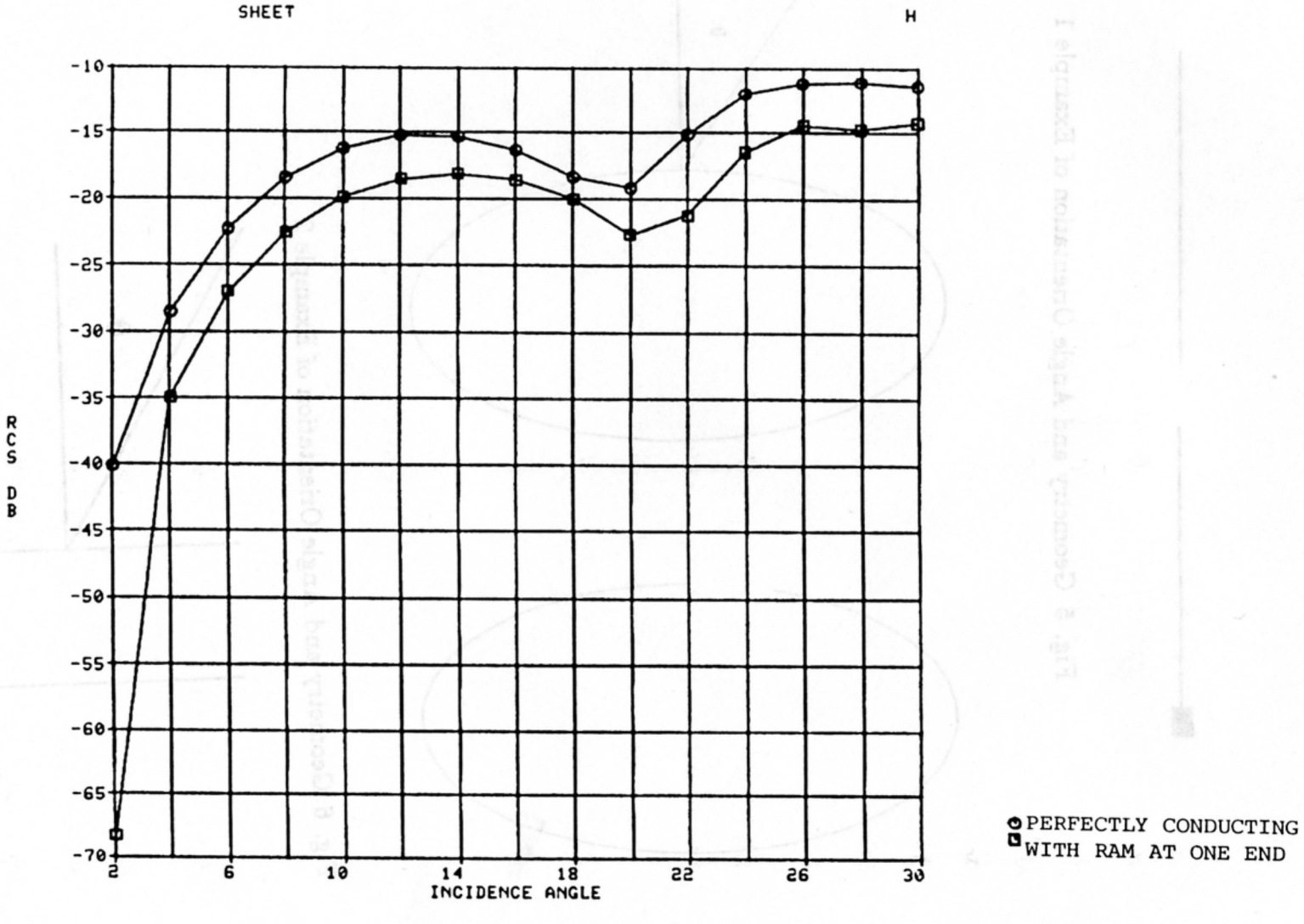

Fig. 8 Scattering Pattern for Example 1

Fig. 9 Scattering Pattern for Example 2

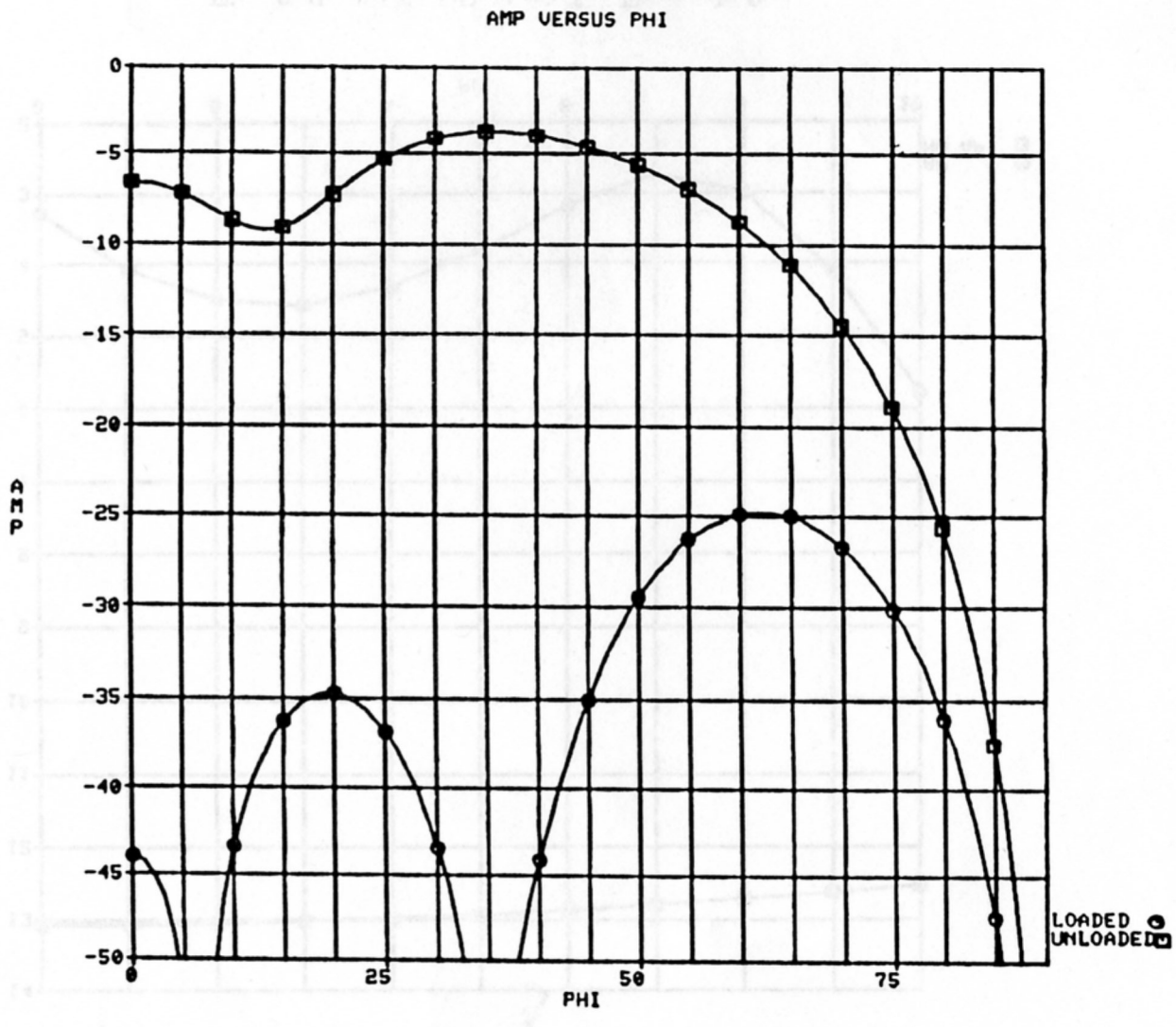

Fig. 10 Scattering Pattern for Example 3

The Effects of Heavy Charged Particle Irradiation of MOSFET Devices

William Eichinger, Patrick O'Reilly, and Chistopher Lehner
Department of Physics, United States Military Academy
West Point, New York 10996

Ionizing cosmic particle radiation poses a serious threat to electronic devices (such as metal-oxide semiconductor, field effect transistors - MOSFETs) that are used in outer space. The physical process in which a bombarding ion creates electron-hole pairs in the SiO_2 layer of a MOSFET, the subsequent collection of charge at the SiO_2-substrate interface and its effect on the operating characteristics of the transistor is modeled with two second order, coupled differential equations. The coupled equations are solved using the finite difference technique known as the Alternating Direction Implicit Method, ADI. Preliminary verification of the computer code was performed using a low energy proton accelerator. The measured change in MOSFET operating characteristics compared favorably with the predicted results. The results show that the damage due to ionizing particles is greatly dependent on the energy of the bombarding particle, its angle of incidence, and the magnitude of the bias applied to the MOSFET.

Introduction.

As our technological exploitation of space progresses, so does our dependence on the reliable operation of electronic devices in the harsh environment of outer space. Cosmic particles (consisting of 85% protons and 14% alpha particles)[1] are a primary threat to the reliable functioning of commonly used electronic devices such as metal-oxide semiconductor, field effect transistors (MOSFETs). MOSFETs are often used because they are easy to fabricate, are relatively impervious to radiation, and have a low noise backround, enabling the amplification of extremely weak signals. Payload, weight and speed constraints require that these electronics devices be miniaturized. Unfortunately, as the device parameters decrease, their vulnerability to the ionizing radiation of a single particle (termed a single event upset, SEU) increases, as well as the long term effects of low levels of ionizing radiation. If the effects of ionizing radiation could be understood, then electronic devices could be designed to maximize their survivability in space. The purpose of this paper is to present the results of a computer code which models the effects of ionizing radiation due to heavy ions in MOSFET devices and preliminary results which verify the code predictions.

Operation of MOSFET Devices.

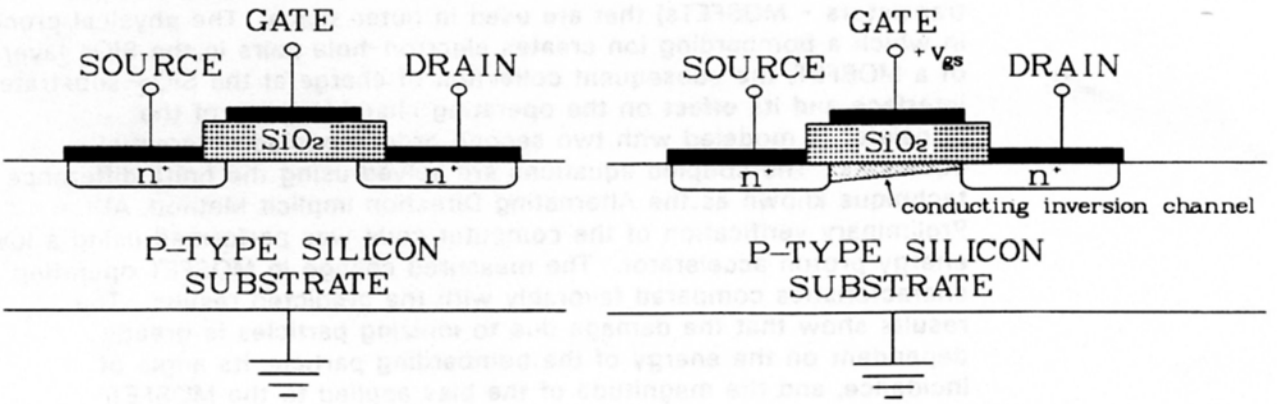

Figure 1a. No Gate Voltage Figure 1b. Positive Gate Voltage
N-Channel Enhancement MOSFET

The electronic device modeled is an enhancement MOSFET (Figure 1a). In the case of an n-channel device, an SiO_2 layer is used to insulate the gate from the p-doped silicon substrate. Although there is not an intrinsic conduction path between the drain and the source, a conducting channel is formed when a positive electric potential (V_{gs}) is placed between the gate and the substrate. This is due to the attraction of electrons to the top of the substrate layer (see figure 1b). These electrons act as the majority carriers in a current (I_d) between the source and the drain which is related to the minimum (or threshold) potential (V_t) required to form the n-channel by:

$$I_d = k(V_{gs} - V_t)^2 \qquad (1)$$

where $V_{gs} > V_t$ and k is a device dependent constant. Figure 2 shows the device characteristics for a typical n-channel enhancement MOSFET. P-channel devices may also be constructed which operate in a similar manner[2].

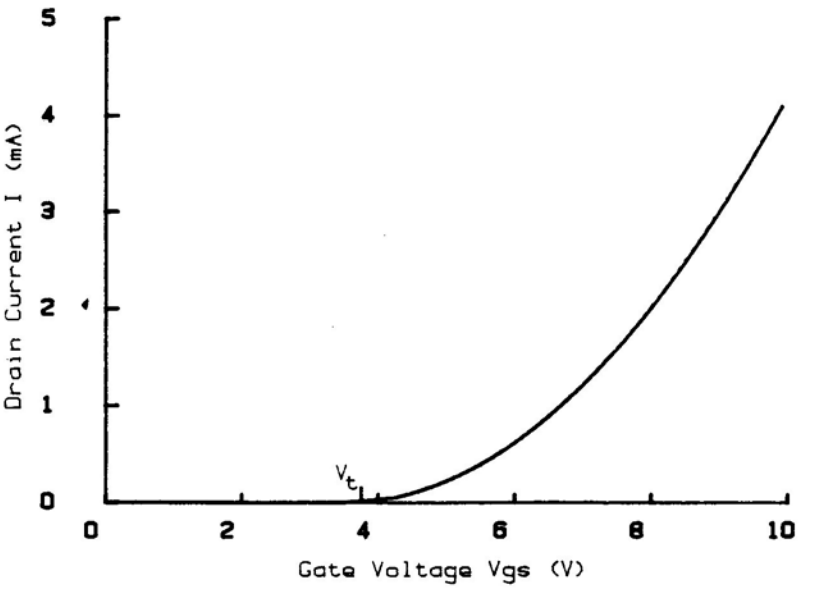

Figure 2. Typical I-V Curve For An N-Channel Enhancement MOSFET.

Damage Mechanisms of Ionizing Radiation In MOSFET Devices.

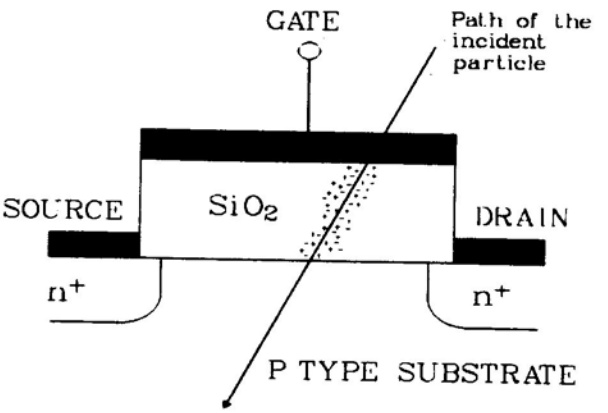

Figure 3. Electron-Hole Generation By Ion Bombardment

When a heavy ion strikes a MOSFET, lattice atoms are ionized as the ion travels through the materials leaving a column of electron-hole pairs as shown in figure 3. In the SiO_2 layer, the electrons are quickly swept away through the gate when V_{gs} is positive. Many of these electrons recombine with the holes as they move toward the gate. The holes which have not recombined will

move to the bottom of the SiO_2 layer, forming a semipermanent concentration of positive charge trapped along the substrate-SiO_2 interface. Consequently, this positive charge will attract electrons in the substrate to the SiO_2-substrate interface decreasing the amount of potential that must be applied to form the n-channel. Thus V_t is reduced by

$$\Delta V_t = - \frac{Q_o f}{C_{ox}} \qquad (2)$$

where Q_o is the total amount of positive charge deposited in the SiO_2 by the incident particle, f is the fraction of the total charge which does not recombine, and C_{ox} is the SiO_2 capacitance. Sufficient irradiation can cause the required threshold voltage to go to zero, thus permanently forming the n-channel (the transistor will remain on).

Mathematical Model of the Effects of Ionizing Radiation.

The result of a heavy ion's traverse through a layer of SiO_2 was modeled as a concentrated column of electron-hole pairs (figure 4a). The initial volume density of the electron-hole pairs decreases radially from the center of the incident ion's path as represented by:

$$n(r) = \frac{N_o}{\pi b^2} e^{-r^2/b^2} \qquad (3)$$

where n(r) is the volume density of electron-hole pairs, N_o is the linear density of electron-hole pairs, b is the radius of the column and r is the radial distance from the center of the column.

The density of the holes in the SiO_2 is dependent upon the rate of recombination, the rate of diffusion, and the rate of drift of the holes and electrons due to an applied electric field. This dependence is mathematically expressed by the following coupled set of equations:

$$\frac{\partial n_+(r,t)}{\partial t} = D_+ \nabla^2 n_+(r,t) + \mu_+ E_x \frac{\partial n_+(r,t)}{\partial x} - \alpha n_+(r,t)\, n_-(r,t) \qquad (4)$$

$$\frac{\partial n_-(r,t)}{\partial t} = D_- \nabla^2 n_-(r,t) - \mu_- E_x \frac{\partial n_-(r,t)}{\partial x} - \alpha n_+(r,t)\, n_-(r,t) \qquad (5)$$

where $D_\pm$ is the diffusion coefficient, $\mu_\pm$ is the mobility of the electrons or holes as appropriate, E_x is the component of the electric field perpendicular to the column, α is the recombination coefficient and n_+ and n_- are the hole and electron volume densities respectively. These equations were first proposed by George Jaffee in 1913 [3]. The solution to these equations will yield the fraction of the original number of holes which escape recombination and begin to migrate towards the SiO_2 - substrate interface. The first term represents the diffusion of holes in the oxide due to the radial density gradient of the electron-hole pairs. The middle term represents the drift of the holes due to the applied electric field. Since the mobility of the holes is much less than the mobility of the electrons, the holes are essentially stationary for times much longer than the time required for the collection of electrons at the gate (10^{-13} seconds). The last term of the equations represents the loss of electrons and holes due to recombination.

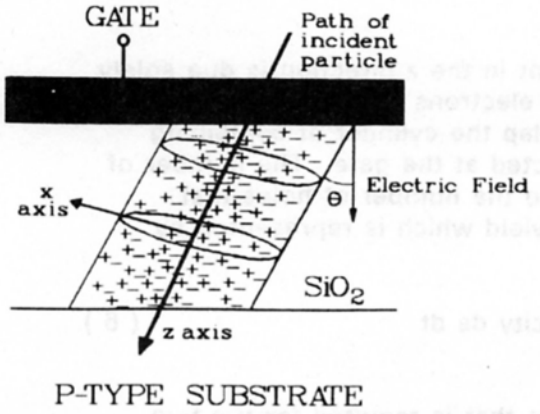

Figure 4a. At Time Equal 0

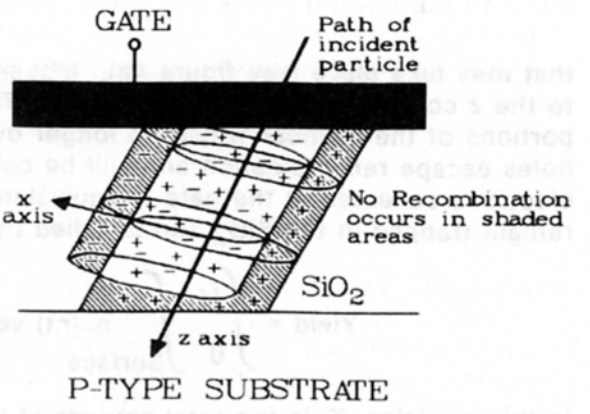

Figure 4b. At Later Times

Figure 4. Charge Movement With Time

Unfortunately, equations 4 and 5 are coupled differential equations which can not be solved analytically using traditional methods of analysis. Thus Jaffee only solved for approximate solutions by ignoring the recombination term and then later attempting to reintroduce its effects. However, with the advent of numerical methods executed by computers, the accurate solution of these equations and the prediction of the effects of ionizing radiation on the MOSFET devices is now possible.

The Computer Model.

The model we have used assumes that two concentric cylinders are formed by the passage of the ion through the SiO_2 layer (see figure 4a). One of the cylinders represents the electron distribution, the other the distribution of holes. The axis of the two concentric cylinders is taken to be the z axis. The angle between the z axis and the normal to the SiO_2-substrate surface is θ. The electron/hole volume density function is assumed to be gaussian in the x-y plane and symmetric about the z axis and given by equation 3 [4]. The linear energy deposition (and thus the electron-hole linear density) of the ion is assumed to be constant over the axial length of the cylinder. This assumption enables the use of a two dimensional solution of the Jaffee Equation since the electrons will not diffuse along the length of the cylinder. The only motion in the axial direction is due to the electric field which will be considered later. The x axis is orthogonal to the cylinder axis and chosen such that the electric field can be expressed completely by its components in the x and z directions.

Each column is conceptually divided into planes which are perpendicular to the column axis. Each plane is subdivided into elements of equal area based upon the choice of Δx and Δy. The electron and hole distribution is evaluated for each element in each time step. These calculated distributions are representitive of distributions at any similar point along the z axis. The movement of the cylinders is due to diffusion and the applied electric field. Recombination occurs only where the cylinder of electrons overlaps the cylinder of holes. Movement in the x direction as a result of the x component of the electric field moves the cylinders apart and limits the amount of recombination

that may take place (see figure 4b). Movement in the z direction is due solely to the z component of the electric field. The electrons remaining in those portions of the cylinder which no longer overlap the cylinder of containing holes escape recombination and will be collected at the gate. The number of electrons collected at the gate is equivalent to the number of holes that remain trapped in the SiO_2 and is called the yield which is represented by:

$$\text{Yield} = \int_0^{T_f} \int_{\text{Surface}} n_-(r,t) \text{ velocity } ds\, dt \qquad (6)$$

In this equation, T_f is the total amount of time that is required for the two cylinders to pass each other due to the z component of the electric field.

$$T_f = \frac{L}{\mu_- E \cos^2\theta} \qquad (7)$$

where L is the SiO_2 thickness and E is the magnitude of the electric field.

For the purposes of this model, it is assumed that all of the holes that remain in the SiO_2 will eventually move to the SiO_2-substrate interface and become trapped there. By experimentally measuring the threshold voltage shift, the actual number of holes that became trapped at the interface can be measured with the use of equation 2.

Due to the method in which the code calculates the charge collected, the model tends to underestimate the number of electrons collected at the gate (and thus holes that survive) at early times. In most cases, the majority of the recombinations that do occur happen very rapidly and at times on the order of 10^{-15} seconds or less. Fortunately, the majority of the charge which is collected is that portion that survives recombination and remains in the cylinders after the two columns have separated in the x direction. Thus the amount of charge collected at early times is generally only a small fraction of the total charge collected. The exceptions to this are those occasions when large amounts of recombination occur throughout the time required for collection of the electrons. Small electric fields and large linear energy depositions are examples where large amounts of recombinations occur.

The Computer Code.

Previously, attempts to solve the Jaffee equation have utilized explicit numerical analysis techniques[5]. The computer method we used to solve the coupled differential equations for this physical system was the Alternating Direction Implicit Method (ADI), also known as the Peachman-Rachford Method[6]. This method is an improvement over the usual explicit method in that it is nearly always stable and convergent. The ADI method involves the solution of a tridiagonal matrix equation which is much simpler and straightforward than the solution to an implicit method system in two dimensions.

For the first half cycle, the calculations proceed along the x axis with the finite elements being implicit in the x direction and explicit in the y direction. This results in the following expression for the electron volume density which is a discrete version of equation 5:

$$\left[\frac{D\Delta t}{2(\Delta x)^2} - \frac{\mu E \Delta t}{4\Delta x}\right] n_{i-1,j}^{k+1} - \left[\frac{D\Delta t}{(\Delta x)^2} + 1\right] n_{i,j}^{k+1} + \left[\frac{D\Delta t}{2(\Delta x)^2} + \frac{\mu E\, \Delta t}{4\Delta x}\right] n_{i+1,j}^{k+1}$$

$$= -\left[\frac{D\Delta t}{2(\Delta x)^2}\right] n_{i,j-1}^{k} + \left[\frac{D\Delta t}{(\Delta x)^2} + \frac{\alpha \Delta t}{2} - 1\right] n_{i,j}^{k} - \left[\frac{D\Delta t}{2(\Delta x)^2}\right] n_{i,j+1}^{k} \qquad (8)$$

During the second half cycle, the calculations proceed along the y axis with the finite elements being explicit in the x direction and implicit in the y direction. This results in the following expression:

$$\left[\frac{D\Delta t}{2(\Delta x)^2}\right] n_{i,j-1}^{k+1} - \left[\frac{D\Delta t}{(\Delta x)^2} + 1\right] n_{i,j}^{k+1} + \left[\frac{D\Delta t}{2(\Delta x)^2}\right] n_{i,j+1}^{k+1}$$

$$= -\left[\frac{D\Delta t}{2(\Delta x)^2} - \frac{\mu E \Delta t}{4\Delta x}\right] n_{i-1,j}^{k} + \left[\frac{D\Delta t}{(\Delta x)^2} + \frac{\alpha \Delta t}{2} - 1\right] n_{i,j}^{k} - \left[\frac{D\Delta t}{2(\Delta x)^2} + \frac{\mu E \Delta t}{4\Delta x}\right] n_{i+1,j}^{k} \qquad (9)$$

It should be recognized that there is a similar set of equations for the hole density with a reversed sign on the drift term which is solved similtaneously.

The advantage of the ADI method should become clear at this point. Each of the matrix equations that require solution are tridiagonal and may be efficiently solved by LU decomposition[7]. The program begins by calculating the initial cell centered density of electrons and holes for each of the cells. The lower and upper matrix elements are calculated for the initial time element. The main cycling routine consists of the calculation of the known values of equation 8 and the solution of the equation for one row in the x direction. After solving for each of the rows in the x direction, the routine will perform a similar set of calculations based upon equation 9 progressing through each column in the y direction. There being no component of the electric field in the y direction, the problem is symmetric across the x axis and only a half cylinder need actually be calculated.

At the end of each time step the number of electrons that are collected at the gate is calculated. The number collected is related to the portion of the electron cylinder which no longer overlaps the hole cylinder. That portion of the cylinder is indicated in figure 4b. The length of this cylinder element is the product of the electric field along the z axis, the electron mobility in silicon dioxide, and the time element dt. Thus the number of electrons arriving at the gate (and thus the number of holes remaining trapped in the SiO_2) during any time period dt is the total number of electrons in the portion of the cylinder representing the non-recombined electrons which is found by:

$$\text{Yield} = \sum_i \sum_j n(i,j)\ (\Delta x \Delta y)\ (\text{element thickness}) \qquad (10)$$

The process is considered complete when the recombination rate for any one step is less than .05 percent of the total number of electrons remaining. At this point, the solution assumes that no more recombination will occur and all of

the electrons that currently remain in the column will be collected at the gate. The ratio of the number of holes that survive to the total number of electron-hole pairs created is called the fractional yield.

The values used in this analysis for the various constants are given below:[8]

electron mobility	$\mu_- = 40\ cm^2/V\text{-}s$
hole mobility	$\mu_+ = 10^{-5}\ cm^2/V\text{-}s$
recombination coefficient	$\alpha = 1.88 \times 10^{-5}\ cm^3/s$
diffusion coefficient	$D_- = 0.261\ cm^2/s$
diffusion coefficient	$D_+ = 6.5 \times 10^{-8}\ cm^2/s$
column width	b = 3.5 nm

The thickness of the SiO_2 layer, electric field strength, angle of incidence and linear density of electron-hole pairs are considered to be variables in the program and are required input. As the program cycles, the electron and hole volume densities along the x axis are plotted for each cycle on the screen. While this plotting does slow the program, it is a useful tool in understanding the physics of what is happening inside the cylinders. The final output of the program is a recapitulaton of the initial parameters, the fractional yield and the change in threshold voltage per particle.

Results and Analysis.

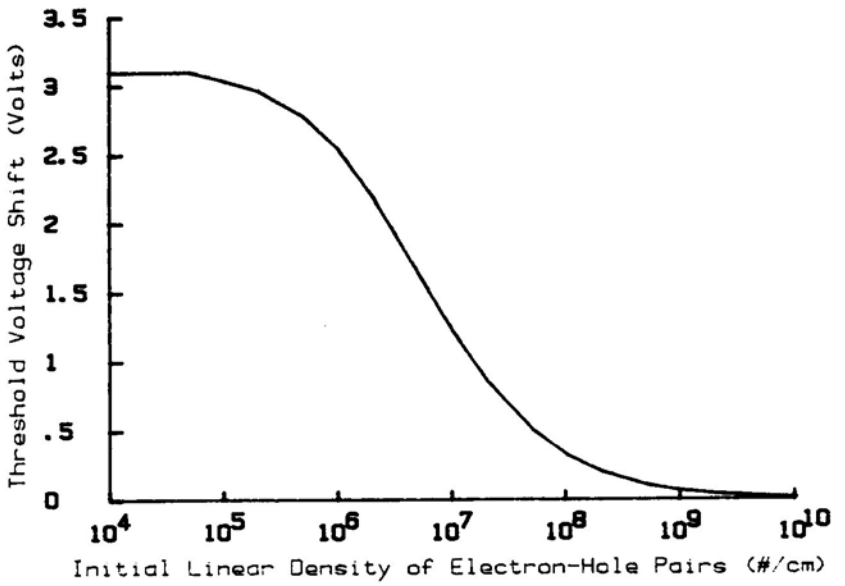

Figure 5. Threshold Voltage Shift vs Initial Linear Pair Density.

Figure 5 is a plot of the predicted threshold voltage shift vs the initial electron-hole linear density (and thus the initial linear energy density). The plot is made for particles impacting at an angle of incidence of 45 degrees on a device with a 350 nm oxide layer under a 5 volt gate voltage (E = 1.4 MV/cm). A dose of 1 krad is assumed for all cases. Note that while the energy

deposited is constant, the damage done varies considerably with the initial linear energy density. This implies that while the high energy, extremely heavy ions in cosmic rays (for example iron) will deposit large amounts of energy in the device, the damage due to ionization effects from these ions will be small. This is because their high linear energy density leads to large amounts of recombination.

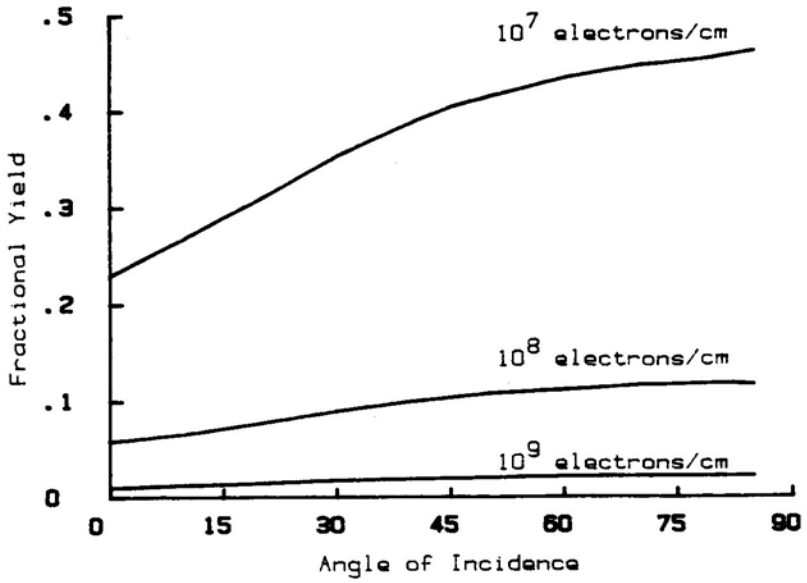

Figure 6. Fractional Yield vs The Angle of Incidence For Various Initial Energy Densities.

Figure 6 is a plot of the fractional yield vs the angle of incidence for various initial electron-hole linear densities. The plot is made for a device with a 350 nm oxide layer under a 5 volt gate voltage (E = 1.4 MV/cm). This graph helps to explain the observed dependence of the threshold voltage shift with angle for protons which was observed by Tallon[9]. He also observed that for low proton energies (which have a high linear energy density) the variation in threshold voltage shift with angle between 45 degrees and 80 degrees became almost nonexistent, while for high proton energies (low linear density) the variation was clear. The computer model also predicts such behavior as a result of the high initial density of electron-hole pairs. At high densities, the initial recombination rate is so high that the rate of separation becomes meaningless. This model demonstrates that the effect is not caused by a buildup of charge on the SiO_2-substrate interface which reduces the effective electric field as Tallon believed but is a consequence of the high linear energy deposition of the particles.

Preliminary Experimental Verification.

Several n-channel devices were irradiated with protons at the USMA Particle Accelerator Laboratory. The gate size of each device was 3 μm by 8 μm with

an oxide thickness of approximately 960 nm. The devices were bombarded with either a diffuse 340 keV or 500 keV proton beam. The proton energies are known with less than 1 percent uncertainty based upon the (p, γ) resonances of boron (163.1 keV) and fluorine (340.6 keV). Proton flux was measured before each irradiation by passing the beam through collimators of known area and collecting the charge deposited with a current integrator. Each device was irradiated with a dose of 500 krads. This was done by rotating the device into the beam for a calculated amount of time based upon the desired dose, proton flux and device size, and then rotating it out of the beam. The threshold voltage for each device was measured before and after irradiation by graphically plotting the I-V curve for the device. The gate voltage (V_{GS}) was maintained at 5 volts during irradiation and until the I-V curve could be measured.

The linear energy density is found from the stopping power equation for protons[10]:

$$\frac{\partial E}{\partial x} = \frac{4.978\ S_{high}\ S_{low}}{S_{high} + S_{low}} \quad keV/\mu m \qquad (11)$$

$$S_{low} = 4.7\ E^{0.45}$$

$$S_{high} = (3329/E)Ln[\ 1 + (550/E) + (0.01321\ E)]$$

Where E is then energy of the bombarding proton in keV. The energy required to create one electron-hole pair is 18 eV[11]. Thus the stopping power is directly related to the linear density of electron or holes.

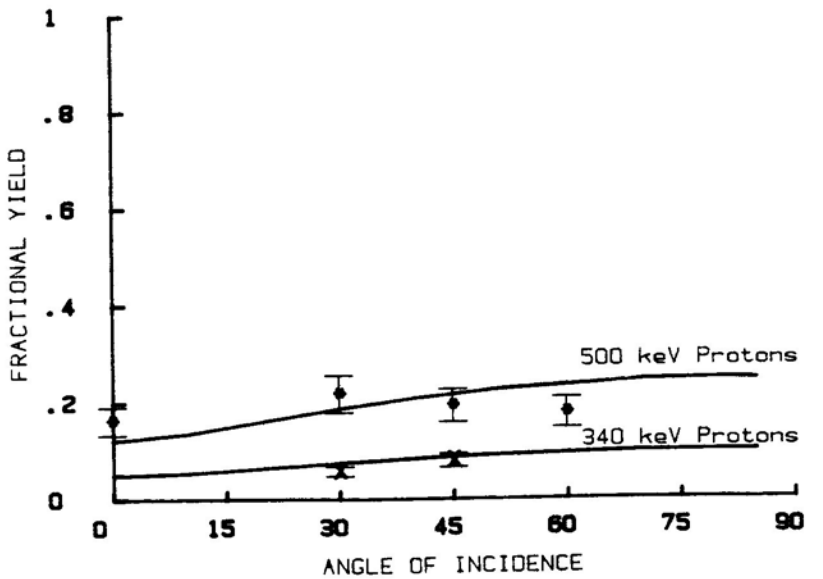

Figure 7. Comparison of Computer Predictions and Test Samples For Proton Energies of 340 keV and 500 keV

The results of the test devices are shown in figure 7. Because of the uncertainties associated with the magnitude of the dose, the uncertainty in the fractional yield is quite high. However, the results do indicate that further and more accurate testing is warranted to verify the predictions made above.

Conclusion.

One of the most interesting results of this work is that while radiation damage is commonly measured in rads (energy deposited), our results show that the amount of damage produced by one rad of radiation can vary greatly (as measured by the threshold voltage shift). The damage done to a device is a complex function of many of the physical parameters, most notably the angle of incidence and the magnitude of the applied electric field, as well as the rate of linear energy deposition (stopping power) of the incident particle.

A logical extension of this work is that the damage done by electrons (thus x rays and gamma rays as well) should be considerably greater than the damage done by an ion which deposits the same amount of energy. The high recombination rate observed in this study is the result of the high electron-hole density along the path of the ion. Since electrons lose their initial direction and tend to have a much more diffuse energy deposition[1,2], the recombination rate will be much less and the damage will be greater for the same amount of energy deposited.

There are some improvements yet to be made on the computer code. Charge would be better modeled as being stripped off in an elliptically shaped cylinder with a thickness based upon the total electric field strength rather than only the z component. More precise measurements on electronic devices must be made to further confirm or disprove the details of the model. The validity of the assumption that all of the holes left in the SiO_2 layer will travel to the SiO_2-substrate interface is uncertain. Prompt measurements of the threshold voltage shifts after irradiation and extending over time should enable measurement of the amount of recombination that occurs as the holes move to the interface.

Acknowledgments

The authors would like to thank Dr. T. R. Oldham and Dr. J. M. McGarrity, without whose assistance this study would not have been possible. A special thanks is due Mr. R. Ronson who machined the device holders and accelerator parts required.

References

1. M. Eisenbud, ENVIRONMENTAL RADIOACTIVITY (Academic Press, New York, 1973), pp. 192-6.
2. A. Bar-Lev, SEMICONDUCTORS AND ELECTRONIC DEVICES, (Prentice/Hall, London, 1979), p. 193-9.
3. G. Jaffee, Annalen der Physik, 42, (1913), p. 303.
4. Solutions to the problem are not sensitive to the shape of initial distribution assumed and vary by less than 10% as long as the peak linear density is constant.

5. T. R. Oldham, CHARGE GENERATION AND RECOMBINATION IN SILICON DIOXIDE FROM HEAVY CHARGED PARTICLES, (Harry Diamond Laboratories, HDL-TR-1985, Adelphi, Md)
6. The program is written is QUICK BASIC for an IBM PC or compatable. A copy of the program may be obtained by sending a diskette to the authors.
7. L. W. Johnson, R. D. Riess, NUMERICAL ANALYSIS, (Addison-Wesley, Reading, Ma., 1982), p. 40-1.
8. T. R. Oldham, op. cit.
9. R. W. Tallon, W. T. Kemp, M. R. Ackerman, M. H. Owen, and A. H. Hoffland, RADIATION DAMAGE IN MOS TRANSISTORS AS A FUNCTION OF THE ANGLE BETWEEN AN APPLIED ELECTRIC FIELD AND VARIOUS INCIDENT RADIATIONS (PROTONS, ELECTRONS, AND CO-60 GAMMA RAYS), IEEE Transactions on Nuclear Science, Volume NS-34, Number 6, December 1987.
10. J. F. Ziegler, THE STOPPING POWER AND RANGES OF IONS IN MATTER 3, (Pergammon Press, New York, 1977).
11. V. A. J. van Lint, T. M. Flanagan, R. E. Leadon, J. A. Naber, and V. C. Rogers, MECHANISM OF RADIATION EFFECTS IN ELECTRONIC MATERIALS, Vol 1, (Wiley and Sons, New York, 1980), p. 222.
12. N. Tsoulfanidis, MEASUREMENT AND DETECTION OF RADIATION, (McGraw-Hill, New York, 1983), p. 118-30.

HF GROUND CONSTANT MEASUREMENTS AT THE LAWRENCE LIVERMORE NATIONAL LABORATORY (LLNL) FIELD SITE

By

George H. Hagn
Information Sciences and Technology Center
SRI International
1611 North Kent Street
Arlington, Virginia 22209

ABSTRACT

The SRI International open-wire-line (OWL) kit was used 3-5 July 1987 to measure the HF ground constants at the Lawrence Livermore National Laboratory (LLNL) field site in Livermore, CA. Data were acquired at 11 locations about 250 ft west of the LLNL facility fence in the vicinity where a longwire and broadband dipole were erected in August 1987 for making impedance measurements for the purpose of validating the Numerical Electromagnetics Code (NEC). An additional location was measured to the north of the antenna site where field strength data were to be taken. Several samples were taken at most locations. Best estimates of the conductivity, relative permittivity (relative dielectric constant), dissipation factor and skin depth were computed as the median values versus frequency for 2 through 30 MHz. Data were acquired at 1-MHz intervals from 2 MHz through 8 MHz, and the interval was increased to 2 MHz from 8 MHz to 30 MHz. The maximum and minimum values were also determined as bounds on the conductivity and relative permittivity values for use in parameter sensitivity analyses. The conductivity values for the relatively dry, densely packed light brown clay fell between those typical of pastoral land and rich agricultural land at about 4×10^{-2} S/m. The relative permittivity values exhibited more variation with frequency. At the low end of the HF band, the relative permittivity values exceeded those of a non-flooded rice paddy (e.g., about 150 at 2 MHz); whereas, at the high end of the band, the relative permittivity approximated values typical of rich agricultural land (about 17 at 30 MHz). The skin depth varied from about 2 m at 2 MHz to 0.7 m at 30 MHz. The dissipation factor was about 1.5, so the soil acted almost as a semiconductor rather than as a lossy conductor or a lossy dielectric. Both the relative dielectric constant and conductivity are important in modeling antennas and propagation over the ground at the LLNL site. Data from nearby wells indicated that the water table was at least 20 m below the surface. Therefore, a one-layer slab model adequately described the ground at this site for HF down to the skin depth.

1. INTRODUCTION

The Lawrence Livermore National Laboratory (LLNL) has developed a method-of-moments model, the Numerical Electromagnetics Code (NEC),[1-3] for modeling antenna characteristics over real ground. The model requires the specification of the wire geometry and the electrical characteristics of the ground over which the antenna is installed. The most recent version, NEC-3,[3] which handles wires that penetrate the earth's surface, has had only limited validation with field measurements. The antenna measurement possibilities include:

- Input impedance;
- Directivity pattern shape;
- Absolute gain; and,
- Ground-wave field strength versus distance from the antenna.

During a previous group of studies, the first three quantities were modeled with NEC-3 and measured in the HF band by SRI International (SRI) for a 7.5-ft vertical monopole with sixteen 40-ft radials buried 7 inches at several sites with different soils.[4-6] The NEC model predictions compared favorably with the measurements when measured ground conductivity and permittivity (i.e., relative dielectric constant) values were used.[7] These values of "ground constants" were obtained using the SRI open-wire-line (OWL) kit designed for this purpose.[8-10]

The LLNL has planned additional NEC validation work at their field site near Livermore, CA, using a broadband dipole and a sloping long-wire.[11] Input impedance and ground-wave field strength values will be measured in the HF band (2-30 MHz). SRI was asked to measure the ground constants in the HF band at the LLNL site for use by LLNL in this validation effort.[12] This paper describes the SRI measurements and presents the ground constants results. The NEC validation results are presented in Ref. 11.

2. DESCRIPTION OF EQUIPMENT

The SRI open-wire line (OWL) ground constants kit consists of a set of 0.5-inch diameter aluminum probes of various lengths from 3 inches to 36 inches, a probe adapter, an HP 4193A Vector Impedance Meter, an HP85B computer, and appropriate software. The kit is powered from generators, and a metered variac is used to maintain the correct voltage at the instrumentation when a long power cord is used. A power-line filter with spike suppression is sometimes used. The kit is shown schematically in Figure 2.1, and it is shown in use at Livermore in Figure 2.2.

The SRI OWL kit semiautomatically measures the soil conductivity and relative permittivity vs frequency in the band 0.5 to 110 MHz. The frequency spacing for measurements between 0.5 and 2 MHz is 0.5 MHz, from 2 MHz to 8 MHz the spacing is 1 MHz, and from 8 to 30 MHz the spacing is 2 MHz. A 4-MHz spacing is used from 30 MHz to 110 MHz.

3. SAMPLING STRATEGY AND MEASUREMENT SITE AND LOCATION DESCRIPTIONS

3.1 Sampling Strategy

The general sampling strategy evolved from consideration of the following:

- Sampling Locations:
  - Proposed antenna locations;
  - Proposed field strength measurement location;
  - Land accessability;
  - Possibility of small-scale lateral inhomogeneities;
  - Availability of water well data; and,
  - Surface vegetation differences.
- Sample Depths:
  - The need for observing variations (if any) in soil electrical properties with depth; and,
  - The depth to which it was possible to penetrate the soil and retrieve the probes.

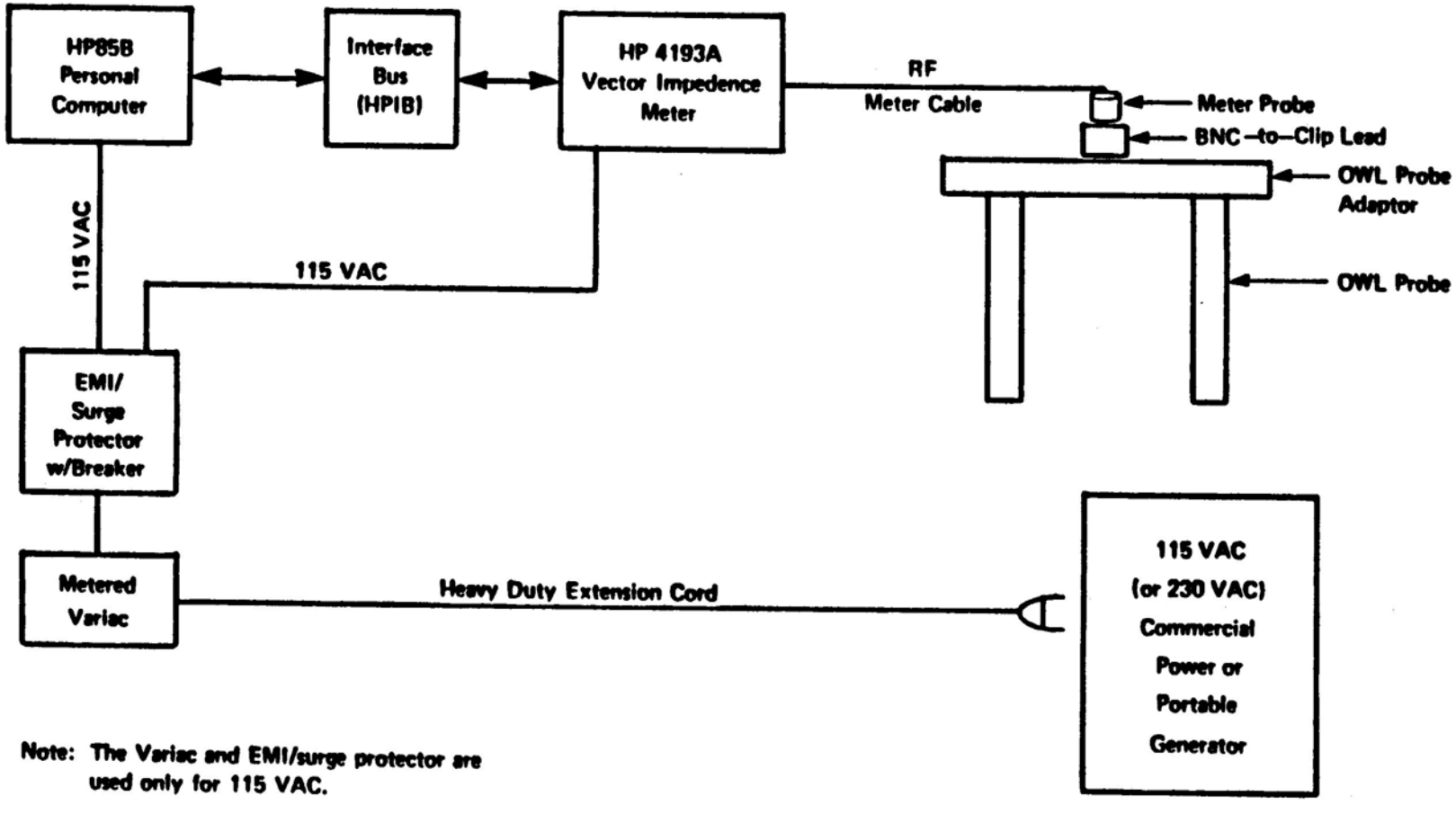

Figure 2.1 BLOCK DIAGRAM OF THE SRI OWL KIT FOR MEASURING RF GROUND CONSTANTS

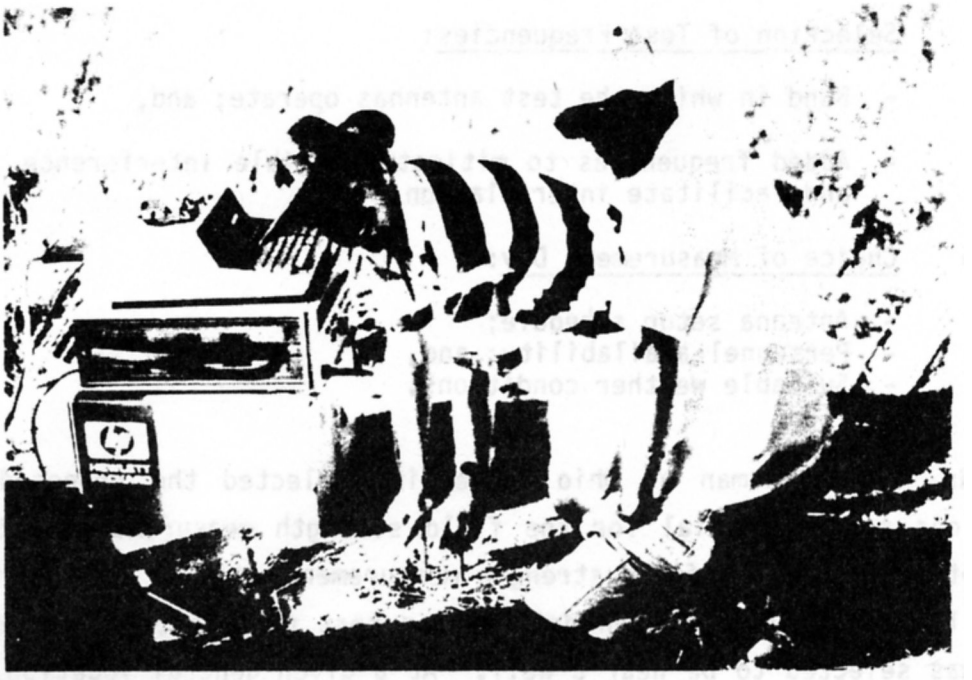

a) Probe Insertion

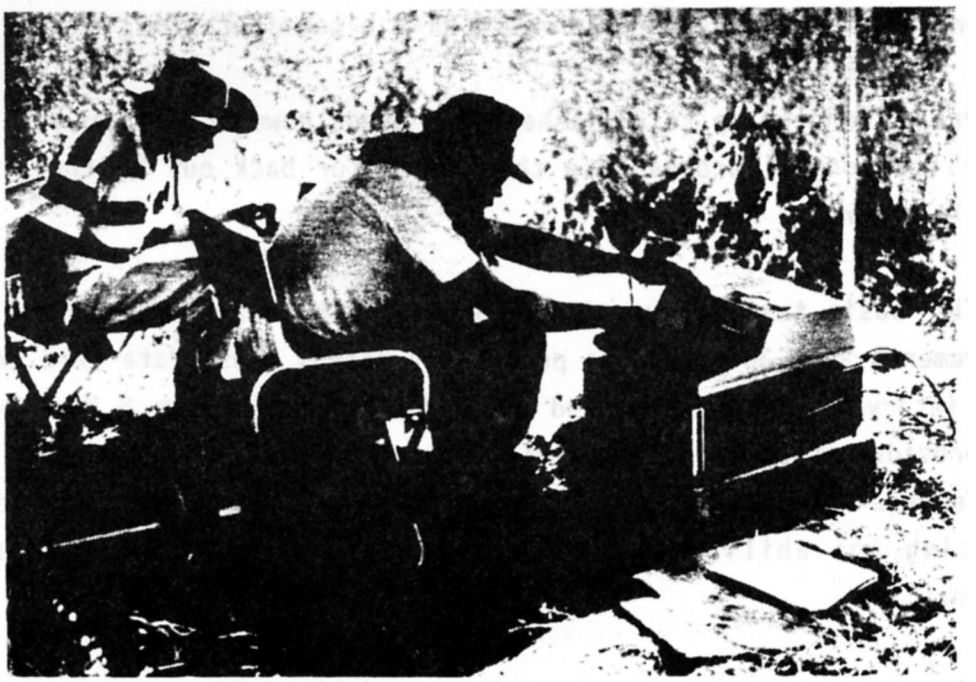

b) Data Acquisition

Figure 2.2 SRI OWL KIT IN USE AT LIVERMORE

- Selection of Test Frequencies:
  - Band in which the test antennas operate; and,
  - Added frequencies to mitigate possible interference and facilitate interpolation.
- Choice of Measurement Day:
  - Antenna setup schedule;
  - Personnel availability; and,
  - Suitable weather conditions.

Mr. Al Christman of Ohio University selected the proposed antenna locations and the radial for the field strength measurements. Some land was not available for field strength measurements due to use by livestock. Several water wells had been drilled for test purposes,[13] and one location was selected to be near a well. At a given general location, several sample points usually were identified within about 1 m of each other to check for small-scale variations. Differences (if any) that might relate to changes in surface vegetation were also a consideration.

Probe lengths up to 36 inches were used; however, it was not possible to get the longest probes into the ground (or back out of the ground) at every location.

The basic test frequencies were in the HF band (defined for the OWL measurements as 2-30 MHz). As previously noted, these data were taken at a 1-MHz interval from 2-8 MHz and at 2-MHz intervals from 8 MHz to 30 MHz. This provided enough samples on different frequencies so that data taken on interference- contaminated frequencies (if any) could be discarded without impacting the ability to estimate the ground constant values versus frequency.

The measurement day was a possible variable. Data were taken on three consecutive days (3-5 July 1987) in order to sample all the locations selected. No locations were repeated on different days at this site due to the extreme difficulty in getting the probes into and out of the ground.

There was no rain during the test period, and it had not rained for some weeks before. Therefore, no significant change in ground constant values with measurement day was expected.

At a given location (an area within a radius of several meters of the stake marking the location), samples were taken at several sample points within about 1 m of each other in order to check the small-scale variations. The 3-inch probe spacing was used, and this approximates a 300-ohm line. An alphanumeric coding system was used to identify the location number, probe configuration, and sample number at that location. For example, L1P3S2 indicates Location 1, a probe spacing of 3 inches and Sample 2. Two identical OWL kits were used at most of the locations, and the data from Kit 1 was assigned odd sample numbers and Kit 2 was assigned even sample numbers.

3.2 General Site Description

The LLNL Livermore, CA test site was located to the west of the scientific compound about 250 feet from the outer security fence. The land is quite flat, and it is covered with dry grass about 1-2 feet high (see Figure 3.1). Occasional green thistles are present and a few small leafless bushes about 3-4 feet high were the tallest vegetation on the site. The soil was a light brown clay containing occasional small rocks.

3.3 Specific Measurement Locations

Twelve measurement locations were selected (see Figure 3.2). Locations 1, 2 and 3 represent the feedpoint, center and termination point where the longwire antenna was erected. Locations 4, 5, 6 and 7 are 25 ft away from the longwire, 75 ft from its center, and Locations 8, 9, 10 and 11 are 75 ft from the longwire at 25 ft from its center. Locations 4 through 11 are symmetrically located around Location 2 to document the area where the broadband dipole was erected. Location 12 was along the line of the longwire beyond Location 3 at the end of the lab fence. It was selected to be along a radial where the field strength data would be taken.

Figure 3.1 PHOTO OF LLNL FIELD SITE

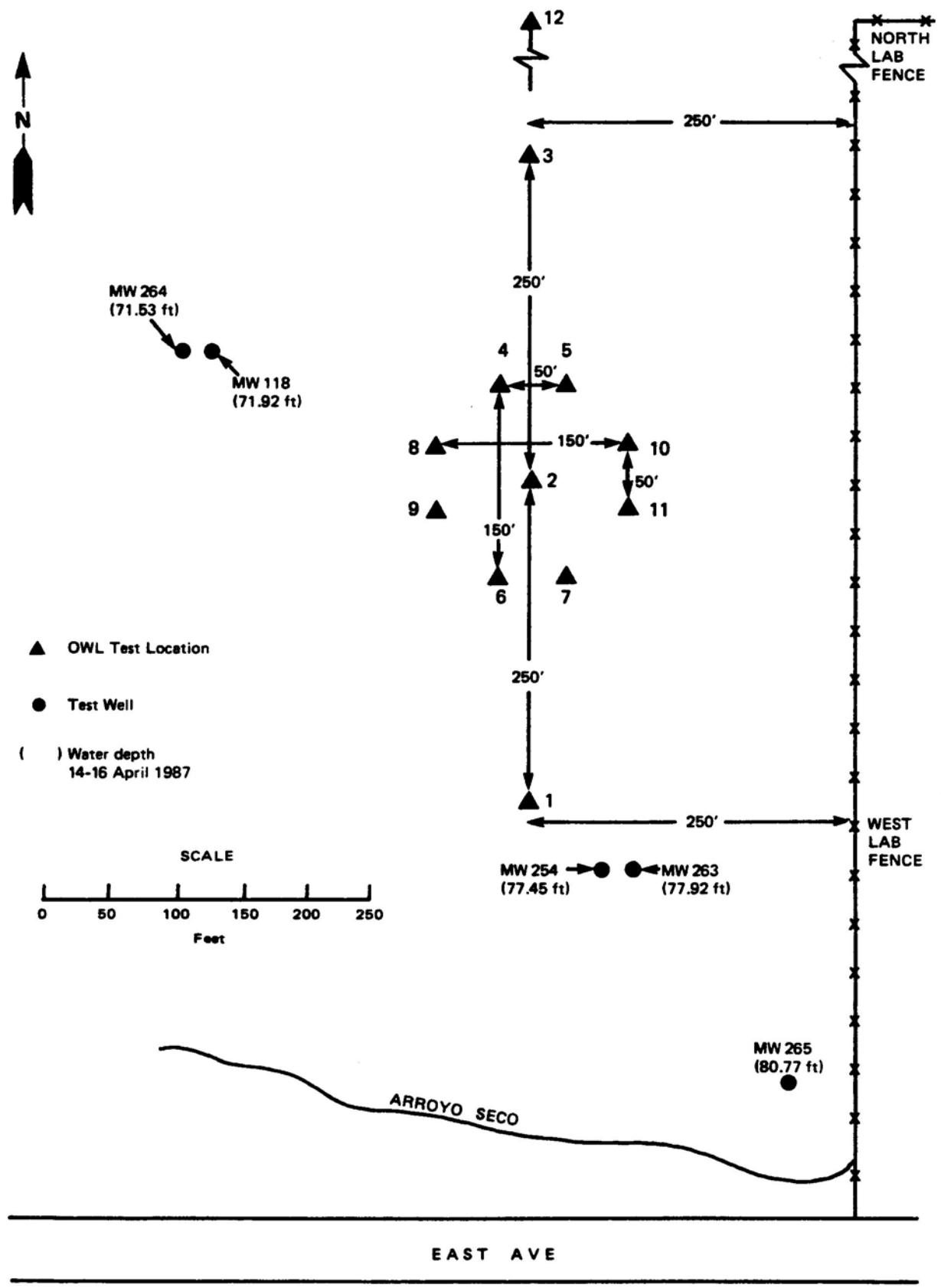

Figure 3.2 LOCATIONS OF OWL MEASUREMENTS AND TEST WELLS AT LIVERMORE SITE

All of the locations appeared very similar to the eye. The 0.5-inch steel rod used to create the hole for the aluminum OWL probe was very difficult to drive into the dry ground using a sledge hammer (see Figure 3.3). Frequently the pointed steel rod would only penetrate less than 1 inch per hit, although it was somewhat easier to drive at Locations 1 (beside a road near the well), 4 and 8.

There was a band about 10 yards wide with no vegetation at Location 5. The ground at this site was very hard, and 3 driving rods were broken trying to drive into it. At the other locations, it was necessary to clear the vegetation prior to making the holes for the probes (see Figure 3.4 taken at Location 12). The vegetation at Location 8 consisted of dried grasses 1-2 ft high, and several 3- to 4-ft bushes (the tallest at the site) were nearby. Several green thistles about 3 ft high were near Location 12, and they were the only green vegetation at the entire site (exclusive of trees along the security fence).

4. SOIL DESCRIPTION

The soil was highly compacted light brown clay with some occasional small (1-2 inch) smooth rocks. The surface moisture content, temperature and pH were measured at each location. These results are summarized in Table 4.1. Surface soil samples were taken at Locations 1, 2 and 3 for use in estimating soil moisture content by measuring the percent of change in weight before and after heating, but the ground was so hard that it was not practical with only a pick and shovel to take samples at different depths except at Location 1 (where additional samples were taken at 1 ft and 2 ft). Regretably, these soil samples were lost when the sample pans melted in the microwave oven. It was observed that the samples were successively more moist as the sample depth increased. The sealed pan for the sample taken at 2 ft had condensation on the inside several days later. Therefore, it is assumed that there was a gradient of moisture content which increased with depth.

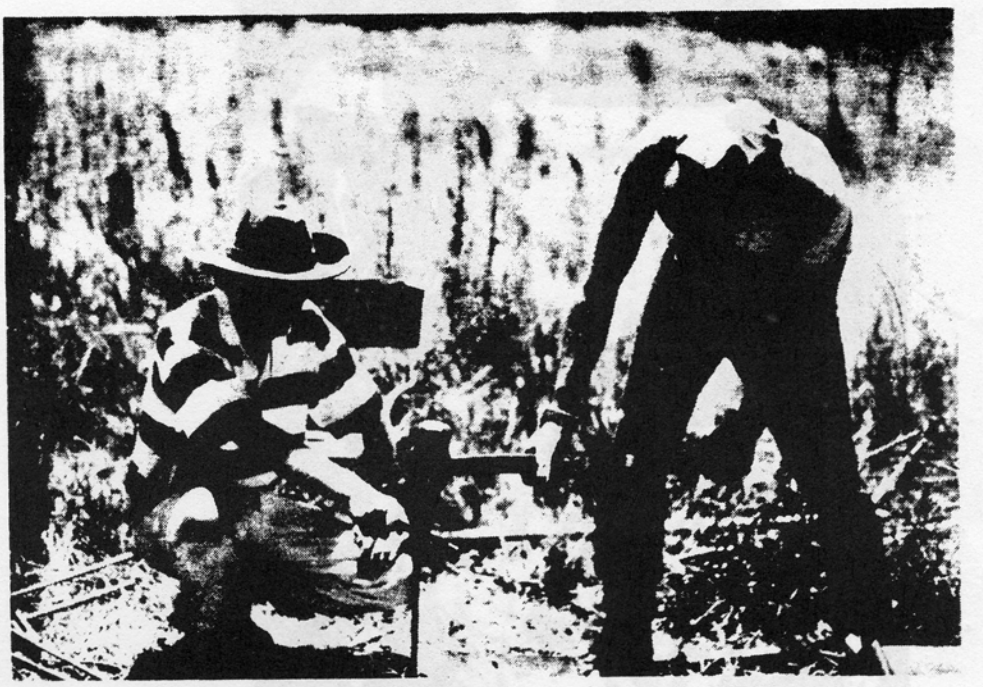

Figure 3.3 DRIVING STEEL AT LIVERMORE

Figure 3.4 CLEARING THE VEGETATION AT LOCATION 12
(With Supervision from Advisors)

TABLE 4.1

Summary of Soil Measurements at LLNL Site

Location Number	M.C.*	Temp. (°C)	pH	Comments
1	1	24.5	7.0	Soil less compacted
2	1	23.0	6.9	Soil very compacted
3	1	22.0	6.9	
4	1	28.5	7.0	Soil less compacted
5	1	27.0	7.0	Soil very compacted
6	1	28.0	7.0	
7	1	28.5	7.0	
8	1	28.0	7.0	Soil less compacted
9	1	28.0	7.0	
10	1	30.0	7.0	
11	1	27.5	7.0	
12	1	24.0	7.0	Soil very compacted

* M.C. = Moisture Content (on a scale from 1 = dry to 8 = wet)

The water table can cause a very significant change in effective ground constants if it occurs closer to the surface than a skin depth at the radio frequency of interest. Fortunately, the LLNL site has been recently surveyed using the test wells shown in Figure 3.2.[13] The water table was between 71 and 81 feet below the surface at the test site. The water depth, measured on 14-16 April 1987, is given in parentheses beside each test well shown on the map of ground constant measurement locations (Figure 3.2).

5. DATA REDUCTION AND ANALYSIS

5.1 Data Reduction

Data were taken at 12 locations. The number of samples per location ranged from one to four. Thirty-one samples were taken in all, but two were discarded due to excessive separation of the soil from the probes near

the surface or the inability to get the probes completely into the ground (see Table 5.1). OWL probe lengths up to 36 inches were used at 8 locations, and lengths up to 24 inches were used at 4 locations due to the difficulty in probe insertion and extraction. The data were recorded on thermal printer paper and on magnetic cassettes using the HP 85B. Figure 5.1 is an example of the raw data for the 3- and 6-inch probe lengths, and Figure 5.2 shows the reduced data for these samples.

TABLE 5.1

Summary of Data Samples

Location Number	Number of Samples	Longest Probe (Inches)
1	4	36
2	4	36
3	2	36
4	1	24
5	2	36
6	4	36
7	3	36
8	1	24
9	1	24
10	2	36
11	2	24
12	3	36

There was a considerable spread in the measured results for a given frequency, so a statistical data reduction was required.

5.2 Data Analysis

Three types of estimates of the ground constants versus frequency are required for subsequent use by LLNL in the NEC validation:

- Estimate for sloping longwire;
- Estimate for broadband dipole; and,
- Estimate for field strength.

SITE NAME	LIV
LOCATION NUMBER	5
SAMPLE NUMBER	1
DATE	07-05-87
TIME (HOURS)	16.30
OPERATOR'S ID	GHH
PROBE CONFIG NO.	3
PROBE KIT NUMBER	1

3 INCH PROBES IN GROUND

FREQ.	/Z/	θ	Er	SD
2.0	1856	-48.7	45	7.32
3.0	1431	-50.8	37	5.59
4.0	1197	-49.9	34	4.15
5.0	1073	-52.3	28	3.83
6.0	934	-51.7	28	3.11
7.0	871	-51.0	26	2.63
8	781	-52.4	24	2.45
10	759	-39.0	33	.97
12	731	-62.2	14	2.76
14	620	-60.0	15	2.09
16	525	-62.7	14	2.19
18	475	-60.2	14	1.72
20	440	-61.0	13	1.63
22	400	-59.6	14	1.39
24	375	-56.7	14	1.09
26	364	-53.3	15	.83
28	352	-51.9	16	.71
30	369	-49.4	16	.55

6 INCH PROBES IN GROUND

FREQ.	/Z/	θ	Er	SD
2.0	783	-48.1	55	7.26
3.0	585	-47.4	48	5.00
4.0	493	-42.2	48	3.19
5.0	467	-42.2	40	2.73
6.0	404	-40.6	41	2.15
7.0	410	-38.7	36	1.80
8	355	-36.6	39	1.43
10	471	-46.6	18	2.06
12	360	-51.4	18	2.09
14	308	-53.6	17	1.99
16	256	-57.0	16	2.04
18	232	-50.8	18	1.42
20	212	-51.3	17	1.34
22	200	-46.7	17	1.03
24	199	-43.5	18	.84
26	203	-42.6	16	.76
28	210	-41.8	15	.69
30	218	-46.8	12	.83

Figure 5.1 EXAMPLE OF RAW DATA

LIV

LOCATION # 5
SAMPLE # 1
PROBE CONFIGURATION 3 in.
PROBE LENGTH 3 in.

FREQ	Er	COND.	D.F.	S.D.
2	45	5.39E-003	1.08	7.32
3	37	6.36E-003	1.04	5.59
4	34	8.28E-003	1.11	4.15
5	28	8.11E-003	1.04	3.83
6	28	9.95E-003	1.08	3.11
7	26	1.15E-002	1.15	2.63
8	24	1.19E-002	1.10	2.45
10	33	4.17E-002	2.26	.97
12	14	7.64E-003	.84	2.76
14	15	1.06E-002	.92	2.09
16	14	9.53E-003	.79	2.19
18	14	1.24E-002	.89	1.72
20	13	1.27E-002	.87	1.63
22	14	1.53E-002	.92	1.39
24	14	2.05E-002	1.07	1.09
26	15	2.88E-002	1.29	.83
28	16	3.43E-002	1.41	.71
30	16	4.73E-002	1.80	.55

LIV

LOCATION # 5
SAMPLE # 1
PROBE CONFIGURATION 3 in.
PROBE LENGTH 6 in.

FREQ.	Er	COND.	D.F.	S.D.
2	55	5.90E-003	.97	7.26
3	48	8.11E-003	1.01	5.00
4	48	1.31E-002	1.23	3.18
5	40	1.40E-002	1.26	2.73
6	41	1.82E-002	1.34	2.15
7	36	2.10E-002	1.49	1.80
8	39	2.78E-002	1.61	1.43
10	18	1.25E-002	1.23	2.06
12	18	1.18E-002	.99	2.09
14	17	1.19E-002	.90	1.99
16	16	1.12E-002	.77	2.04
18	18	1.72E-002	.97	1.42
20	17	1.78E-002	.95	1.34
22	17	2.41E-002	1.13	1.03
24	18	3.05E-002	1.30	.84
26	16	3.29E-002	1.39	.76
28	15	3.54E-002	1.51	.69
30	12	2.50E-002	1.29	.83

Figure 5.2 EXAMPLE OF REDUCED DATA

The estimate for the sloping longwire was made by computing the median values for each frequency from Locations 1 through 7. The estimate for the broadband dipole was obtained by computing the comparable median values from Locations 2 and 4 through 11. The estimate for the field strength was obtained by computing the site median values using data from all 12 locations. For each of these types of estimates, the appropriate data (taken as a set) were used to perform the following steps:

- Compute the median values of conductivity and relative dielectric constant for each measurement frequency used;
- Compute median dissipation factor and skin depth using the median relative dielectric constant and conductivity; and,
- Tabulate and plot the results vs frequency.

6. DISCUSSION OF RESULTS

6.1 Results

The results for Locations 1-7, pertinent to the longwire, are given in Table 6.1. The upper and lower bounds (i.e., the maximum and minimum observed values) are given for the conductivity and relative dielectric constant. The median conductivity was approximately 4×10^{-2} S/m across the band; whereas, the median relative dielectric constant decreased from 182 at 2 MHz to 17 at 30 MHz. The upper and lower bounds were separated by about one order of magnitude for the conductivity and about half that separation was typical for the relative dielectric constant. The dissipation factor was about 1.5 and the skin depth varied from about 1.5 m at 2 MHz down to about 0.7 m at 30 MHz.

Comparable data were obtained for the area where the broadband dipole is to be erected (Locations 2, 4-11). These data are summarized in Table 6.2 for the conductivity and relative dielectric constant. The overall site median values (Locations 1-12) for these same parameters are tabulated in Table 6.3.

TABLE 6.1

Summary of Data for Longwire Antenna
(Locations 1 through 7)

Frequency (MHz)	Best Estimate		Lower Bound		Upper Bound	
	ε_r	σ (S/m)	ε_r	σ (S/m)	ε_r	σ (S/m)
2	182	4.72 X 10-2	82	1.16 X 10-2	455	1.56 X 10^{-1}
3	141	7.10 X 10-2	71	2.15 X 10-2	371	2.04 X 10-1
4	92	6.09 X 10-2	73	2.55 X 10-2	328	2.73 X 10^{-1}
5	71	3.93 X 10-2	52	2.10 X 10-2	301	3.36 X 10^{-1}
6	71	4.98 X 10-2	49	2.51 X 10-2	293	4.35 X 10^{-1}
7	62	5.45 X 10-2	38	2.62 X 10-2	217	3.06 X 10^{-1}
8	51	5.00 X 10-2	22	2.67 X 10-2	213	3.68 X 10^{-1}
10	46	5.18 X 10-2	28	2.01 X 10-2	78	1.12 X 10^{-1}
12	39	4.32 X 10-2	19	1.56 X 10-2	58	8.38 X 10-2
14	31	3.67 X 10-2	19	1.59 X 10-2	54	9.59 X 10-2
16	30	3.54 X 10-2	19	1.87 X 10-2	52	1.04 X 10^{-1}
18	24	3.09 X 10-2	17	1.91 X 10-2	46	8.83 X 10-2
20	23	3.11 X 10-2	16	2.08 X 10-2	44	9.32 X 10-2
22	22	3.80 X 10-2	14	1.03 X 10-2	28	5.55 X 10-2
24	20	3.91 X 10-2	12	1.53 X 10-2	31	6.80 X 10-2
26	20	4.48 X 10-2	10	1.32 X 10-2	27	6.43 X 10-2
28	18	4.45 X 10-2	10	1.22 X 10-2	26	6.98 X 10-2
30	17	4.33 X 10-2	9	1.26 X 10-2	24	7.23 X 10-2

TABLE 6.2

Summary of Data Broadband Dipole
(Locations 2, 4 through 11)

Frequency (MHz)	Best Estimate		Lower Bound		Upper Bound	
	ε_r	σ (S/m)	ε_r	σ (S/m)	ε_r	σ (S/m)
2	137	2.72 X 10-2	54	1.16 X 10-2	314	9.22×10^{-2}
3	112	3.52 X 10-2	49	1.00 X 10-2	230	1.10×10^{-1}
4	87	3.73 X 10-2	45	1.17 X 10-2	266	2.14×10^{-1}
5	71	3.93 X 10-2	42	1.78 X 10-2	189	1.63×10^{-1}
6	63	3.49 X 10-2	33	1.01 X 10-2	205	2.73×10^{-1}
7	57	4.46 X 10-2	28	1.27 X 10-2	163	2.36×10^{-1}
8	48	3.70 X 10-2	22	1.47 X 10-2	150	2.48×10^{-1}
10	45	4.66 X 10-2	22	1.18 X 10-2	78	1.12×10^{-1}
12	39	4.37 X 10-2	19	1.46 X 10-2	58	8.38 X 10-2
14	32	4.24 X 10-2	19	1.81 X 10-2	54	9.59 X 10-2
16	32	4.55 X 10-2	19	1.87 X 10-2	52	1.04×10^{-1}
18	23	2.99 X 10-2	17	1.91 X 10-2	46	8.83 X 10-2
20	22	3.11 X 10-2	16	2.08 X 10-2	44	9.32 X 10-2
22	20	3.41 X 10-2	10	1.01 X 10-2	28	5.55 X 10-2
24	22	4.80 X 10-2	11	1.40 X 10-2	31	7.09 X 10-2
26	20	5.05 X 10-2	10	1.28 X 10-2	27	6.53 X 10-2
28	18	4.26 X 10-2	9	1.22 X 10-2	26	6.98 X 10-2
30	17	3.80 X 10-2	9	1.26 X 10-2	24	6.67 X 10-2

TABLE 6.3

Summary of Data for Field Strength Tests
(Locations 1 through 12)

Frequency (MHz)	Best Estimate		Lower Bound		Upper Bound	
	ε_r	σ (S/m)	ε_r	σ (S/m)	ε_r	σ (S/m)
2	153	3.55 X 10-2	54	6.37 X 10^{-3}	455	1.56 X 10^{-1}
3	129	4.18 X 10-2	49	1.00 X 10-2	371	2.04 X 10^{-1}
4	109	4.74 X 10-2	45	1.17 X 10-2	328	2.73 X 10^{-1}
5	77	3.82 X 10-2	42	1.78 X 10-2	301	3.36 X 10^{-1}
6	60	3.41 X 10-2	33	1.01 X 10-2	293	4.35 X 10^{-1}
7	56	4.43 X 10-2	28	1.27 X 10-2	217	3.06 X 10^{-1}
8	48	3.91 X 10-2	22	1.47 X 10-2	213	3.68 X 10^{-1}
10	45	4.34 X 10-2	22	1.18 X 10-2	78	1.12 X 10^{-1}
12	39	4.35 X 10-2	19	1.46 X 10-2	58	8.38 X 10-2
14	32	4.10 X 10-2	19	1.59 X 10-2	54	9.59 X 10-2
16	29	3.34 X 10-2	19	1.87 X 10-2	52	1.04 X 10^{-1}
18	23	3.03 X 10-2	17	1.91 X 10-2	46	8.83 X 10-2
20	23	3.07 X 10-2	16	2.08 X 10-2	44	9.32 X 10-2
22	21	3.59 X 10-2	10	1.01 X 10-2	28	5.55 X 10-2
24	22	4.14 X 10-2	11	1.40 X 10-2	31	7.09 X 10-2
26	20	4.61 X 10-2	10	1.28 X 10-2	27	6.53 X 10-2
28	18	4.36 X 10-2	9	1.22 X 10-2	26	6.98 X 10-2
30	17	3.96 X 10-2	9	1.26 X 10-2	24	7.23 X 10-2

6.2 Horizontal Homogeneity

There are two scales of horizontal homogeneity to consider: variations among samples taken on a given frequency with the probes inserted within about 1 m of each other at a given location, and variations with location across the entire antenna field. The small-scale variations seemed rather large (see the bounds given in Appendix A of Ref. 12 for the data on a given frequency at each location), but the small-scale variation seemed to decrease with increasing measurement frequency. The median values for each location showed relatively little variation (for this type of data) across the entire antenna field (with a few minor exceptions), as discussed below.

The median data were quite similar for the three groupings. This is to be expected because the data sets were not mutually exclusive. The horizontal (lateral) homogeneity across the entire site can be considered by focussing on a few selected frequencies. Table 6.4 summarizes the conductivity and relative dielectric constants data for 7, 14 and 30 MHz.

TABLE 6.4

Summary of Median Data for 7, 14 and 30 MHz

Location No.	7 MHz		14 MHz		30 MHz	
	ϵ_r	σ(S/m)	ϵ_r	σ(S/m)	ϵ_r	σ(S/m)
1	55	4.35×10^{-2}	23	1.86×10^{-2}	16	4.12×10^{-2}
2	62	5.77×10^{-2}	32	4.31×10^{-2}	17	4.33×10^{-2}
3	63	5.56×10^{-2}	41	5.45×10^{-2}	21	5.56×10^{-2}
4	54	4.00×10^{-2}	31	3.61×10^{-2}	12	2.42×10^{-2}
5	67	5.45×10^{-2}	39	4.84×10^{-2}	22	5.48×10^{-2}
6	50	3.38×10^{-2}	29	2.77×10^{-2}	16	3.18×10^{-2}
7	66	5.91×10^{-2}	31	3.67×10^{-2}	21	5.54×10^{-2}
8	54	4.46×10^{-2}	31	3.96×10^{-2}	14	3.59×10^{-2}
9	41	2.10×10^{-2}	33	4.24×10^{-2}	11	2.07×10^{-2}
10	59	5.02×10^{-2}	37	4.91×10^{-2}	16	3.80×10^{-2}
11	57	4.40×10^{-2}	34	4.24×10^{-2}	21	5.57×10^{-2}
12	37	1.99×10^{-2}	22	1.80×10^{-2}	17	3.62×10^{-2}

These frequencies are approximately octavely related across the HF band. At 7 MHz, the location median values are very similar except at Locations 9 and 12. At each of these locations there was some difficulty with the soil breaking away from the top of the probe holes as the holes were being made. This added air may have caused the OWL kit readings to be biased to the low side. The data reduction equations assume that the soil is touching the rods for their full length. The suspicion that the air holes caused reduced readings was verified by using the same set of probe holes twice. The second readings, taken in the enlarged holes (with more air), gave lower values. The problem caused by the dry brittle soil was not unique to these two locations, but it was more pronounced there. Excluding these two locations, the conductivity values varied between 3.38×10^{-2} S/m and 5.91×10^{-2} S/m, and the relative dielectric constant values varied between 50 and 67. At 14 MHz, the data from Locations 1 and 12 were low relative to the other locations. Excluding these two locations, the conductivity values varied from 2.77×10^{-2} S/m to 5.45×10^{-2} S/m, and the relative dielectric constant values varied from 29 to 41. At 30 MHz, the data at Locations 4 and 9 were lower for both the conductivity and relative dielectric constant. At Location 9, the problem of air around the probes was probably responsible for the values being lower. At Location 4, the surface soil (pertinent to the 9-inch probes used to obtain the data at 30 MHz) was much less compacted, and this resulted in the lower values. As noted in Table 4.1, the soil was less compacted at Locations 1, 4 and 8. The Location 8 data for all three frequencies seems to be very similar to the data from the other locations even though the steel rods were somewhat easier to drive at this location.

The conclusion is that the site is relatively horizontally homogeneous from a statistical standpoint--with the possible exception of Locations 9 and 12.

6.3 Vertical Homogeneity

As mentioned in Section 3, there was a vertical gradient of moisture content with the soil getting more moist with increasing depth down to 2 or 3 ft. The water table was at 71 to 81 feet below the surface. Therefore,

it was not a factor since the skin depth was only about 3 to 6 feet. Next, the variation of the relative dielectric constant (most closely correlated with volumetric moisture content)[14] with depth at the same location is considered by comparing the results obtained for several probe lengths on the same frequency at Location 2.

The relative dielectric constant data for Location 2 are given in Table 6.5 for the seven probe lengths for the following frequencies: 2, 4, 7, 14 and 30 MHz. These data show that there is a variation of relative

TABLE 6.5

Examples of Variation of Relative Dielectric Constant with Depth for Selected Samples and Frequencies at Location 2

Loc. No.	Sample No.	Freq. (MHz)	Probe Length (inches)						
			3	6	5	12	18	24	36
2	1	2	32	59	59	84	138	95	141
2	1	4	24	45	45	74	99	85	i.d.*
2	1	7	23	63	47	65	53	55	i.d.
2	1	14	12	15	17	22	30	39	i.d.
2	1	30	16?	17	12	17	i.d.	i.d.	i.d.
2	2	2	20	37	45	128	212	266	197
2	2	4	16	28	35	73	114	176	169
2	2	7	14	25	24	40	71	94	1.d.
2	2	14	11	13	16	27	54	i.d.	i.d.
2	2	30	10	9	11	20	i.d.	i.d.	i.d.
2	3	2	22	97	72	100	63	76	89
2	3	4	17	64	74	126?	68	81	i.d.
2	3	7	16	80	76	101	36	38	i.d.
2	3	14	10	18	18	22	18	19	i.d.
2	3	30	16?	16	12	15	18	i.d.	i.d.
2	4	2	25	29	65	51	104	92	250
2	4	4	18	22	41	41	54	79	i.d.
2	4	7	15	20	32	35	34	62	i.d.
2	4	14	11	12	16	17	26	45	i.d.
2	4	30	13?	10	10	11	i.d.	i.d.	i.d.

* i.d. = invalid data; ? = questionable data.

dielectric constant with probe depth for a given frequency that generally increases with increasing probe depth up to 18 or 24 inches, except at 30 MHz where little real variation is apparent. All four samples were obtained within 2 meters of each other; Samples 1 and 3 (Kit 1) and Samples 2 and 4 (Kit 2) were within 1 meter of each other for a given kit. The conclusion is that the moisture content and the resulting ground constants varied considerably over relatively short distances, and that it would be necessary to sample several times at a given location and use some measure of central tendency (e.g., the median) to describe the soil as it would be seen by a passing radio wave with a wavelength in the medium which is larger than the scale of variation being observed.

6.4 Comparison of Livermore Data with Generic Curves and Data from Other Sites

In 1980, the author developed some "generic curves" for the ground constants vs frequency, and they were first published in 1982.[15] These curves provide estimates of the ground constants for different terrain categories of the types described in handbooks.[16,17] These curves for the HF band for conductivity, relative dielectric constant, dissipation factor and skin depth, are reproduced here (from Ref. 5) as Figures 6.1 through 6.4, respectively. Also shown on these curves are data taken at other sites as presented and discussed in Ref. 18. The Livermore median values for all 12 locations are shown on Figures 6.1 through 6.4 to facilitate the comparison. The closest fit for the Livermore data to the generic curves is with rich agricultural land. The Livermore data are almost identical to the results obtained earlier by SRI on a farm near Delta, UT, where again rich agricultural land seemed an apt description.[4,5]

A useful parameter for NEC modeling is the wavelength in the soil at the radio frequency of interest. This parameter is needed in order to determine the number of segments needed for NEC-3 for the wire which has penetrated the air-ground interface. A set of generic curves for this parameter were developed recently by Hagn.[19] using the equations in Table 6 of Ref. 18 or Table 1 of Ref. 19. The curves of wavelength in the soil

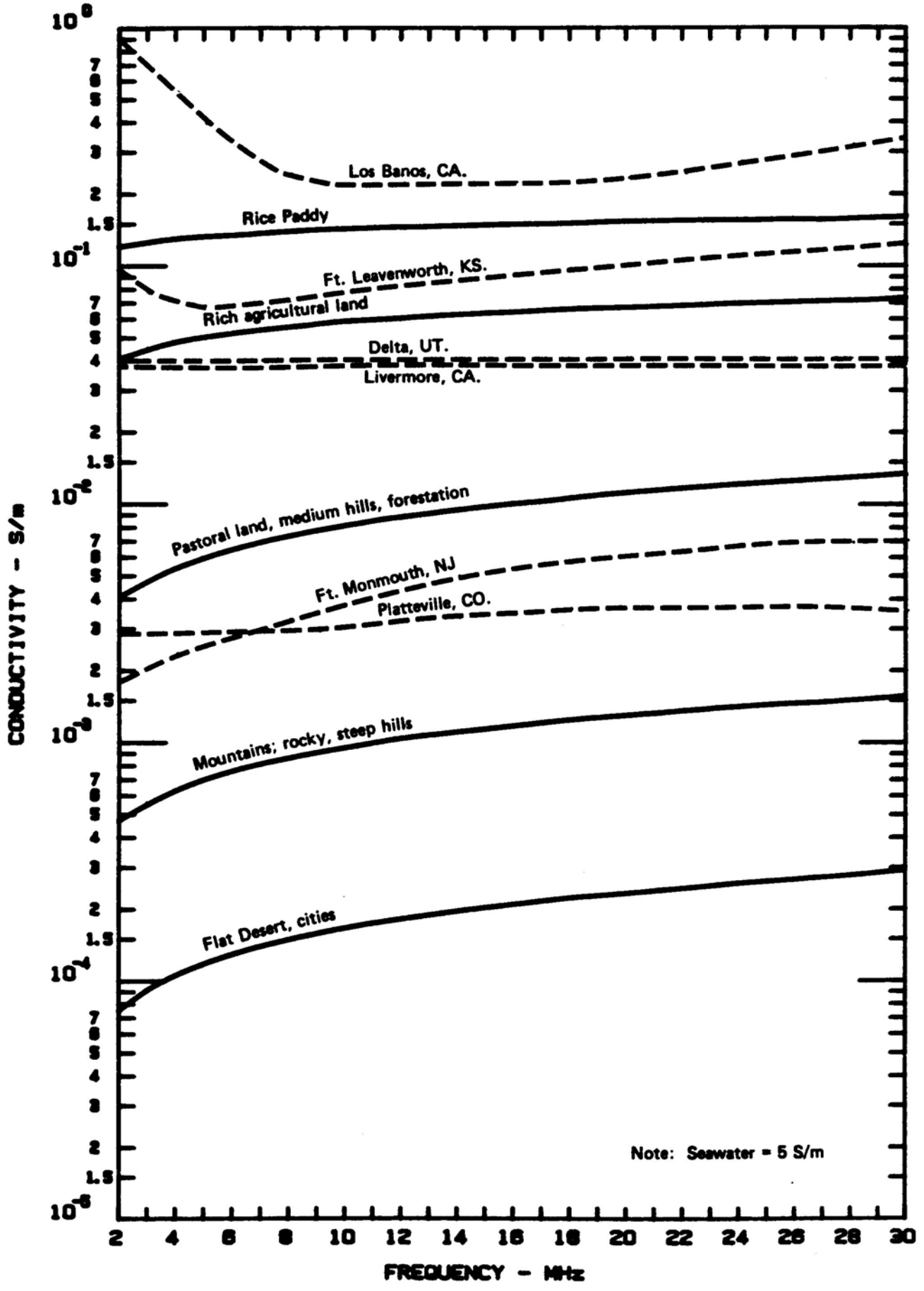

Figure 6.1 EFFECTIVE GROUND CONDUCTIVITY FOR SIX ANTENNA TEST FIELD SITES VS SRI GENERIC CURVES FOR SELECTED TERRAIN CATAGORIES

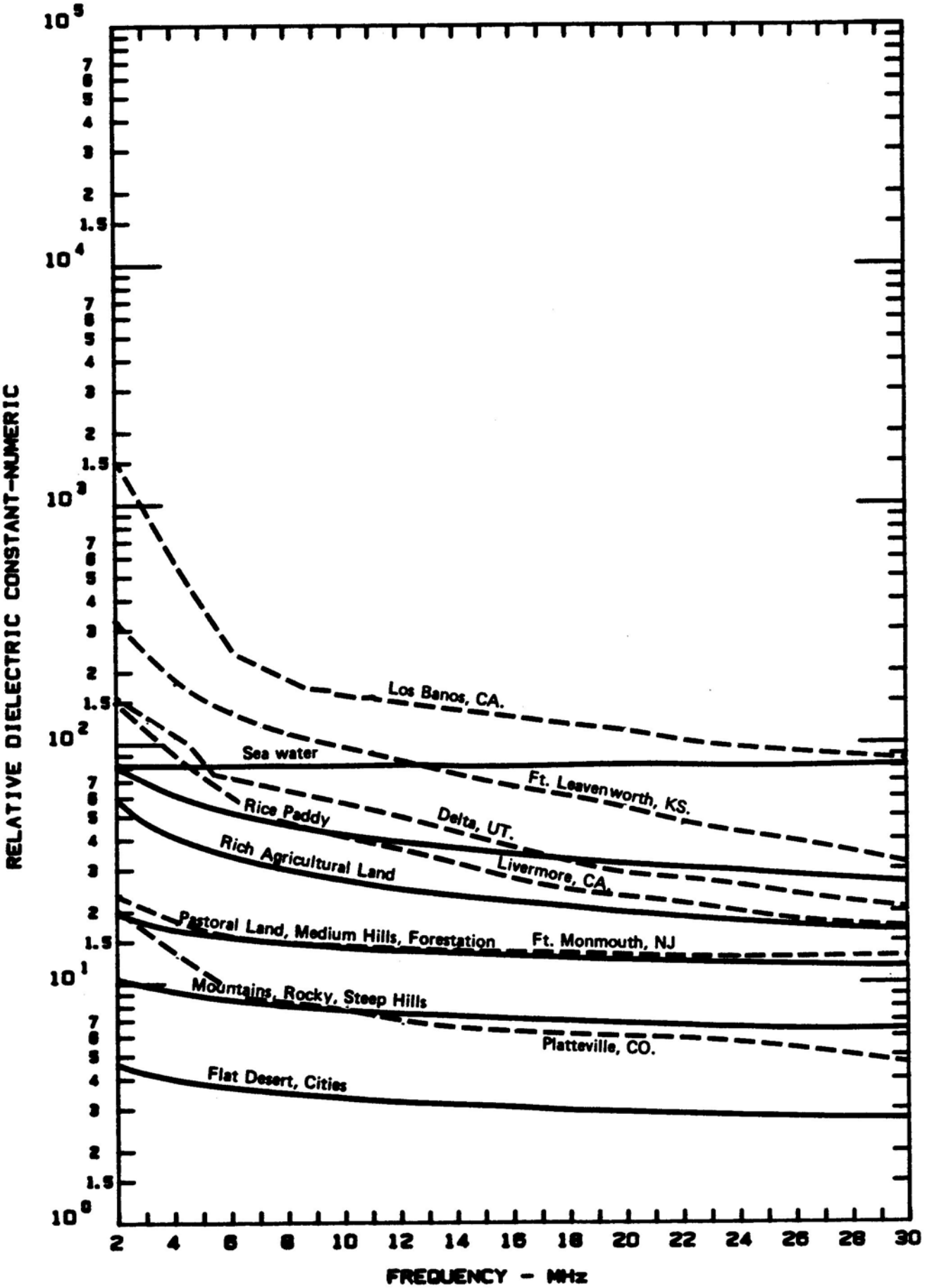

Figure 6.2 EFFECTIVE RELATIVE DIELECTRIC CONSTANT FOR SIX ANTENNA TEST FIELD SITES VS SRI GENERIC CURVES FOR SELECTED TERRAIN CATAGORIES

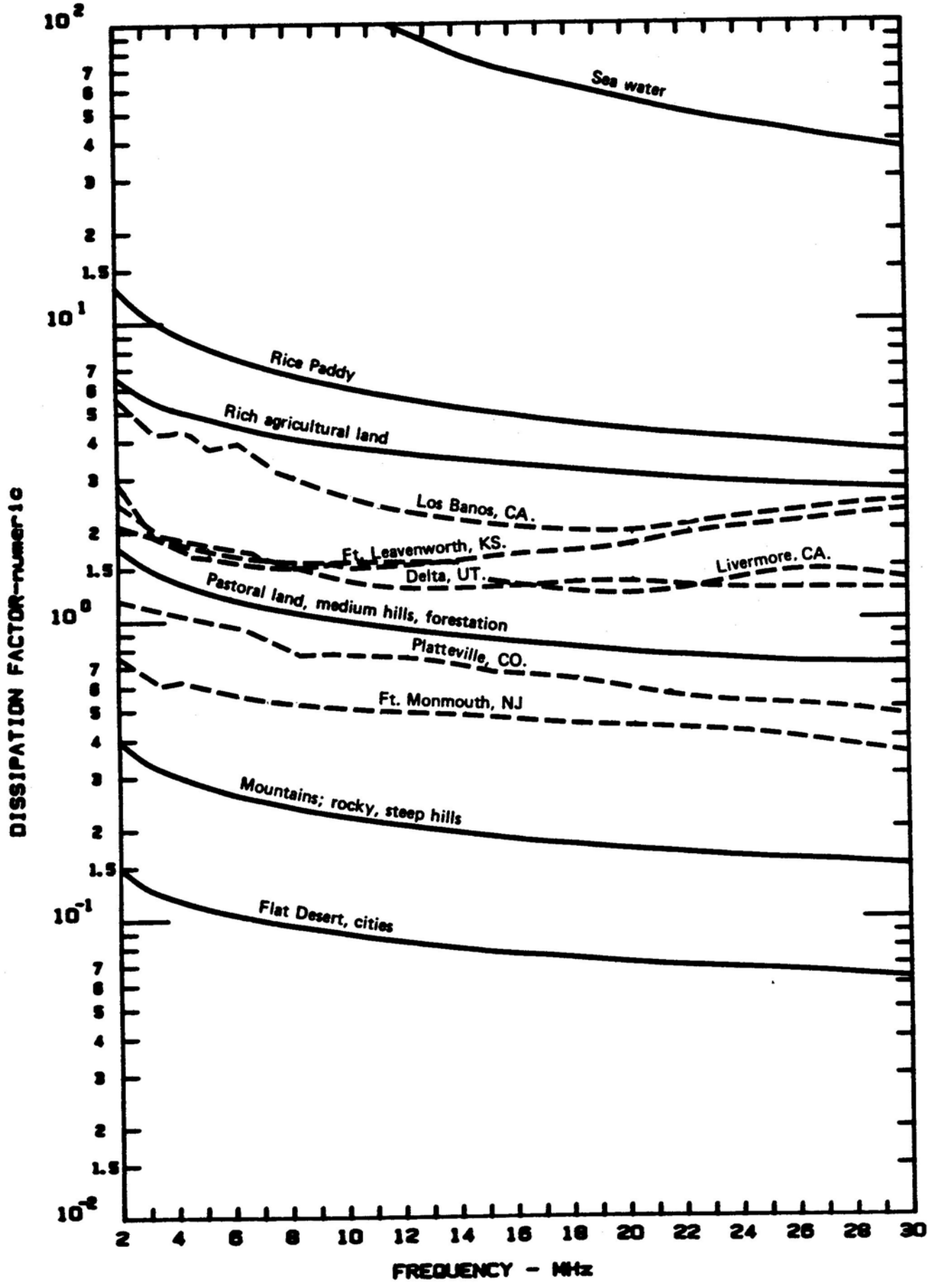

Figure 6.3 EFFECTIVE GROUND DISSIPATION FACTOR FOR SIX ANTENNA TEST FIELD SITES VS SRI GENERIC CURVES FOR SELECTED TERRAIN CATAGORIES

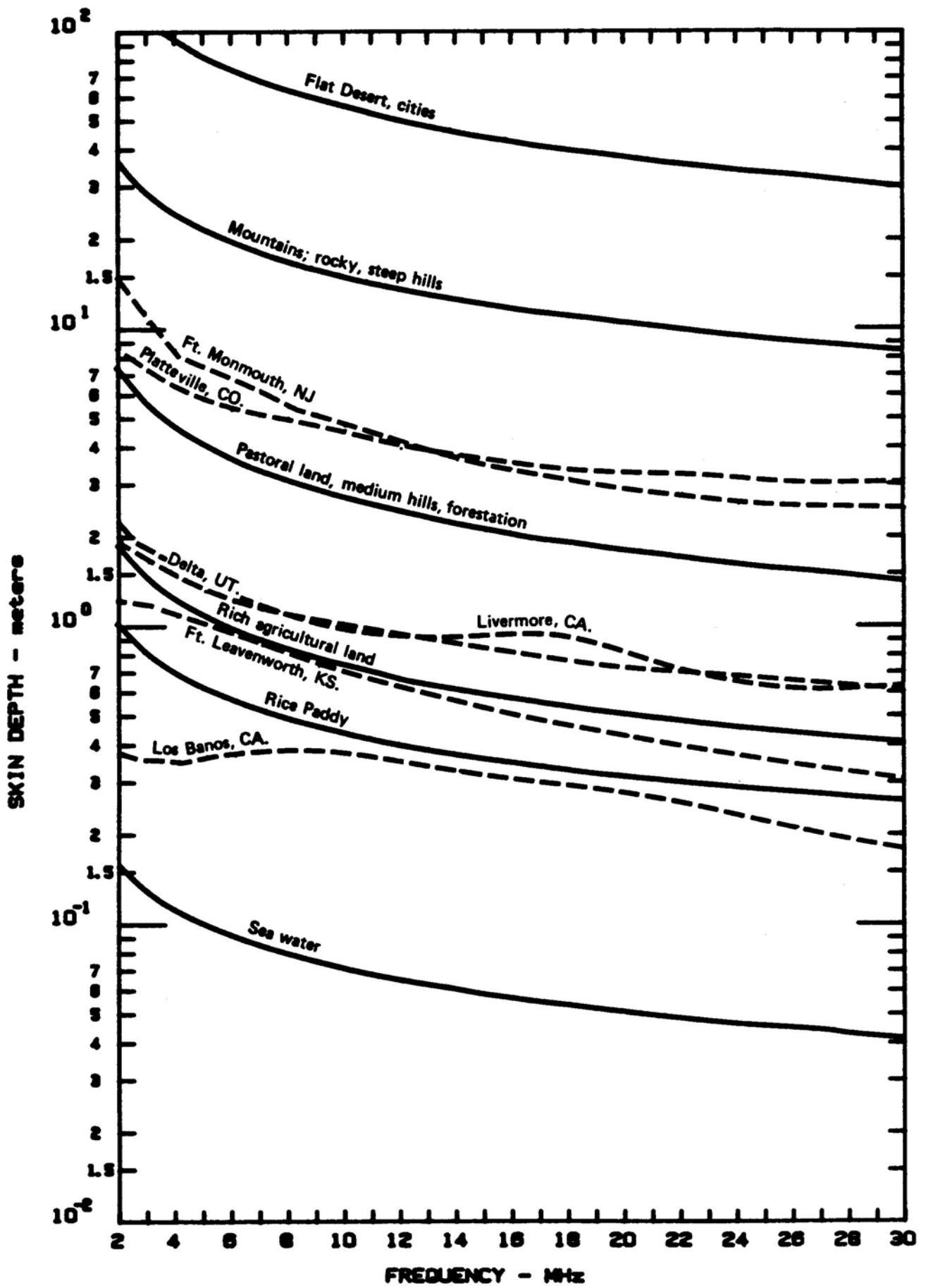

Figure 6.4 EFFECTIVE SKIN DEPTH FOR SIX ANTENNA TEST FIELD SITES VS SRI GENERIC CURVES FOR SELECTED TERRAIN CATAGORIES

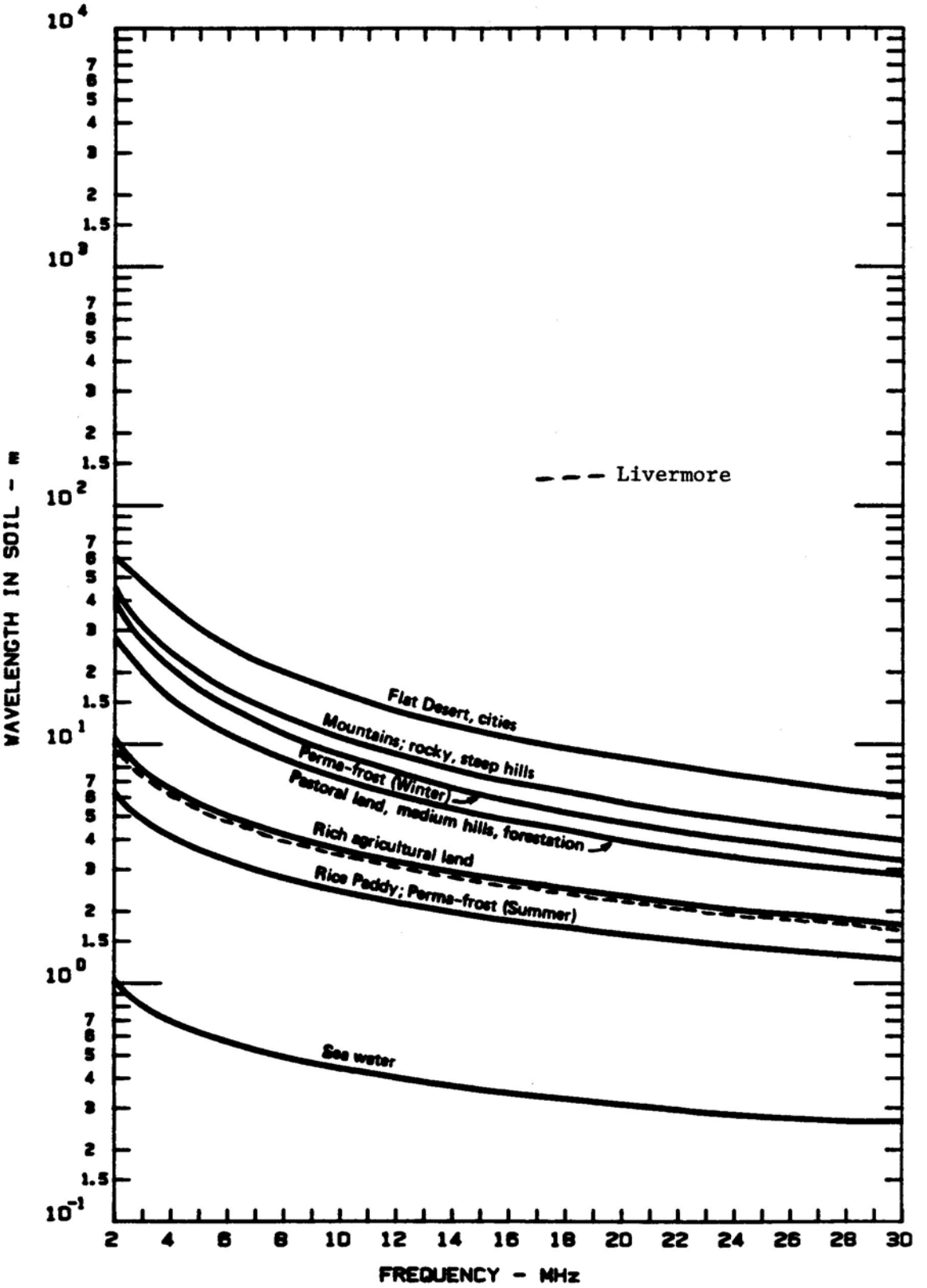

Figure 6.5 LIVERMORE DATA AND SRI GENERIC CURVES OF WAVELENGTH IN SOIL VS FREQUENCY FOR SELECTED TERRAIN CATEGORIES

(or sea water) vs frequency are plotted in Figure 6.5. The data from the Livermore site are plotted for comparison.

6.5 Accuracy Considerations

Accuracy checks with the HP 4193A on a 52.0-ohm dummy load, as measured at DC with a Micronta Model 2-211 two-jewel meter, provided values less than 0.6 ohm different across the HF band on the measurement frequencies. The phase angle difference was never more than 1.9 degrees, and it was 1 degree or less for frequencies below 16 MHz. The frequency accuracy is $\pm$ 0.01 percent. The HP 4193A features built-in test equipment (BITE), and the front-panel display flashes "PASS" or a "NOT READY" light comes on. This ensures that the instrument is operating properly prior to data acquisition.

The resulting accuracy of measurement of the ground constants is better than 25 percent.

7. CONCLUSIONS AND RECOMMENDATIONS

7.1 Conclusions

The following conclusions were reached:

- The ground constants data were particularly difficult to obtain at Livermore due to the hardness (and brittle nature) of the soil at this site.
- There was a significant variation of the data for a given frequency at a given location and between locations, and this necessitated a statistical analysis to obtain best estimates of the ground constants at the Livermore site suitable for use in NEC validation.
- These small-scale variations could have been caused by localized variations in moisture content or by differing amounts of air around the probes (biasing the reading to be too low), or by both effects.
- The data from selected locations required grouping

together to obtain the sample set for the two antennas (longwire and broadband dipole) and for the field strength test.

- The location median values of the conductivity and relative dielectric constant were reasonably consistent across the antenna field.

- The spreads between the bounds about the median formed by the maximum and minimum observed values were about an order of magnitude for the conductivity and about half that for the relative dielectric constant. These are typical of the spreads observed at other locations where there was less of a problem with air around the probes.

- The effective skin depth is less than about 2 meters in the HF band at Livermore, and it decreases to about 0.7 m at 30 MHz. Therefore, the water table (which is over 20 m down) has no significant effect on HF antennas or propagation at this site.

- The ground at the Livermore site behaves as a lossy conductor in the HF band with an effective dissipation factor that is relatively constant with frequency at about 1.5.

- The conductivity also is relatively constant in the HF band at about 4×10^{-2} S/m; whereas, the relative dielectric constant decreases with increasing frequency from about 150 at 2 MHz to about 17 at 30 MHz.

- The SRI OWL kit, adapted from the approach of Kirkscether,[20] is an effective tool for estimating effective ground constant values for the HF band when appropriate sampling techniques are used and when appropriate statistical processing of the valid data is performed.

7.2 Recommendations

The following recommendations are offered:

- The median values of conductivity and relative dielectric constant given in Tables 6.1 through 6.3 should be used to estimate (by interpolation) the values for the NEC validation computations for the longwire and broadband dipole input impedance and the field strength vs distance.

- A parameter sensitivity analysis should be performed using the bounds given in Tables 6.1 through 6.3 of Ref. 11 as input values for NEC. Priority should be given to the upper bounds due to the problem with air around the top of the probes at some locations which probably biased those values low.

- The vertical electric field strength data vs distance from the longwire should be fit using an SRI program or the NEC while varying the ground constants. Any ground constant estimates obtained through such curve fitting should be compared with the data from the OWL kit.

- The moisture content vs depth should be measured and correlated with the relative dielectric constant data vs probe length of the type given in Table 6.5. The soil samples for this comparison should be taken from the same volume sampled by the OWL kit (a cylinder approximately twice the probe spacing and as deep as the probes) to check the small-scale variations in relative dielectric constant and to determine if they are caused by highly localized moisture content variations or by different amounts of air around the probes near the top of the holes. It may be necessary to carefully drill the holes for the probes and to use a core drill for the soil samples.

ACKNOWLEDGMENTS

The author is pleased to acknowledge the assistance of the following individuals during data acquisition: Al Christman, Jim Breakall, Dick Adler and Warren Averill. It took the combined efforts of this group, working with the author, to extract the data (and OWL probes) from the very hard ground at the LLNL site. The author also appreciated the loan of electronic and other equipment by LLNL so that two OWL kits could be run in parallel to acquire twice the amount of data originally envisioned. Cheryl Hagn assisted with data reduction and computed the sample medians. The author is grateful to all of these individuals for their help. The author and LLNL also appreciate the encouragement and support of Ward Nair, Janet McDonald and Lee Corrington of USAISEIC, Ft. Huachuca, AZ, who provided the funds for the NEC validation. Any errors of commission or omission are those of the author alone.

DISCLAIMER

The findings in this report are not to be construed as an official Department of Energy or Department of Defense position unless so designated by other authorized documents. Citation of trade names in this report does not constitute an official endorsement or approval of the use of such commercial items by SRI International or by the Lawrence Livermore National Laboratory, or by the USAISEIC.

REFERENCES

1. G.J. Burke and A.J. Poggio, "Numerical Electromagnetics Code (NEC) -- Method of Moments," NOSC Technical Document 116, Volume 1, Contract MIPR-N0095376MP, Lawrence Livermore Laboratory, Livermore, CA, January 1981.

2. J.K. Breakall, G.J. Burke and E.K. Miller, "The Numerical Electromagnetics Code (NEC)," Proceedings of the 6th Symposium and Technical Exhibition on Electromagnetic Compatibility, pp. 301-308, Zurich, March 1985.

3. G.J. Burke, "Numerical Electromagnetics Code - User's Guide Supplement for NEC-3 for Modelling Buried Wires," Lawrence Livermore Laboratory, Livermore, CA, October 1983.

4. L.O. Harnish, G.H. Hagn and J.H. Faulconer, "Advanced Development Model Tactical HF Antenna Kits and Related Field Tests," Quarterly Technical Status Report: 2 December 1984 - 21 March 1985, Contract DAAB07-84-C-K545, SRI Project 7439, SRI International, Arlington, VA, 21 March 1985.

5. L.O. Harnish, G.H. Hagn and J.H. Faulconer, "Advanced Development Model Tactical HF Antenna Kits and Related Field Tests," Quarterly Technical Status Report: 22 March - 21 June 1985, Contract DAAB07-84-C-K545, SRI Project 7439, SRI International, Arlington, VA, 21 March 1985.

6. L.O. Harnish, G.H. Hagn and M. Lee, "Full-Scale Measurements of the Boresight Elevation-Plane Directivity Pattern and Gain of an HF Beverage Antenna Array," Final Report, Contract P.O. NB2149, SRI Project 2624, SRI International, Arlington, VA, 15 December 1986.

7. L.O. Harnish, M. Lee and G.H. Hagn, "Comparison of Measured and NEC-Calculated Characteristics of a Vertical Monopole with Buried Ground Radials," Proceedings of the 3rd Annual Review of Progress in Applied Computational Electromagnetics, Monterey, CA, March 1987.

8. N.E. Goldstein, H.W. Parker and G.H. Hagn, "Three Techniques for Measurement for Ground Constants in the Presence of Vegetation," Special Technical Report 30, Contract DA-36-039 AMC-00040(E), SRI Project 4240, Stanford Research Institute, Menlo Park, CA, March 1967. AD 672 496.

9. G.H. Hagn and J.C. Gaddie, "Medium and High Frequency (MF and HF) Ground Electrical Parameters Measured during 1982 at Seven Locations in the United States with the SRI OWL Probe Kit," Presented to URSI Com. A., National Radio Science Meeting, Boulder, CO, Abstract, p. 78, 11-14 January 1984.

10. G.H. Hagn and L.O. Harnish, "Measurement Techniques for HF Tactical Antennas," Proceedings of the DARPA-AFCEA-IEEE conference on Tactical Communications: The Next Generation, Fort Wayne, Indiana, 22-24 April 1986.

11. J.K. Breakall and A.M. Christman, "Experimental Antenna Measurements for the Validation of the Numerical Electromagnetics Code (NEC), Proceedings of the 4th Annual Review of Progress in Applied Computational Electromagnetics, Monterey, CA, March 1988.

12. G.H. Hagn, "HF Ground Constant Measurements at the Lawrence Livermore National Laboratory (LLNL) Field Site," Letter Report, Purchase Order No. 214 7603, SRI Project 3942, SRI International, Arlington, VA, August 1987.

13. C.P. Webster-Scholten, M.D. Dresen, W.A. McConachie, R.O. Devany, D.S. Thompson and D.N. Homan, "LLNL Ground Water Project," Report No. UCAR-10160-87-5, Environmental Protection Investigations and Corrections Series, Lawrence Livermore National Laboratory, Livermore, CA, 15 March - 15 April, 1987.

14. R.W.P. King, S. Smith, M. Owens and T.T. Wu, Antennas in Matter, The MIT Press, Cambridge, MA, 1981.

15. G.H. Hagn, B.M. Sifford and R.A. Shepherd, "The SRICOM Probabilistic Model of Communication System Performance -- A Users Manual for Engineers, Applications Programmers, and System Programmers," Final Report, Contract NT-81-RC-16011, SRI Project 3603, SRI International, Arlington, VA, May 1982.

16. F.E. Terman, Radio Engineer's Handbook, McGraw Hill Book Company, Inc., New York, p. 709, 1943.

17. ITT, Reference Data for Radio Engineers, Howard W. Sams and Company, Inc., 7th Edition, New York, 1985.

18. G.H. Hagn, "Ground Constants at High Frequencies (HF)," Proceedings of the 3rd Annual Review of Progress in Applied Computational Electromagnetics, Monterey, CA, March 1987.

19. G.H. Hagn, "HF Ground Constant Measurements at the Lawrence Livermore National Laboratory (LLNL) Field Site," Proceedings of the Fourth Annual Review of Progress in Applied Computational Electromagnetics, Monterey, CA, 22-24 March 1988.

20. E.J. Kirkscether, "Ground Constant Measurements Using a Section of Balanced Two-Wire Transmission Line," IEEE Trans. Ant. and Prop., Vol. AP-8, No. 3, pp. 307-312, May 1960.

NUMERICAL INTEGRATION OF MARCUSE'S POWER LOSS FORMULA

JAMES P COUGHLIN, PhD
MATHEMATICS DEPARTMENT
TOWSON STATE UNIVERSITY
TOWSON, MARYLAND

ALBERT D. KRALL
ADVANCED TECHNOLOGY AND RESEARCH CORP.
LAUREL, MARYLAND

ROBERT H. BARAN
U.S. NAVAL SURFACE WEAPONS CENTER
SILVER SPRING, MARYLAND

MEMBERS, I.E.E.E.

Introduction: D. Marcuse [1] has derived a power loss formula to calculate the power losses from an electromagnetic wave traveling down a tapered dielectric rod. He first considers the losses at a step and then approximates the tapered rod by a series of steps. He assumes that, when the radius of the rod is a, the constants describing the bound mode will be the same as for an infinite rod. When the radius changes, so do the coefficients. Further, there is an additional change due to power taken from the bound mode and converted into the radiation modes. For a full discussion of the model, the interested reader is referred to [1]. Here, we are concerned only with the numerical integration of his formula.

In order to understand his formula, it is necessary to include lengthy abstracts from Marcuse's original paper. To begin with, the bound mode fields inside the rod are:

$$E_z = A\, J_\nu(\kappa r)\, \cos(\nu\phi)$$

$$H_z = B\, J_\nu(\kappa r)\, \sin(\nu\phi)$$

$$E_r = -i/\kappa^2 \{ \kappa\beta_0 A\, J'_\nu(\kappa r) + \omega\mu B\, \nu/r\, J_\nu(\kappa r) \}\, \cos(\nu\phi) \qquad (1)$$

$$E_\phi = 1/\kappa^2\{\ \beta_0\ A\ \nu\ /r\ \ J_\nu(\kappa r) + \kappa\ \omega\ \mu\ B\ J'_\nu\ (\kappa r)\ \}\ \ \sin(\nu\phi)$$

$$H_r = -i/\kappa^2\{\ n^2\omega\ \epsilon_0\ A\ \nu/r\ J_\nu(\kappa r) + \kappa\ \beta_0\ B\ J'_\nu\ (\kappa r)\ \}\ \sin(\nu\phi)$$

$$H_\phi = -i/\kappa^2\ \{n^2\kappa\omega\epsilon_0 A\ J'_\nu\ (\kappa r) + \beta_0 B\ \nu/r\ \ J_\nu(\kappa r)\ \ \}\ \cos(\nu\phi)$$

While the fields outside the rod may be written:

$$E_z = C\ H_\nu^{\ 1}(i\gamma r)\ \cos(\nu\phi)$$

$$H_z = D\ H_\nu^{\ 1}(i\gamma r)\ \sin(\nu\phi)$$

$$E_r = 1/\gamma^2\{\ i\gamma\beta_0 C H_\nu^{\ 1'}(i\gamma r)\ \ + \omega\mu\nu/r\ D H_\nu^{\ 1}(i\gamma r)\ \}\ \cos(\nu\phi) \qquad (2)$$

$$E_\phi = -1/\gamma^2\ [\ \beta_0\nu/r\ \ C H_\nu^{\ 1}(i\gamma r) + i\omega\gamma\mu D H_\nu^{\ 1'}(i\gamma r)]\ \sin(\nu\phi)$$

$$H_r = 1/\gamma^2[\ \omega\epsilon_0\nu/r\ \ C H_\nu^{\ 1}(i\gamma r) + i\gamma\beta_0 D H_\nu^{\ 1'}(i\gamma r)\ ]\ \sin(\nu\phi)$$

$$H_\phi = \ 1/\gamma^2\ [\ i\gamma\omega\epsilon_0 C H_\nu^{\ 1'}(i\gamma r) + \beta_0\nu/r\ D H_\nu^{\ 1}(i\gamma r)]\ \cos(\nu\phi)$$

It is necessary that these fields satisfy the usual continuity conditions where they meet, namely that the tangential components of H and E are continuous and the normal component of D. This gives rise to the "eigenvalue" equation (We specialize to the lowest order mode, ν=1)

$$\left\{\ n^2 a\gamma^2/\kappa\ [\ J_0(\kappa a)/J_1(\kappa a)\ -1/\kappa a\ ]\ \ + \gamma a\ i\ H_0^{\ 1}(i\gamma a)/H_1^{\ 1}(i\gamma a)\ \ - 1\right\} *$$

$$\left\{a\gamma^2/\kappa[\ J_0(\kappa a)/J_1(\kappa a)\ -1/\kappa a\ ]\ \ + \gamma a i\ H_0^{\ 1}(i\gamma a)\ \ /H_1^{\ 1}(i\gamma a)\ \ - 1\right\}$$

$$= \ [\ \ (n^2-1)\beta_0 k/\kappa^2\ \ ]^{\ 2} \qquad (3)$$

where $k^2 = 4\pi^2 f^2 \mu_0 \epsilon_0$

β_0= *the solution of the eigenvalue problem*

$\kappa^2 = n^2k^2 - \beta_0^{\ 2}$ $\qquad$ $\mu = \mu_r * \mu_0$

n^2 = *the dielectric constant*

$\gamma^2 = \beta_0{}^2 - k^2$ $\qquad$ μ_r = relative magnetic permeability

$H = iH_0{}^1(i\gamma a) / H_1{}^1(i\gamma a)$

When this equation is satisfied we can compute the values of A and B and therefore the fields inside the rod from:

$$B/A = -\sqrt{\epsilon_0/\mu_0}\ ka\ (\kappa a)^2 \left[n^2/\kappa a \{J_0(\kappa a)/J_1(\kappa a) - 1/\kappa a\} + 1/\gamma a \{ H - 1/\gamma a \} \right] / [\beta_0 a(1+\kappa^2/\gamma^2)] \qquad (4)$$

and

$$p=\pi/4 * \left[k\beta_0/\kappa^4 * \left\{ (\kappa a)^2 [J_0{}^2(\kappa a) + J_1{}^2(\kappa a)] - 2J_1{}^2(\kappa a) \right\} * \{n^2+\mu_0/\epsilon_0\ B^2/A^2\} + k\beta_0/\gamma^4 * \{ (\gamma a)^2 * \{1-H^2\} + 2 \} * J_1{}^2(\kappa a) * \{ 1 + \mu_0/\epsilon_0\ B^2/A^2\} + 2\sqrt{\mu_0/\epsilon_0}\ B/A \{ (\beta_0{}^2+n^2k^2)/\kappa^4 - (\beta_0{}^2+k^2)/\gamma^4 \}\ J_1{}^2(\kappa a) \right] \qquad (5)$$

$$* A^2 \sqrt{\epsilon_0/\mu_0}$$

The equations thus far describe the "so called" bound mode. In addition to this, radiation modes will be created by the taper and, if we write:

$\sigma^2 = n^2k^2 - \beta^2$

$\rho^2 = k^2 - \beta^2$

Then:

$E_z = F\ J_\nu(\sigma r) \cos \nu\phi$

$H_z = G\ J_\nu(\sigma r) \sin \nu\phi$

$E_r = -i/\sigma^2 \{ \sigma\beta\ F\ J_\nu'(\sigma r) + \omega\mu\nu/r\ G\ J_\nu(\sigma r) \} \cos \nu\phi$

$$E_\phi = 1/\sigma^2 \{\beta\nu/r\ F\ J_\nu(\sigma r) + \sigma\mu\omega\ G\ J'_\nu(\sigma r)\} \sin\nu\phi \qquad (6)$$
$$H_r = -i/\sigma^2 \{ n^2\omega\epsilon_0\nu/r\ F\ J_\nu(\sigma r) + \sigma\beta\ G\ J'_\nu(\sigma r)\} \sin\nu\phi$$
$$H_\phi = -i/\sigma^2 \{ n^2\sigma\omega\epsilon_0\ F\ J'_\nu(\sigma r) + \beta\nu/r\ G\ J_\nu(\sigma r)\} \cos\nu\phi$$

give the radiation modes inside the rod while:

$$E_z = [H\ J_\nu(\rho r) + I\ Y_\nu(\rho r)] \cos\nu\phi$$
$$H_z = [K\ J_\nu(\rho r) + M\ Y_\nu(\rho r)] \sin\nu\phi \qquad (7)$$
$$E_r = -i/\rho^2 \left\{ \rho\beta[H\ J'_\nu(\rho r) + I\ Y'_\nu(\rho r)] + \omega\mu\nu/r\ [K\ J_\nu(\rho r) + M\ Y_\nu(\rho r)] \right\} \cos\nu\phi$$
$$E_\phi = 1/\rho^2 \left\{ \beta\nu/r\ [H\ J_\nu(\rho r) + I\ Y_\nu(\rho r)] + \rho\omega\mu\ [K\ J'_\nu(\rho r) + M\ Y'_\nu(\rho r)] \right\} \sin\nu\phi$$
$$H_r = -i/\rho^2 \left\{ \omega\epsilon_0\nu/r\ [H\ J_\nu(\rho r) + I\ Y_\nu(\rho r)] + \rho\beta\ [K\ J'_\nu(\rho r) + M\ Y'_\nu(\rho r)] \right\} \sin\nu\phi$$
$$H_\phi = -i/\rho^2 \left\{ \rho\omega\epsilon_0\ [H\ J_\nu'(\rho r) + I\ Y'_\nu(\rho r)] + \beta\nu/r\ [K\ J_\nu(\rho r) + M\ Y_\nu(\rho r)] \right\} \cos\nu\phi$$

give the fields outside the rod.

Let:

$$b = \rho/\sigma\ J'_1(\sigma a)\ Y_1(\rho a)$$
$$c = (n^2-1)k\beta/\ a\rho\sigma^2\ \ J_1(\sigma a)\ Y_1(\rho a)$$
$$d = \rho/\sigma\ J'_1(\sigma a)\ J_1(\rho a) \qquad (8)$$
$$e = J_1(\sigma a)\ J'_1(\rho a)$$

$$f = (n^2-1)k\beta/\, ap\sigma^2 \;\; J_1(\sigma a) \;\; J_1(\rho a)$$

$$g = J_1(\sigma a) \;\; Y_1'(\rho a)$$

Then:

$$F/G = +/- \sqrt{\mu_0 \epsilon_0} \sqrt{\frac{(g-b)^2+(e-d)^2+c^2+f^2}{(g-n^2b)^2+(e-n^2d)^2+c^2+f^2}} \qquad (9)$$

and

$$\begin{aligned} P=(\pi/2)^3 a^2 \beta/\rho\, \omega\epsilon_0 \{ & [g-n^2b + c\sqrt{\mu_0/\epsilon_0}\;\; G/F]^2 + \\ & [e-n^2d + f\sqrt{\mu_0/\epsilon_0}\;\; G/F]^2 \\ & [c + (g-b)\sqrt{\mu_0/\epsilon_0}\;\; G/F]^2 \qquad (10) \\ & [f + (e-d)\sqrt{\mu_0/\epsilon_0}\; G/F\,]^2 \;\; \} F^2 \end{aligned}$$

where F and G are the analogs of A and B in the bound modes. The square root in the first formula introduces an ambiguity of sign which we shall comment on later.

For the present, we compute the four partial derivatives:

$$\begin{aligned} \frac{\partial H}{\partial a} = \pi\rho/2 \Big[& \Big\{ a(\sigma^2-n^2\rho^2)/\sigma\; J_0(\sigma a)\; [Y_0(\rho a) - Y_1(\rho a)/\rho a\,] \\ & + [\; 2/\rho a - \rho a + n^2(\rho a - 2\rho a/a^2\sigma^2)]\; J_1(\sigma a)\; Y_1(\rho a) \\ & + [n^2\rho^2/\sigma^2 - 1]\; J_1(\sigma a)\; Y_0(\rho a) \Big\}\; F \end{aligned}$$

$$\begin{aligned} & + (n^2-1)k^2\beta/\omega\epsilon_0\sigma^2\rho \; * \qquad (11) \\ & \Big\{ \sigma J_0(\sigma a)\; Y_1(\rho a) + \rho J_1(\sigma a)\; Y_0(\rho a) \\ & \qquad - 2/a\; J_1(\sigma a)\; Y_1(\rho a) \Big\}\; G \;\; \Big] \end{aligned}$$

$$\frac{\partial I}{\partial a} = -\pi\rho/2 \Big[\Big\{ a(\sigma^2 - n^2\rho^2)/\sigma \; J_0(\sigma a) \; \{ J_0(\rho a) - J_1(\rho a)/\rho a \; \}$$
$$+ [2/\rho a - \rho a + n^2(\rho a - 2\rho a/a^2\sigma^2) \;] \; J_1(\sigma a) J_1(\rho a)$$
$$+ (n^2\rho^2/\sigma^2 - 1) \; J_1(\sigma a) \; J_0(\rho a) \; \Big\} F$$
$$+ (n^2 - 1)k^2\beta/\omega\epsilon_0\sigma^2\rho \; * \qquad (12)$$
$$\Big\{ \sigma J_0(\sigma a) \; J_1(\rho a) + \rho \; J_1(\sigma a) \; J_0(\rho a) - 2/a \; J_1(\sigma a) \; J_1(\rho a) \Big\} \; * \; G \Big]$$

$$\frac{\partial K}{\partial a} = \pi\rho/2\sigma \; (n^2 - 1)k^2 \Big[$$
$$\beta \; / \; \omega\mu\rho\sigma \Big\{ \sigma J_0(\sigma a) \; Y_1(\rho a) + \rho J_1(\sigma a) Y_0(\rho a) - 2/a J_1(\sigma a) \; Y_1(\rho a) \Big\} F$$
$$+ \Big\{ a J_0(\sigma a) \; \{ \; Y_0(\rho a) - Y_1(\rho a)/\rho a \;) + 2 \; / \; \rho\sigma a \; J_1(\sigma a) Y_1(\rho a) \qquad (13)$$
$$- 1/\sigma \; J_1(\sigma a) Y_0(\rho a) \Big\} * G \Big]$$

$$\frac{\partial M}{\partial a} = -.5\pi\rho/\sigma \; (n^2 - 1)k^2 \Big[\beta/\omega\mu\rho\sigma$$
$$\Big\{ \sigma J_0(\sigma a) \; J_1(\rho a) + \rho J_1(\sigma a) J_0(\rho a) - 2/a \; J_1(\sigma a) J_1(\rho a) \Big\} F$$
$$+ \Big\{ \; a J_0(\sigma a) \; [\; J_0(\rho a) - J_1(\rho a)/\rho a \;] \qquad (14)$$
$$+ 2/\rho\sigma a \; J_1(\sigma a) J_1(\rho a) \; - \; 1/\sigma \; J_1(\sigma a) J_0(\rho a)$$
$$\Big\} \; * \; G \Big]$$

And now we are in a position to compute the first integrand:

$$I(\rho, a) = \frac{\pi}{4\rho^2\gamma^2 \, P} \; J_1(\kappa a) \; *$$

$$\left\{ (\beta_0+\beta)\gamma\rho\omega \left(\epsilon_0 A \frac{\partial H}{\partial a} + \mu_0 B \frac{\partial K}{\partial a}\right) * \right.$$

$$\left[a\frac{\gamma J_0(\rho a)+\rho J_1(\rho a)\; iH_0^{\,1}(i\gamma a) \,/\, H_1^{\,1}(i\gamma a)}{\gamma^2+\rho^2} - \frac{J_1(\rho a)}{\gamma\rho} \right]$$

$$+\{ (\beta_0+\beta)\gamma\rho\omega \left(\epsilon_0 A\frac{\partial I}{\partial a} + \mu_0 B\frac{\partial M}{\partial a}\right) \} * \qquad (15)$$

$$\left[a\frac{\gamma Y_0(\rho a)+\rho Y_1(\rho a)\; iH_0^{\,1}(i\gamma a) \,/\, H_1^{\,1}(i\gamma a)}{\gamma^2+\rho^2} - \frac{Y_1(\rho a)}{\gamma\rho} \right]$$

$$+(k^2+\beta_0\beta) \left[\left(A\frac{\partial K}{\partial a} + B\frac{\partial H}{\partial a}\right) J_1(\rho a) + \left(A\frac{\partial M}{\partial a} + B\frac{\partial I}{\partial a}\right) Y_1(\rho a) \right] \right\}$$

Corresponding to each choice of sign for the square root in equation 9, there will be a function, $I(\rho,a)$. By $I_+(\rho,a)$ we mean the function corresponding to the positive choice of the sign and by $I_-(\rho,a)$ we mean the function corresponding to the negative choice. This corresponds completely to the even and odd symmetry present in the slab dielectrics. Now calculate:

$$p(\rho) = \int_0^L I_+(\rho,a)\, a'(z) \exp\left[-i \int_0^z (\beta_0-\beta)\, ds\right] dz \qquad (16)$$

$$q(\rho) = \int_0^L I_-(\rho,a)\, a'(z) \exp\left[-i \int_0^z (\beta_0-\beta)\, ds\right] dz \qquad (17)$$

And then the fractional power loss is given by:

$$\Delta P/P = \oint \{ |p|^2 + |q|^2 \} |\beta|/\rho \, d\beta \qquad (18)$$

The Eigenvalue Equation: The first step in integrating this expression is the evaluation of the integrand and this begins with a solution of the eigenvalue equation. In practice it was found easier to solve for γ ($= \sqrt{\beta_0^2 - k^2}$ than for β_0 because there is one root at $\gamma = 0$ and we are looking for the smallest positive root. The function on the right was

expanded in a power series in the two variables γa and $\ln(\gamma a)$, as shown in appendix I. (See also [2] and [3].) Only the lowest order terms were retained and the resulting formula led to the approximation

$$\gamma a = 1.123 \exp\left[-\tfrac{1}{2}\frac{n^2+1}{\kappa_0 a}\quad\frac{J_0(\kappa_0 a)}{J_1(\kappa_0 a)}\right]$$

This formula was extremely accurate for $ka < 1$ and provided a useful starting point for an iteration scheme whenever $\kappa_0 a$ was less than 2.4 (ie: the first zero of the Bessel function), that is: as long as all higher order modes are choked off.

When the eigenvalue is determined, the bound mode is completely described by equations (4) and (5). In the calculation, fifty values of γ, A and B were calculated at points spaced at equal intervals down the rod. These values were then stored in a table to be used as needed.

The Singularities: With the bound mode available, the inner integrand may be calculated from equations (7)-(14). A value of $I(\rho,a)$ is needed for each value of β from -k to +k inclusive. At each of these (end) points, $\rho = 0$, the denominator of (18) vanishes and a singularity (which must be dealt with) is created. It is to be hoped that $p(\rho)$ and $q(\rho)$ will be proportional to $\sqrt{\rho}$ or better. Unfortunately equation (14) does not have $\sqrt{\rho}$ but $1/\rho^2$. Now a factor of $\rho^{5/2}$ must be sought from the rest of the terms and the search leads us a merry chase. The details are included in appendix I. When $|p|$ and $|q|$ were plotted for values of β close to k, the graph rose steeply. (Indeed, it was this that led to the calculations described in appendix II.) After the results of appendix II were available, the integrand was calculated for values of β each of which was only half as far from k as its predecessor. The graph rose sharply revealing a burst of power very close to $\beta = k$. The preliminary calculations had missed this entirely and underestimated the power lost. With the aid of appendix II, the revised calculations used much smaller steps near $\beta = k$ and were much more accurate as we shall show.

Another, albeit simpler, singularity was found at $\beta = 0$. It was easily mended. Now a straightforward Simpson's law integration scheme could be (and was) written. It worked moderately well for short rods but failed utterly when applied to long rods. This led to an investigation which showed that the problem lay in the periodic nature of the integrand.

The Inverse Square Law and the Validation of the Program: Starting

with the power loss formula:

$$\Delta P/P = \oint \{ |p|^2 + |q|^2 \} \, |\beta|/\rho \, d\beta \qquad (18)$$

where:

$$p(\rho) = \int_0^L I_+(\rho,a)\, a'(z) \exp[-i \int_0^z (\beta_0-\beta)\, ds\,]\, dz \qquad (16)$$

$$q(\rho) = \int_0^L I_-(\rho,a)\, a'(z) \exp[-i \int_0^z (\beta_0-\beta)\, ds\,]\, dz \qquad (17)$$

If z is large, so is the argument of the imaginary exponential function and that creates the problem. The period of the integrand is small compared to the spacing, Δx. So we wind up taking a quasi-random sample of the integrand.

Let us suppose that the antenna is self-similar in that the radius depends only on the ratio x=z/L. Substituting this in the integral:

$$p(\rho) = \int_0^1 I_+(\rho,a[x])\, \frac{da}{dx} L \exp\{ -i \int_0^x [\, \beta_0(a[x]) - \beta\,] L\, ds\}\, dx$$

Now set $u = \int_0^x [\, \beta_0(a[x]) - \beta\,]\, ds$.

$$p(\rho) = \int_0^{u_1} \phi(u) \exp\{-iLu\}\, du \qquad (19)$$

where

$$\phi(u) = I_+(\rho, a[x])\, \frac{da}{dx} \; / \; [\, \beta_0(a[x]) - \beta] \qquad (20)$$

and the quantities to be evaluated are understood to be functions of u. Integrating by parts and multiplying by L:

$$Lp(\rho) = i \exp(-iLu)\, \phi(u) \,|_0^{u_1} - i \int_0^{u_1} \phi(u) \exp\{-iLu\}\, du$$

$$Lp(\rho) = i \exp\{-iLu_1\}\, \phi(u_1) - i\phi(0) - iT_+$$

and $$Lq(\rho) = i \exp\{-iLu_1\}\, \psi(u_1) - i\psi(0) - iT_-$$

$$L^2 \Delta P/P = \int_{-k}^{k} [\phi^2(u_1) + \phi^2(0) + \psi^2(u_1) + \psi^2(0)]\, |\beta|/\rho \, d\beta$$

$$-2 \int_{-k}^{k} [\phi(u_1)\, \phi(0) + \psi(u_1)\, \psi(0)\,] \cos(Lu_1)\, |\beta|\, /\rho \, d\beta$$

$$
\begin{aligned}
{}_{-k}\int^{k} \Big[\;& \phi(u_1)\,\{\, T_+ \exp(iLu_1) + T_+^{*} \exp(-iLu_1) \;\} \\
& + \psi(u_1)\,\{\, T_- \exp(iLu_1) + T_-^{*} \exp(-iLu_1) \;\} \\
& - \phi(0)\,\{\, T_+ + T_+^{*} \,\} \\
& - \psi(0)\,\{\, T_- + T_-^{*} \,\} \\
& T_+^{*} T_+ + T_- T_-^{*} \Big] \, |\beta| \,/\, \rho \; d\beta
\end{aligned}
$$

Now the limits of T_+ and T_- as L goes to infinity are both zero as noted above and the third integral grows smaller as L grows larger. We claim that the same is true for the second integral as well. Observe that the integrand :

$$\{\, \phi(u_1)\,\phi(0) + \psi(u_1)\,\psi(0) \,\}\, |\beta| \,/\, \rho$$

is continuous except possibly at $\beta=0$ and $\rho=0$. By appendix II, even in these three exceptional cases the integrand is continuous . Accordingly the integral goes to zero (Riemann- Lebesgue Lemma)

Hence, as L goes to infinity, $L^2 \Delta P/P$ approaches:

$${}_{-k}\int^{k} \{\, \phi^2(u_1) + \phi^2(0) + \psi^2(u_1) + \psi^2(0) \,\}\, |\beta| \,/\rho \; d\beta$$

and by using this formula we can compute the value of the constant appearing in the inverse square law. The agreement initially was not very good, and a more sophisticated integration -- the one of van der Vooren and van Linde [4] (which owes some filial respect to the scheme of Filon) was introduced.. This scheme is designed for integrating:

$$\int_0^{2N\pi} f(x) \cos(\omega x)\, dx$$

and

$$\int_0^{2N\pi} f(x) \sin(\omega x)\, dx$$

by approximating f(x) by an appropriate polynomial.

The first hurdle that we must clear in order to use this scheme stems from the fact that our integral is not exactly in this form since

u_1 is not, in general, a multiple of 2π. So we choose N to be the greatest integer that does not exceed $u_1 / 2\pi$. The integral from $2n\pi$ to u_1 is then found by a Simpson Law scheme. Before evaluating the remainder by the van der Vooren - van Linde scheme, we have one more hurdle to cross. This scheme requires that the integrand be evaluated at integral submultiples of $2N\pi$. But u must be constructed from a numerical integration scheme and the values of u that are available are not always at the required points. To overcome this difficulty, the most straightforward imaginable solution was used: linear interpolation. We did not have time to carry out a thorough analysis of the errors involved in such a scheme, but we did test it by generating a value of u from the quadratic function:

$$u = 2\pi x - \pi x^2/10$$

By setting $x = n/5$ for n=1 to 50, we generated a table of values of u The following four integrals were then evaluated:

$$I_1 = \int_0^{10\pi} u^5 \cos(u)\, du \qquad I_2 = \int_0^{10\pi} u^5 \sin(u)\, du$$

$$I_3 = \int_0^{10\pi} u^4 \cos(u)\, du \qquad I_4 = \int_0^{10\pi} u^4 \sin(u)\, du$$

in three different ways. The first was a straightforward application of integral calculus and repeated integrations by parts (exact). The second used the vdVvL scheme just as it stands and the third chose a value of u as the scheme demands, but then interpolated linearly in the table to find the value of z and then got back to u from the interpolated value of z by using the formula. The results are in the table below:

	exact	vdVvL	mod. vdVvL
I_1	$.48112369 \times 10^7$	$.48218 \times 10^7$	$.48183 \times 10^7$
I_2	$-.29985613 \times 10^8$	$-.29986 \times 10^8$	$-.29983 \times 10^8$
I_3	$.1232712 \times 10^6$	$.12340 \times 10^6$	$.12332 \times 10^6$
I_4	$-.96224739 \times 10^6$	$-.96225 \times 10^6$	$-.96214 \times 10^6$

The modified scheme does not seem markedly inaccurate - the errors are all less than a quarter of a percent. To obtain exact error bounds a complete analysis would have to be undertaken and the results might well be too complicated to apply to our problem in any simple way This table seems sufficient to us to warrant our confidence in the results obtained by the use of this scheme.

It was hoped that the introduction of this scheme would remedy all the problems and bring the long antenna results and the inverse square law results together. This did not occur and a further search revealed the power spike just below $\beta = k$ alluded to earlier. When both programs were corrected to use much smaller steps near $\beta = k$, the desired agreement was forthcoming, as the following figures show.

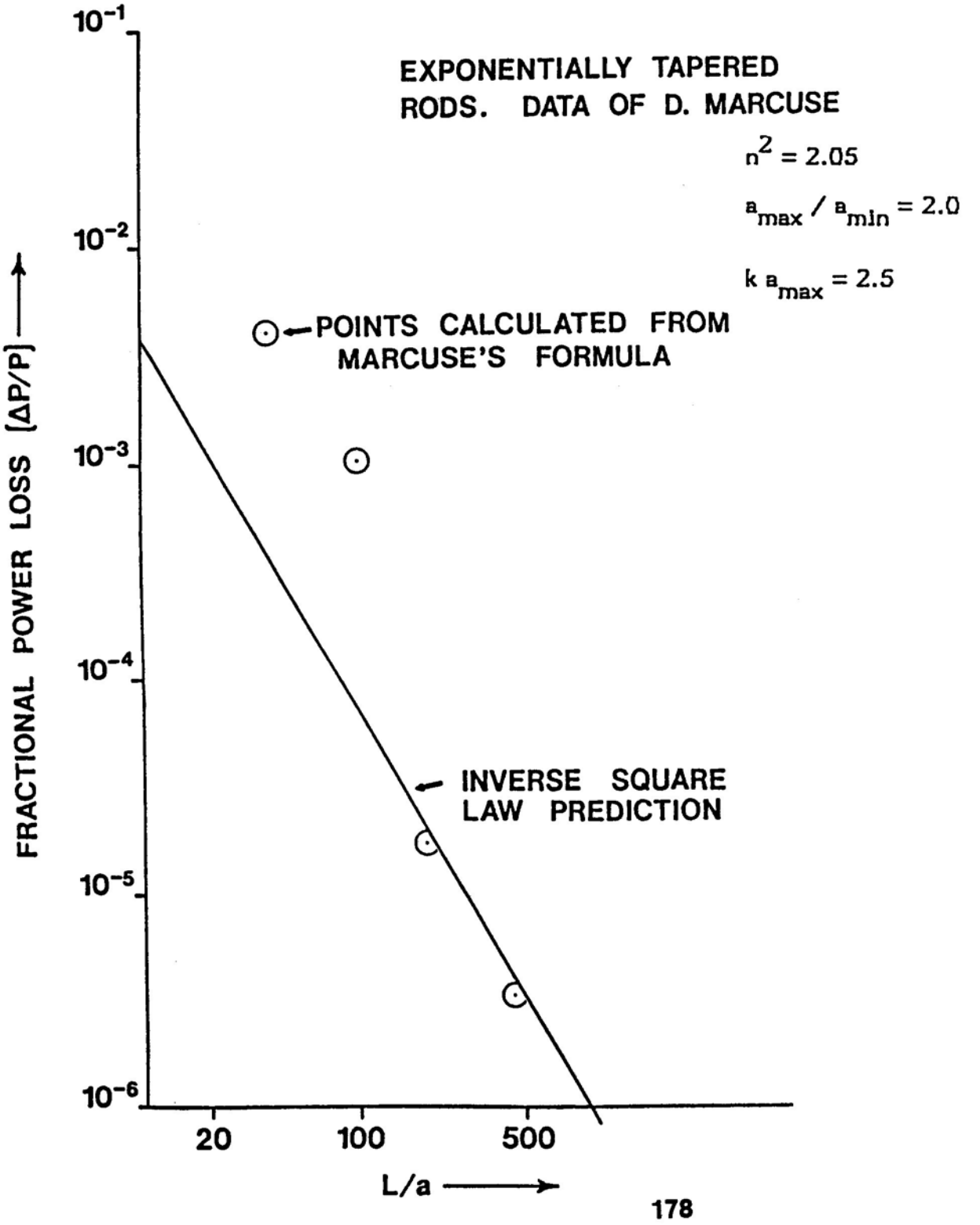
EXPONENTIALLY TAPERED
RODS. DATA OF D. MARCUSE
$n^2 = 2.05$
$a_{max} / a_{min} = 2.0$
$k\, a_{max} = 2.5$
POINTS CALCULATED FROM
MARCUSE'S FORMULA
INVERSE SQUARE
LAW PREDICTION
FRACTIONAL POWER LOSS [ΔP/P]
10^{-1}
10^{-2}
10^{-3}
10^{-4}
10^{-5}
10^{-6}
20
100
500
L/a

MARCUSE'S DIELECTRIC ROD CALCULATED POWER LOSSES AND INVERSE SQUARE LAW PREDICTIONS LINEAR TAPER

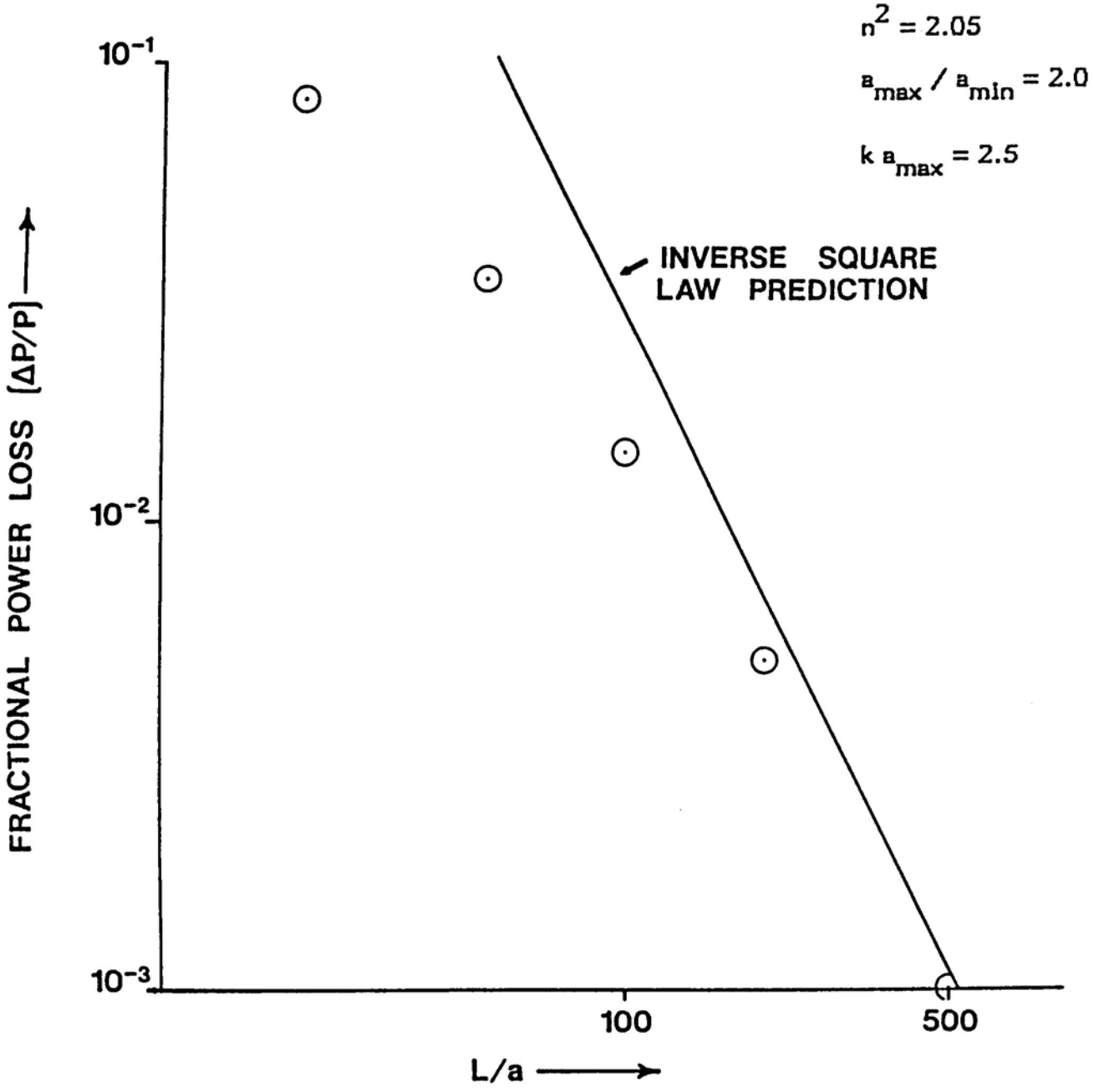

⊙ Calculated directly from Marcuse's Equations

$n^2 = 1.2$
Linear Taper
$a_{max} = .0642\,m$
$a_{min} = .0315\,m$

$f = 4 \times 10^9\,Hz$

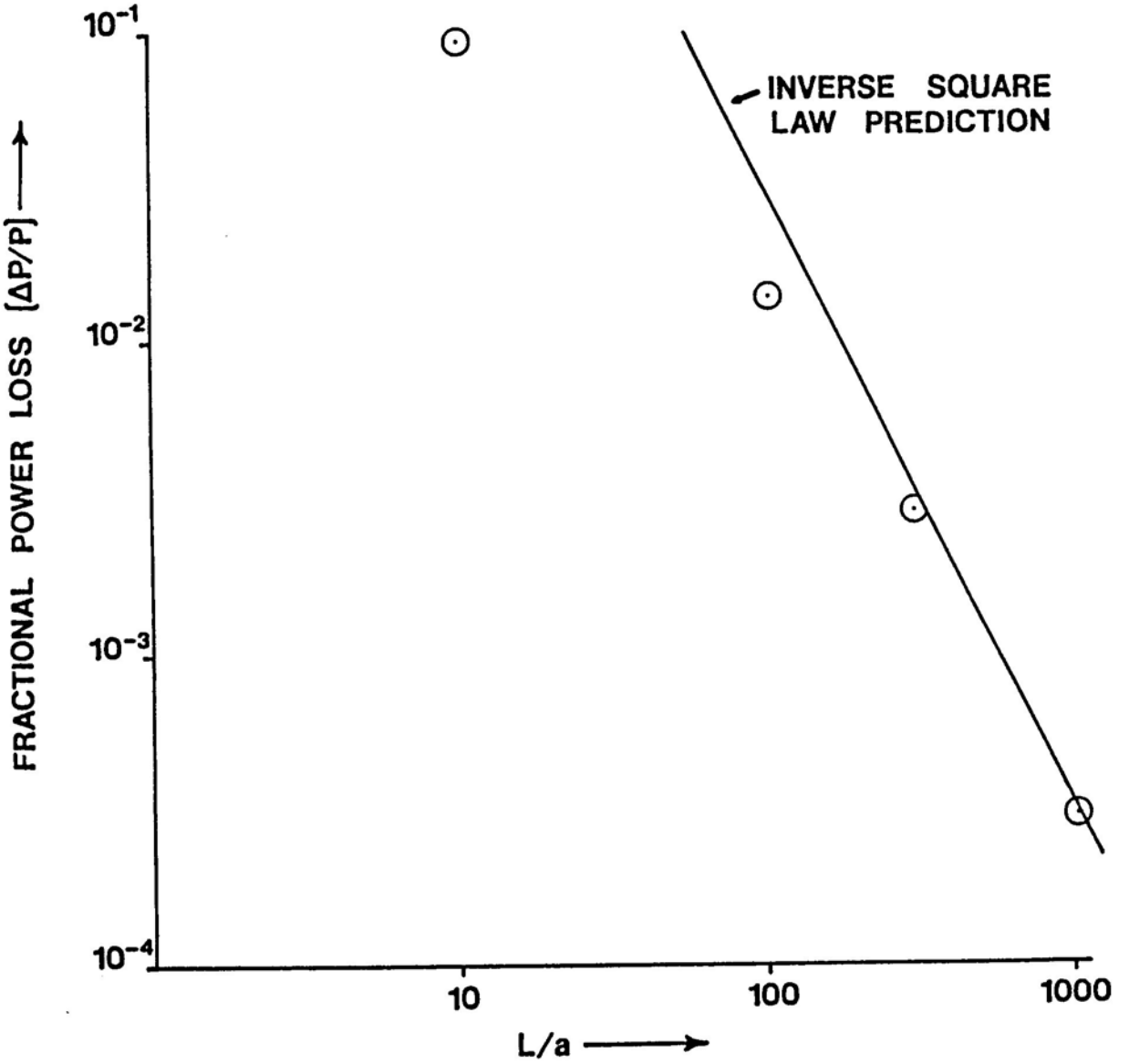

⊙ Calculated directly from Marcuse's Equations

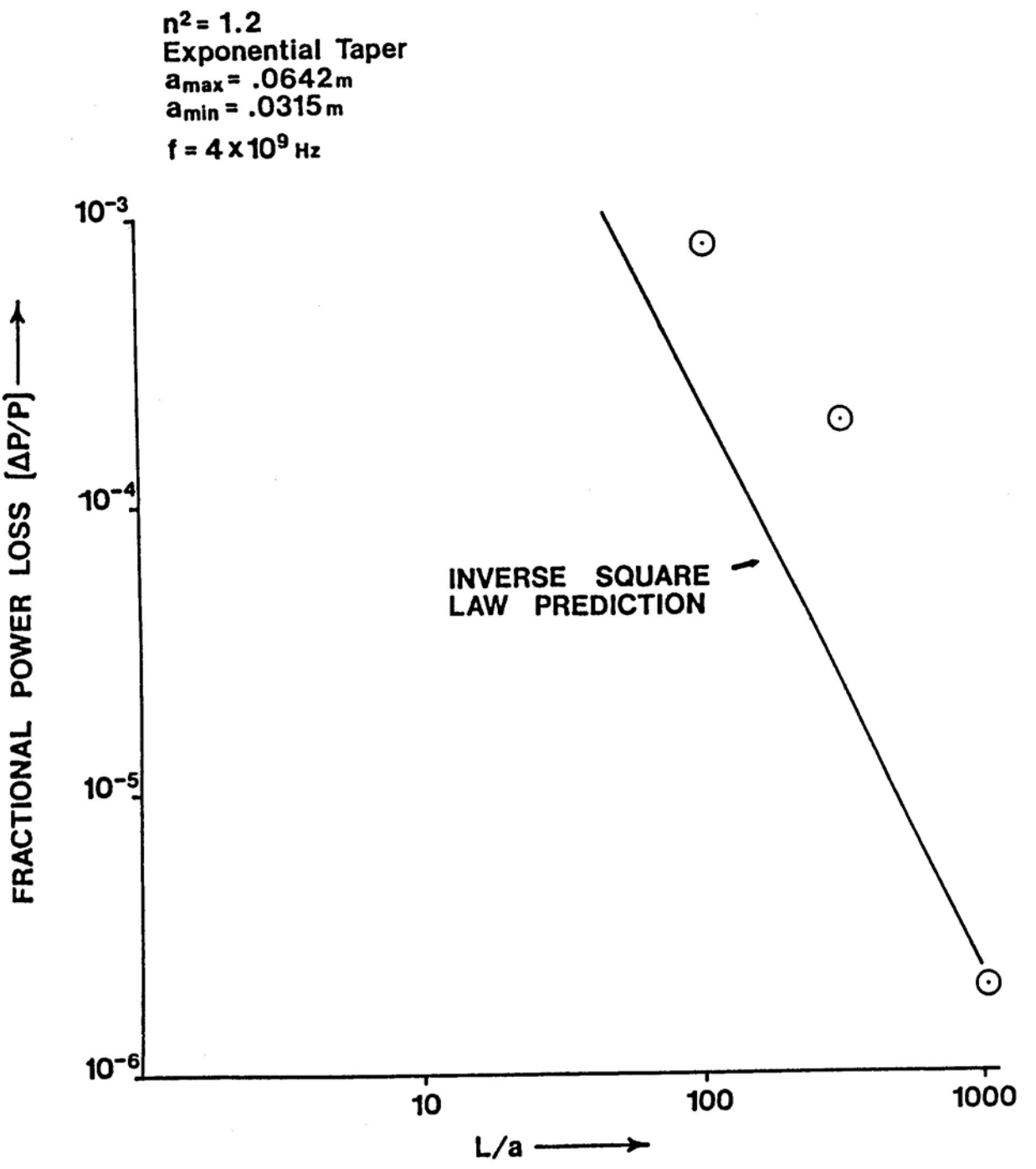

⊙ Calculated directly from Marcuse's Equations

$n^2 = 1.5$
Linear Taper
$a_{max} = .04057m$
$a_{min} = .024748m$
$f = 4 \times 10^9$ Hz

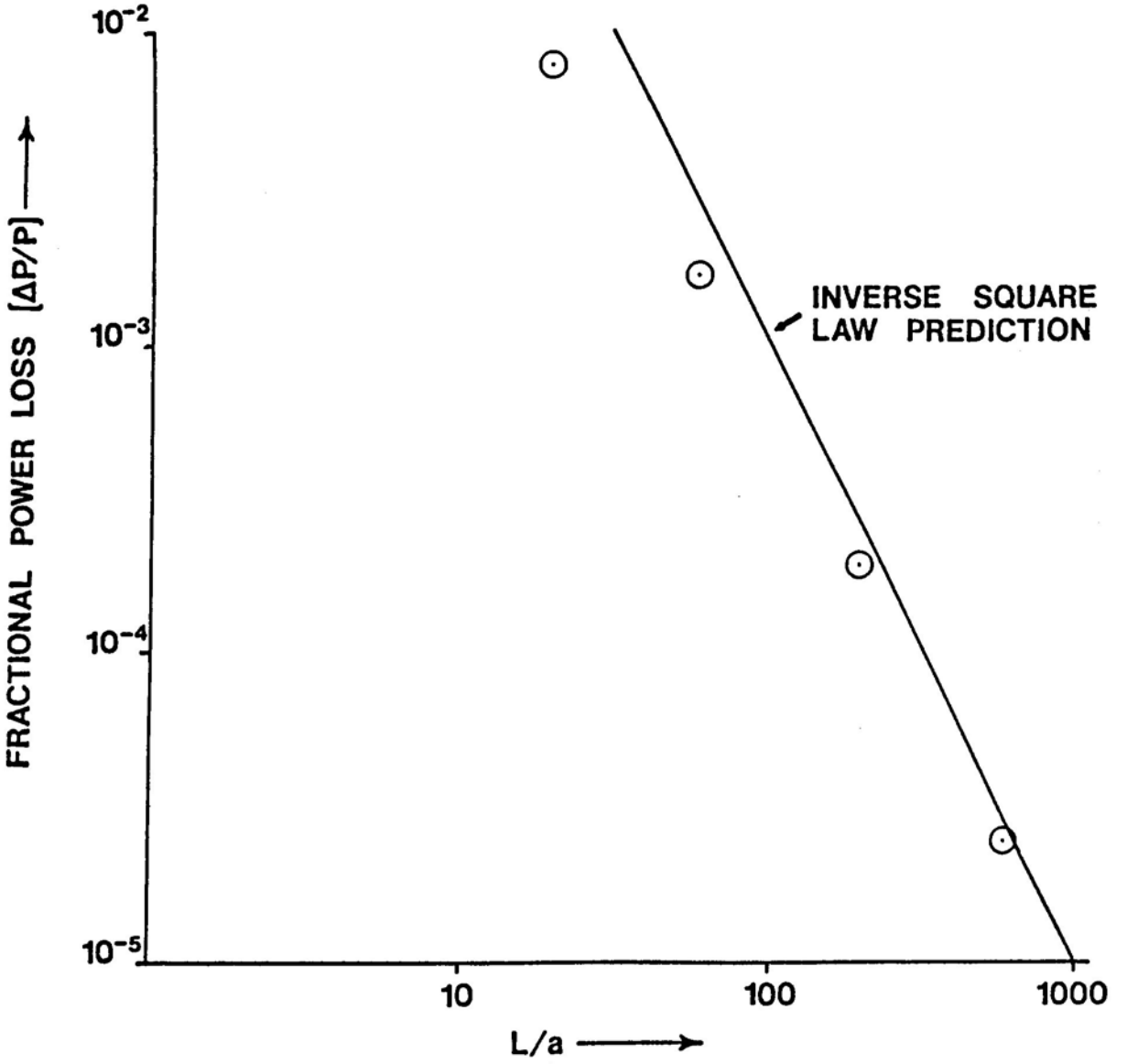

⊙ Calculated directly from Marcuse's Equations

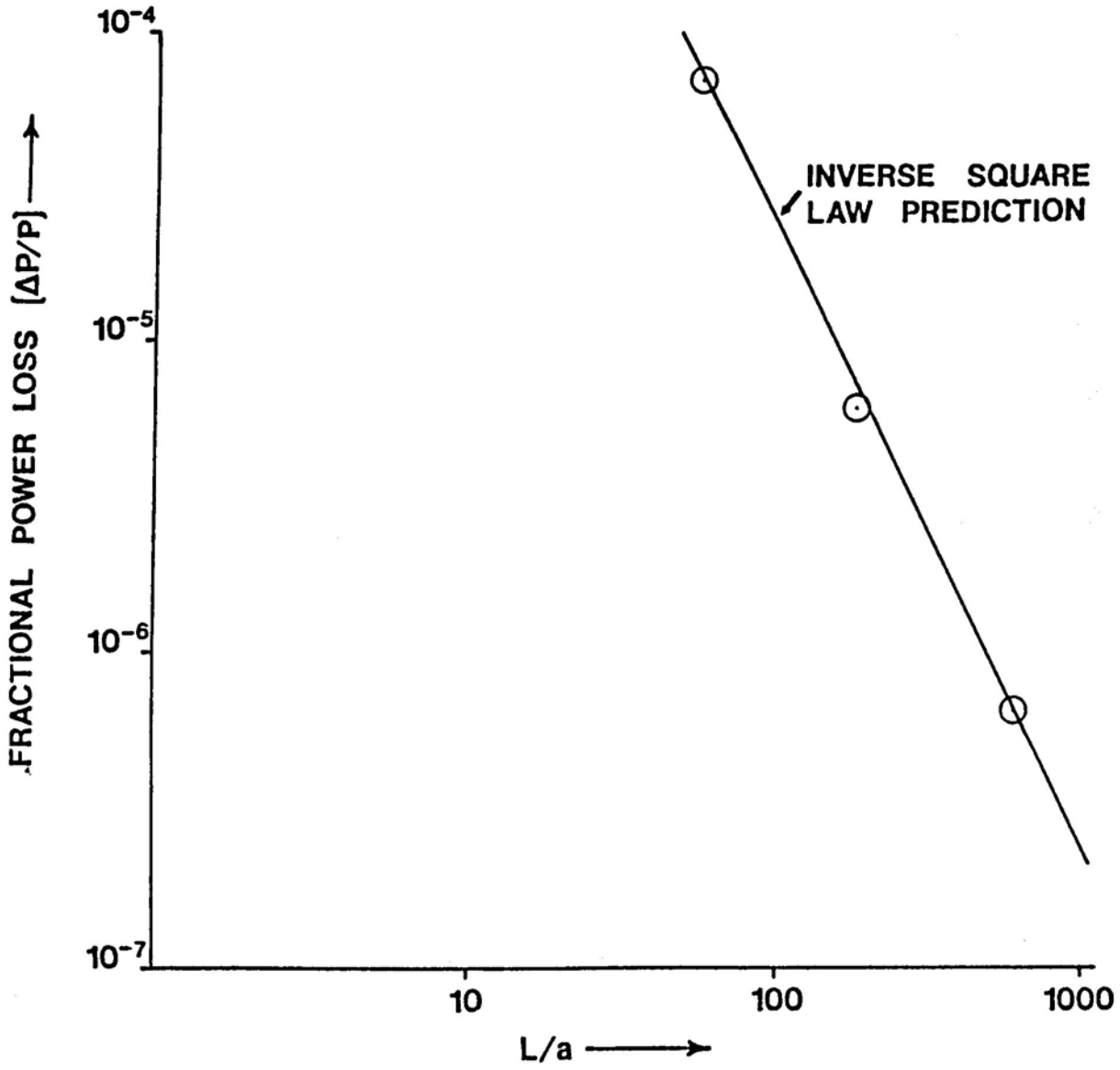

⊙ Calculated directly from Marcuse's Equations

$n^2 = 2.56$
Linear Taper
$a_{max} = .02297m$
$a_{min} = .013047m$

$f = 4 \times 10^9$ Hz

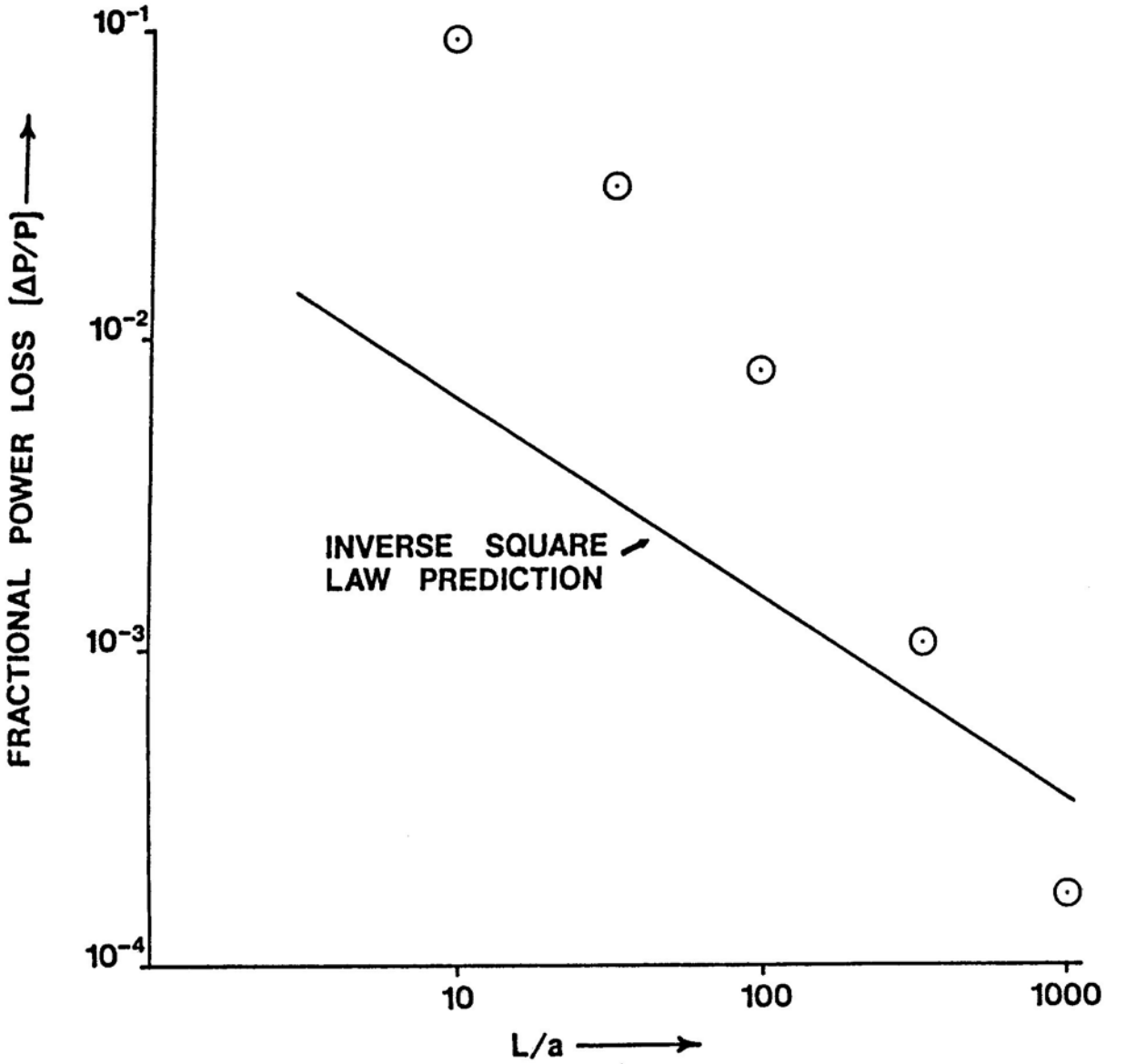

⊙ Calculated directly from Marcuse's Equations

$n^2 = 2.56$
Exponential Taper
$a_{max} = .02297m$
$a_{min} = .013047m$
$f = 4 \times 10^9$ Hz

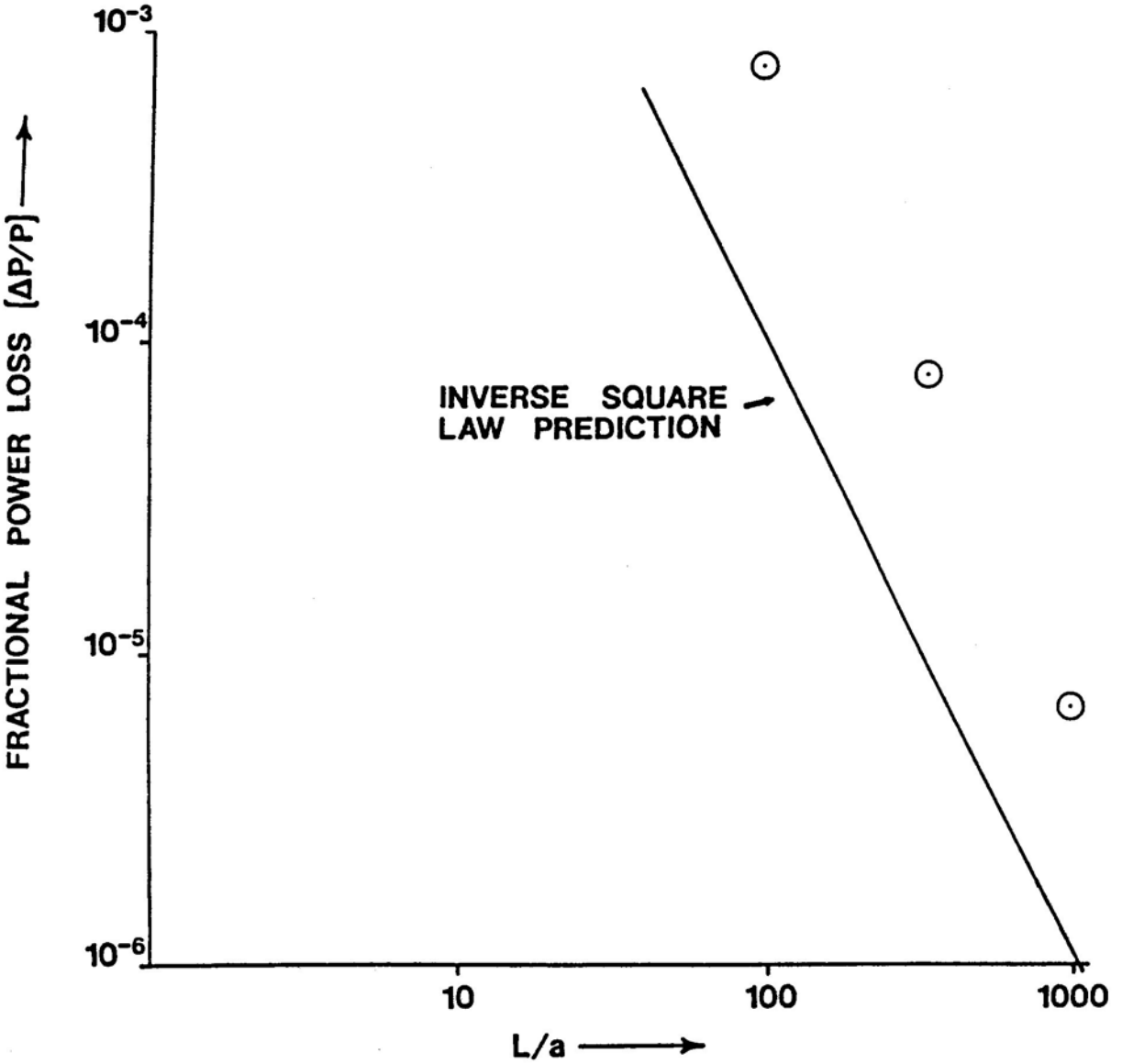

⊙ Calculated directly from Marcuse's Equations

$n^2 = 10$
Linear Taper
$a_{max} = .009563\,m$
$a_{min} = .0069332\,m$
$f = 4 \times 10^9\,Hz$

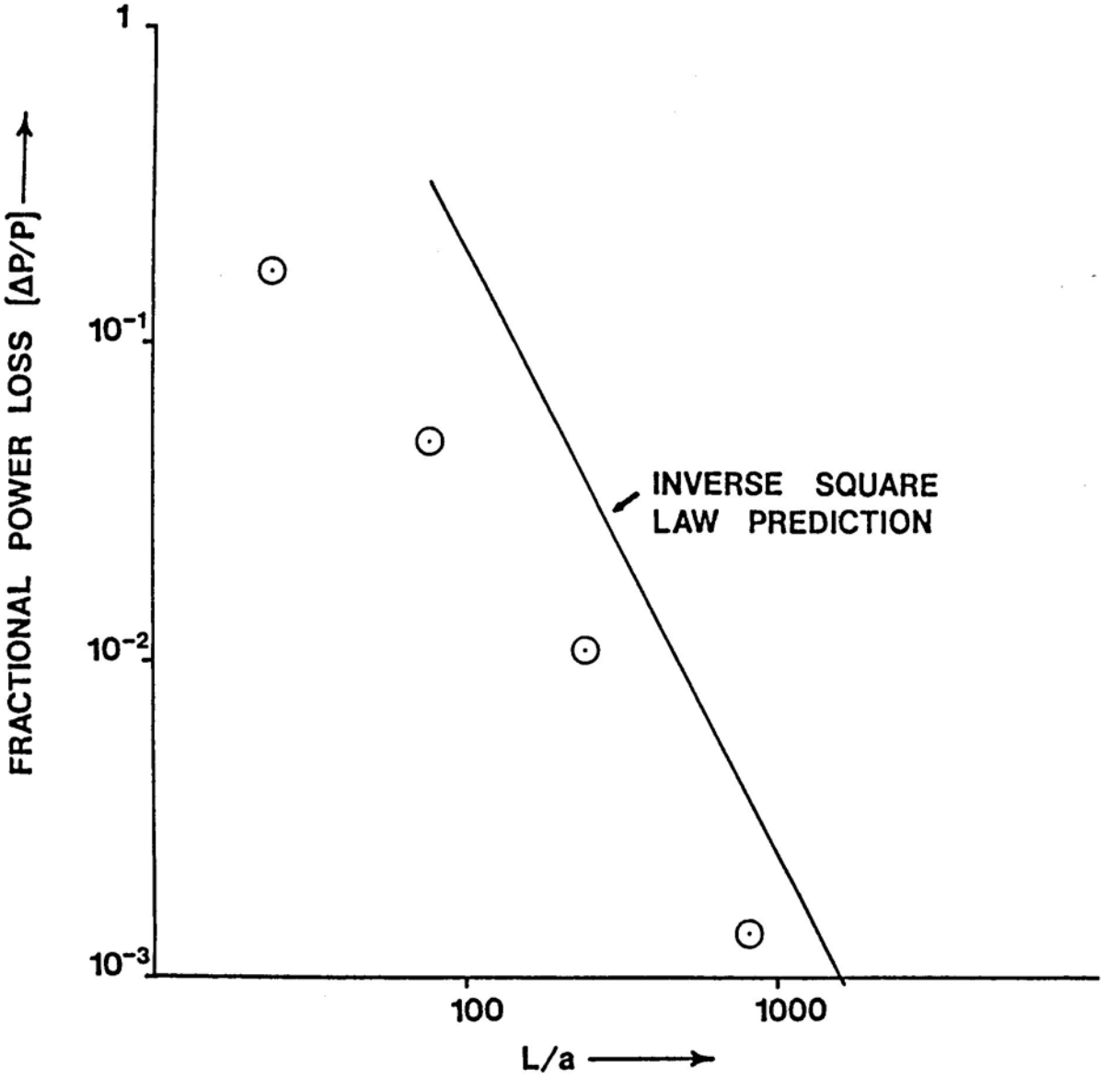

⊙ Calculated directly from Marcuse's Equations

$n^2 = 10$
Exponential Taper
$a_{max} = .009563\,m$
$a_{min} = .006932\,m$
$f = 4 \times 10^9\,Hz$

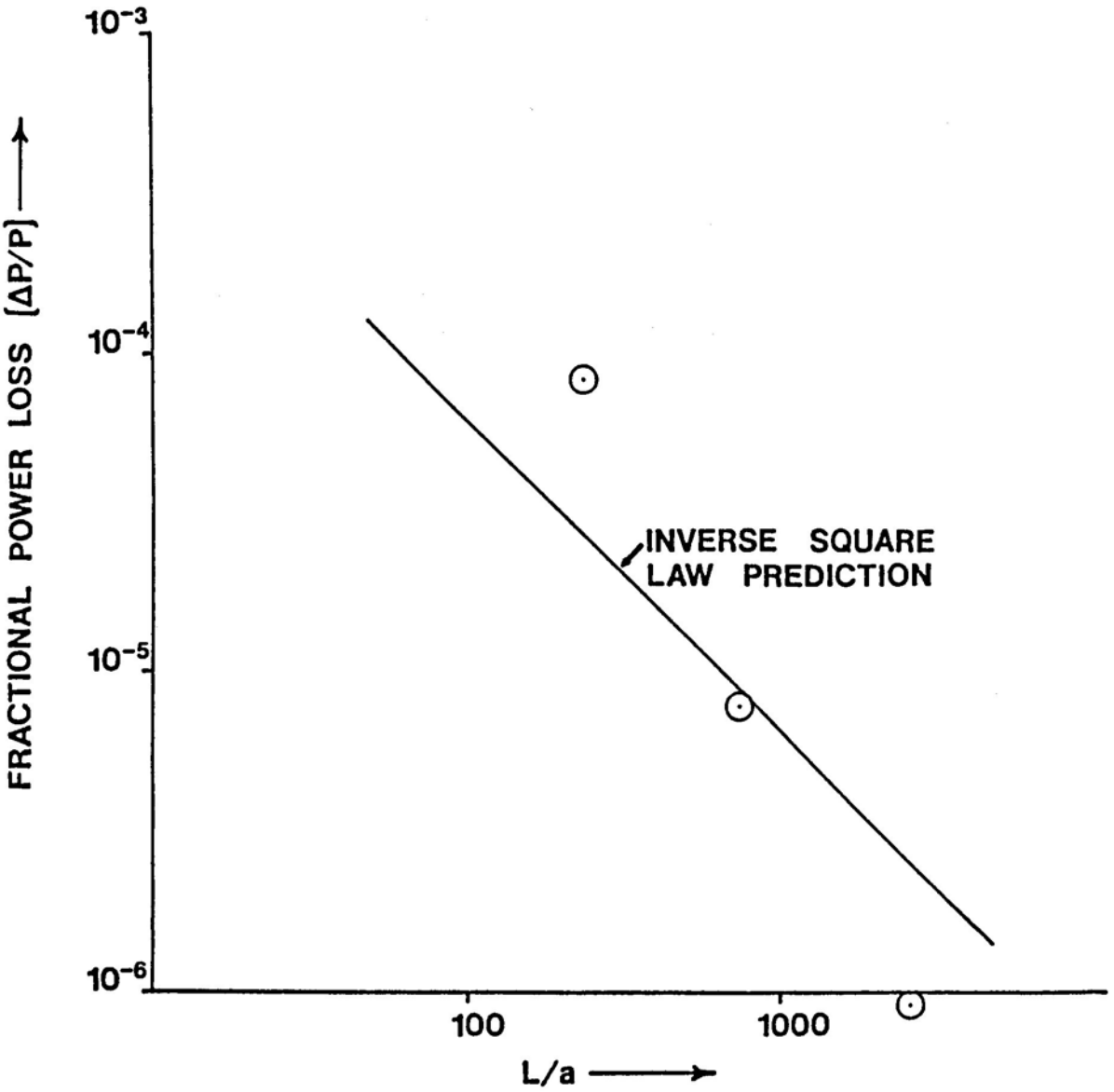

⊙ Calculated directly from Marcuse's Equations

Bibliography

[1] Marcuse, Dietrich: Radiation Losses of the Dominant Mode in a Round Dielectric Waveguide. Bell System Technical Journal 49 (8) October 1970

[2] Coughlin, James P.: Baran, Robert H. and Krall, Albert D. : The Mathematics of Marcuse's Power Loss Equation. IEEE Antennas and Propagation Society / URSI Radio Science Meeting. Syracuse, New York 6-10 June 1988

[3] Coughlin, James P. Calculation of Losses from a Dielectric Rod NSWC - TR 81-299 July 1981

[4] van de Vooren, A.I. and van Linde, H.J.: Numerical Calculation of Integrals with strongly Oscillating Integrand. Mathematics of Computation 20 (1966)

[5] Abramowitz, Milton and Stegun, Irene : Handbook of Mathematical Functions. U.S. Department of Commerce. 1964

APPENDIX I

$$\left\{\frac{\gamma^2 a^2 J_\nu'(\kappa a)}{\kappa a \; J_\nu(\kappa a)} + i\gamma a \frac{H_\nu^{(1)'}(i\gamma a)}{H_\nu^{(1)}(i\gamma a)}\right\} *$$

$$\left\{\frac{n^2\gamma^2 a^2 J_\nu'(\kappa a)}{\kappa a \; J_\nu(\kappa a)} + i\gamma a \frac{H_\nu^{(1)'}(i\gamma a)}{H_\nu^{(1)}(i\gamma a)}\right\} =$$

$$\frac{\nu^2 (n^2-1)^2 k^2 \beta_0^2}{\kappa^4}$$

This is the equation that determines whether the ν^{th} mode can propagate down the rod. A careful study of this equation will reveal that it is not possible to satisfy it for arbitrary ν and a. Indeed unless a has a certain minimum value, there will, in general, be no solution. The only exception to this rule is the case $\nu=1$, where the above equation has a solution for all values of a. Accordingly, $\nu=1$ is the lowest order mode that can propogate down the rod (lower than $\nu = 0$!). If we specialize to this case, the resulting equation becomes:

$$\left[\frac{n^2 a^2 \gamma^2}{\kappa a}\left\{\frac{J_0(\kappa a)}{J_1(\kappa a)} - \frac{1}{\kappa a}\right\} + \gamma a \frac{iH_0^{(1)}(i\gamma a)}{H_1^{(1)}(i\gamma a)} - 1\right] *$$

$$\left[\frac{a^2\gamma^2}{\kappa a}\left\{\frac{J_0(\kappa a)}{J_1(\kappa a)} - \frac{1}{\kappa a}\right\} + \gamma a \frac{iH_0^{(1)}(i\gamma a)}{H_1^{(1)}(i\gamma a)} - 1\right]$$

$$= (n^2-1)^2 \beta_0^2 k^2 / \kappa^4$$

where the derivatives of the Bessel functions have been eliminated by using well known identities (cf. Abramowitz and Stegun[5])

We can expand the Hankel functions as follows:

$$i\gamma a H_0^{(1)}(i\gamma a) / H_1^{(1)}(i\gamma a) \simeq -\gamma^2 a^2 \left(\gamma_1 + \ln\left(\frac{\gamma a}{2}\right)\right) + O(\gamma^2 a^2)$$

where γ_1 is Euler's constant. This expansion is not, strictly speaking,

a valid MacLaurin series for the Hankel functions, since the natural logarithm term is extremely large near $\gamma a = 0$. But we will make the substitution anyway, leading to:

$$\left\{1-\gamma^2 a^2\left(\ln\left(\frac{\gamma a}{2}\right) + \gamma_1\right) + \frac{n^2\gamma^2 a^2}{\kappa_0 a}\, t_1 \qquad +O(\gamma^2) \right\}$$

$$* \left\{1-\gamma^2 a^2\left(\ln\left(\frac{\gamma a}{2}\right) +\gamma_1\right) + \frac{\gamma^2 a^2}{\kappa_0 a}\, t_1 \quad + O(\gamma^2) \right\} = \frac{(n^2-1)^2 k^2 (k^2+\gamma^2)}{[(n^2-1)k^2-\gamma^2]^2}$$

where

$$t_1 = \left\{ \frac{J_0(\kappa_0 a)}{J_1(\kappa_0 a)} - \frac{1}{\kappa_0 a} \right\}$$

Expand the left hand side in a power series in γa and subtract the right hand side to obtain:

$$\frac{1+2/(n^2-1)}{k^{*2}} + 2\gamma_1 + 2\ln\frac{\gamma a}{2} \qquad \frac{(n^2+1)}{\kappa_0 a}\, t_1 = O(\gamma^2)$$

(where $k^* = ka$) and in view of the behavior of the logarithm near $\gamma=0$, this equation cannot be satisfied unless

$$\ln\frac{\gamma a}{2} = -\left[\gamma_1 + \frac{n^2+1}{2\kappa_0 a}\, t_1 + 2\frac{n^2+1}{n^2-1}\, k^{*2}\right]$$

And, if this equation is solved for γa, we get:

$$\gamma a \simeq 2\exp(-\gamma_1)\exp\left(-\frac{n^2+1}{2\kappa_0 a}\,\frac{J_0(\kappa_0 a)}{J_1(\kappa_0 a)}\right)$$

This is a very useful approximate formula for computing the solution to the eigenvalue problem. As the table below shows, the results are quite good for small values of ka and even for large values they form a good starting point for an iteration scheme.

TABLE II

ka	γ_a (formula)	γ_a (computer calculation)
.5	1.5×10^{-5}	1.48×10^{-5}
.625	9.74×10^{-4}	9.76×10^{-5}
.75	9.45×10^{-3}	9.50×10^{-3}
.875	3.77×10^{-2}	3.77×10^{-2}
1.0	1.08×10^{-1}	9.32×10^{-2}
1.5	4.72×10^{-1}	5.48×10^{-1}

APPENDIX II

We now return to the expression for $I(\rho,a)$ given by formula 15. Corresponding to each choice of sign for the square root in equation 9, there will be a function, $I(\rho,a)$. By $I_+(\rho,a)$ we mean the function obtained from the positive choice for the sign and by $I_-(\rho,a)$, we mean the function corresponding to the negative choice. Now calculate:

$$p(\rho) = \int_0^L I_+(\rho,a)\, a'(z)\, \exp[-i \int_0^z (\beta_0-\beta)\, ds\,]\, dz$$

$$q(\rho) = \int_0^L I_-(\rho,a)\, a'(z)\, \exp[-i \int_0^z (\beta_0-\beta)\, ds\,]\, dz$$

And then the fractional power loss will be given by:

$$\Delta P/P = \int_{-k}^{k} \{\, |q|^2 + |p|^2 \,\}\, |\beta| \,/\rho \; d\beta$$

Now since $\rho = \sqrt{(k^2-\beta^2)}$, it is clear that this last named integrand has a singularity at each end point of the interval of integration. This singularity is rendered doubly difficult because each limit as β approaches k or -k must be handled separately for each choice of sign for F/G.

$$\lim_{\beta \Rightarrow k} \; I_+(\rho,a) \,/\, \sqrt{\rho}$$

$$\lim_{\beta \Rightarrow -k} \; I_+(\rho,a) \,/\, \sqrt{\rho}$$

$$\lim_{\beta \Rightarrow k} \; I_-(\rho,a) \,/\, \sqrt{\rho}$$

$$\lim_{\beta \Rightarrow -k} \; I_-(\rho,a) \,/\, \sqrt{\rho}$$

vanish. To see this we shall outline the derivation for the first of these four limits, since that is the most difficult of the four. First we show:

$$\lim_{\beta \Rightarrow k} F/G = \sqrt{\epsilon_0/\mu}$$

and, then:

$$\lim_{\beta=>k} [\, F/G - \sqrt{\epsilon_0/\mu}\,] / \rho^2 = L_1 = 0$$

With the aid of these, we can show

$$\lim_{\beta=>k} [\, \ln(\rho) * F/\rho^{-1/2}\,] = F_1 = 0$$

And now we are prepared to look at the integrand. To save writing, we will use H^* in place of $iH_0^1(i\gamma a)/H_1^1(i\gamma a)$. Then

$$\lim_{\beta=>k} I(\rho,a)/\sqrt{\rho} = \lim_{\beta=>k} \pi J_1(\kappa a) / 4\, P\, \gamma^2\, \rho^{5/2} *$$

$$\Big\{ (\beta_0+\beta)\gamma\rho\, (\omega\epsilon_0 A \frac{\partial H}{\partial a} + \omega\mu B \frac{\partial K}{\partial a}) * \Big[a \frac{\gamma J_0(\rho a)+H^* \rho J_1(\rho a)}{\gamma^2+\rho^2} - \frac{J_1(\rho a)}{\gamma\rho} \Big]$$

$$+ (\beta_0+\beta)\gamma\rho(\omega\epsilon_0 A \frac{\partial I}{\partial a} + \omega\mu B \frac{\partial M}{\partial a}) * \Big[a \frac{\gamma Y_0(\rho a)+H^* \rho Y_1(\rho a)}{\gamma^2+\rho^2} - \frac{Y_1(\rho a)}{\gamma\rho} \Big]$$

$$+(k^2+\beta_0\beta) * \Big[(A \frac{\partial K}{\partial a} + B \frac{\partial H}{\partial a}) * J_1(\rho a) + (A \frac{\partial M}{\partial a} + B \frac{\partial I}{\partial a}) Y_1(\rho a) \Big]$$

This limit gives rise to the following four limits:

$$L_1 = \lim \rho^{-5/2} \{ (\beta_0+\beta)\gamma\rho\omega\epsilon_0 \frac{\partial H}{\partial a} \Big[a \frac{\gamma J_0(\rho a) + \rho J_1(\rho a) H^*}{\gamma^2+\rho^2} - \frac{J_1(\rho a)}{\gamma\rho} \Big]$$
$$+(k^2+\beta_0\beta) \frac{\partial K}{\partial a} J_1(\rho a) \}$$

$$L_2 = \lim_{\beta_0=>k} \rho^{-5/2} \{ (\beta_0+\beta)\gamma\rho\omega\epsilon_0 \frac{\partial I}{\partial a} \Big[a \frac{\gamma Y_0(\rho a) + \rho H^* Y_1(\rho a)}{\gamma^2+\rho^2} - \frac{Y_1(\rho a)}{\gamma\rho} \Big]$$

$$+(k^2+\beta_0\beta) \frac{\partial M}{\partial a} Y_1(\rho a) \}$$

$$L_3 = \lim_{\beta \Rightarrow k} \rho^{-5/2} \Big\{ (\beta_0+\beta)\gamma\rho\omega\mu \frac{\partial K}{\partial a} \Big[a\frac{\gamma J_0(\rho a) + \rho H^* J_1(\rho a)}{\gamma^2+\rho^2} - \frac{J_1(\rho a)}{\gamma\rho} \Big]$$

$$+(k^2+\beta\beta_0) J_1(\rho a) \frac{\partial H}{\partial a} \Big\}$$

$$L_4 = \lim_{\beta \Rightarrow k} \rho^{-5/2} \Big\{ (\beta_0+\beta)\gamma\rho\omega\mu \frac{\partial M}{\partial a} \Big[a\frac{\gamma Y_0(\rho a) + \rho H^* Y_1(\rho a)}{\gamma^2+\rho^2} - \frac{Y_1(\rho a)}{\rho\gamma} \Big]$$

$$+(k^2+\beta\beta_0)\frac{\partial I}{\partial a} Y_1(\rho a) \Big\}$$

Then the limit of $I(\rho,a)/\sqrt{\rho}$ will be

$$I_0 = \pi J_1(\kappa a)/(4\gamma^2 P) \Big\{ A(L_1+L_2) + B(L_3+L_4) \Big\}$$

$$L_1 = L_1' + L_1''$$

$$L_1' = \lim_{\beta_0 \Rightarrow k} \rho^{-5/2} \Big[(\beta_0+\beta)\gamma\rho\omega\epsilon_0 \frac{\partial H}{\partial a} \Big]^* \Big\{ a \frac{\gamma J_0(\rho a) + \rho H^* J_1(\rho a)}{\gamma^2+\rho^2} - \frac{J_1(\rho a)}{\rho\gamma} - \frac{a}{2\gamma} \Big\}$$

$$=0$$

$$L_1 = L_1'' = \lim_{\beta \Rightarrow k} \rho^{-5/2} \Big\{ (\beta_0+\beta)\omega\epsilon_0 a\rho/2\gamma \frac{\partial H}{\partial a} + (k^2+\beta_0\beta) J_1(\rho a) \frac{\partial K}{\partial a} \Big\}$$

$$= .25\, \pi a F_1 (L^{iii} + L^{iv} + L^{v})$$

$$L^{v}=0$$

$$L_1^{iii} = \lim[\ln(\rho)]^{-1} * \frac{Y_1(\rho a)}{\rho a} \{ \sigma a J_0(\sigma a) - 2J_1(\sigma a) \}^*$$

$$\Big[-(\beta_0+\beta)\omega\epsilon_0 + (\beta_0+\beta)(n^2-1)k^2\beta G/F/\sigma^2 +$$

$$(k^2+\beta_0\beta)\left\{2J_1(\rho a)/\rho a\right\}\left\{\beta/\omega\mu\right\}\left\{(n^2-1)k^2/\sigma^2\right\}$$

$$-(k^2+\beta_0\beta)\left\{2J_1(\rho a)/\rho a\right\} G/F$$

$$L_1^{iii} = -2/\pi a^2 * [\,\sigma_0 a J_0(\sigma_0 a) - 2J_1(\sigma_0 a)\,] * \{\,L_1^{vi} + L_1^{vii}\,\}$$

$$L_1^{vi} = \lim_{\beta \Rightarrow k} \frac{(k^2+\beta_0\beta)\,[2J_1(\rho a)/\rho a]\,[(n^2-1)k^2/\sigma^2]\,[\beta/\omega\mu] - (\beta_0+\beta)\omega\epsilon_0}{\rho^2 \ln(\rho)}$$

$$L_1^{vi} = 0$$

$$L_1^{vii} = \lim_{\beta \Rightarrow k} \frac{(\beta_0+\beta)(n^2-1)k^2/\sigma^2\ \beta\ G/F - (k^2+\beta_0\beta)\ G/F\ [2J_1(\rho a)/\rho a]}{\rho^2 \ln(\rho)}$$

$$L_1^{vii} = 0$$

$$L_1 = .25\ \pi a\ F_1 * \lim_{\beta \Rightarrow k} \frac{Y_0(\rho a)}{\ln(\rho)} *$$

$$\{\quad (\beta_0+\beta)\omega\epsilon_0[\,\sigma a J_0(\sigma a) - J_1(\sigma a)\,]$$

$$+(\beta_0+\beta)\omega\epsilon_0 * (n^2-1) * k^2/\sigma^2\ \ \beta/\omega\epsilon_0\ G/F\ J_1(\sigma a)$$

$$+(k^2+\beta_0\beta)\ [2J_1(\rho a)/\rho a]\ [\,(n^2-1)k^2/\sigma^2]\ [\beta/\omega\mu]\ J_1(\sigma a)$$

$$+(k^2+\beta_0\beta)\ [2J_1(\rho a)/\ \rho a]\ [(n^2-1)k^2/\sigma^2]\ G/F\ *$$

$$[\,\sigma a J_0(\sigma a) - J_1(\sigma a)\,] \quad \}$$

$L_1 = F_1 a\, \sigma_0 a J_0(\sigma a)\ (\beta_0 + k) k \sqrt{\epsilon_0/\mu}$

$L_2 = -L_1$

$L_3 = F_1\, k\, (\beta_0 + k) \sigma_0 a J_0(\sigma_0 a)\, a$

$L_4 = -L_3$

1988 INSTITUTIONAL MEMBERS

ANTENNA TECHNOLOGIES
6 Shields Dr Box 618
Bennington, VT 05201

NOKIA-MOBIRA
P O Box 86 24101 Salo
Finland

LOCKHEED MISSILES & SPACE CO
Adv Systems Tech Laboratory
3251 Hanover St.
Palo Alto, CA 94304

W RICHARD GREEN & ASSOC.
3200 Wilkinson Rd
Cameron Park, CA 95682

HUNTING ENGINEERING LTD
Redding Wood, Ampthill
Bedford England MK45 2HD

ROSEMONT AEROSPACE
14300 Judicial Rd
Burnsville, MN 55337

TEXAS INSTRUMENTS
2501 W University
P O Box 801/MS 8019
McKinney, TX 75069

KERSHNER, WRIGHT & HAGAMAN
5730 General Washington Dr.
Alexandria, VA 22312

DELFIN SYSTEMS
1349 Moffett Park Dr
Sunnyvale, CA 94089

SCALA ELECTRONIC CORP
P O Box 4580
Medford, OR 97501

HELSINKI UNIV OF TECHNOLOGY
Otakaari 5A Espoo 15
Finland

AWA DEFENCE & AEROSPACE
P O Box 96
North Ryde NSW,
Australia 2113

NEW MEXICO STATE UNIVERSITY
Box 3548/Physics/Science Lab
Las Cruces, NM 88003

TRW
One Space Park
Redondo Beach, CA 90278

CULHAM LABORATORY
UK Atomic Energy Authority
Abingdon Oxfordshire
England OX14 3DB

U.S. AIR FORCE
Base Library Bldg 437
485 EIG/EIEUS
Griffiss, AFB, NY 13441

KATHREIN-WERKE KG
Postfach 260
D-8200 Rosenheim 2
West Germany

OAR CORPORATION
10447 Roselle St.
San Diego, CA 92121

SCIENCE APPLICATIONS INTERNATIONAL CORP
5151 East Broadway, Suite 900
Tucson, AZ 85711

U.S. COAST GUARD
2100 2nd St. SW
Washington, DC 20593-0001

STG NATIONAL LIGHT-EN
Ruimtevvart Laboratorium
1059 CM Amsterdam
Netherlands

TELECOM RESEARCH LABS
770 Blackburn Rd
CLayton, Victoria, Australia 3168

HONEYWELL INC
401 DEFENSE HIGHWAY
Annapolis, MD 21401

IIT RESEARCH INSTITUTE
185 Admiral Cochrane Dr
Annapolis, MD 21401

FORD AEROSPACE
3939 Fabian Way MS T96
Palo Alto, CA 94303

ITT AEROSPACE/OPT DIVISION
P O Box 3700
Ft Wayne, IN 46801

NYNEX CORPORATION
500 Westchester Ave
White Plains, NY 10604

BUSINESS MANAGEMENT SYSTEMS
Sproughton House
Sproughton, Ipswich
Suffolk, England Ip8 3AW

FFV ELEKTRONIK AB
S-351 80 VAXJO
Ljungadalsgatan 2
Sweden 0470-420-0

VISTA RESEARCH
100 View St Box 998
Mountain View, CA 94042

TASC
55 Walkers Brook Dr.
Reading, MA 01867

PILKINGTON
Pilkington Tech Center, L
Lathom, Ormskirk
Lancashire, England L40-SUF

TCI
1625 Stierlin Rd
Mountain View, CA 94043

TELEX COMMUNICATIONS INC.
8601 Northeast Hwy 6
Lincoln, NE 68505

ROCKWELL INTERNATIONAL
1745 Jeff Davis Hwy, Suite 1
Arlington, VA 22202

KATHREIN INCORPORATED
26100 Brush Ave, Suite 319
Euclid, OH 44132

I.D.S. INGEGNERIA SISTEMI
Via Roma 50
Pisa, Italy 56100

CELWAVE RF
Frejasvey 30
Hillerod, Denmark 3400

MIT, LINCOLN LAB
P.O. Box 73
Lexington, MA 02173-0073

FGAN/FHP
Neuenahrer Str. 20
Wachtberg-Werthoven
W Germany, D5307

GEORGIA INSTITUTE OF TECHNOLOGY
GTRI/ECSL/ERB Bldg, Rm 242
Atlanta, GA 30332

RADIO FREQUENCY SYSTEM
AUSTRALIA PTY LTD.
Box 191 Croydon
Victoria, Croydon, Australia 3136

SRI International

SRI INTERNATIONAL is one of the largest research, development and consulting organizations with a human resource base composed of over 110 disciplines. Our activities focus around contracted projects with our client base which includes domestic and international businesses and governments. Our unique environment encourages substantial individual contribution as well as team activities based on our matrix organization.

The Engineering Research Group at SRI is looking for experienced individuals at the Bachelors, Masters and PhD levels for technical and technical management positions in any one of the following areas:

Research and Development at SRI International

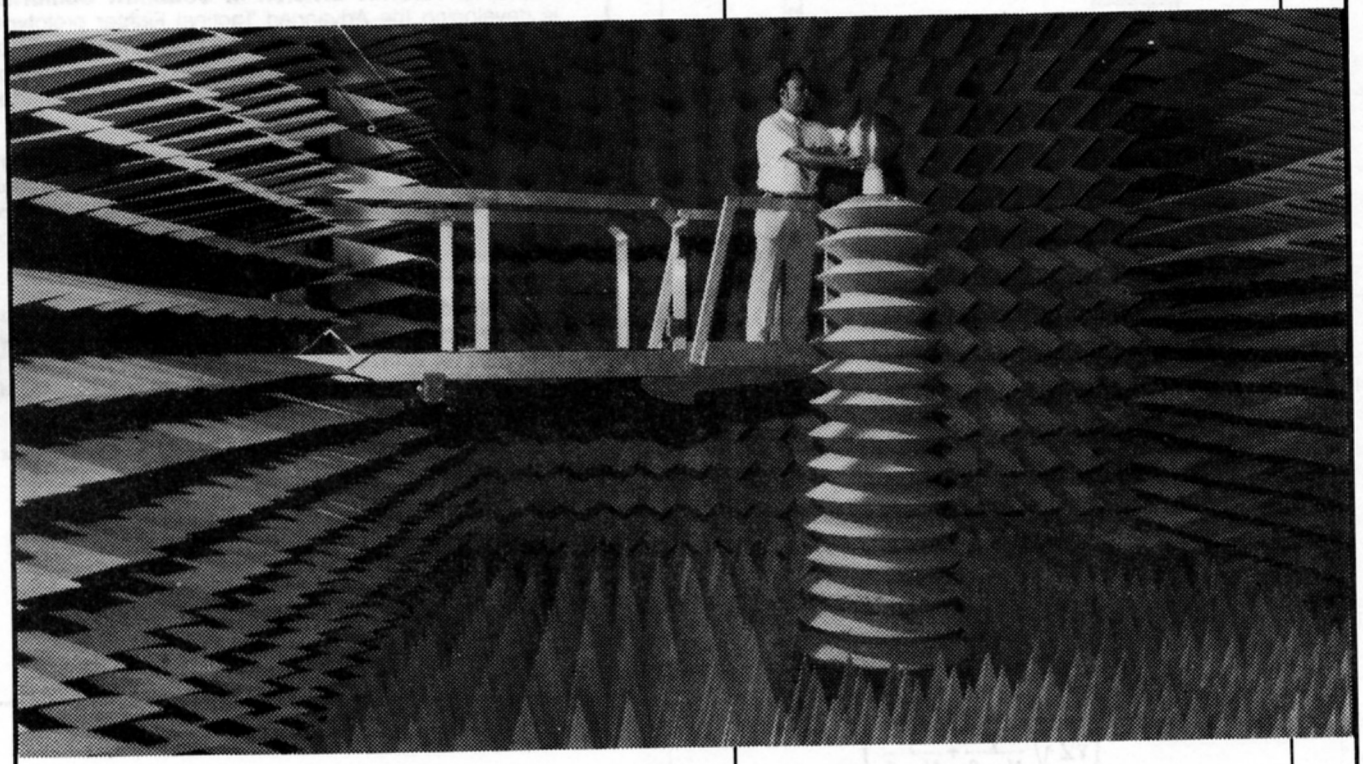

- ***Radar Cross Section***
- ***Image Processing***
- ***Systems Analysis***
- ***Over-the-Horizon Radar***
- ***Electromagnetic Modeling***

A technician adjusts a calibration sphere in our Anechoic chamber prior to tests for RCS measurements. The chamber is utilized for a variety of research projects.

For immediate consideration, please send resume to Michael Patrick, Professional Staffing, Engineering Research Group, Dept. ACE-1288, SRI INTERNATIONAL, 333 Ravenswood Avenue, Menlo Park, CA 94025. An equal opportunity employer. U.S. Citizenship required.

Equations Made Easy

with

Expressionist 2.0

For the Macintosh

The Personal Mathematical Equation Editor

"An excellent toolkit that all technical people should have..."
– Jean Louis Gassée, President, Apple Computer, Inc.

1.) Select the DA ...

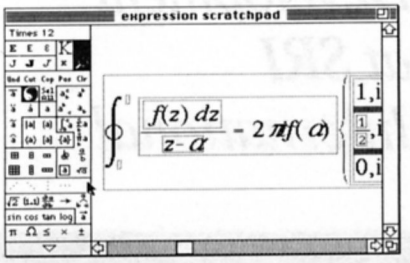

2.) Create your equation ...

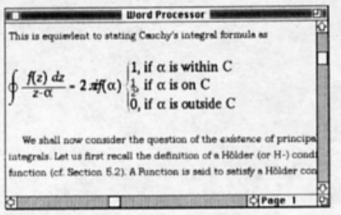

3.) Copy & paste into your word processor!

and get

Results like this:

$$\nabla^2 \mathbf{E} - \frac{\mu\varepsilon}{c^2}\frac{\partial^2 \mathbf{E}}{\partial t^2} = 0$$

$$\nabla^2 \mathbf{B} - \frac{\mu\varepsilon}{c^2}\frac{\partial^2 \mathbf{B}}{\partial t^2} = 0$$

$$\operatorname{erfc}\left(\frac{|z_1 - z_2|}{\sqrt{2}\sqrt{\frac{1}{N_1 - 3} + \frac{1}{N_2 - 3}}}\right)$$

$$f_o(z) = \frac{1}{2\pi i}\int_C \frac{u_o(z')\,dz'}{(z' - z)}$$

Send $129.95 for the complete package, or for a brochure and FREE Demo disk write to:

allan bonadio associates
814 Castro Street #110
San Francisco, CA 94114
(415) 282-5864

Aircraft Division

ELECTROMAGNETIC SPECIALIST

Northrop Aircraft Division in Southern California is developing the Advanced Tactical Fighter prototype. Our Electromagnetic Engineering Department is investigating special designs of RF antenna and sensor, as well as communications components for Advanced Tactical Aircraft applications.

Develop prediction tools for low observable antenna and radome design, integrating scattering prediction techniques and antenna analysis methods. Advanced degree and 5+ years electromagnetic design experience preferred.

For immediate consideration, please forward your resume including daytime phone number (discretion assured) to: Gloria Daniels, NORTHROP AIRCRAFT DIVISION, Technical Staffing, P.O. Box 2282, Dept. 1222/AJ, ACE/1931, Hawthorne, CA 90251-2282.

U.S. CITIZENSHIP REQUIRED. Northrop is an Equal Opportunity Employer M/F/H/V.

NORTHROP

Electronics Division
Electronics Systems Group